Understanding and exploiting metrological fiber networks for Sagnac sensing, frequency dissemination and geosensing

Mads Bebe Krog Tønnes

PSL UNIVERSITÉ PARIS

THÈSE DE DOCTORAT
DE L'UNIVERSITÉ PSL

Préparée à l'Observatoire de Paris
au Laboratoire Systèmes de référence Temps-Espace

Understanding and exploiting metrological fiber networks for Sagnac sensing, frequency dissemination and geosensing

Soutenue par
MADS BEBE KROG TØNNES

Le 21 novembre 2022

École doctorale nº 564
Physique en Île-de-France

Spécialité
Physique

Composition du jury :

Pascale DEFRAIGNE Professeur, ORB	Rapporteuse
François VERNOTTE Professeur, UFC	Rapporteur
Cecilia CLIVATI Chercheuse, INRIM	Examinatrice
Carlo SIRTORI Professeur, PSL-ENS	Examinateur
Anne AMY-KLEIN Professeur, USPN	Invitée
Paul-Éric POTTIE Ingénieur, PSL-OP	Encadrant de thèse
Sébastien BIZE Chercheur, PSL-OP	Directeur de thèse

l'Observatoire de Paris | PSL

Acknowledgements

I have now been at SYRTE for a little more than four years, which includes one year of master's thesis and three years of PhD. This has been an amazing experience which I will never forget. In a very uncertain time, amazing colleagues and supervisors ensured that I could always make scientific progress, and more importantly that I never felt alone in my work.

First of all I would like to thank my supervisor Paul-Éric Pottie. Doing an experimental thesis during the COVID outbreak was far from trivial, but Paul-Éric managed to steer me and my work in the right directions, so I could finish my thesis on time, even with three months working remotely from Denmark. In a busy schedule he has always prioritized me, both for online meetings or face-to-face discussions. I have felt that he truly cared about me and my work, and how he could send me towards the next step in my career in the best way possible.

I would like to thank my closest colleagues, the fiber link team at SYRTE, which has changed during my PhD: Etienne Cantin, who patiently taught me a lot, especially in my first year. This includes both physics, as well as where to find the best Neapolitan restaurants in Paris. I want to thank Dan Xu, who I worked closely with in the laboratory, and who likewise taught me a lot when I first started. I have enjoyed my close work with Maxime Mazouth-Laurol, who I shared office with for large parts of my time at SYRTE, and more importantly our daily talks about football, and Caroline Lim, who together with Maxime acted important support in the stressful ending of my thesis. Furthermore Florian Frank, Eva Bookjans, Phillip Tuckey, Mikkel Ibsen, Jérôme Fils, Hendrix Montalvan Leyva and Florian Dedieu, have constituted an amazing team to work in.

Our close colleagues at LPL, especially Anne Amy-Klein, Olivier Lopez and Christian Chardonnet, deserves a big thank you as well. Anne co-supervised a lot of my work, and has shown me amazing support. She always took time to read my reports, and have meetings to answer my many questions. In the writing of my articles she was invaluable. In this context I would like to thank the rest of the collaborators in the REFIMEVE network, including the colleagues from iXblue (formerly MuQuans).

I would like to thank the optical frequencies group at SYRTE as well, with a special thank you to Sébastien Bize who has directed my thesis. I would like to thank our close colleagues working on the cavities and combs: Rodolphe Le Targat, Hector Álvarez Martínez, Christian Bærentsen, Angélique Lartaux, and Benjamin Pointard. Their collaboration have been invaluable anytime I

would come asking questions about the source signals. Furthermore, Jérôme Lodewyck has been very helpful in the context of comparison campaigns.

The electronic department and mechanical workshop deserves a big thank you as well, with a special mention to Jose Pinto who I worked closely with for a time. Also the IT department, with Pascale Blondé and Maxime Laiguillon, have shown me amazing support when needed. The adminstrative department, with especially Marine Pailler, has likewise been a big help throughout my stay.

A last thank you goes out to our European colleagues at NPL, PTB, and INRIM. Working in such a big colaboratory experiment has been exciting, and they have all been very nice and helpful, answering any questions I had about either the experiments, or the procedures of data sharing.

Contents

List of Figures

List of Tables

Introduction

Time is always ticking, no matter if we measure it or not. Keeping track of time has however always been paramount, as it allows the distinction between night and day, between seasons, and between years. In that sense, time metrology is one of the oldest scientific fields, and has been around just as long as the humans. The definition of time has changed through the ages. Together with six other fundamental units, it is a crucial part of the Système International d'Unités (SI). These units are illustrated in figure 1. The seven fundamental units include the second, meter, kilogram, ampere, kelvin, mole, and candela. Of those seven units, the second is used to define the meter, the ampere, and the candela. Indeed, the second is one of the absolute cornerstones of modern metrology. For hundreds of years, it has been possible to measure the second with clocks. However, as no two clocks will be identical, a synchronization and comparison between different clocks is necessary. Historically, people in the city have been able to synchronize their clocks with transportable watches, or the bells of the churches at noon, to name a few. Modern society runs much faster, with global exchange and mobility at a World scale, accurate synchronization and syntonization, with waves much faster than acoustic waves, are needed. Since the last century or so, with the discovery of radio-transmission (G. Marconi, N. Tesla and others), electromagnetic waves are used to transmit signals, for telecommunication, and comparing clocks around the world.

Clocks can be compared with optical fibers, which is the subject of this thesis. There are many methods that can take benefits of the guided propagation over fiber networks to synchronize and syntonize clocks. Some very widely used processes over the internet synchronizes clocks in computers for the daily life. Here, the subject of this thesis is about ultra-precise state-of-the-art frequency dissemination of optical frequencies.

Here, I describe the use of a new research infrastructure in France for time and frequency dissemination that is a coherent, long-range, optical fiber network

FIGURE 1: Système International d'Unités (SI). Figure from the BIPM website [1].

for clock comparisons, as well as for high-resolution spectroscopy, a wide range of precision measurement, and for geophysical sensing applications. I describe the necessary tools, and an in-depth study, in order to understand the physical properties of the fiber network, which will then be used to determine the uncertainty contribution of fiber links, as well as an exploration of two applications of fiber network for Earth science: a first observation of the Sagnac effect for increasing areas in a fiber link forming a closed loop, where a non-reciprocal phase is expected, and a first study on seismic detection with a fiber network.

I will start with an explanation on the field of time and frequency metrology. I will briefly discuss the advancements of optical atomic clocks, and thereby motivate the need for ultra-stable and accurate time and frequency dissemination tools. I will describe the ensemble of clocks at SYRTE, and briefly introduce the French fiber network REFIMEVE.

In chapter 2, I will explain the basic principles of frequency transfer through fiber links, insisting on the fundamental hypothesis that underlays the operation of the system, and the techniques we apply. I will describe the challenges arising for long-haul fiber links, as well as describe the fundamental limits we face. Lastly, I will describe the fiber links of the REFIMEVE network, that is the name of the French research infrastructure for time and frequency dissemination over the French fiber network for education and research, RENATER.

In the third chapter, I will describe the noise processes of the fiber links, both in the high and low frequency spectrum. I will show how I use these characteristics to simulate the noise of the links, which is a necessary tool when studying the effects of missing data.

In chapter 4, I evaluate the effects arising from missing data in our statistical evaluation of the links. I discuss ways of handling the missing data in detail, and present a novel way in the context of fiber links, based on the noise model elaborated in chapter 3. Then, I use these tools I built for a case study, for the first time evaluating the statistical properties of a fiber link over the span of five years, where missing data are unavoidably present and significant.

In the following chapter, I will discuss the European connections of the REFIMEVE network to Germany, United Kingdom, and Italy, in the context of the clock comparisons such a network allows. I will discuss the challenges we face in the French REFIMEVE network in such a comparison, and how the French links performed. I present an uncertainty budget of the French links for a one-month-long clock comparison campaign. I will end with an evaluation of the links' uncertainty contribution in the presence of missing data, where I will not only consider the missing data from the link itself, but also the downtime of other subsystems in the comparison.

In chapter 6 I will explore the use of fiber links themselves as sensors in 2 different studies. First, I will explain the use of a fiber link enclosing a large area in Paris as a gyrometer, and compare with the situation of a spooled fiber, where the enclosed area is orders of magnitudes smaller. Afterwards, I show a quantitative study of the use of a fiber network to detect seismic waves, arising from earthquakes around the world.

I will end with a conclusion, summarizing the most important points from throughout the thesis.

Chapter 1

Frequency metrology

The principle of an atomic clock as introduced by Essen and Parry at NPL in the early 1950s is to servo-loop the output frequency of a local oscillator to the atomic response [3]. The general sketch of an atomic frequency standards is given in figure 1.1.

The output of a frequency standard has to be a practically usable oscillatory electromagnetic signal whose frequency is connected to the atomic transition.

The output of the frequency standard with a frequency offset and frequency noise, can be written as:

$$\omega(t) = \omega_{ef}(t) \cdot (1 + y(t) + \epsilon), \tag{1.1}$$

where ω_{ef} is the frequency of the atomic transition between the ground state e and the excited state f, $y(t)$ represents the statistical relative frequency fluctuations, and ϵ a systematic shift as compared to the frequency of the atomic transition. In such an expression, one assumes that $y(t)$ is stochastic and has a mean value of $\langle y(t) \rangle = 0$.

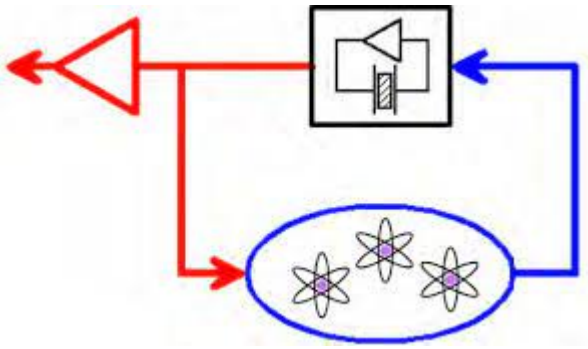

FIGURE 1.1: Principle of an atomic frequency standard. Figure extracted from [2].

The essential properties of atomic frequency standards are therefore its accuracy, which is evaluated quantitatively by its overall uncertainty on ϵ, and its stability, evaluated quantitatively by the statistical properties of $y(t)$. The latter is characterized by its deviation, denoted $\sigma_y(\tau)$, where τ is the integration time.

The relative frequency fluctuations can be expressed as:

$$y = \frac{\delta f}{f_0}$$

where δ_f is the frequency fluctuation over a given measurement time and $f_0 = \omega_{ef}/(2\pi)$. So, if one keeps the same error in the frequency fluctuations, the higher the carrier, the lower is the relative frequency deviations.

The relative frequency fluctuations and its systematic offset are the observables under consideration. The time difference between the realized clock and an ideal realization is simply given by the integral of $(y+\epsilon)$ over the integration time, from an arbitrary initial instant to time T:

$$\Delta t = \int_0^T (y + \epsilon)\ dt$$

If the realization of a frequency standard suffers from systematic bias $\epsilon \neq 0$, the time indicated by the clock will drift, as compared to an ideal realization. Comparing the time difference between two independent atomic clocks over large integration times is therefore a stringent test of their inaccuracies.

The way of realization of a frequency standard over the age is then a resulting trade-off between the fundamental understanding of the laws of physics, available technologies, and some practical considerations, so that the standard can be used by the scientists and the society.

The second has been defined by the rotation of the Earth around itself and/or, the rotation of the Earth around the Sun, with oscillation frequencies of 11.5 µHz, and 31 nHz respectively. For a long time, it was the only universally available regular and periodic phenomena. Besides observing the movement of Earth in Space, manufacturing clocks was essentially a matter of (classical) mechanics, noticeably to help for navigation: this was the case for the famous Harrisson clock, used by the British marines.

The situation drastically changed with the discovery of piezo-electricity and its application to excite crystals. The quartz oscillators were developed, using an oscillator frequency of kHz to GHz, enabling the discovery of time variations in the rotation of the Earth.

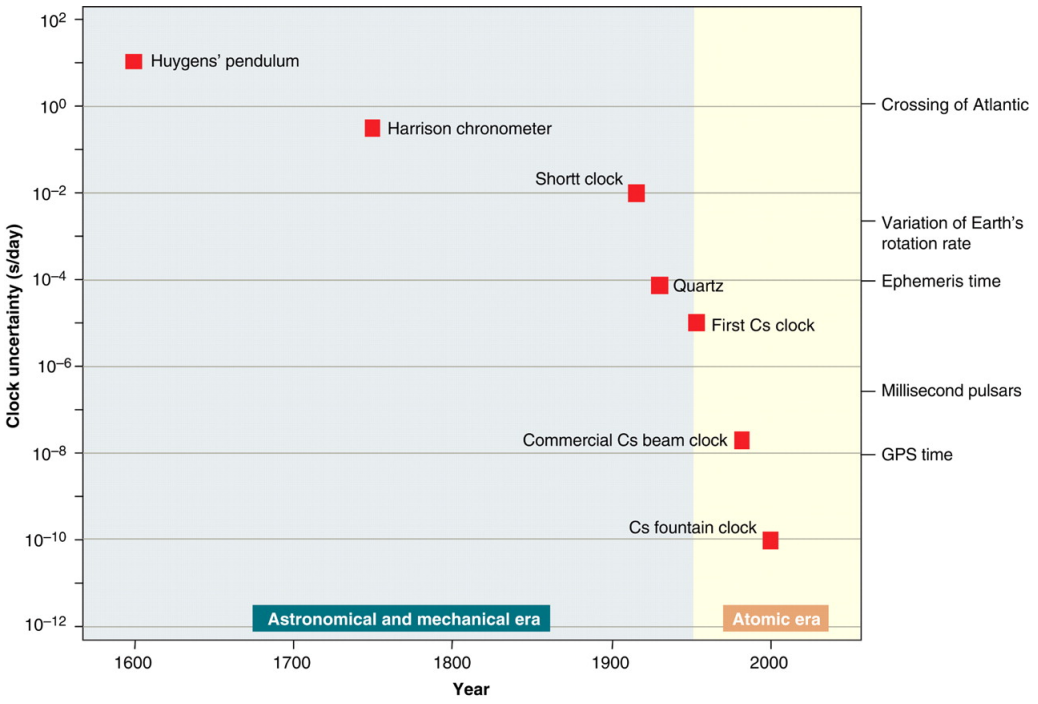

FIGURE 1.2: Improvement of clocks over the last 400 years. Figure extracted from [4].

In the mid-20$^{\text{th}}$ century, the atomic clocks were introduced, with atomic transition frequencies in the GHz range (H-Masers, Cesium, Rubidium...), and nowadays with optical atomic clocks, that servo loops the frequency of laser on atomic transitions, with frequencies at hundreds of THz. Nowadays, there are several atomic species, neutral or with an electric charge, that are operated (Strontium, Mercury, Ytterbium...).

Comparing ultra-precise atomic clocks is therefore a very exciting challenge, for its impact on the realization of atomic time scales and the expected re-definition of the SI second, for tests of fundamental physics that can be performed with an ensemble of atomic clocks co-located or set apart, and its impact in society for cutting-edge research in spectroscopy, astronomy, and telecommunication, to name a few.

1.1 Optical reference signals

1.1.1 Optical clocks

Since the development of the first atomic clock, they have steadily improved over the years. This is illustrated in figure 1.3. The uncertainty of microwave clocks since 1960 is shown in blue, which have reached an uncertainty at the level

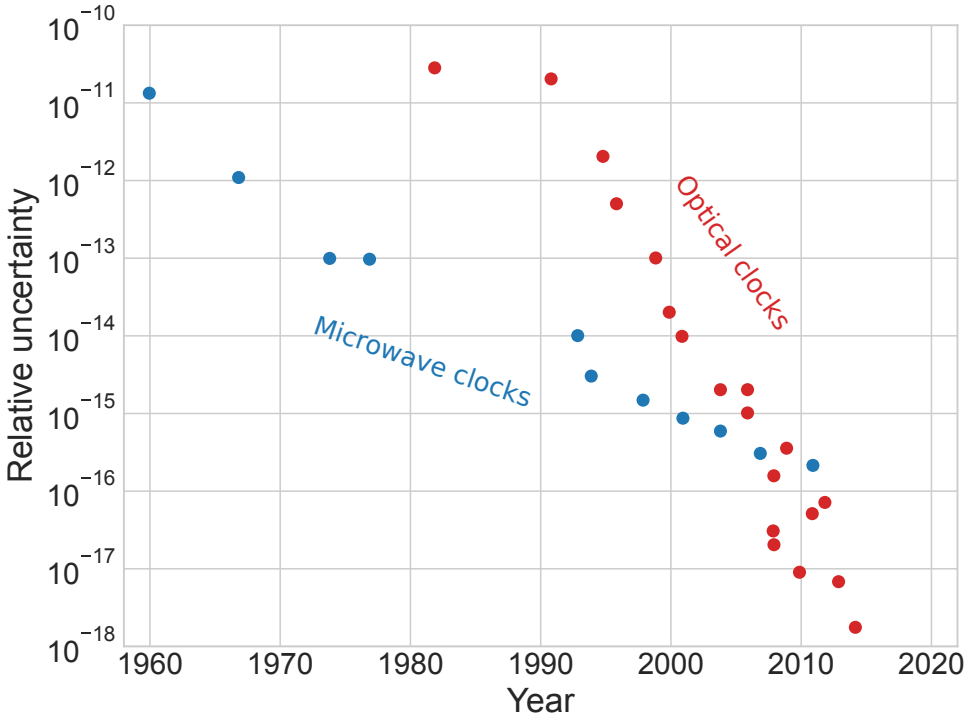

FIGURE 1.3: Decrease in uncertainty of optical and microwave clocks over the last decades. Figure derived from BIPM.

of 10^{-16}. These microwave standards include clocks built on the primary frequency standard of Cs, as well as secondary frequency standards like Rb. Since the introduction of clocks based on optical transitions, the improvements have accelerated, with state-of-the-art optical atomic clocks reaching uncertainties in the low 10^{-18}.

With such orders of magnitudes difference between the current definition of the SI second, and the uncertainty of state-of-the-art optical clocks, work have started towards a redefinition of the SI second. Before such a redefinition can be realized, a number of criteria must be met. In 2016, the Consultative Committee for Time and Frequency (CCTF) defined the following roadmap:

1. Three different optical clocks (either in different laboratories or of different species) but shows a relative uncertainty at the level of $1 \cdot 10^{-18}$.

2. Three independent comparisons of optical clocks, either by transportable clocks or by remote means of comparison, must be realized with a relative uncertainty $< 5 \cdot 10^{-18}$.

3. Regular contributions to International Atomic Time (TAI) from optical clocks.

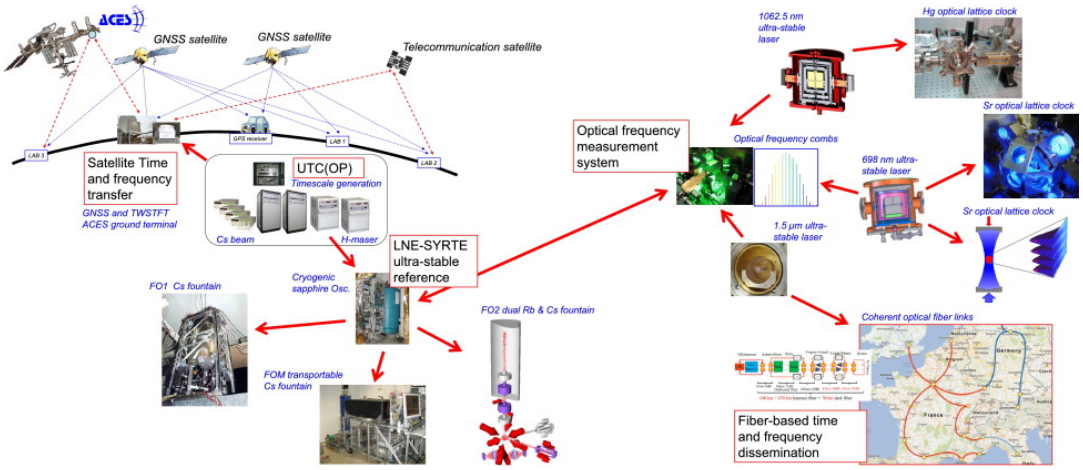

FIGURE 1.4: Overview of the LNE–SYRTE atomic clock ensemble at the Observatoire de Paris. Figure extracted from [5].

4. Comparisons between at least five optical clocks, to the level of $< 5 \cdot 10^{-18}$, with each frequency ratio measured by at least two different, independent laboratories.

It is evident, that the comparison of optical frequency standard is a cornerstone towards the future redefinition of the SI second. In this thesis, I explore such remote comparisons with coherent optical fiber links.

1.1.2 Optical reference signals at LNE-SYRTE

Laboratoire national de métrologie et d'essais (LNE) - Système de Références Temps-Espace (SYRTE) is the French national metrology institute (NMI), and is part of l'Observatoire de Paris. It is here the French national timescale, Coordinated Universal Time (UTC)(OP), is realized. This timescale is realized from the microwave fountain atomic clocks, FO1-Cs and FO2. FO1-Cs is a Cs fountain clock, and FO2 is dual clock, which operates two independent clocks, FO2-Cs and FO2-Rb [6, 7]. FO1-Cs and FO2-Cs are primary frequency standards, and FO2-Rb is a secondary frequency standard based on ^{87}Rb, which represents a secondary representation of the second. Furthermore, an ensemble of optical clocks are operated at SYRTE. These include one Hg clock, two Sr clocks, and a transportable Yb clock which is currently under construction. Several hydrogen masers (H-masers), with excellent long-term stabilities, are used as timekeepers as they are continuous, and one of them is used as the central frequency comparator (*pivot*). A Global Navigation Satellite System (GNSS) connection to the German NMI Physikalisch-Technische Bundesanstalt (PTB) in Braunschweig ensures the comparison of the French frequency standards to

the German pivot institute, from where their contribution to the international atomic timescale TAI is calculated. Around 40-50 % of the total contribution to TAI is generated in Paris. From the TAI, the timescale UTC is calculated by adding leap seconds, corresponding to the decreasing rotation rate of the Earth. Since 1972, 27 leap seconds have been added.

1.2 Remote frequency comparisons

It is possible to compare two clocks simply by physically transporting them to the same location. However, this does not always prove the most convenient method, and it is not straightforward that the clock will keep ticking at the same frequency when transported back to its usual location. As such, remote comparisons are, when viable, an utmost desired solution. With the improvement of optical clocks, as illustrated in figure 1.3, similar advancements were made in the means of remotely comparing the clocks, which are located throughout the world. Microwave frequency standards were, and still are, compared by means of GNSS. Such comparisons of microwave clocks are performed continuously and very reliably. However, with the recent advancements of optical frequency standards, optical means of comparison have likewise become necessary. A mean of comparison which relies on optical frequencies indeed shows the ability to compare state-of-the-art optical frequency standards, without a degradation of the performance of the clocks. These means include optical free-space time and frequency transfer, as well as comparisons through coherent optical fiber cables. The latter is the subject of this thesis.

1.2.1 Optical fiber links

Coherent optical fiber links shows some of the most promising prospects as a remote mean of comparison optical clocks. The development of optical fiber networks has been underway for more than 20 years, and is currently accelerating in Europe and China. In France, this has culminated in the construction and operation of the reseau fibré metrologique à vocation européenne (REFIMEVE) network: currently spanning more than 3 300 km throughout France, as well as ensuring international connections to three neighboring countries, REFIMEVE delivers reliably stabilized optical signals, with a high availability, to a handful of research laboratories. This indeed enables the comparison of optical clocks between four NMIs in Europe, which, as discussed above, is a necessity on the road map towards the future redefinition of the SI second. REFIMEVE also

continuously generates data, from the measurement of the fiber noise that has to be compensated for, and from the assessment of the residual frequency error of the frequency transfer. A large part of my studies used such data acquired by the REFIMEVE network.

Chapter 2

Optical frequency transfer over fiber links

In this chapter, I will start with showing the experimental principles of optical frequency transfer over fiber links. I will discuss some of the challenges in the operation of long-haul fiber links, and which principles we utilize in the REFIMEVE network in order to coherently operate links which are hundreds of kilometers long. Here, I will discuss both technical as well as fundamental limitations.

Afterwards, I will discuss the French REFIMEVE network. I will introduce the different fiber links in the network, and give some general information about them and their operation, before their statistical properties will be analyzed in-depth in chapter 3.

2.1 Principles of optical fiber links

The goal of frequency dissemination is to transfer a frequency from a local to a remote site, while ensuring the smallest possible degradation of the accuracy and stability of the signal. For modern optical fiber networks like REFIMEVE, the requirements of both the accuracy, stability, availability, and evaluations of the signal are high. This has been ensured through many years of development and testing, where the technology has reached a very mature level, with critical systems now being manufactured and operated by industrial partners [8, 9].

2.1.1 Michelson interferometry

The basic principle of an optical fiber link as introduced by Ma et al. in the early 90s [10] is built on the principles of Michelson interferometry [11]. This

is illustrated in figure 2.1. A coherent light source is coupled into the interfer-

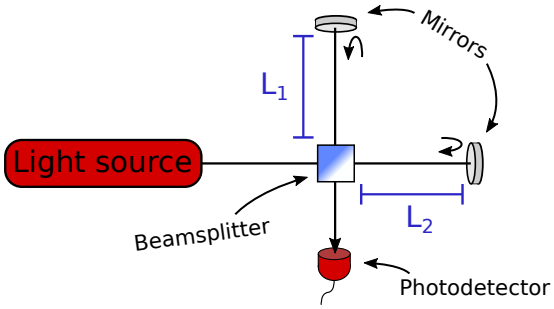

FIGURE 2.1: Illustration of a Michelson interferometer.

ometer. Using a beamsplitter, the light is separated in two beams. Each of the two signals travels an optical length of L_1 or L_2. Mirrors reflect the light, which travels back through the same path, and gets combined on a photodetector. If the optical distance the light travels in the arms, of $2L_1$ and $2L_2$, is shorter than the coherence length of the light source, an interference pattern will be detected by the photodetector. This interference pattern will vary if the length of either arm changes. These principles are widely used for many detectors. For instance, with arm lengths of 4 km, these interferometers are used for large-scale interferometric experiments like Virgo and LIGO, measuring the changes in the optical length due to gravitational waves [12]. For fiber links, the interferometer will be strongly imbalanced. One arm will be in the order of a few centimeters long, and made as stable as possible, while the other arm can be hundreds of kilometers long. This puts a strict requirement on the coherence length of the light source, which must be more than a few thousand kilometers long. In our systems, the polarization is not maintained after propagation in the fiber, as we are using *simple* single-mode fiber. The mitigation strategy consists in employing Faraday mirrors instead of mirror at the ends of the interferometer [13].

2.1.2 Multipath in a fiber

One of the strengths of using the optical fiber to guide the light, is that the path is unambiguous. This means that for an ideal optical fiber, there is only one path for the light to reach a unique and well localized spot. The arrival time of the light is however not perfectly known, as the effective index of refraction of the fiber is known only at the 0.1 % level. In addition, back reflections in fibers deployed in-field generate ambiguity in the arrival time. Even more stray lights and non-linearities are additional issues that impose a system to lift path ambiguities. Therefore, an acousto-optic modulator (AOM) is placed at the

remote end just before the mirror. This is a crystal in which the acoustic wave and the optical wave will be summed up. By conservation of the momentum and the energy, one can show that such devices changes the optical frequency of the signal by a very well controlled quantity [14]. This AOM changes the frequency of the signal with a constant value, typically $\sim 40 - 80$ MHz. With AOMs set at the two ends of the fiber link, the light that experiences a round-trip into the fiber will be shifted by exactly twice the sum of the acoustic frequencies, driving the two AOMs. Let's denote this frequency shift f_b. Generating the beat note between the local laser field experiencing a round-trip in the short arm, and the traveling laser field in the long arm, using a heterodyne detection technique, one obtains a complex frequency spectra, but where the beat-note found at f_b corresponds uniquely to the light that experiences the full round-trip in the long arm. In practice, this frequency shift enables the distinction between the light which has traveled twice through the AOM, and has experienced twice the fixed, known frequency shift, and the light which arrives at the photodetector from reflections and back-scattering.

The ultra-stable signal, which has traveled back and forth in the interferometer, can be written of the form [15]

$$V(t) = [V_0 + \epsilon(t)] \sin\left(2\pi\nu_0 t + \phi\left(t\right)\right),$$

with V_0 being the nominal amplitude, and $\epsilon(t)$ being the amplitude variation of the signal. The nominal frequency, ν_0, is at 194.4 THz throughout the network. The phase variation $\phi(t)$ can be written as

$$\phi(t) = 2\pi\nu(t)\tau_D(t),$$

with the propagation delay of the signal in the long arm of the interferometer

$$\tau_D(t) = \frac{n(t)L(t)}{c},$$

where $n(t)$ is the refractive index of the fiber, and c is the speed of light in vacuum. The derivative of the phase, being the frequency variation, can be written as the sum

$$\frac{d\phi(t)}{dt} = 2\pi\frac{d\nu(t)}{dt}\tau_D + 2\pi\nu(t)\frac{d\tau_D(t)}{dt}.$$

The first term, $2\pi\frac{d\nu(t)}{dt}\tau_D$, describes the variation of the frequency of the signal source. The second term, $2\pi\nu(t)\frac{d\tau_D}{dt}$, describes the variation of the delay in the

fiber, corresponding to a time-dependent Doppler-shift. Assuming reciprocity of the path, the fiber delay of the signal traveling back and forth in the fiber, $\tau_D^{\rightarrow}$ and $\tau_D^{\leftarrow}$, will be the same:

$$\tau_D = \tau_D^{\rightarrow} + \tau_D^{\leftarrow} = 2\tau_D^{\rightarrow} = 2\tau_D^{\leftarrow}.$$

The assumption of reciprocity of the path, and to which extent it holds true, will be discussed throughout this manuscript, as this indeed can lead to sources of error.

Detection At the photodetector, the light is detected with *self-heterodyne beat note detection*: the light from the short arm is combined with the light from the long arm. Assuming that the polarization of the two signals are parallel when arriving at the photodetector, the intensity measured by the photodetector is given by

$$I(t) = \frac{V_{0,1}^2}{2} + \frac{V_{0,2}^2}{2} + V_{0,1}V_{0,2}\cos\left(2\pi\left(\nu_1(t) - \nu_2(t)\right)t\right), \tag{2.1}$$

with $V_{0,1}$ and $V_{0,2}$ denoting the amplitudes, and

$$\nu_1(t) = \nu_0 + \frac{1}{2\pi}\frac{d\phi_1(t)}{dt}$$
$$\nu_2(t) = \nu_0 + \frac{1}{2\pi}\frac{d\phi_2(t)}{dt}.$$

Here, $\phi_1(t)$ and $\phi_2(t)$ corresponds to the perceived phase fluctuations from the optical paths 1 and 2 respectively. In equation 2.1, I have discarded any terms consisting of $\cos(\nu_1)$, $\cos(\nu_2)$ and $\cos(\nu_1 + \nu_2)$, as these frequencies are of the order of THz, which is too high to be detected by the photodetector. The beat note at the frequency $\nu_1 - \nu_2$ will typically be in the order of tens of MHz, and since it is self-heterodyne, any common noise will be canceled.

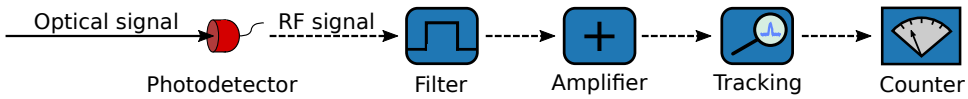

FIGURE 2.2: Illustration of the electronic radio frequency (RF) chain used to measure the fiber link signal: after detection by the photodetector, the signal is filtered, amplified, and tracked, before it is measured by the frequency counter.

Figure 2.2 illustrates the electronic radio frequency (RF) chain of the detection. The signal from the photodetector will be very small, around -50 dBm or even lower. It will have a poor signal-to-noise ratio (SNR), and there will

be many spurious signals with a similar frequency. Therefore, the RF signal is filtered, amplified, and tracked, with a tracking bandwidth typically between 10 kHz - 100 kHz. This allows a measurement of the frequency of the signal by a dead-time free frequency counter. The signals of the links are often recorded with counters both operated in Λ and Π mode [16], but unless stated otherwise, I will assume Λ-counted data throughout this manuscript. Technicalities of the counters are discussed further in chapter 5.3.

2.1.3 Fundamental limits of a fiber link

In the back-and-forth path in the long arm in the interferometer, reciprocal fiber noise is assumed. This is however not strictly the case, as non-reciprocal effects like the Sagnac effect will be present. These non-reciprocal effects will affect counter-propagating signals differently, even if they share the same fiber at the same time. The Sagnac effect is studied in chapter 6.1.

The most limiting fundamental limit of fiber links arise from the finite propagation time of the light in the fiber. This limit arises if one wishes to use the signal, which has traveled to one end of the fiber and back, for any type of compensation. Specifically, any perturbations faster than four times the propagation delay of the light, $4\tau_D$ [17, 18], can not be compensated. The travel path back and forth in the fiber, between a local and a remote site, is illustrated by the red and red/green arrows in figure 2.3. This finite propagation time furthermore limits the possible loop gain, as first shown in [17]. For a fiber link with a fiber noise density $S_{\text{free}}(f)$, and propagation delay τ_D, the limit of compensation using a feedback loop is given by [17]

$$S_{\text{ANC}}(f) = \frac{(2\pi f \tau_D)^2}{3} S_{\text{free}}(f), \tag{2.2}$$

for any frequencies $f < 1/(4\tau_D)$.

A different scheme can be considered, where light is, at the same time, sent from the local to the remote laboratory, and from the remote to the local laboratory. This is illustrated by the green and red/green arrows in figure 2.3. Since this scheme only requires half the travel time of the signal, assuming perfect synchronization between the two laboratories, the limit above can be improved by a factor 4 [19, 20]:

$$S_{\text{TW}}(f) = \frac{(2\pi f \tau_D)^2}{12} S_{\text{free}}(f). \tag{2.3}$$

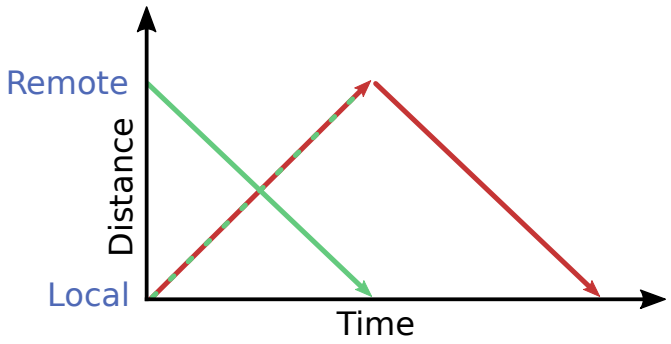

FIGURE 2.3: Illustrative comparison between travel times of signals in a fiber, in an active compensation scheme (red and red/green arrows), and a two-way scheme (green and red/green arrows). Plot derived from Claudio Calosso.

Doing a two-way (TW) comparison on actively compensated links does however not bring additional noise compression [21] Below, I will give examples of both types of schemes, and how they are implemented in the REFIMEVE network.

2.1.4 Active noise compensation

Along the path of the fiber link, the phase of the light will undergo Doppler shifts from any changes in the optical path length, or equivalently changed in the fiber delay τ_D, as discussed above. These changes primarily arise from acoustic perturbations, but also from temperature and humidity variations. To ensure a phase-coherent dissemination of the light at a remote site, an active noise compensation (ANC) is applied to the signal. This scheme is illustrated in figure 2.4.

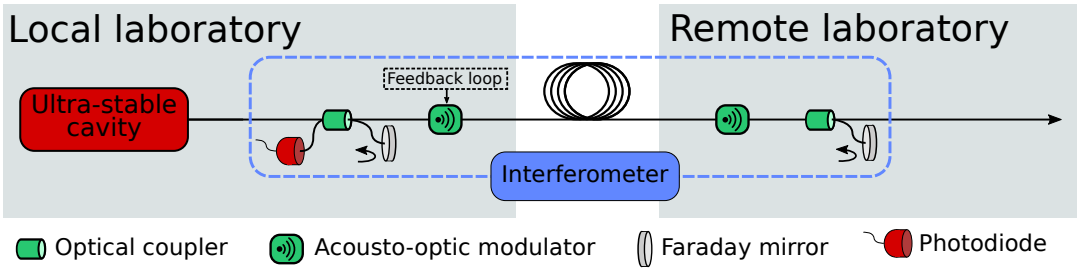

FIGURE 2.4: Illustration of active noise compensation of a fiber link. Ultra-stable light is coupled into the interferometer. At the remote end, part of the signal will get reflected back by a Faraday mirror, which is used to apply a correction to the signal using a feedback loop.

The ultra-stable laser light is coupled into the interferometer, indicated by the blue region in figure 2.4. For fibered interferometers, optical couplers are used in place of the beamsplitter shown in figure 2.1. At the local end, the

frequency difference measured by the photodiode will correspond to the Doppler broadening of the light, which has traveled to the remote laboratory and back. This signal is called the *round-trip* signal, and represents twice the noise of the fiber link. Using an AOM placed at the local site as an actuator, a feedback loop stabilizes the phase of the signal, compensating continuously for the Doppler broadening. As the signal is stabilized by the phase, which is called a phase locked loop (PLL), it ensures the phase coherence of the fiber link. For frequency changes slower than $1/(4\tau_D)$, the beat note measured at the photodiode will be

$$\nu_{\text{beat}}(t) = \frac{1}{\pi}\frac{d\phi_{\text{link}}(t)}{dt} + 2\left(\nu_{\text{AOM}}^{\text{local}} + \nu_{\text{corr}}(t)\right) + \nu_{\text{AOM}}^{\text{remote}}, \tag{2.4}$$

where $\nu_{\text{AOM}}^{\text{local}}$ and $\nu_{\text{AOM}}^{\text{remote}}$ are the fixed frequencies of the local and remote AOMs respectively, and $\phi_{\text{link}}(t)$ is the phase perturbations induced by the noise of the link. Here it has been assumed that the noise experienced by the light will be reciprocal. $\nu_{\text{corr}}(t)$ is the correction applied by the PLL, which will be $\nu_{\text{corr}}(t) = -\frac{1}{2\pi}\frac{d\phi_{\text{link}}(t)}{dt}$, ensuring a complete compensation of the noise, under the two conditions:

1. the noise processes are slower than $4\tau_D$, and
2. the noise is reciprocal.

Noise processes that does not apply to any of the two conditions will either not be compensated at all, or only partially compensated. Under these conditions, the frequency of the signal at the remote end will be $\nu_{\text{USC}} + \nu_{\text{AOM}}^{\text{local}} + \nu_{\text{AOM}}^{\text{remote}}$, with ν_{USC} being the frequency of the local ultra-stable cavity.

2.1.5 Passive noise compensation

While ANC ensures the quality of a disseminated signal, one can alternatively apply passive noise compensation schemes. One such scheme is the TW technique [19, 22]. This can be useful for the comparison of two separated oscillators, by applying the correction in post-processing instead of on the signal itself. The technique is valid as long as the emission time from the two ends is synchronous [23]. The two approaches may have different strengths and weaknesses, depending on the application. In practice, it can be useful to use a combination of the two approaches. Hybrid approaches have been investigated [24].

Figure 2.5 illustrates a TW comparison setup. Two ultra-stable cavities are placed in independent laboratories, separated by an optical fiber. Similar to in the ANC setup, AOMs with a fixed frequency are placed at each laboratory, to

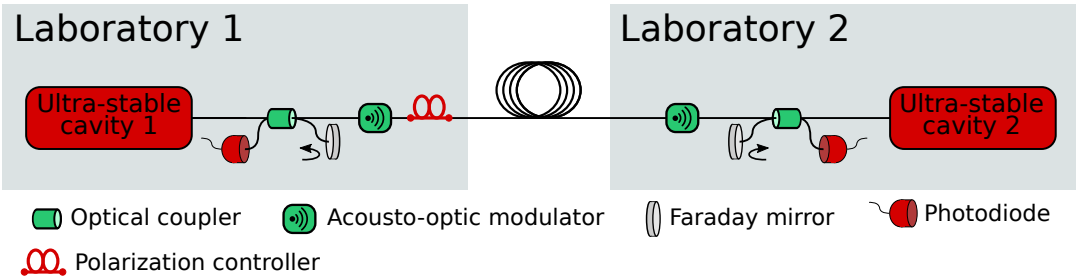

FIGURE 2.5: Illustration of a two-way comparison scheme, between two ultra-stable cavities. Separate beat notes are measured at each laboratory, which can be combined in post-processing.

be able to tell the disseminated light from reflections and back-scatterings. An interferometer is placed in each laboratory, enabling a beat note measurement between the local signal and the signal arriving from the other end. A polarization controller is needed in one end, enabling the adjustment of the polarization of the signal, ensuring an optical beat note amplitude at both ends. The two photodetectors, at laboratory $\#1$ and $\#2$, measures the signals:

$$\nu^1_{\mathrm{PD}}(t) = \nu^1_{\mathrm{USC}}(t) - \left(\nu^2_{\mathrm{USC}}(t) + \frac{1}{2\pi}\frac{d\phi_{\mathrm{link}}(t)}{dt}\right) \text{ and}$$
$$\nu^2_{\mathrm{PD}}(t) = \nu^2_{\mathrm{USC}}(t) - \left(\nu^1_{\mathrm{USC}}(t) + \frac{1}{2\pi}\frac{d\phi_{\mathrm{link}}(t)}{dt}\right)$$

respectively, assuming reciprocal link noise. Assuming perfect synchronization between the two laboratories, one can in post-processing either obtain an evaluation of (twice) the noise of the fiber link:

$$\nu^1_{\mathrm{PD}}(t) + \nu^2_{\mathrm{PD}}(t) = -\frac{1}{\pi}\frac{d\phi_{\mathrm{link}}(t)}{dt}, \tag{2.5}$$

or (twice) a comparison of the two cavities:

$$\nu^1_{\mathrm{PD}}(t) - \nu^2_{\mathrm{PD}}(t) = 2\left(\nu^1_{\mathrm{USC}}(t) - \nu^2_{\mathrm{USC}}(t)\right). \tag{2.6}$$

Since the TW comparison is passive noise compensation, there is no feedback or gain, which is equivalent to en infinite impedance between the two compared systems.

2.1.6 Evaluation of the disseminated signal

For users of a fiber network, it is paramount to have an evaluation of the disseminated frequency signal. This allows users to access the performance of the

link at any time, allowing them an uncertainty evaluation for their experiments. This is likewise essential for the comparison of optical clocks using a fiber network, where a strict uncertainty evaluation of the fiber link is needed at any given time. This is discussed in chapter 5.3. In the REFIMEVE network, this evaluation is ensured by the end-to-end (E2E) measurement, which is illustrated in figure 2.6. Part of the signal disseminated from the local to the remote labo-

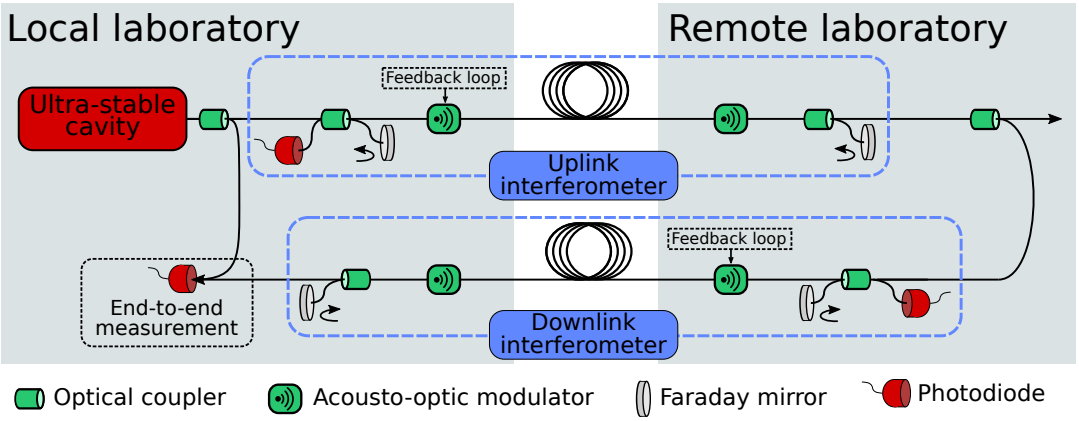

FIGURE 2.6: Illustration of the experimental setup required to perform the end-to-end measurement. This is twice the setup illustrated in figure 2.4, one for the uplink signal, and one for the downlink signal.

ratory, called the uplink signal, is looped back in an identical ANC scheme, as the one illustrated in figure 2.4. This requires a second, parallel fiber. As the telecommunication industry uses two parallel fibers in a unidirectional configuration, cable providers often rent out fibers in pairs. This means the two fibers will be part of the same fiber bundle.

The signal which is disseminated from the remote to the local laboratory, is measured against the local laser light, using a photodetector. This is the E2E beat note, which provides an out-of-loop evaluation of the disseminated signal. Unless stated otherwise, I will be referring to the E2E signal, when discussing the signal of a fiber link throughout this manuscript.

2.1.7 Technical limitations

Several technical limitations can deteriorate the quality of the disseminated signal, in the case of an actively compensated fiber link, or a comparison of cavities using the TW method.

Temperature and humidity variations A number of studies have shown that temperature variations can limit the performance of a fiber link on longer

timescales [21, 25, 26]. This arises from interferometric noise induced to the phase of the signal in the short arm of the interferometer, which by construction will not be actively compensated. However, With a record of the temperature variations inside the interferometer, it is possible to apply a correction in post-processing [25]. More recently, it was found that humidity variations induces a similar perturbation to the phase of the signal [27]. These effects can be reduced by using a free-space interferometer, which will be less sensitive to temperature and humidity variations as compared to a fibered one [28]. Furthermore, increasing isolation of the interferometer will reduce its sensibility. Work has also gone into interferometers with integrated optics [29].

Polarization asymmetry Due to polarization mode dispersion, a single-mode optical fiber will not be functioning strictly as single-mode. A second mode will arise from birefringence, as different parts of the fiber will be experiencing different levels of stress. This effect can occur by a simple bend in the fiber cable, and induces an asymmetry, which the polarization of the light is especially sensitive to [27]. In optical fiber links, we mitigate this effect by using Faraday mirrors, that guarantees that the light that retraces its path back is always orthogonal to the entrance state. In that case, the propagation delay is different in the two propagation directions, but the fluctuations of the difference of the propagation delays is much smaller and compatible with uncertainty at the 10^{-20} level (see below). One method of reducing this effect is by actively scrambling the polarization of the signal, averaging out the asymmetric effect [30].

2.2 Long-haul fiber links

In the following, I will describe some of the challenges arising when constructing long-haul fiber links. I will try to give a sense of the practical range limitations, with the different hardware and techniques employed in the REFIMEVE network.

For frequencies below a cutoff frequency [17], typically around 10-100 Hz depending on the link, the noise of an uncompensated fiber link consists mainly of white frequency noise. This noise level is roughly linearly proportional with the length of the link [17]. The level of white frequency noise of the uncompensated fiber links is shown in figure 2.7, for the *first spans* of the five links in the REFIMEVE network. These links are introduced in chapter 2.3. A black dotted line shows a fit to the linear function $b_{-2}(L) = \kappa L$, with κ being the

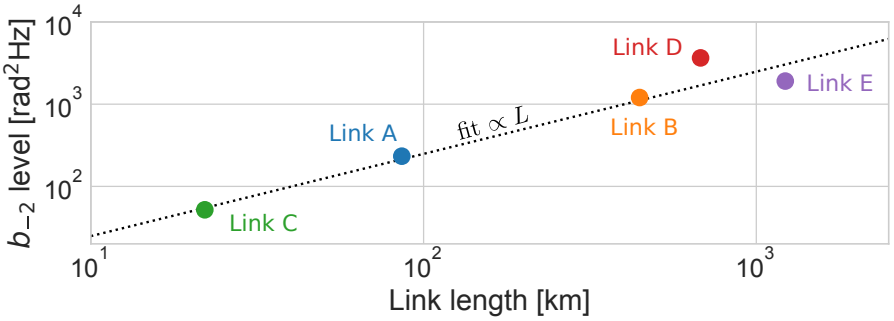

FIGURE 2.7: The level of white frequency noise b_{-2} for the noise of the first spans of the five links in the REFIMEVE network, as a function of their respective lengths L (colored dots). The dotted line shows a fit with slope κL. The links are explained in chapter 2.3.

level of white frequency noise per km fiber link. The expected linear tendency is clear, showing a good agreement with the fit. For the REFIMEVE network, $\kappa \approx 2.5$ rad^{2}Hz/km. This value is similar to values reported previously for optical fiber links around the world [31, 32]. As such, the total amount of noise of the fiber link can be written as a function of the length of the link, in dBm as

$$\mathcal{N} = N_0 + 10\log_{10}(\kappa L f_{\mathrm{BW}}). \tag{2.7}$$

For the tracking bandwidth, I will assume a typical value of $f_{\mathrm{BW}} \sim 10$ kHz, used in the network. The input noise level at SYRTE is estimated at $N_0 \approx -110$ dBm at a 1 Hz bandwidth. Empirically, we have found the amplitude of the signal to typically deteriorate with $\alpha \sim 23$ dB per 100 km, which can be expressed as

$$\mathcal{S} = S_0 - \alpha L,$$

with the initial amplitude of the signal of $S_0 \approx -24$ dBm. From the signal and the noise, the SNR can be calculated as

$$\rho = \mathcal{S} - \mathcal{N}.$$

If the SNR gets too low in the tracking bandwidth, the tracking will fail, which will induce *cycle slips*. Cycle slips in the context of fiber links are discussed further in chapter 3.1. The cycle slips will appear seemingly at random, but their probability, and thus their occurrence frequency, will increase the lower the SNR. The mean time between cycle slips can be calculated by [33]

$$\bar{T} = \frac{\pi^2 \rho}{2 f_{\mathrm{BW}}} \left[I_0\left(\rho\right)\right]^2, \tag{2.8}$$

with $I_0(\cdot)$ being the modified Bessel function of zeroth order.

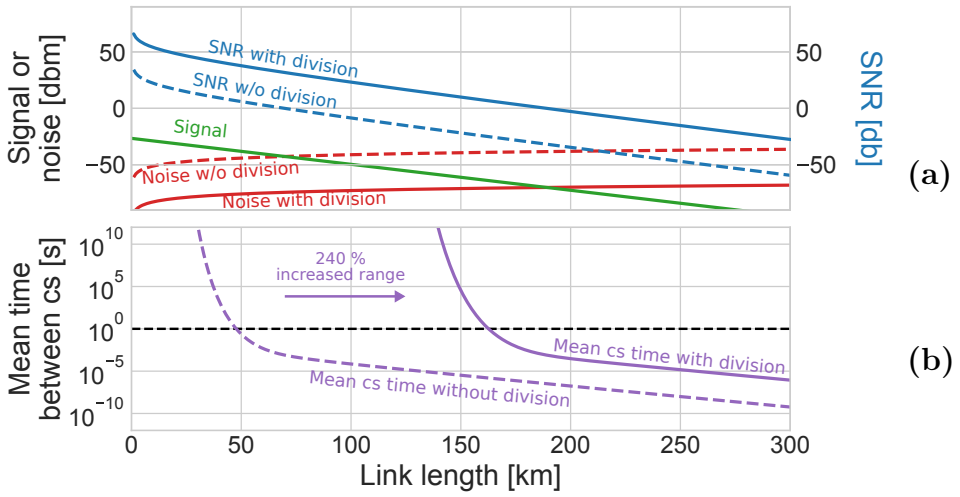

FIGURE 2.8: (a): Signal (green), noise (red), and signal-to-noise ratio (SNR) (blue), in a 1 Hz bandwidth, as a function of the length of a fiber link. (b): Corresponding mean time between cycle slips $\bar{T}$, calculated with the SNRs in (a), by equation 2.8. Dashed lines indicate noise, and corresponding SNR and $\bar{T}$, without a division factor (according to equation 2.7). Continuous lines corresponds to noise which is divided down (equation 2.9).

Figure 2.8(a) shows the signal (green continuous line) and the noise (red dashed line) of a fiber link, as a function of the length of the link. The corresponding SNR is shown as a dashed blue line. The SNR drops linearly with the length of the link, as the linear deterioration of the optical signal with link length, αL, is the most dominating contribution to the decrease in SNR. Figure 2.8(b) shows in the dashed purple curve the corresponding mean time between cycle slips, as calculated by equation 2.8. With a fiber link length larger than ~ 50 km, the mean time between cycle slips drops below 1 s. For this orders-of-magnitudes-study, I define the maximal length of the fiber link, as the length at which the mean time between cycle slips drops below 1 s. With a typical measurement time of $\tau_G = 1$ s, such a case would result in a link only consisting of cycle slips, and it would not be considered operational. Therefore, division of the noise is required for the operation of long-haul links.

2.2.1 Noise division

One way to reduce the amount of noise is to implement a *divider*, which divides the amount of noise with a factor N. With such a divider, the expression of the

noise of the link becomes

$$\mathcal{N} = N_0 + 10\log_{10}(\kappa L f_{\mathrm{BW}}) - 10\log_{10}(N). \tag{2.9}$$

When $N \to \infty$, it is evident that $\rho \to \infty$, and therefore $\bar{T} \to \infty$. So, theoretically, a link can be arbitrarily long, as long as the division of the noise is high enough. I will assume a division factor $N \to 1500$, which is a typical value used for long-haul links in the REFIMEVE network.

The continuous curves in figure 2.8 show the signal, SNR, and mean time between cycle slips, with a noise division of $N = 1500$. This addition to the measurement scheme pushes the limit of the fiber link to $150 - 180$ km, more than tripling the range. Notice that equation 2.8 is not linear with the SNR ρ around $\bar{T} \sim 1$, which makes the length increase of a fiber link as a function of N non-trivial, where doubling the division factor leads to an increase of the possible length of 12 km. Increasing the division factor to 10 000 will is this example barely get the limit of the link above 200 km.

2.2.2 Signal amplification

Several different technologies can be used to amplify the signal in the fiber link. These include Raman amplification, fibre-Brillouin amplifiers (FBAs), which is used in the German fiber network, and erbium-doped fiber amplifiers (EDFAs), which is the technology implemented in the REFIMEVE network[1]. EDFAs are commonly used by the telecommunication industry as well, and is a very mature and reliable technology. As explained in chapter 2.1, the fiber links are bidirectional, and so must the EDFAs be.

On average, one amplifier is installed every 70-100 km of a fiber link. Due to risks of self-oscillations in the fiber link, the gain of the amplifier, β, cannot be set to perfectly match the deterioration of the signal, α. Usually the gain is ~ 15 dB, which corresponds to a net loss of $\alpha - \beta \approx 8$ dB for every 100 km. The amplified signal can be written as

$$\mathcal{S} = S_0 - \alpha L + \beta L,$$

where βL approximates the gain to be continuous, rather than in the form of discrete amplification steps. The noise increases with the amplification as well,

[1] Bi-directional EDFAs of the brand Keopsys by Lumibird is implemented throughout the network.

which ultimately leads to a decrease in the SNR, as

$$\mathcal{N} = N_0 + 10\log_{10}(\kappa L f_{\mathrm{BW}}) - 10\log_{10}(N) + F_{\mathrm{EDFA}} L.$$

The noise figure of the amplifiers is $F_{\mathrm{EDFA}} = 5$ dB, so with one amplifier approximately every 100 km on average, this corresponds to a noise figure of $F_{\mathrm{EDFA}} \approx 5$ dB/100 km.

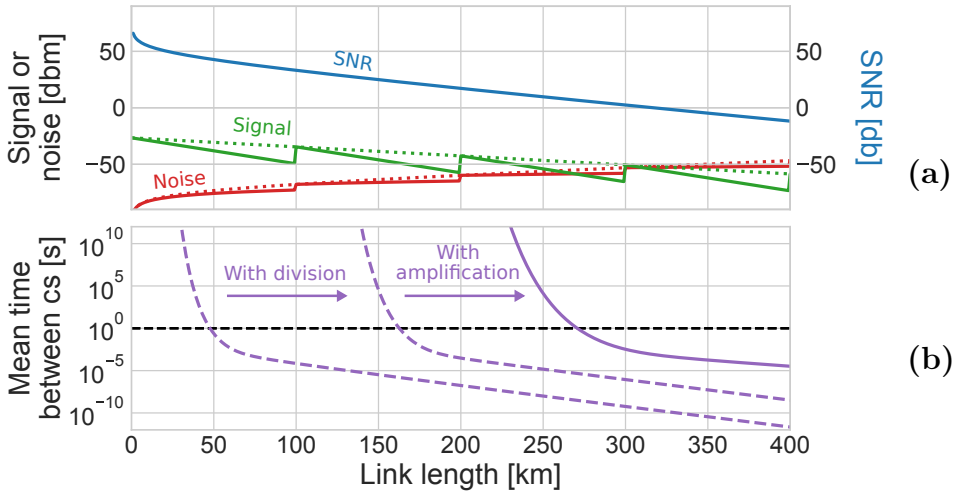

FIGURE 2.9: (a): Signal (green), noise (red), and signal-to-noise ratio (SNR) (blue), in a 1 Hz bandwidth, as a function of the length of a fiber link, with amplifiers along the link. Dotted lines show a continuous approximation of amplifiers, and continuous lines shows the discrete amplification steps. (b): The corresponding mean time between cycle slips $\bar{T}$ of the amplified signal. Dashed lines show $\bar{T}$ for the non-amplified signal, without and with division, also shown in figure 2.8.

The green curve in figure 2.9(a) shows the amplified signal, with the red curve showing the noise of the amplified signal. Dotted curves show the continuous approximations of the amplification, and the continuous curves shows the discrete amplification steps every 100 km. The SNR is calculated from the continuous approximations. As illustrated in figure 2.9(b), the maximal length of the link can be as long as $250 - 300$ km.

2.2.3 Signal regeneration

To further extend the length of the fiber links, the signal needs to be regenerated from a new laser source. In the refimeve network, this is done with repeater laser stations (RLSs) [34] and multi-branch laser stations (MLSs) [28].

The RLS is a type of regeneration terminal that is used throughout the network. These stations effectively *cascade* the fiber link, i.e. splits it up in shorter segments. The RLS has two main objectives:

1. Locking a local diode laser to the received signal, it copies the phase of the ultra-stable REFIMEVE signal for further dissemination, but with the SNR of the local laser [35, 36].

2. It compensates the next segment of the link [34, 37]. By splitting up the compensation of the full link into shorter spans, the loop bandwidth is reduced from the whole link, to the bandwidth of each segment. Two benefits are gained: 1) a higher loop bandwidth means a larger part of the spectrum is compensated, and 2) the limit of compensation, which depends on the length, is increased. This limit is discussed in chapter 2.1.

The RLS has one input, one main output, and a second output with lower power for local dissemination. Therefore, it is used for one-way dissemination of fiber links. The MLS is a kind of RLS, which is able to sustain several links at once, and can be used as network hubs.

The RLS can regenerate the signal to its initial level. However, even the cascaded approach will have a limited range, as the stations will decrease the SNR with an average of $F_{\mathrm{RLS}} \sim 2$ dB/100 km [34]. Here, F_{RLS} includes the regeneration, power attenuation, as well as the increase in fiber noise with the length of the link, κL. As such, the signal and noise can respectively be written as:

$$\begin{aligned} \mathcal{S} &= S_0 \\ \mathcal{N} &= N_0 + F_{\mathrm{RLS}} L - 10 \log_{10}(N). \end{aligned}$$

According to this model, the average signal can be considered constant, since the RLS, unlike the EDFAs, is able to restore the signal amplitude without risks of self-oscillations. With such a regeneration scheme, the maximum length of the fiber link is increased to the order of $1500 - 2000$ km, which is shown in figure 2.10. As seen below, the longest links in the REFIMEVE network are very close to this limit.

These evaluations of the obtainable ranges of a fiber link are heavily parameter dependent. Here, I have shown expected values for hardware and settings employed in the REFIMEVE network, and as such the result above should not be seen as a prediction, that a fiber link can not be above 2000 km long. However, it does indicate that it would probably not be possible to employ a link

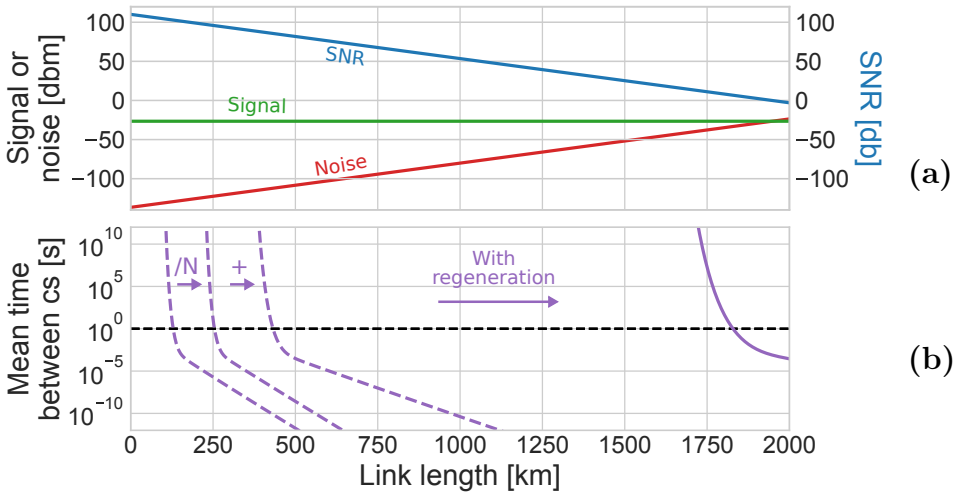

FIGURE 2.10: (a): Signal (green), noise (red), and signal-to-noise ratio (SNR) (blue), at 1 Hz bandwidth, as a function of the length of a fiber link, with repeater laser stations (RLSs) along the link. (b): The corresponding mean time between cycle slips $\bar{T}$ of the regenerated signal. Results of $\bar{T}$ shown in figures 2.8 and 2.9 shown in dashed lines.

between the European west coast and the American east coast, using purely these technologies. Indeed, techniques like intermediate clean-up oscillators, in the form of ultra-stable cavities, would most likely be needed for fiber networks exceeding a European scale.

2.3 The REFIMEVE network

The REFIMEVE network is a French national metrological network [38]. It aims at disseminating ultra-stable optical frequency and time references, through optical fiber cables to more than 30 partner laboratories throughout France, for scientific use such as narrow-linewidth spectroscopy [39]. This fiber infrastructure is shown in figure 2.11, where continuous lines indicate operational links, and dotted lines show links which are yet to be deployed. This has enabled international connections to European partner NMIs, which has enabled the comparison of optical atomic clocks [40], which would otherwise have a limited performance below that of the clocks, through traditional means of comparison with the GNSS. These international connections are shown by continuous blue lines in figure 2.11, which since 2015 includes the German and the English networks, and since 2021 the Italian Quantum Backbone (IQB) [41] (former Italian Link for Frequency and Time (LIFT)). REFIMEVE is a close collaboration between the laboratories SYRTE and Laboratoire de Physique des Lasers (LPL),

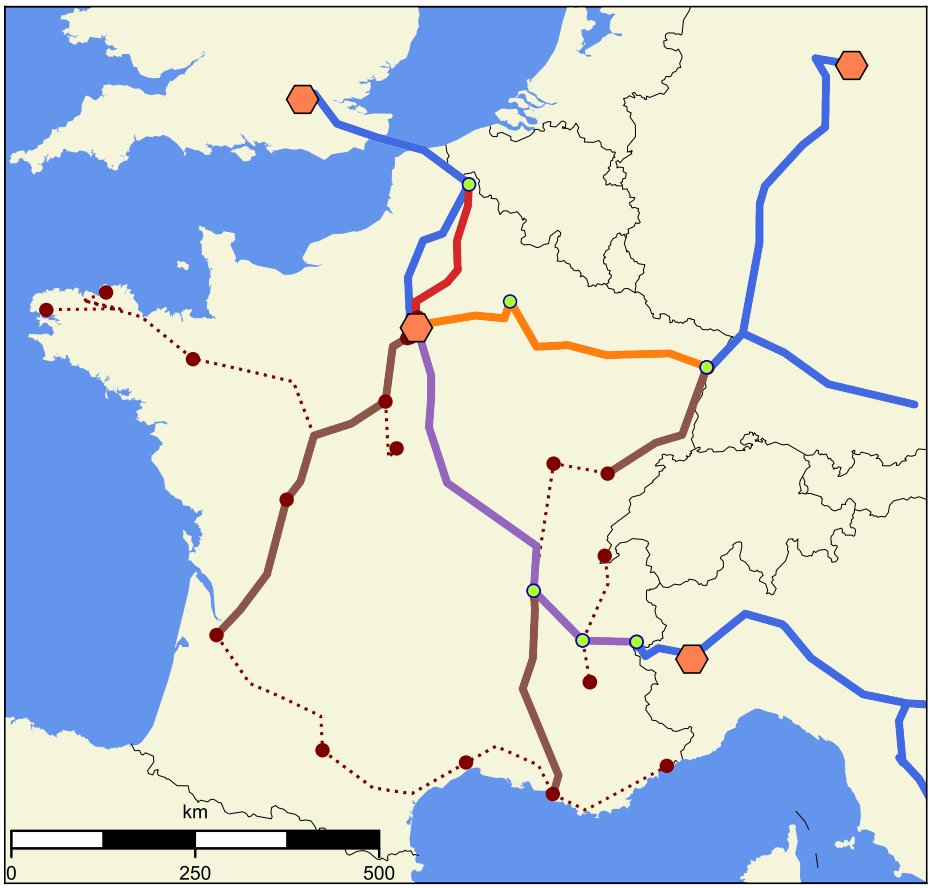

FIGURE 2.11: A map of the REFIMEVE network, including its international connections. Continuous orange, red, and purple lines shows the nationals links B, D and E respectively. Continuous brown lines show other deployed links, which are in operation but not studied in this thesis. Red dotted lines indicates national links which are yet to be deployed. RLSs are indicated by yellow dots along the links. Blue lines show international links and networks, and national metrology institutes (NMIs) are shown by orange hexagons.

and the public organization that operates and manages the national research and education network (NREN), reseau national de télécommunications pour la technologie, l'enseignement et la recherche (RENATER). REFIMEVE was acknowledged as a national research infrastructure in 2021. The ultra-stable frequency signal is realized at SYRTE, from a narrow-linewidth laser locked to an ultra-stable cavity. The cavity is actively dedrifted by an H-maser, which is used as a pivot. Furthermore, as the Paris Observatory realizes the French national timescale, UTC(OP), through an ensemble of primary and secondary frequency standards, the REFIMEVE signal is directly traceable to UTC(OP).

Since 2020, the REFIMEVE project has been expanded to include synchronization delivered with the White Rabbit technology [42]. This service will both be delivered to users of the network, as well as for synchronization of the network itself, which is a vital necessity. This is described in chapter 5.3.

Since the start of the operational network in 2015, five different national links have been deployed. The specifics of links are summarized in table 2.1. In this manuscript, I will be referring to the links by the letters A, B, C, D, and E. I will show many plots of measurements performed on the five links, where I will be consistently using the color code presented here.

	Link A	**Link B**	**Link C**	**Link D**	**Link E**
Length [km]	2×43	2×700	2×11	2×340	2×858
Delay [ms]	0.4	6.6	0.1	3.2	8.0
EDFAs	0	16	0	8	13
RLSs or MLSs	2	5	2	2	7

TABLE 2.1: Information about the five operational links in the REFIMEVE network. The long-haul links B, D and E are shown in figure 2.11 with the same color code. The information includes the length and corresponding time delay of the links, as well as the number of optical amplification steps (erbium-doped fiber amplifiers (EDFAs)), and regeneration steps (a combination of repeater laser stations (RLSs) and multi-branch laser stations (MLSs)).

1. **Link A**: The oldest of the five links, Link A is 2×43 km long, and spans between the laboratories SYRTE in Paris, and LPL in the city of Villetaneuse, North of Paris. Apart from being a testbed for link development [43], and providing a reference for laser stabilization and accurate spectroscopy at LPL [44, 39], the link has been used for the comparison of optical clocks with the English NMI National Physical Laboratory (NPL) in Teddington. The link has been operational in different configurations since 2002, but went out of service in 2020.

2. **Link B**: The oldest of the long-haul fiber links. Link B spans from SYRTE to University of Strasbourg (UoS) in Strasbourg, where it is used for optical clock comparisons with the German NMI PTB [40] in Braunschweig. Before December 2018, the link spanned directly from SYRTE to Reims, and then to Strasbourg. Since then, the link has been split up. The first span, between SYRTE and a data center in Paris called Telehouse2 (TH2), became Link C, and the span between TH2 and Strasbourg remained Link B. The fiber path between TH2 and Strasbourg was also changed in 2021, for a slightly shorter path, as the RENATER network was updating its backbone. In this study Link B is 2×700 km long, and is regenerated by an RLS once in Reims. Nowadays, Link B is 2×650 km long, still regenerated by an RLS once in Reims. The operation of Link A and Link B is described in-depth in [28].

3. **Link C**: Operational since December 2018, Link C is with its 2×11 km the shortest operational fiber link in the REFIMEVE network. Link C is the most critical of all the links, as it provides the ultra-stable reference signal to the MLS in the data center TH2. The links B, D, and E, who all starts at TH2, depends on the signal from this link.

4. **Link D**: 2×340 km long, Link D has since September 2017 spanned from SYRTE to the city of Lille. This link is the first link which was deployed by the company iXblue (formerly µquans), with commercial RLSs that they have developed, following a knowledge transfer from LPL and SYRTE.

5. **Link E**: The newest link in the REFIMEVE network presented in this study [2], and with its length of 2×858 km the longest. The link spans from TH2 to the town Modane, located on the French-Italian alpine border. This link has been operational since March 2020, and enables the comparison of atomic clocks between SYRTE and the Italian NMI Istituto Nazionale di Ricerca Metrologica (INRIM) in Torino [45]. The signal gets regenerated two times between TH2 and Modane: once in Lyon, and once in Grenoble.

All links include at least two RLSs or MLSs: one in the local laboratory, and one in the remote laboratory. As such, the signals from all links gets regenerated at least once, at the remote site.

[2] REFIMEVE have extended to Marseille in 2021 and to Bordeaux in 2022

Chapter 3

Noise processes of coherent fiber links

In the previous chapter, I described the experimental principles of optical frequency dissemination through fibers. I discussed the experimental techniques, as well as the fundamental limits such pose. In this chapter, I will describe the noise processes in optical fiber links, and how to engineer and design a fiber link. Studying all the links in the REFIMEVE network, I will discuss how the advantages and disadvantages of the experimental techniques are seen in the quality of the disseminated signal. I will show how to model the noise of the fiber links, using different statistical tools, and how the noise of the links can be summarized efficiently for future reference and comparison. Knowledge of the noise properties and behavior of the links are essential in the evaluation of uncertainty contribution that a link brings to the disseminated signal. This is important both for users of the ultra-stable reference signal, and for state-of-the-art optical clock comparison. Furthermore, knowledge of the nominal behavior of the links are needed as a reference, if one wishes to use the optical fiber links for sensing geodesic or fundamental physical effects. I will end with discussing how this knowledge can be used to simulate the links, and show a case study of a simulation of a long-haul fiber link.

3.1 Ensuring a phase coherent fiber link

The dissemination of light in coherent optical fiber links is a very well controlled process. Compared to dissemination techniques through air like GNSS techniques, the guiding of the light through a fiber is both less noisy, as well as being reciprocal to a very high degree, as discussed in chapter 2.1. The environmental conditions are however under a smaller degree of control and isolation

as compared to "completely" controlled systems like atomic clocks. This constraints the assumptions on the stationarity of the noise of the links, as the amount of acoustic noise changes with days and seasons: there is less noise during the night when the city sleeps, or during the summer vacation when people seek away to avoid the Parisian heat. The change in nominal noise level of

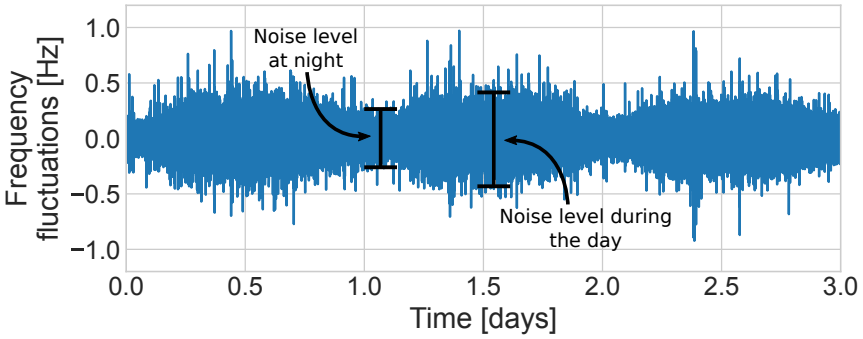

FIGURE 3.1: Frequency fluctuations of Link B over the span of 3 days. The difference in the nominal noise level during the day and during the night is highlighted.

Link B (see chapter 2.3 for link description) is illustrated in figure 3.1. Here, the frequency fluctuations are shown over the span of 3 days, which shows a visible difference in the nominal noise during the day and during the night. Indeed, to this degree the links are only stationary at a wide sense, as these events happen at a periodic basis, of 1 day and 1 year respectively for the mentioned examples.

In the following, I will describe the principles behind the design and engineering of a phase coherent fiber link. I will discuss the importance of minimizing the amount of cycle slips in the operation of a link, and I will use the concept of the β-separation line as a guiding tool for the upper bound of the desired noise of a link [46]. I will show studies of the five links in the REFIMEVE network, evaluating their noise limits and individual contributions to the broadening of the linewidth of the disseminated signal.

3.1.1 Cycle slips

An essential consideration in the design and engineering of a coherent fiber link is to minimize the amount of cycle slips in the PLL of the link stabilization, as discussed in chapter 2.2. A cycle slip happens when the accumulated noise of the link equals more than one optical cycle. These events result in a frequency measurement of an integer values of one optical cycle, or equivalently in phase jumps of an integer values of 2π. Similarly, half-cycle slips can occur when phase fluctuations exceeds π. An occurrence of a cycle slip in the E2E signal of

Link A is shown in figure 3.2, which shows the (a): frequency fluctuations and (b): phase fluctuations over a duration of 25 minutes. The nominal frequency

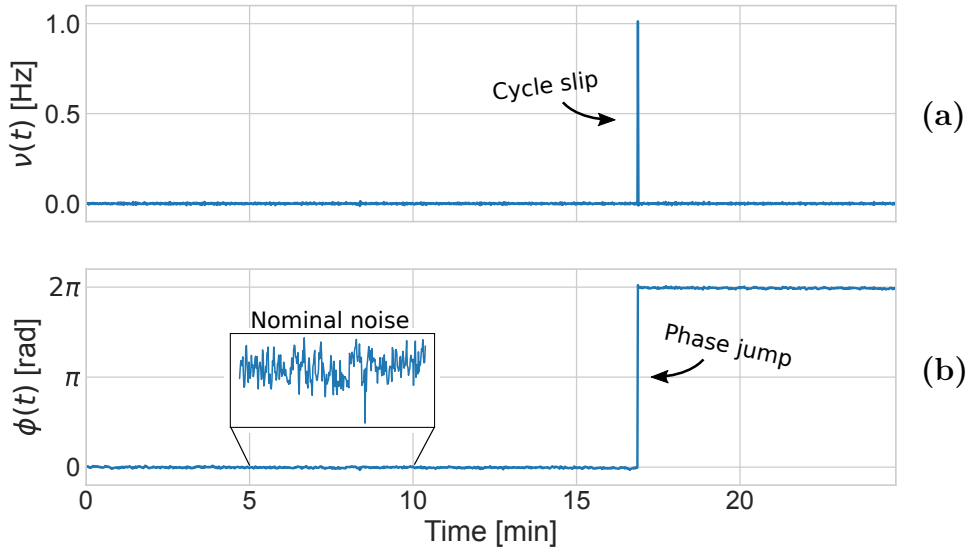

FIGURE 3.2: (a): Frequency fluctuations and (b): phase fluctuations of Link A over a duration of 25 minutes. A cycle slip around the 17$^{\text{th}}$ minute is highlighted. Insert showing nominal phase fluctuations.

fluctuations of the link in figure 3.2(a) have a standard deviation of ~ 3.3 mHz. The cycle slip is easily identifiable, in the form of a single frequency deviation measurement of a little more than 1 Hz, corresponding to 1 optical cycle. This results in a phase jump of 2π, which is shown in figure 3.2(b). The insert shows the nominal phase fluctuations of Link A at a fraction of a radian, highlighting the importance of minimizing the amount of cycle slips if a links needs to stay phase coherent.

3.1.2 The β-line: a convenient tool

The β-separation line (β-line for short) was to my knowledge first introduced in [46], and is given by[1]

$$\beta(f) = \frac{8\ln(2)}{f\pi^2}. \tag{3.1}$$

[1]There is a factor of f^2 between the definition of the β-line in [46] and what is used in this manuscript. This factor comes from the conversion between phase power spectral density (PSD) and frequency PSD, which is used in [46].

The β-line is a function, separating the phase PSD into two distinct regions of low-modulation index and high-modulation index:

$$S_\phi(f) \ll 1 \text{ optical cycle when } S_\phi(f) \ll \beta(f),$$
$$S_\phi(f) \gg 1 \text{ optical cycle when } S_\phi(f) \gg \beta(f).$$

Here we consider $S_\phi(f)$ as being the phase PSD of the E2E signal of the fiber link. As explained in [46], when $S_\phi(f) < \beta(f)$, the noise level is small compared to its Fourier frequency, which results in a fast frequency modulation. Equivalently, in the regions where $S_\phi(f) > \beta(f)$, the noise level is high compared to its Fourier frequency, which results in a slow frequency modulation with a high modulation index. For an introduction to the concept of the PSD, see appendix A. A phase noise density exceeding that of 1 optical cycle, producing a high modulation index, results in an increase in cycle slips, which in the worst case breaks the phase coherence of the link. Using the β-line as a guide for limiting the phase noise proves a convenient tool in the design of long-haul fiber links, which is illustrated in figure 3.3. This shows the phase PSD of Link A

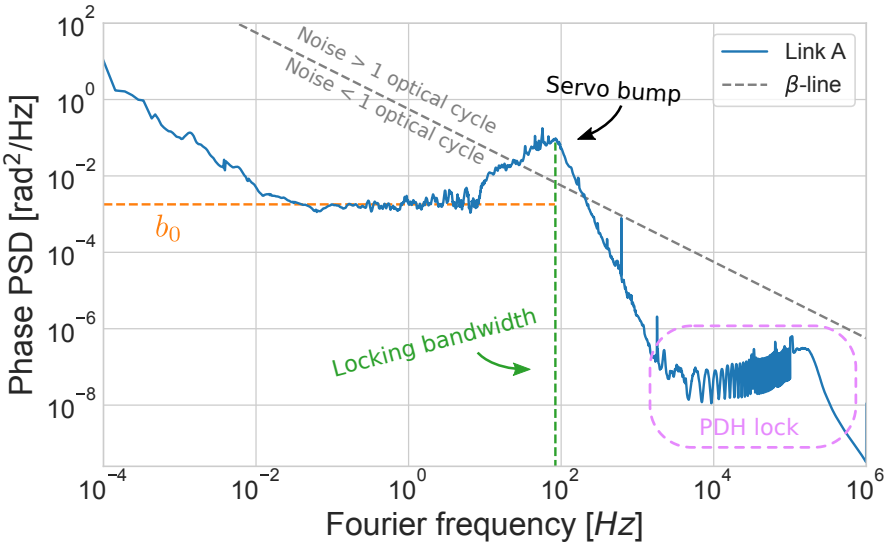

FIGURE 3.3: Phase power spectral density (PSD) of Link A (blue). Lines represent the level of white phase noise b_0 (orange), its locking bandwidth (green), and the β-line (gray). The pink box highlights the Pound–Drever–Hall (PDH) lock limit.

in blue[2], ranging from a Fourier frequency of 0.1 mHz to 1 MHz. The white phase noise level b_0 and locking bandwidth are highlighted by orange and green dashed lines respectively. The high end of the spectrum above ∼ 10 kHz is limited by the Pound–Drever–Hall (PDH) lock of the transfer laser to the ultra

[2]Measurement made with Symmetricom S5120A phase noise test set.

stable cavity [47]. The β-line is shown in gray, indicating the separation where the phase noise density gets high enough to induce cycle slips. The β-line is useful for inferring some general guidelines for planning and engineering a link, which is discussed below. At low Fourier frequencies, $f < 10^{-2}$ in figure 3.3, the noise changes from white phase noise to white frequency noise, increasing with lower frequencies. This region of the spectrum is discussed in chapter 3.2.

Optimal locking of a link

The PLL of a fiber link ensures the compensation of the noise along the link at Fourier frequencies lower than the locking bandwidth. The locking bandwidth of Link A is illustrated by the green vertical line in figure 3.3 around 80 Hz. Too low a locking bandwidth will result in a smaller compensation range, resulting in a smaller part of the spectrum being compensated, increasing the level of white phase noise b_0. Furthermore, it can result in more cycle slips, as a bigger part of the servo bump will be above the β-line. The limit of the servo bandwidth of a linear time-independent system is given by $1/(4\tau_D)$ [17, 18], with τ_D being the delay of the light in the fiber. For Link A, as illustrated in figure 3.3, the time delay is 0.4 ms, resulting in a bandwidth limit of $\sim$ 623 Hz. The locking bandwidth of Link A could have been set significantly higher, resulting in better compensation of the noise. Lastly, the β-line can be used as a guide when tuning the gain of the lock, as a high gain means higher noise compensation, but too high a gain results in an excess of cycle slips, due to a higher servo bump.

As discussed in chapter 2.1, the fundamental limit of the compression of the noise in the fiber arises from the finite travel speed of the light, which leads to the limit given by equation 2.2. Figure 3.4 shows in thick lines the phase PSD[3] of the E2E signal of the five links, and in dashed thin lines the noise of the first span of each link, at Fourier frequencies 10 mHz to 500 Hz. The PSD of the noise of the first span of the link, $S_\phi^{\text{noise}}(f)_{\text{span1}}$, has been scaled to represent the noise of the full length of the link with

$$S_\phi^{\text{noise}}(f)_{\text{full}} \approx \frac{L_{\text{full}}}{L_{\text{span1}}} S_\phi^{\text{noise}}(f)_{\text{span1}}, \tag{3.2}$$

where L_{full} is the total length of the link, and L_{span1} being the length of the first span of the link. This approximation assumes a uniform noise distribution along the link, which will not be entirely true, especially for Link B and Link E

[3] Averaged PSD curves, resulting in a linear distribution of points, are shown in the PSD plots throughout the manuscript. This is intended to be more easily readable, than when all points are shown.

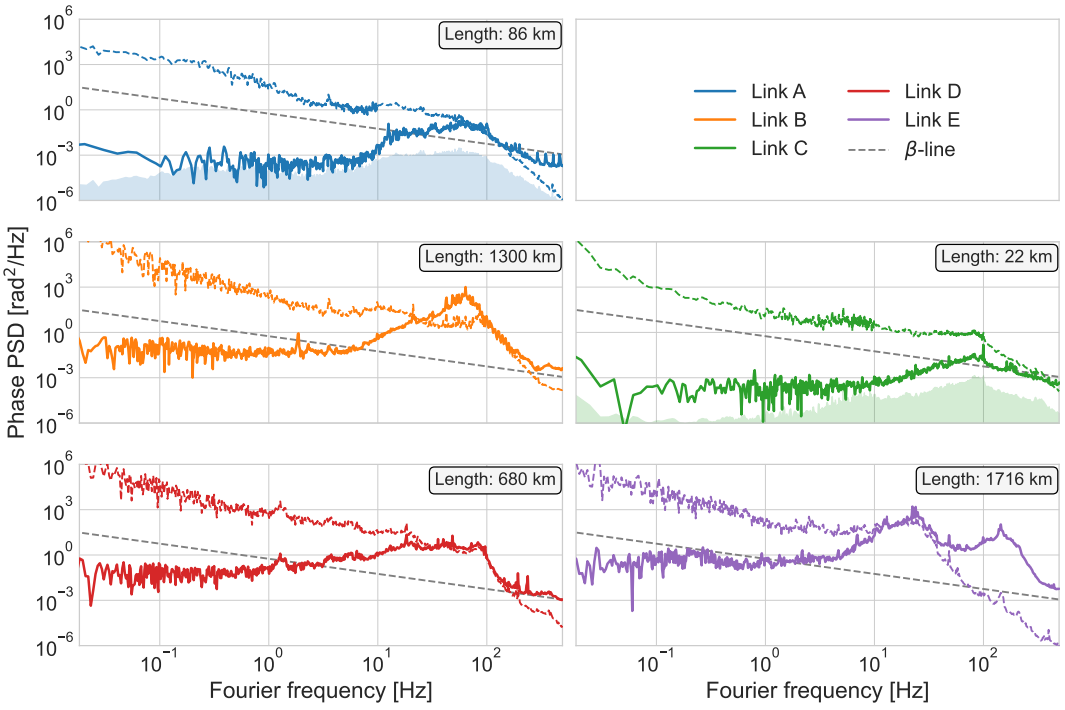

FIGURE 3.4: Phase power spectral density (PSD) of the end-to-end signals (thick, continuous curves) and noise of the first spans (dashed curves) of the five links in the REFIMEVE network. Shaded areas indicate the noise compensation limit, as given by equation 2.2.

which are cascaded in several spans. Moreover, it assumes no correlated noise between the fiber pairs, which will also not be entirely true. The limit of the compensated fiber link is shown as shaded areas in figure 3.4, which are calculated from equation 2.2 using the scaled noise of the links from equation 3.2.

All the links except Link C, the shortest of them all of 22 km, follows the limit of compensation well at frequencies lower than 10 Hz. Links A, B, C and E shows an excess of noise at higher frequencies, which is likely due to suboptimal tuning of the lock. However, part of this discrepancy could also arise from the excess of noise from some spans of the link where the noise is not recorded.

Link E shows a large deviation from the limit at high frequencies, which has a significant oscillation around 150 Hz. This can arise from cross-talk between different servos in the long frequency chain, or RF noise at regeneration points, which gets demodulated by the link.

The best agreement with the theoretical limit is seen in Link D, which shows almost perfect agreement. This link is only cascaded once, whereas the two other long links, Link B and Link E, are cascaded 3-5 times respectively. As such, the noise recorded in Link D gives to a high degree a picture of the noise of the full link.

3.1.3 Linewidth broadening of the disseminated signal

The REFIMEVE network is first and foremost a service, delivering an ultra-stable frequency reference to the many partner laboratories. Many such laboratories uses the signal for high-precision spectroscopy, and as interaction times in modern spectroscopy ranges from 10s of MHz, to several 10s of seconds, the linewidth of the delivered signal at a given interaction time can be crucial for the users of the network. In the following, I will calculate the broadening of the disseminated linewidth from the fiber links with two different approaches, and show that the REFIMEVE signal indeed is, to a varying degree, viable for many applications in high-precision spectroscopy.

According to [46], the linewidth of a signal $\Delta\nu$ can be calculated by

$$\Delta\nu = \sqrt{8\ln(2)A}, \tag{3.3}$$

where A is the area of the frequency spectrum that exceeds the β-line:

$$A = \int_{1/T}^{f_h} H\left\{S_\phi(f) - \beta(f)\right\} S_\phi(f) f^2 \, df, \tag{3.4}$$

with $H\{\cdot\}$ being the Heaviside step function, and T the measurement time. f_h is the upper limit of the frequency, at which the linewidth is measured.

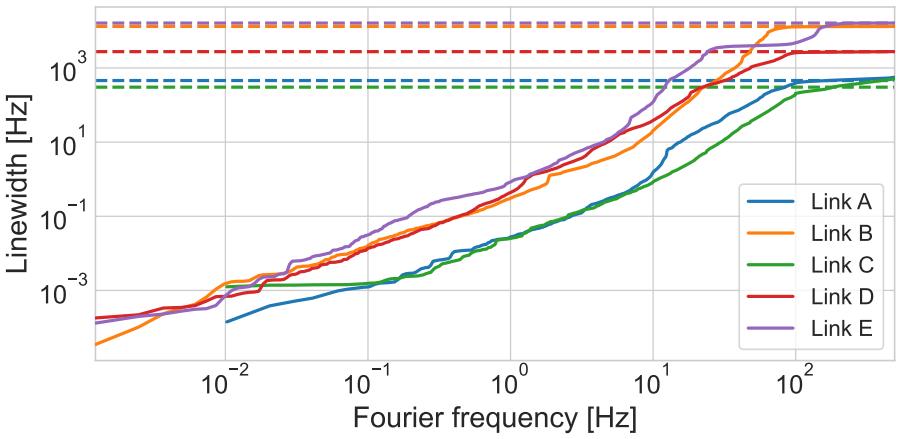

FIGURE 3.5: Linewidth broadening contribution of the 5 links in the REFIMEVE network. Dashed lines show the linewidth contributions as calculated using equation 3.3. Continuous lines show the cumulative linewidth contribution, as calculated using equation 3.6.

	Link A	**Link B**	**Link C**	**Link D**	**Link E**
$\Delta\nu_{\text{E2E}}$ [kHz]	0.47	11.07	0.43	2.32	13.67
$\Delta\nu_{\text{user}}$ [kHz]	0.33	7.83	0.30	1.64	9.66

TABLE 3.1: Linewidth broadening contributions of the five links in the REFIMEVE network, calculated from equation 3.3, with a bandwidth of 500 Hz. The user linewidth is calculated from the end-to-end (E2E) linewidth using equation 3.5.

As seen in figure 3.4, a substantial part of the spectrum of the three long links (Link B, D and E) is above the β-line. This is unavoidable for such long links, even with optimal tuning of the lock. Calculating the linewidth broadening of the five links using equation 3.3, at a bandwidth of 500 Hz, yields broadenings between 426 Hz and 13.67 kHz, which are summarized in table 3.1, and shown as horizontal dashed lines in figure 3.5. These linewidth broadenings are calculated from the E2E measurement of the links, and will not be perfectly representative of the signal at the user's side. Assuming no correlation in the uplink and the downlink of the E2E measurement, which is not strictly true [48, 27], the linewidth at the user's side can be approximated by

$$\Delta\nu_{\text{user}} = \frac{1}{\sqrt{2}}\Delta\nu_{\text{E2E}}. \tag{3.5}$$

This approximation of the delivered linewidth is likewise given in table 3.1.

The contribution to the linewidth broadening of a link varies at different parts of the spectrum. By approximating the linewidth broadening to not only include the part of the spectrum above the β-line, as in equation 3.4, but to include the whole spectrum, the linewidth broadening can be written as a function of the upper cutoff frequency f_h as

$$\Delta\nu(f_h) = \sqrt{8\ln(2)\int_{1/T}^{f_h} S_\phi(f) f^2 \, df}. \tag{3.6}$$

This is the *cumulative linewidth contribution*, and shows which parts of the spectrum contributes the most to the linewidth broadening. This is shown for the five links in figure 3.5 as continuous lines, calculated over the spectra shown in figure 3.4. The linewidth contributions saturate after the servo bumps above $\sim$ 100 Hz, converging with the values calculated using equation 3.3, demonstrating the validity of the approach. A linewidth below 1 Hz is sufficient for most high-precision spectroscopy applications, such as demonstrated with the REFIMEVE network in [44, 39] using Link A. The long-haul links reaches a linewidth broadening of 1 Hz after $\sim$ 1 s averaging time. This is already reached after $\sim$ 10 ms for the two short links, which is a factor of 10 faster. The cascading approach implemented in the REFIMEVE network adds noise outside the bandwidth of measurement [34], which does degrade the linewidth of the disseminated signal, as shown here. This effect gets multiplied by the long-haul links, which gets regenerated several times. To reach the performance of the short links, clean-up oscillators, which are essentially intermediate remote ultra-stable cavities, can be deployed to preserve the linewidth of the disseminated signal of cascaded links. However, it would not be possible to preserve the phase-coherence of the signal on timescales shorter than the new locking bandwidth.

3.2 Modeling the noise profile of a fiber link

For most applications of optical fiber links like optical clock comparisons, spectroscopy, VLBI and geodesic sensing, measurements are performed and averaged for tens to thousands of seconds, making the long-term noise behavior of the links critical for most scientific applications. In the following, I will describe the phase noise of fiber links over half a day, with a measurement bandwidth of $f_{\mathrm{BW}} = 0.5$ Hz, or equivalently a gate-time of the frequency counter of $\tau_G = 1$ s.

The phase evolution of the E2E signal of a fiber link can be separated as

$$\phi(t) = \phi(t)_{\text{stochastic}} + \phi(t)_{\text{periodic}}, \tag{3.7}$$

where $\phi(t)_{\text{stochastic}}$ is the stochastic phase evolution, and

$$\phi(t)_{\text{periodic}} = \sum_n A_n \sin(2\pi f_n t) \tag{3.8}$$

being a sum of any periodic perturbations to the phase. Here A_n denotes the modulation amplitude, and f_n the modulation frequency of a given perturbation. In the following, I will describe the statistical properties of the five links in the network, highlighting their distinctly different features and common points.

3.2.1 Phase noise density

The phase PSD of the link can be calculated from the Fourier transform of the auto-correlation function of the phase. This is explained in appendix A. For a link with a phase evolution as equation 3.7, the phase PSD becomes

$$S_\phi(f) = b_0 + b_{-1} f^{-1} + b_{-2} f^{-2} + \frac{1}{2} \sum_n A_n^2 \delta(f - f_n). \tag{3.9}$$

The noise coefficients b_0, b_{-1}, and b_{-2} corresponds to the level of white phase noise, flicker phase noise, and white frequency noise respectively, which are the dominating noise terms for a coherent fiber link.

Figure 3.6(a) shows the phase PSD of all five links in the REFIMEVE network, with dotted lines indicating fitted functions to the power law of equation 3.9 [4], and the gray dashed line indicating the β-line as given by equation 3.1. The level of white phase noise of the two short links (Link A and Link C) is much lower than that of the longer, cascaded links (Link B, D and E), since the noise level scales with the length of the links, as discussed in chapter 3.1. At Fourier frequencies lower than 5 mHz, the noise of Link C approaches that of the three long links. This noise arises from the MLS in the data center TH2, being the common denominator between all the links but Link A. The environment of the MLS in this data center is much noisier than that of the MLSs of Link A, being placed in the laboratories at SYRTE and LPL.

Since the fits do not take the periodic modulations into account, it results in a difference between the fit and the data, which mainly affects Link C at long term.

[4] The amplitude of the periodic term is equal zero.

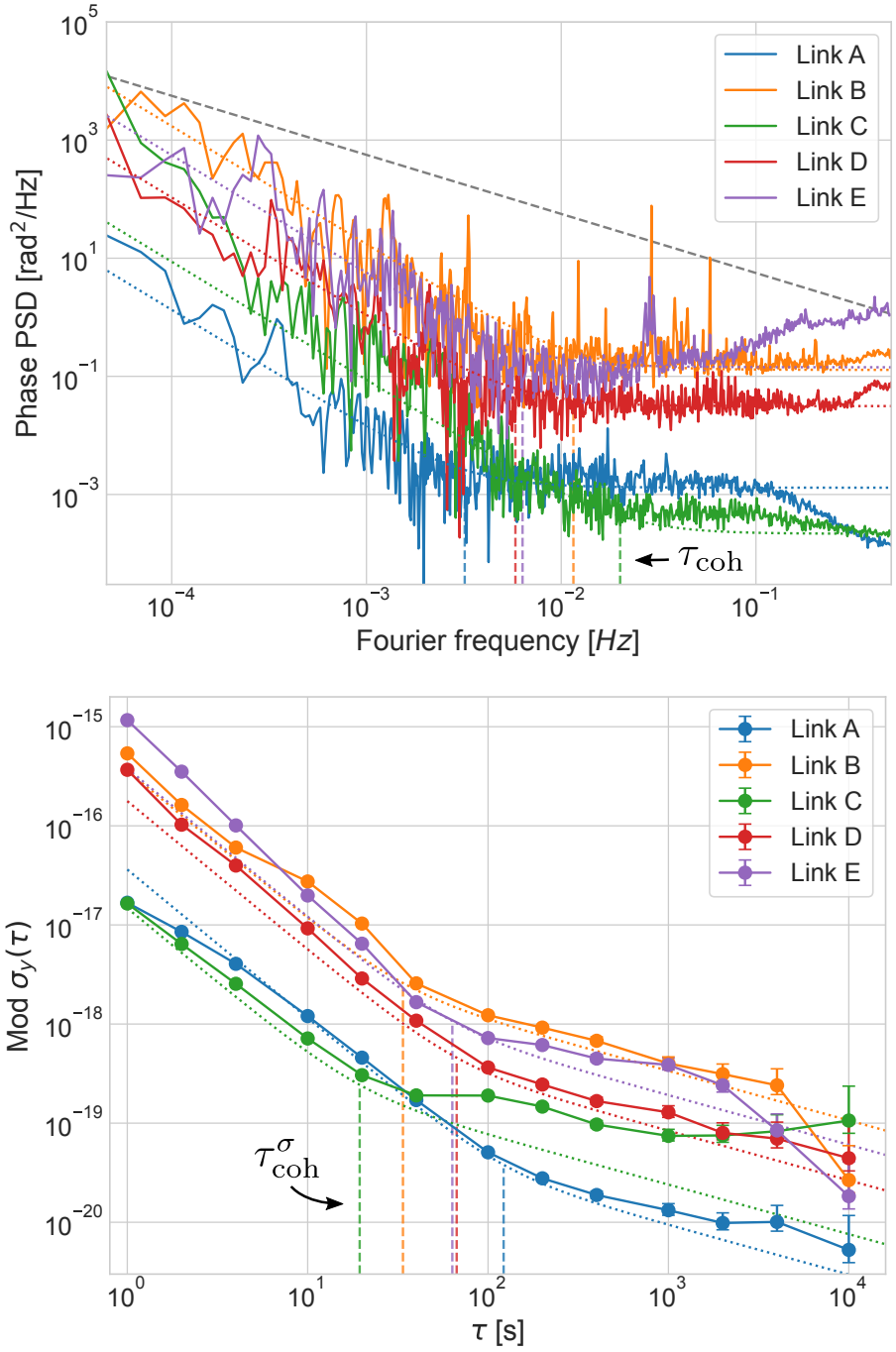

FIGURE 3.6: (a): Phase power spectral density (PSD) and (b): modified Allan deviation of the five national links in the REFIMEVE network, measured with a 0.5 Hz bandwidth. Dotted lines shows fits to equation 3.9 (without modulation terms) of links with the same color code. The dashed gray line shows the β-line as defined by equation 3.1. Vertical dashed lines show the coherence times, as calculated with the "+" solutions in (a): equation 3.11 and (b): equation 3.14. See chapter 2.3 for descriptions and labeling of the links.

Many periodic perturbations are observed for the three long links between 10 mHz and 100 mHz, which are fewer and much smaller for the two short links. These are due to temperature [21, 25, 36] and humidity [27] variations in the interferometers of the stations: as discussed in chapter 2.1, a free-space interferometer is less sensitive to temperature variations than a fibered interferometer. The MLSs at SYRTE and TH2, which are comprising Link A, are free-space interferometers [28]. Furthermore, the laboratory at SYRTE is temperature controlled. We measure the temperature every 10 minutes, and it typically stays within 1 degree Celsius during a day. The long links include RLSs and MLSs, which include 1-5 additional interferometers, which are all fibered, increasing their temperature and humidity sensitivity. Furthermore, these stations are placed in data centers with a less strict temperature control in the rooms as compared to the laboratories. The noise coefficients of the fits in figure 3.6(a), as well as amplitudes and modulation frequencies of the periodic perturbations, are summarized further below in table 3.2.

Determining periodic perturbations from the PSD

From the phase PSD, it is possible to determine the modulation frequencies f_n and amplitudes A_n of the corresponding periodic perturbations. The modulation frequencies are simply given by the frequency of the peak in the PSD, whereas the amplitudes needs to be converted to phase fluctuations. The conversion factor between a periodic perturbation as given by equation 3.8, A_n, and the amplitude of the peak inferred from the phase PSD, A_n^{PSD}, can be approximated by

$$A_n \approx 2\sqrt{\frac{A_n^{\mathrm{PSD}}}{T f_{\mathrm{ENBW}}}}. \tag{3.10}$$

Here T is the duration of the data set, and f_{ENBW} is the *equivalent noise bandwidth* [49], which is $f_{\mathrm{ENBW}} = 1.5$ (unitless) for the Hann window used to calculate the PSD in figure 3.6. The uncertainty of this approach arises from the determination of the amplitude A_n^{PSD} and frequency f_n, due to the limited resolution of the PSD.

Coherence time

The coherence time of a fiber link describes the timescale up until which the link is phase coherent[5]. This can be interpreted in two different ways:

[5] The coherence time of the fiber link it not equivalent to the coherence time of the disseminated laser signal. However, it corresponds to the timescale after which the fiber link adds white frequency noise to the disseminated laser signal.

1. as the crossing point between white phase noise (b_0), and flicker phase noise and white frequency noise (b_{-1}+b_{-2}), corresponding to the frequency at which $b_0 = b_{-1} + b_{-2}$, or

2. as the crossing point between white phase noise and flicker phase noise (b_0+b_{-1}), and white frequency noise (b_{-2}), corresponding to the frequency at which $b_0 + b_{-1} = b_{-2}$.

The two interpretations of the coherence time are described by the equation

$$\tau_{\text{coh}} = \frac{2b_0}{\pm b_{-1} + \sqrt{b_{-1}^2 + 4b_0 b_{-2}}}, \tag{3.11}$$

where the "+" solution corresponds to interpretation #1, and the "−" solution corresponds to interpretation #2. I will from here on use interpretation #1 to calculate the coherence time, as the distinction between white phase noise and flicker phase noise often is desirable when describing coherent fiber links.

The flicker phase noise component will often be negligible, as is the case for all the links but Link E. Equation 3.11 then reduces to

$$\tau_{\text{coh}} = \sqrt{\frac{b_0}{b_{-2}}}. \tag{3.12}$$

In figure 3.6(a), the frequencies corresponding to the coherence time, $f_{\text{coh}} = \tau_{\text{coh}}^{-1}$, of the five links are shown by vertical dashed lines, with the same color code as the PSD traces. The coherence time of the three long links are all between 50 s to 160 s, significantly shorter than the coherence time of the shorter Link A of 313 s. It is expected for a shorter link to show a higher degree of phase coherence, however, as seen in the case of Link C this is not always the case. Here, the limiting low-frequency periodic perturbation of the interferometer in the data center significantly reduces the coherence time of the link.

3.2.2 Stability

When assessing the stability of coherent fiber links, the modified Allan deviation (MDEV) [50] is preferred over the overlapping Allan deviation (OADEV), as it allows the distinction between flicker phase noise and white phase noise. This is similar to choosing interpretation #1 when calculating the coherence time of a fiber link in the presence of flicker phase noise, as discussed above. The MDEV can be obtained from the PSD of the signal, which is explained in appendix A. From the PSD given by equation 3.9, the modified Allan variance (MVAR) for

coherent fiber links becomes

$$\text{Mod } \sigma_y^2(\tau) = \frac{0.0380}{\nu_0^2\tau^3}b_0 + \frac{0.0855}{\nu_0^2\tau^2}b_{-1} + \frac{1}{4\nu_0^2\tau}b_{-2} + \sum_n A_n^2\left[\frac{\tau_G \sin^3(\pi f_n\tau)}{\pi\nu_0\tau^2\sin(\pi f_n\tau_G)}\right]^2, \tag{3.13}$$

with τ being the integration time, and ν_0 being the optical carrier frequency at 194.4 THz.

The MDEV of the five links is shown in figure 3.6(b), with the same color code. Being an equivalent picture to the PSD, the instability of the short links are much lower than that of the three long links. The dotted lines correspond to the fitted noise coefficients to the PSD, converted to MDEV using equation 3.13.

Coherence integration time

The coherence time as defined by the general definition of equation 3.11 can be translated to integration time, corresponding to

$$\tau_{\text{coh}}^{\sigma} = 2\frac{\sqrt{0.0855^2\, b_{-1}^2 + 0.038\, b_0 b_{-2}} \pm 0.0855\, b_{-1}}{b_{-2}},$$

where the interpretation of the "+" and "−" solutions are the same as the ones of equation 3.11. As with the coherence time shown in the PSD in figure 3.6(a), the coherence integration time shown in the MDEV in figure 3.6(b) corresponds to the "+" solution. In the simple case where flicker phase noise is negligible, the coherence integration time simply reduces to

$$\tau_{\text{coh}}^{\sigma} = \sqrt{4\cdot 0.038\frac{b_0}{b_{-2}}} = 0.39\tau_{\text{coh}}. \tag{3.14}$$

Integration time period of periodic perturbations

The fourth term of equation 3.13, which sums up any periodic perturbations, will be visible in the form of "bumps" in the stability curves, bringing an excess of noise to the system. This is visible in the MDEV of Link E (purple) in figure 3.6(b), at an integration time of $\sim$ 1000 s. By locating the top of the bump, it is possible to calculate the corresponding modulation frequency of the periodic perturbation. This is found by considering the instability contribution of the periodic perturbation:

$$\text{Mod } \sigma_y(\tau) = A_n\frac{\tau_G \sin^3(\pi f_n\tau)}{\pi\nu_0\tau^2\sin(\pi f_n\tau_G)}.$$

By differentiation, the top point of the function can be calculated, which results in a conversion factor between the integration time of the top of the bump τ_n and the actual modulation period T_n:

$$T_n = 3.25\tau_n.$$

A more in-depth derivation, including the corresponding conversion factor in the case of classical Allan deviation, is described in appendix A. The biggest source of error of this approach arises from locating the top of the bump in the stability curve, as stability points usually are shown in decades. It is however a decent approach if more precise methods are not available, like using the PSD as described above.

3.2.3 Autocorrelation

The autocorrelation of a signal is a measure of the correlation between a signal and a delayed version of itself. This is defined in appendix A. The autocorrelation can be a useful tool in identifying the amplitude and modulation frequency of a signal with one or more periodic perturbations, as described by equation 3.7. An effective method is to calculate the autocorrelation of the *rolling mean* of the signal, i.e. where each data point is calculated as the mean of the k previous data points. This is illustrated in figure 3.7, which shows the autocorrelation of Link B calculated on the frequency trace without any rolling calculation (purple), with a rolling mean with a window of $k = 5$ s (red), and with a rolling mean with a window of $k = 100$ s (orange).

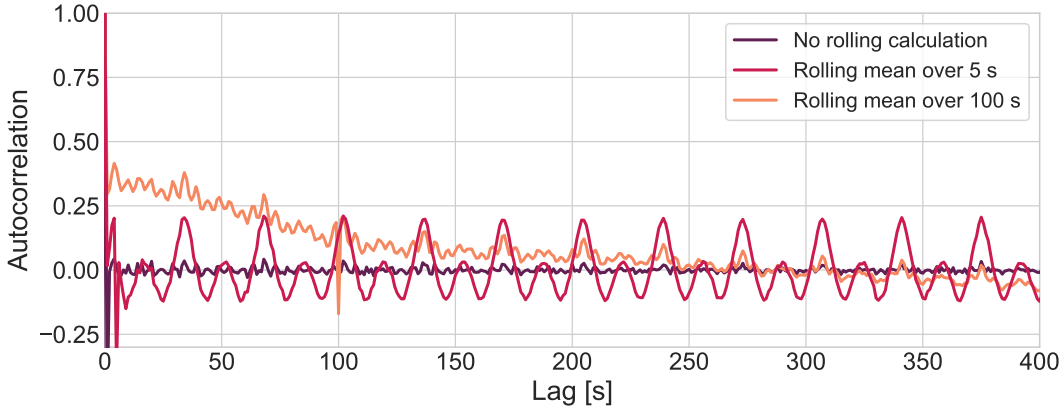

FIGURE 3.7: Autocorrelation of: the frequency deviation of Link B (purple), the rolling mean of the frequency over 5 s (red), and the rolling mean of the frequency over 100 s (orange).

In figure 3.7, the red trace (corresponding to a rolling window of 5 s) clearly highlights the two periodic perturbations in the link at 17 s and 34 s. This is not apparent in the autocorrelation of the signal without any rolling calculation, which shows a correlation of 0 at all timescales. Choosing too big of a rolling window likewise fails to highlight the periodic perturbations of the signal, which is seen in the orange curve. In this case, the short-term periodic perturbations average out, and reveals little more information than when no rolling mean is performed at all. The best results are indeed obtained if the window of the rolling mean is smaller than, or of the order of the periodic perturbations. This method can be effective in highlighting the periodic perturbations, however, choosing a fitting rolling window can be difficult if one has no a priori knowledge of the expected results.

3.2.4 Distribution

The frequency data used to calculate the phase PSD and MDEV of the five links in figure 3.6 are shown in figure 3.8. The distribution of the frequency fluctuations, that is the optical spectrum, can be modeled as a sum of a Gaussian profile, which arises from the inhomogeneous broadening from, for instance, external acoustic noise sources, and a Lorentzian profile, arising from the homogeneous broadening of the fundamental white phase noise of the link. Such a sum of Gaussian and Lorentzian profiles is called the pseudo-Voigt approximation, which can be written as

$$V_p(\Delta\nu, \delta\nu) = wL(\Delta\nu, \delta\nu) + (1 - w)G(\Delta\nu, \delta\nu), \tag{3.15}$$

with w being the *Lorentzian weight*, determining the ratio between the Gaussian and Lorentzian parts, and $\delta\nu$ being the full with at half maximum (FWHM) of the distributions. The Gaussian part is defined as

$$G(\Delta\nu, \delta\nu) = \frac{2\sqrt{\ln(2)}}{\sqrt{\pi}\delta\nu} e^{-4\ln(2)\left(\frac{\Delta\nu}{\delta\nu}\right)^2}, \tag{3.16}$$

and the Lorentzian as

$$L(\Delta\nu, \delta\nu) = \frac{1}{2\pi} \frac{\delta\nu}{\Delta\nu^2 + \frac{1}{4}\delta\nu^2}. \tag{3.17}$$

The distribution of the frequency data in figure 3.8 has been fitted with a pseudo-Voigt distribution according to equation 3.15. This fit is shown by black dotted lines. All the traces but the trace of Link D shows primarily Gaussian

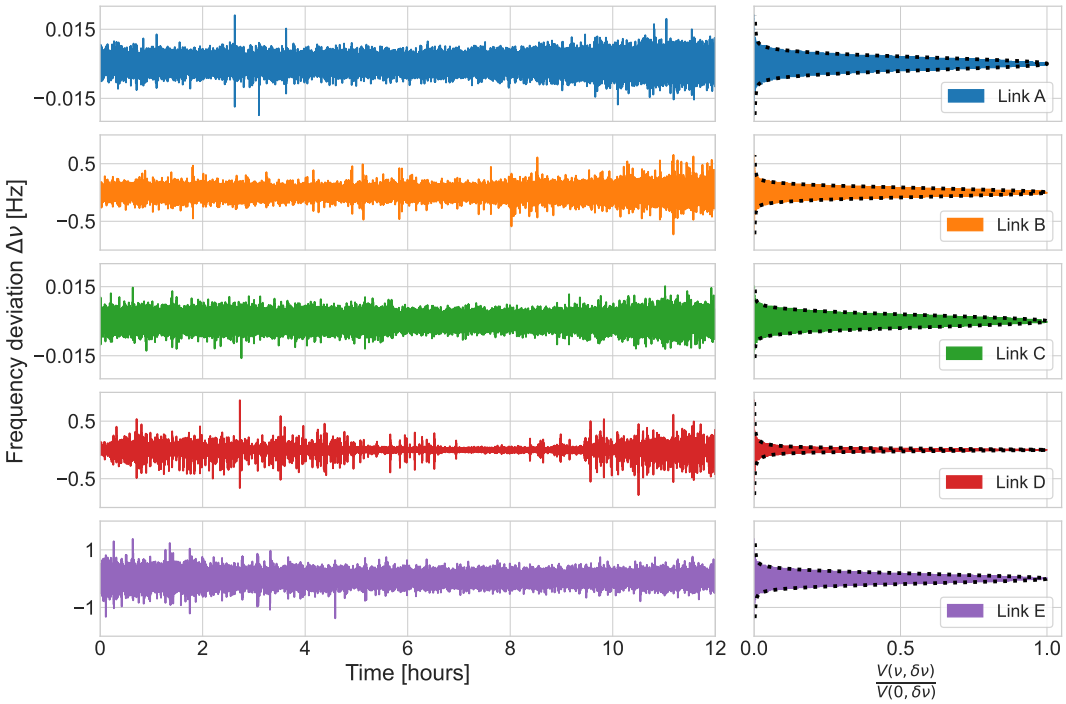

FIGURE 3.8: Frequency fluctuations of the five links over a duration of half a day. The right part shows the distributions of the frequency fluctuations, with black dotted lines corresponding to Voigt fits according to equation 3.15.

components. In the case of Link D, the Lorentzian weight is as high as 0.8. This Lorentzian behavior arises from a number of small spurs, which is evident from the red frequency trace in figure 3.8. These spurs could arise from suboptimal electromagnetic compatibility.

3.2.5 A simple summary

Summarizing the analysis presented here of the phase PSDs and the frequency distributions, I present table 3.2. This table summarizes the noise parameters of the 5 links, and can easily be expanded with the still growing network.

This table allows straightforward comparison between the links, within the same bandwidth. We see the difference in amplitude of the respective noise components of the links, which as summarized above arises from a combination of link length, number of cascades, as well as the environments wherein the different stations are located. However, as the noise of the links is not strictly stationary, a future expanded analysis of the change of these parameters with the time of day, between seasons, and between years, would be compelling to give insight into the degree of stationary and how it changes with time.

Length [km]	**Link A** 2×42	**Link B** 2×700	**Link C** 2×11	**Link D** 2×340	**Link E** 2×858
Lorentzian weight	0.15	0.14	0.09	0.79	0.17
FWHM [mHz]	6	173	6	52	376
b_0 [rad^2/Hz]	$1.3 \cdot 10^{-3}$	$1.3 \cdot 10^{-1}$	$2.2 \cdot 10^{-4}$	$3.1 \cdot 10^{-2}$	$1.4 \cdot 10^{-1}$
b_{-1} [rad^2]	0	0	0	0	$2.7 \cdot 10^{-5}$
b_{-2} [rad^2 Hz]	$1.3 \cdot 10^{-8}$	$1.7 \cdot 10^{-5}$	$8.7 \cdot 10^{-8}$	$1.1 \cdot 10^{-6}$	$5.5 \cdot 10^{-6}$
τ_{coh} [s]	313	87	50	172	157

n	A_n (rad)	f_n (mHz)
#1	$2 \cdot 10^{-3}$	63
#1	$1 \cdot 10^{-1}$	59
#2	$2 \cdot 10^{-1}$	29
#3	$2 \cdot 10^{-2}$	17
#4	$4 \cdot 10^{-2}$	12
#5	$6 \cdot 10^{-2}$	3.3
#6	$9 \cdot 10^{-2}$	1.3
#1	$8 \cdot 10^{-3}$	2.2
#1	$1 \cdot 10^{-2}$	2.1
#2	$8 \cdot 10^{-2}$	0.3
#1	$3 \cdot 10^{-2}$	30
#2	$4 \cdot 10^{-2}$	29
#3	$2 \cdot 10^{-2}$	27
#4	$6 \cdot 10^{-2}$	1.4
#5	$3 \cdot 10^{-1}$	0.3

TABLE 3.2: Top: Summary of the noise parameters of the five links. Values are based on the fits shown in figure 3.6 and figure 3.8. Bottom: Summary of the amplitudes and frequencies of the periodic perturbations of the five links, with same color code.

As discussed in chapter 3.2, it is evident from the second table that the periodic perturbations of the long-haul links (Link B, D and E) are more in number and larger in amplitudes: the amplitudes of the perturbations on the short links does not exceed $8 \cdot 10^{-3}$ rad, whereas all the long links has perturbations up to $8 \cdot 10^{-2}$ rad to $3 \cdot 10^{-1}$ rad, a factor of $10 - 40$ times larger.

3.3 Frequency bias of a fiber link

The estimation of the uncertainty of a system is a crucial task in metrology, and can be difficult, as the determination of an "expected value" is not always straightforward. However, as the noise of the E2E signal of a fiber link is actively compensated, and measured against the outgoing light, the expected average frequency shift, and therefore the induced bias, is 0 Hz. Therefore, the bias can be calculated as the mean value of the data set. The deviation of the bias is given by the long-term OADEV of the frequency data [51, 52]. Figure 3.9

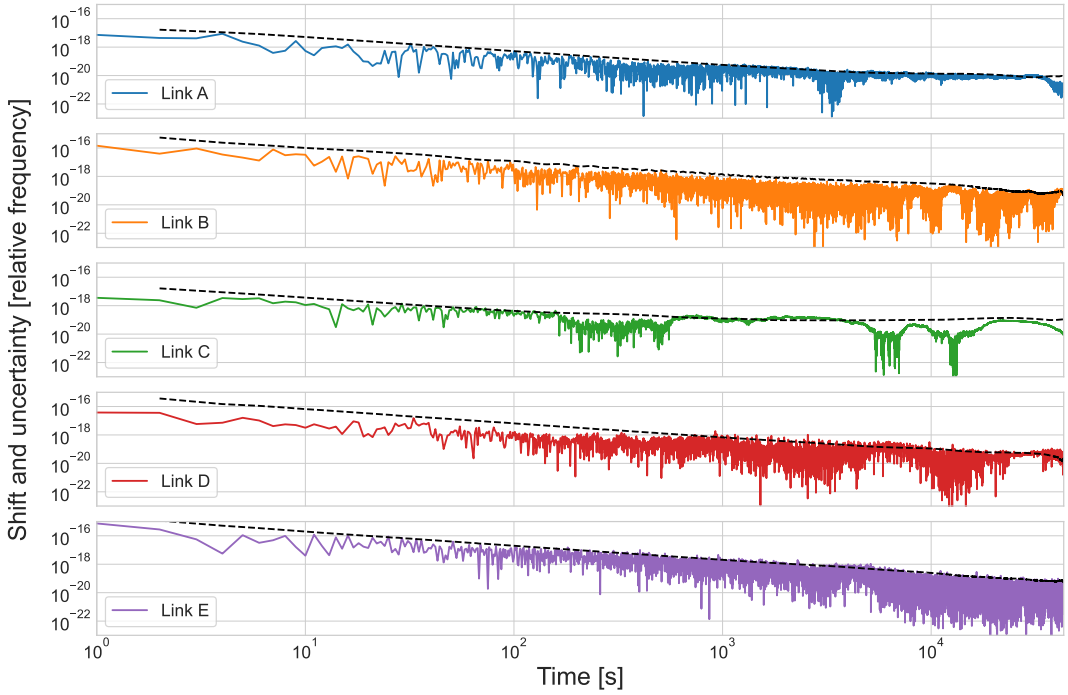

FIGURE 3.9: Cumulative relative frequency shift of the five links in the network of the frequency data presented over half a day in figure 3.8. The black dashed line shows the uncertainty of the shift at a given timescale.

shows the absolute value of the *cumulative shift* of the five links, calculated from the same frequency data as shown in figure 3.8, shown with the same color code. The cumulative shift corresponds to the cumulative mean of the data set,

averaging over an increasing amount of frequency data with time. The shift of all five links decreases with time, and goes down to a few 10^{-21} for the shortest links, and a few 10^{-20} for the longest, after half a day of averaging.

The dashed black curve shows the deviation of the shift at a given timescale. The error follows very well the upper level of the shift, showing the validity of using the OADEV as an estimator of the uncertainty. The longest link, Link E, has a standard deviation of the relative frequency data over the full duration of $9 \cdot 10^{-16}$. This is enough to give a second-to-second fluctuation of the shift of a few orders of magnitudes at half-a-day timescales, showing the importance of the estimation of the uncertainty when considering the bias of a fiber link.

3.4 Simulating a fiber link

In chapter 4 I will study the increase in noise and uncertainty contribution of fiber links in the presence of missing data. Using the knowledge of the noise parameters of the links, I have developed a simulation of the fiber links, able to study the effects of missing data, through any number of iterations, under steady statistical conditions. Artificially keeping the statistical conditions constant is a necessity, since the noise of the links is not strictly stationary. Without the simulation a study of external noise contributions like missing data would be difficult, since it would not be clear if the statistical derivations would arise from external fluctuations of the noise parameters, or from the external effects under study. This is demonstrated here in a case study of Link B.

The generation of artificial data is designed in such a way, that it is possible to use the simulated data to fill in gaps in other data sets. This study is detailed in chapter 4.2. When a data point is missing, the information of the phase evolution is lost. As such, it is not possible to use interpolation techniques to connect the known paths of the phase. This is an essential consideration as the links are phase coherent, so the addition of simulated data should not induce phase jumps.

3.4.1 Generation of simulated data

As the simulation needs to express the noise parameters of the link when creating even a singular data point, three fundamental parameters are considered when tailoring the simulation to a specific link:

- The short-term noise level, corresponding to the 1 s MDEV, or equivalently to the white phase noise coefficient b_0.

- The coherence time of the link, expressing the relationship between the level of white phase noise b_0 and the level of white frequency noise b_{-2} though equation 3.12.
- The Lorentzian weight w of the distribution of the frequencies.

When generating a phase data point $\phi(t_n)$ at a time instant t_n, the data point will be generated from a pseudo-Voigt profile $V_p(\Delta\nu, \delta\nu)$, with weight w of the link. Since the Lorentzian part of the pseudo-Voigt profile, which does not have a well-defined mean, in some cases will not be negligible, a cutoff frequency needs to be introduced. This ensures that the generated data will not have a risk of being arbitrarily big. The cutoff frequency of the distribution are tuned, so that the simulation expresses the desired short-term noise level b_0.

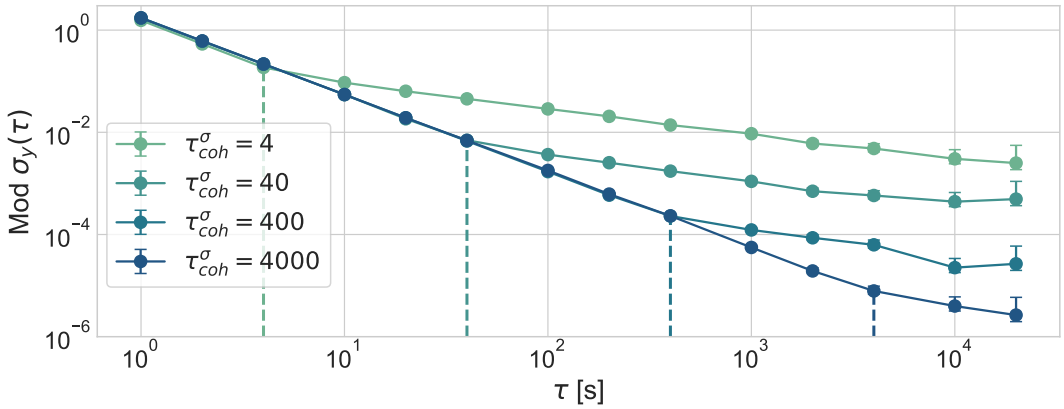

FIGURE 3.10: Illustration of the use of the coherence integration time $\tau^{\sigma}_{\text{coh}}$, defined by equation 3.14, for generating simulated data. The four different stability curves correspond to four different values of $\tau^{\sigma}_{\text{coh}}$. Dashed lines indicate $\tau^{\sigma}_{\text{coh}}$ of each respective simulation.

Due to the link not expressing solely white phase noise, the phase of the link will wander on a timescale defined by the coherence time of the link τ_{coh}. This means that the mean of the distribution $V_p(\Delta\nu, \delta\nu)$, from which the phase data point $\phi(t_n)$ is generated, needs to be defined around the current level of the phase at an earlier timescale. This timescale is given by the coherence integration time of the link, as given by equation 3.14.

Figure 3.10 shows this tuning of the coherence time of the link τ_{coh}, for 4 simulations of arbitrary but identical short-term stabilities. It is evident how the coherence integration time used in the simulations, indicated in the legend and taking the values $\tau^{\sigma}_{\text{coh}} = \{4, 40, 400, 4000\}$, matches perfectly the effective coherence integration time of the simulation.

3.4.2 Simulation of Link B

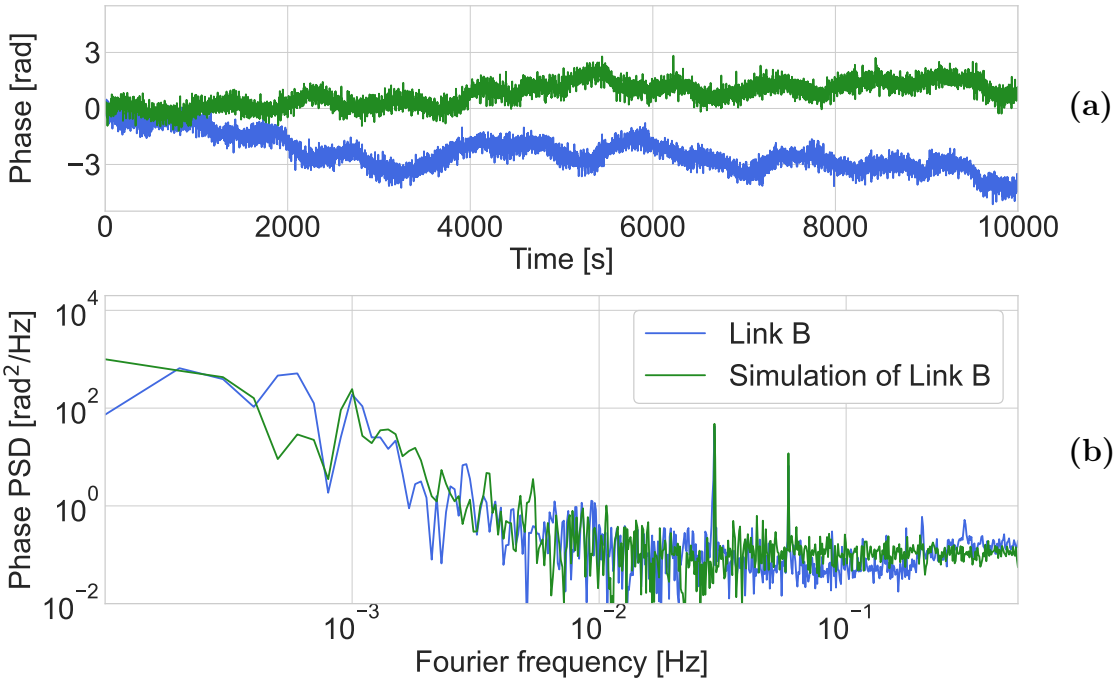

FIGURE 3.11: (a): Phase evolution and (b): phase power spectral density (PSD) of Link B (blue) and a simulation of the link (green).

Applying the knowledge of generating the simulation described above, I present in figure 3.11 the simulation of Link B. Figure 3.11(a) shows the phase of an iteration of a simulation of Link B (green), and compares it to the phase of the link itself (blue) over a duration of 10 000 s. As the simulation is a single realization of stochastic noise processes, the two phases do not equal each other at every given time. However, they do show similar statistical properties, which is illustrated in the phase PSD shown in figure 3.11(b). Here the very good correspondence between the simulation and the link is evident, which allows me to investigate the statistical properties of the link through any number of statistically identical iterations. This study is detailed in chapter 4, where the simulation is both used to represent the fiber link under study, and filling gaps left by missing data points with simulated noise.

3.5 Conclusion

In this chapter, I have discussed the fundamental noise processes of fiber links, and which limitations these induce in the design and engineering of the links. On the engineering of the links in the REFIMEVE network, I found an excess

of high-frequency noise in four out of five links, with only Link D performing at its theoretical limit. I evaluated the linewidth broadening of the disseminated signals induced by each link, and found them compatible with the requirements of the users of the REFIMEVE network. I have shown how to model the noise of optical fiber links, both in time, phase PSD and MDEV. I have introduced the coherence time of a fiber link, and discussed its dual interpretation. A summary of all five links in the network is presented, allowing easy and convenient comparison between the different links. I have shown the converging behavior of the frequency bias of the fiber links, and how it converges with the long-term assessment of the instability. Lastly, I introduce how I use the knowledge of the noise of the links to simulate the fiber links. I show a case study of a simulation of Link B, and find that it does indeed agree with the behavior of the real link. In the following chapter, this simulation is an integral part of a study of missing data in a fiber network, which will inevitably occur, and I will show how to use the advantages of using such at-will generation of noise to fill in gaps left by missing data.

Chapter 4

Missing data in a fiber network

In the previous chapter, I described and modeled the behavior of the noise of coherent optical fiber links, under the assumption of continuous, non-interrupted measurements. This will not always be the case, as missing data will appear in the form of rogue data points and outliers, or even long, continuous invalid durations of data. These arise from cycle slips, polarization adjustments, unlocks of the links, bugs and crashes of the measurement software [28], or terrorist attacks [53]. If one wants to exploit and analyze the long-term behavior of the links, either for the evaluation of the behavior of the links themselves, or for the use of fiber links as a sensor of external geodesic or fundamental physical effects, a rigorous evaluation of the uncertainty and noise contributions missing data brings to a measurement is needed.

Missing data is a well-known problem in data science [54], and have been studied for many different applications like GNSS [55, 56], the comparison of microwave fountain clocks [57], and in tests of fundamental physics [58]. A common conclusion is that the handling of missing data, and the uncertainty it introduces, is dependent on the model of the data. In the context of phase coherent fiber links, only the correction of Allan variance in the presence of missing data has been studied thus far [59, 60]. The strength of optical fiber links is their operation in the phase coherent regime, enabling them to average out noise at a faster timescale, as compared to systems performing uncorrelated measurements like optical clocks, which the links are used to compare. However, this phase coherence raises novel challenges when missing data is present. By consideration of the definition of the phase of the signal:

$$\phi(t) = 2\pi \int \Delta\nu(t)\ dt,$$

a missing frequency data point will split up the integral, leading to an unknown phase offset, damaging the phase coherence of the link.

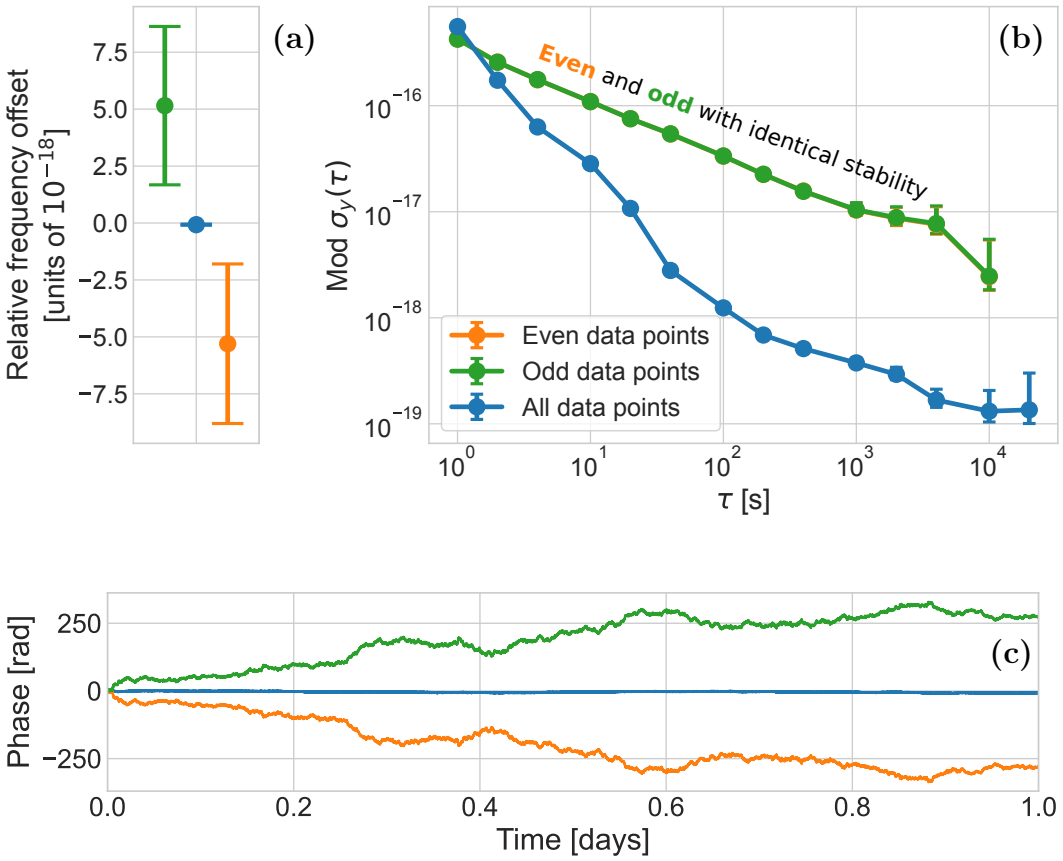

FIGURE 4.1: (a): Uncertainty, (b): modified Allan deviation, and (c): phase evolution of one full day of Link B, using the full data set (blue), or only using the even (orange) or odd (green) points.

An extreme case of missing data is illustrated in figure 4.1. The Uncertainty (a), stability (b), and phase evolution (c), of Link B over one day is shown in blue. Orange and green curves shows the same properties, but where the data has been split up in even and odd points respectively. The uncertainty of the full data set of the link over one day is $(-7.4 \pm 2.5) \cdot 10^{-20}$. When removing every second point, a bias of $\sim \pm(5 \pm 3.5) \cdot 10^{-18}$ is introduced, which is almost perfectly symmetrical for the even/odd data sets. This is clearly seen in figure 4.1(c), where the phase evolution of the two split-up signals are diverging in an almost perfectly symmetrical way. This bias is not related to the fiber link itself, but rather to the measurement of the signal. We expect it is related to a technical limitation of the dead-time free frequency counters. The deterioration of the stability of the signals, as seen in figure 4.1(b), is entirely due to another effect: this arises from an increase in frequency noise due to the

periodic sampling of the signal known as the *Dick effect* [61], which will be the topic of this chapter.

In the following, I will introduce the mathematical formalism used to describe missing data. I will discuss different distributions of missing data, and show their convergences and differences. From this, a general formula is derived, describing the decrease of the phase coherence of the link due to missing data. I end with discussing and comparing methods to mitigate some of these sampling effects in post-processing, which arise from missing data. Many of the results presented in this chapter are published in [62].

4.1 Formalism of missing data

To model missing data, I define the *annihilation operator*, $g(t)$, being a function indicating whether a data point is valid or missing at any time instant t_k. The annihilation operator is a discrete function, with a duration between consecutive data points τ_G and total duration T matching that of the data set it describes. Mathematically, this is defined by

$$g(t_k) = \begin{cases} 0 & \text{when data is missing at time } t_k, \\ 1 & \text{when data is available at time } t_k. \end{cases}$$

This annihilation operator is equivalent to the sensitivity function [63], developed to describe the interrogation of a clock transition by a low-noise oscillator. The ratio between the amount of missing data and the amount of valid data is given by the *density of missing data*:

$$h = 1 - \frac{\tau_G}{T} \sum_{k=1}^{T/\tau_G} g(t_k). \tag{4.1}$$

From this definition, the two extreme cases are $h = 0$, describing a complete data set without missing data, and $h = 1$, describing an empty data set. This naturally leads to the mean value of $g(t)$ being $1 - h$. This allows any time instant of any data set to be represented by

$$y^{\text{eff}}(t_k) = y(t_k)g(t_k),$$

where $y(t)$ indicates the full data set without any missing data, and $y^{\text{eff}}(t)$ the *effective data set* where, depending on h, any amount of data points can be unknown.

4.1.1 Distributions of missing data

The distribution of missing data can in principle have any pattern, which may change the statistical properties of a data set in different ways. In figure 4.2 I

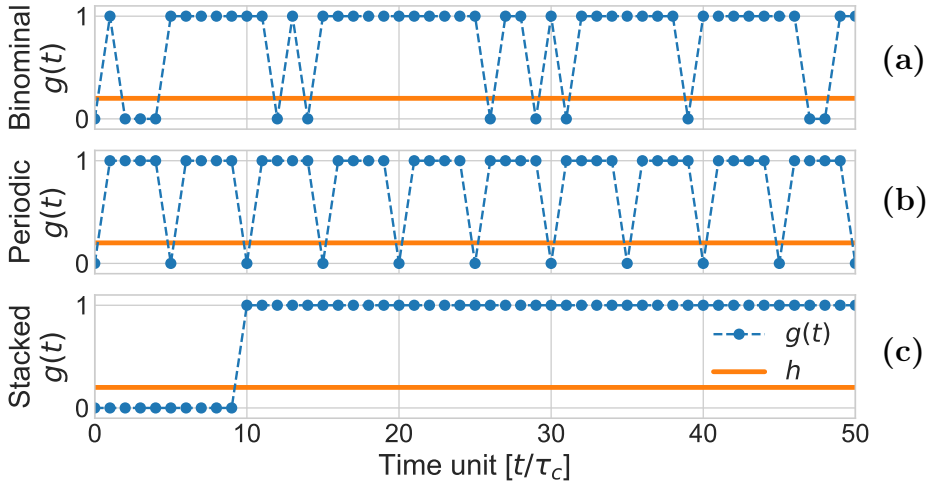

FIGURE 4.2: Illustration of different types of annihilation operators $g(t)$ (blue). (a): binomial, (b): periodic, and (c): stacked. Orange lines show the density of missing data, being the same for all three operators: $h = 0.05$.

illustrate three different patterns of missing data:

1. (a) Binomially missing data: a data point has an h chance of being missing at time t_n, $g(t_n) = 0$, and an $(1-h)$ chance of not being missing, $g(t_n) = 1$. This is commonly known as a Bernoulli trial. With each missing data point being completely independent of previous missing data points, this operator corresponds to a white frequency noise process.

2. (b) Periodically missing data: every τ_G/h data points will be missing. This has been studied with the sensitivity function, and is the cause of the increase in noise due to periodic sampling, known as the Dick effect [61].

3. (c) Stacked missing data: all Nh missing data points will be consecutive, with $N = T/\tau_G$ being the number of data points in the data set.

In the following, I start by discussing the statistical properties of binomially missing data, and show the convergence with the central limit theorem (CLT). Then, I will use the formalism developed for the Dick effect in atomic interrogation, to analytically calculate the increase in noise in fiber links due to the sampling from missing data. I will then show the convergence between the two models, and lastly I introduce a novel method of minimizing these sampling

effects, by replacing the missing data with simulated noise according to the method introduced in chapter 3.4.

4.1.2 Statistical properties of binomially missing data

As explained above, the binomial annihilation operator at each time increment t_n, associates an h chance of taking the value $g(t_n) = 0$. This is written in the notation:

$$\begin{aligned} P(H) &= h, && \text{chance of a data point being missing,} \\ P(E) &= 1 - h, && \text{chance of a data point being valid.} \end{aligned}$$

For an annihilation operator with density of missing data h, the discrete probability function for the distance d between missing data points is given by

$$P(d, h) = P(H) \cdot P(E)^{d-1} = h \cdot (1 - h)^{d-1}, \tag{4.2}$$

which is normalized:

$$\sum_{d=1}^{\infty} P(d, h) = \sum_{d=1}^{\infty} h \cdot (1 - h)^{d-1} = 1.$$

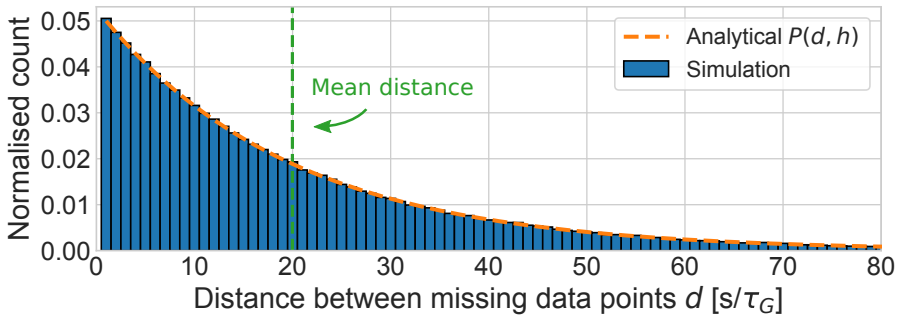

FIGURE 4.3: Monte Carlo simulation of the distance between missing data points for a binomial annihilation operator, with a density of missing data $h = 0.05$. The orange dashed curve shows equation 4.2, and the mean distance is indicated by the vertical green line.

Equation 4.2 is shown by the orange dashed line in figure 4.3, for a density of missing data $h = 0.05$. I have numerically calculated the distances between missing data points for a generated annihilation operator $g(t)$, which is shown by the normalized blue histogram. The numerically calculated values match very well equation 4.2, and shows the validity of the numerical approach.

From equation 4.2 the mean distance between missing data points is found to be

$$\mu_d(h) = \sum_{d=1}^{\infty} P(d) \cdot d = \frac{1}{h}, \tag{4.3}$$

with a variance of the distance between missing data points:

$$\sigma_d^2(h) = \sum_{d=1}^{\infty} P(d) \cdot (d-\mu)^2 = \frac{1-h}{h^2}. \tag{4.4}$$

Figure 4.4 shows a Monte Carlo simulation of (a) $\mu_d(h)$ and (b) $\sigma_d^2(h)$ in blue

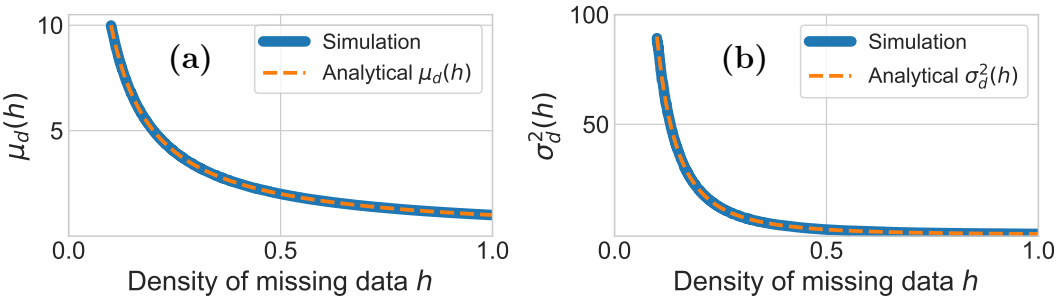

FIGURE 4.4: Monte Carlo simulation of (a): the mean distance $\mu_d(h)$ and (b): variance on the distance $\sigma_d^2(h)$ between missing data points for a binomial annihilation operator, as a function of the density of missing data h. Orange dashed curves show equations 4.3 and 4.4.

curves. Equations 4.3 and 4.4 are shown in dashed orange curves, illustrating the agreement between simulations and predictions.

Repeating the calculation of the mean distance between missing data points of M different binomial annihilation operators, each consisting of N data points, will result in an error of the mean distance of

$$\sigma_\mu^2(h) = \frac{\sigma_d^2(h)}{Nh} = \frac{1-h}{h^3 N}. \tag{4.5}$$

Calculating the mean distance between missing data for a high amount of binomial annihilation operators will, from the CLT, result in a Gaussian distribution:

$$G(d,h) = \frac{1}{\sqrt{2\pi\sigma_\mu^2(h)}} e^{-\frac{1}{2}\frac{(d-\mu_d(h))^2}{\sigma_\mu^2(h)}}, \tag{4.6}$$

with variance $\sigma_\mu^2(h)$ given by equation 4.5, and mean $\mu_d(h)$ by equation 4.3. Figure 4.5 shows a calculation of the mean distance between missing data, for three different densities $h = \{0.2, 0.05, 0.01\}$. A total number of $M = 10^4$

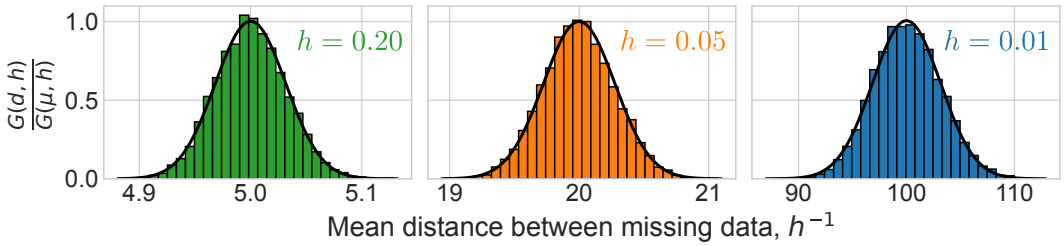

FIGURE 4.5: Mean distance between missing data points, simulated from annihilation operators with length $N = 10^5$, of three different densities of missing data: $h = 0.2$ (green), $h = 0.05$ (orange), and $h = 0.01$ (blue). Black curves corresponds to equation 4.6.

annihilation operators has been averaged to obtain the distributions in figure 4.5, which is sufficient to fulfill the CLT. This is seen in the black lines, being the analytical formula of equation 4.6 for each value of h, showing very good correspondence with the simulation.

4.1.3 Spectral properties of missing data

In chapter 3.2 I showed how the noise of a link depends on a few noise coefficients b_n. The corresponding noise coefficient for the annihilation operator is the density of missing data h, on which the statistical properties depend, which was demonstrated above for the binomial annihilation operator. As one Bernoulli trial is completely independent of previous Bernoulli trials, and will only depend on h, the process corresponds to a white frequency noise process. As such, the Fourier spectrum of the binomial annihilation operator can be written as

$$S(f) = \frac{\sigma^2}{f_{\mathrm{BW}}} = \frac{h(1-h)}{f_{\mathrm{BW}}}, \tag{4.7}$$

where σ^2 is the variance of the annihilation operator, given by $\sigma^2 = h(1-h)$. The spectrum of a binomial annihilation operator is shown by the blue trace in figure 4.6(a), clearly illustrating the white frequency noise behavior. The dashed orange line shows equation 4.7, corresponding to the white frequency noise level. Equation 4.7 is also shown in figure 4.6(b), with the same orange color and dashed lines, for the whole range of which h is defined between 0 and 1. The thicker blue curve shows the noise level of simulated annihilation operators, agreeing well with the analytical formula.

The green spikes in figure 4.6(a) shows the Fourier spectrum of the periodic annihilation operator. This spectrum is 0 at all frequencies other than integer values of h/τ_G, as $S(f) \propto \sum_{n=1}^{\frac{1}{2h}} \delta\left(f - \frac{nh}{\tau_G}\right)$.

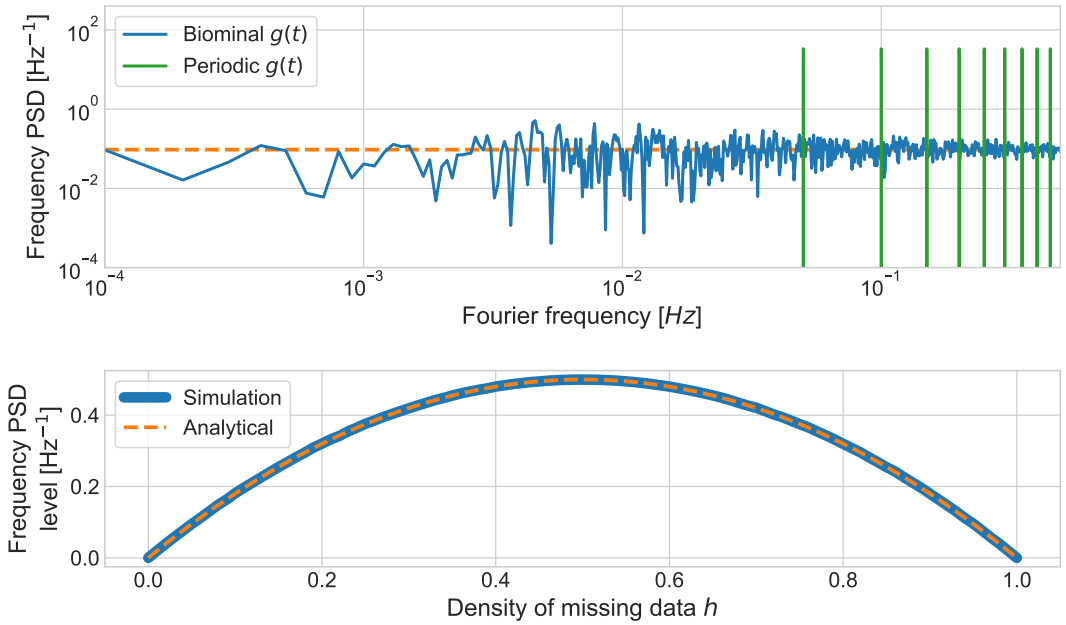

FIGURE 4.6: (a): Spectrum of periodic (green) and binomial (blue) annihilation operators $g(t)$, with a density of missing data $h = 0.05$. (b): Change in white frequency noise level of the binomial $g(t)$ as a function of h. Dashed orange curves in both plots corresponds to equation 4.7.

4.1.4 The Dick effect

Assuming a periodic annihilation operator, the formalism introduced by John G. Dick in the 80s [61] can be applied, describing the increase in noise when interrogating an atomic ensemble with a narrow-linewidth oscillator in non-continuous operation. Following [64], the increase in noise due to the Dick effect as a function of the density of missing data h can be written as

$$S_\phi^{\text{Dick}}(f,h) \approx \frac{2h}{(\tau_G f)^2} \sum_{n=1}^{\infty} \text{sinc}\left(n\pi\left(1-h\right)\right)^2 n^2 S_\phi\left(\frac{nh}{\tau_G}\right), \tag{4.8}$$

where τ_G/h corresponds to the period of the periodic annihilation operator. Assuming a noise profile of the links as described by equation 3.9, and applying the upper limit of summation of $n \leq \lfloor \frac{1}{2h} \rfloor$, with $\lfloor \cdot \rfloor$ indicating the "floor" operation of rounding down, the increase in frequency noise can be written as

$$\begin{aligned} S_\phi^{\text{Dick}}(f,h) &\approx b_0 h^2 \frac{2\lfloor \frac{1}{2h} \rfloor - \frac{1}{\sin(\pi h)} \sin\left(2\pi h \lfloor \frac{1}{2h} \rfloor + \pi h\right) + 1}{\tau_G^2 f^2 2\pi^2 (h-1)^2} \\ &= b_0 \frac{\mathbb{D}(h)}{f^2}. \end{aligned} \tag{4.9}$$

$\mathbb{D}(h)$ is introduced as the *Dick factor*, increasing with the density of missing data h, and vanishing for a complete data set: $\mathbb{D}(0) = 0$. This term indeed shows a Fourier frequency dependence of f^{-2}, corresponding to an increase in the white frequency noise term b_{-2} of the system. This increase in noise depends on the nominal level of white phase noise b_0, showing that the sampling of white phase noise is fundamental and does not discriminate between systems with varying levels of white phase noise. Ultimately, this effect is proportionally the same for phase coherent links of any length. Assuming a noise profile with negligible flicker phase noise dependence, $S_\phi(f) = b_0 + b_{-2}f^{-2}$, the effective PSD of the sampled system can be written as

$$\begin{aligned} S_\phi^{\text{eff}}(f,h) &\approx S_\phi(f) + S_\phi^{\text{Dick}}(f,h) \\ &\approx b_0 + (b_0\mathbb{D}(h) + b_{-2})\, f^{-2}. \end{aligned} \tag{4.10}$$

In the case of a complete data set, equation 4.10 reduces to the PSD of the nominal link, $S_\phi^{\text{eff}}(f,0) = S_\phi(f) = b_0 + b_{-2}f^{-2}$, and when $h \to 1$ the noise term $S_\phi^{\text{Dick}}(f,h)$ will be dominating.

Sampling of a strongly modulated signal

The sampling effects arising from the periodic and the binomial annihilation operators will in many instances be very similar. A special case where they do show different behaviors is when the sampled signal has a strong periodic modulation. To highlight these effects I consider a signal consisting of white phase noise, $\phi(t)_{WP}$, and a strong periodic modulation:

$$\begin{aligned} \phi(t) &= \phi(t)_{WP} + A_m \sin(2\pi f_m t), \\ S_\phi(f) &= b_0 + \frac{1}{2}A_m^2\delta(f - f_m). \end{aligned} \tag{4.11}$$

The amplitude of modulation is chosen to be roughly 4 times larger than the variance of the white phase noise fluctuations, and with a modulation frequency of $f_m = 50$ mHz. Figure 4.7 shows the effective phase PSD $S_\phi^{\text{eff}}(f,h)$ of a simulated signal described by equation 4.11, for 4 different densities of missing data: $h = \{5\cdot10^{-4}, 5\cdot10^{-3}, 5\cdot10^{-2}, 5\cdot10^{-1}\}$. Figure 4.7(a) shows the aliasing of the periodic annihilation operator, and figure 4.7(b) shows the aliasing of the binomial annihilation operator. The sampled simulated data sets have been calculated 10 times for each density of missing data, and the curves shown are the mean phase PSD of the 10 iterations. This serves to average out statistical fluctuations that will be present at each iteration of the stochastic signal. The

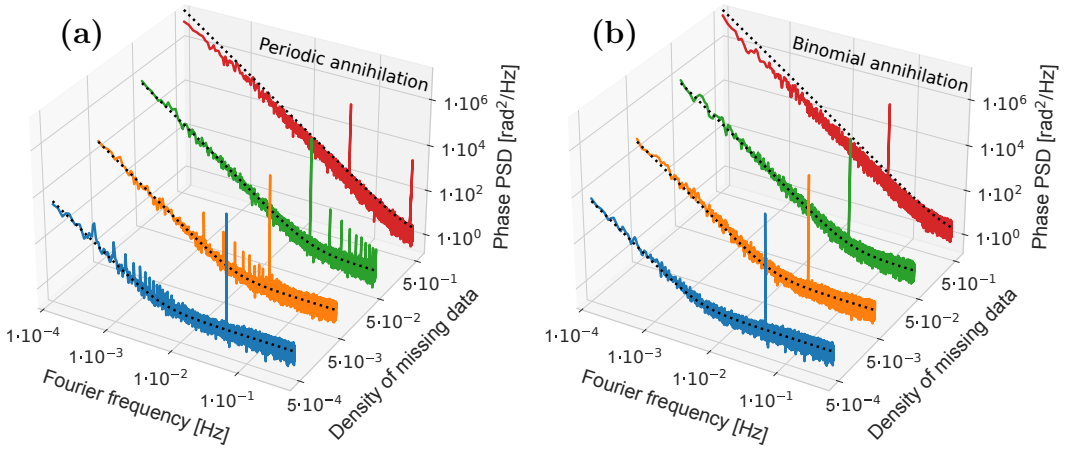

FIGURE 4.7: Aliasing effects of a white phase noise signal with a strong periodic modulation, with an increasing amount of missing data. (a): Periodically spaced missing data, and (b): binomially spaced missing data.

missing data has been replaced with frequency deviation data of 0 Hz, which serves to keep the phase of the signal constant across the gap left by the missing data. As this induces a bias in the short-term noise level, the PSD curves have all been normalized with the mean value of the annihilation operator: $(1-h)$.

The dotted black lines show the predicted noise level of the sampled data according to equation 4.10. There is a good correspondence between the simulation and the predicted noise level, both for the case of the periodic annihilation operator, as well as the binomial annihilation operator, for densities of missing data lower than 50 % (the front 3 curves). This shows indeed that the increase in white frequency noise due to the Dick effect is the same for the two different annihilation operators, and that equation 4.10 can be applied to binomially distributed missing data.

Other than the increase in white frequency noise from the Dick effect, a secondary aliasing effect arises which is not the same for the two annihilation operators: when periodically sampling a signal with a strong carrier, a series of sub-harmonics appear. These appear at integer n counts of the frequencies $f_m \pm nh/\tau_G$, and is an interference between the period of the modulation and the period of the appearance of the missing data. This is not present for the binomial annihilation operator, as it distributes missing data with no periodic order.

Decrease in coherence time due to sampling

Using the simplified definition of the coherence time from equation 3.12, an increase in frequency noise in the system will be directly equivalent to a decrease in coherence time of the link. This effective coherence time of a sampled fiber link can be written as

$$\tau_{\mathrm{coh}}^{\mathrm{eff}}(h) \approx \left(\mathbb{D}(h) + \tau_{\mathrm{coh}}^{-2}\right)^{-\frac{1}{2}}, \tag{4.12}$$

where $\tau_{\mathrm{coh}}^{\mathrm{eff}}(0) = \tau_{\mathrm{coh}}$ is the nominal coherence time of the system without any missing data. The decrease in coherence time of the link is a convenient parameter to use as a metric, as keeping the phase coherence of the link is important if they are to be used for the comparison of state-of-the-art optical clocks.

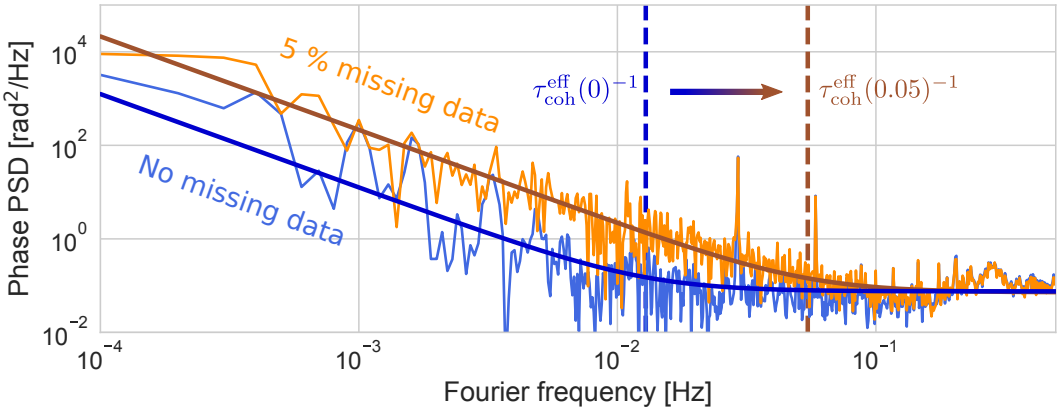

FIGURE 4.8: Phase power spectral density (PSD) of Link B without missing data (blue), and with 5 % of the data removed (orange). Thick lines show the power law model of each data set, and the decrease in effective coherence time is indicated by vertical dashed lines.

The decrease in coherence time when sampling Link B is shown in figure 4.8. Here, the phase PSD of the link without any missing data is shown in blue. After removing 5 % of the data points using the binomial annihilation operator, the coherence time decreases correspondingly. This is seen in the orange trace, which shows the phase PSD of the data set where 5 % of the data is missing. The thick blue and orange lines shows the power law of the link, where it is evident that the level of white phase noise b_0 is kept, and there is an increase in noise according to the white frequency power law f^{-2}, as predicted by the noise arising from the Dick effect. Especially the decrease in coherence time is visible, highlighted by the two vertical dashed lines. In the following, I will discuss the mitigation of the effects of missing data, using the effective coherence time as a metric in the comparison between different approaches.

4.2 Mitigating the effects of missing data

As missing data inevitably occur in fiber links, one needs proper techniques to be able to mitigate the effects of missing data when evaluating the statistical properties of the link. I have previously studied three different approaches for handling missing data, which can be found in [65]:

1. **Ignoring the problem**: One can concatenate the remaining data, effectively ignoring the problem. This creates a length mismatch of the effective data set, which is problematic if one needs to be able to evaluate the frequency data at certain time increments $\nu(t_n)$. This is the case for clock comparisons when evaluating the quality of the frequency comparison at all times during the comparison, as well as in the frequency dissemination to users of the network who needs to know the quality of the signal during measurement periods. For the statistical evaluation of the signal, the length mismatch creates a Fourier frequency bias, making the evaluation of periodic perturbations difficult. This is shown and discussed in [65]. Lastly, it does not address the deterioration of the coherence time of the signal, as given by equation 4.12.

2. **Keeping the phase constant across the missing data**: Keeping a constant value for the phase across the gap left by the missing data will keep the length intact, yielding a more meaningful Fourier analysis. This is accomplished by inserting a frequency value of 0 Hz into the gap left by the missing data, which creates a bias in the short-term noise level of the signal. Lastly, just as in approach #1, this approach does not deal with the increase in noise from the Dick effect.

3. **Replacing missing data with simulated noise**: The last approach is more novel, and uses the techniques in generating simulated noise described in chapter 3.4 to fill the gaps left by the missing data. This has the advantages of approach #2 in keeping the length of the data set intact, avoiding the creation of a bias in the Fourier domain. Contrary to approach #2, this approach does not bias the short-term noise level, as long as the short-term noise level of the generated noise is the same as the original data set. This will only be partly true for a fiber link, as the noise is not strictly stationary, as discussed in chapter 3.1. Lastly, this approach mitigates the deterioration of the coherence time of the link.

To compare approach #2 with approach #3, I have simulated a fiber link consisting of white phase noise and white frequency noise, with the power law of

$S_\phi(f) = b_0 + b_{-2}f^{-2}$, and equivalently coherence time τ_{coh}, using the procedure described in chapter 3.4. Applying the binomial annihilation operator $g(t)$, with density of missing data h, results in the effective data sets $y^{\text{eff}}(t) = y(t)g(t)$:

$$y^{\text{eff}}_{\text{constant}}(t), \quad \text{where the phase is kept constant,}$$
$$y^{\text{eff}}_{\text{replace}}(t), \quad \text{where missing data is replaced.}$$

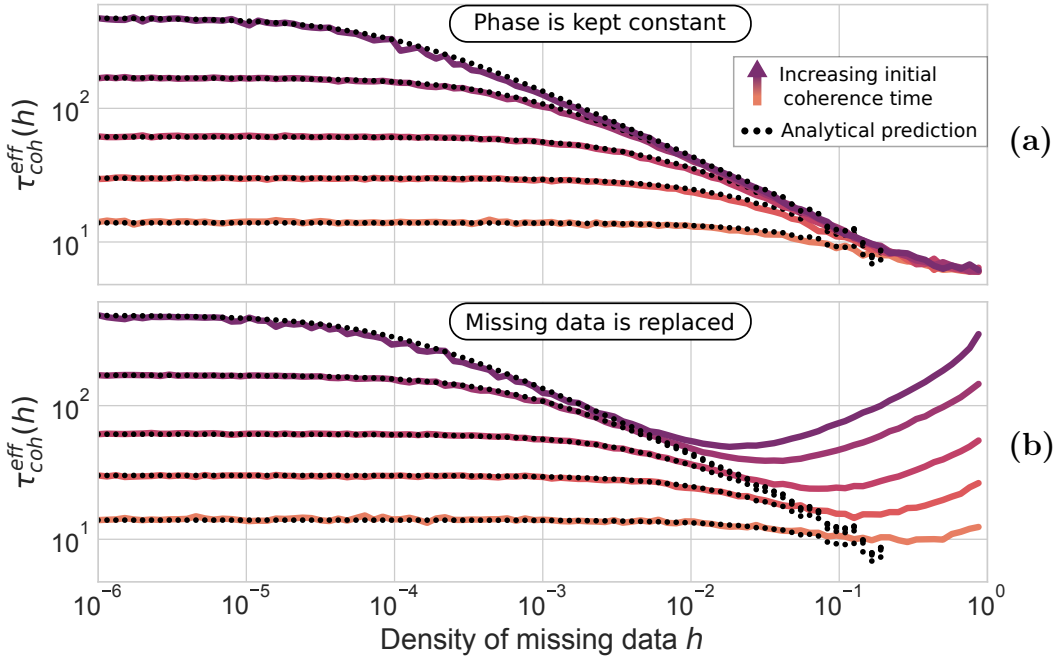

FIGURE 4.9: Effective coherence time of a simulated link $\tau^{\text{eff}}_{\text{coh}}(h)$ as a function of the density of missing data h, where (a): the phase is kept constant across the gap left by missing data, and (b): missing data is replaced with simulated noise. Increasingly purple color indicates increasing initial coherence time of the simulation, with no missing data present. Black dotted curves show equation 4.12.

Figure 4.9 shows the effective coherence time of the signal, as a function of the density of missing data h, when (a): the phase is kept constant across gaps left by missing data, (b): missing data is replaced by simulated noise. The simulation has been repeated for 5 different nominal coherence times, between 15 s - 500 s, symbolized by the increasingly purple color in figure 4.9. The results shown are a mean of 400 iterations of the simulation, which serves to average out any stochastic fluctuations which can arise in individual simulations. It is evident from the figure that with an increasing initial coherence time, the sensitivity to missing data increases: the effective coherence time of a fiber link with a very long coherence time (dark purple) starts to deteriorate with just a

few missing data points. This is in contrast to the link with a coherence time of just 15 s (yellow), which sees no significant decrease until ~ 5 % of the data is removed.

Black dotted lines indicate the expression for the effective coherence time $\tau_{\text{coh}}^{\text{eff}}(h)$, as described by the increase in Dick noise by equation 4.12. This expression describes the approach of keeping the phase constant across the gap left by missing data, as seen in figure 4.9(a), where the overlap between equation 4.12 and the simulation is evident. The approach of replacing missing data with simulated noise shows the same behavior for low densities of missing data. For a higher amount of missing data, the models diverge as the data set starts to consist of a significant amount of simulated noise. In this case, we observe that the coherence time of the link increases towards its nominal value, without any missing data. The point of divergence between the two models is given by

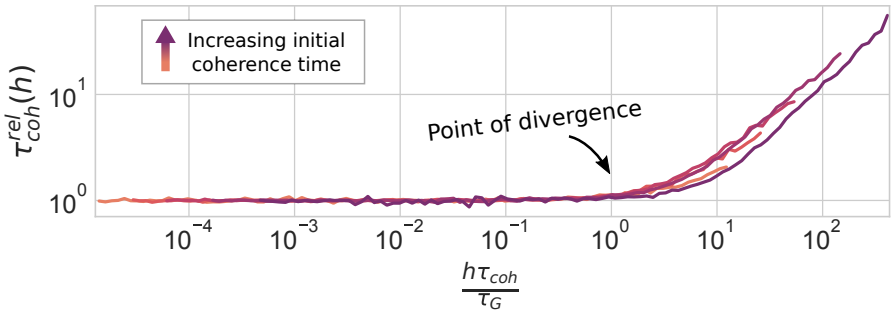

FIGURE 4.10: Relative effective coherence time of the two simulations $\tau_{\text{coh}}^{\text{rel}}(h)$, as defined by equation 4.13, plotted as a function of $\frac{h\tau_{\text{coh}}}{\tau_G}$. Increasingly purple color indicates increasing initial coherence time of the simulation, with no missing data present. The point of divergence between the two approaches is highlighted at $\tau_G/h = \tau_{\text{coh}}$.

the point at which the average duration between missing data points is similar to the initial coherence time of the link: $\tau_G/h = \tau_{\text{coh}}$. This is illustrated in figure 4.10, where the relative effective coherence time,

$$\tau_{\text{coh}}^{\text{rel}}(h) = \frac{\tau_{\text{coh}}^{\text{replace}}(h)}{\tau_{\text{coh}}^{\text{constant}}(h)}, \tag{4.13}$$

between the two approaches are plotted as a function of $\frac{h\tau_{\text{coh}}}{\tau_G}$. Figure 4.10 illustrates the similarity between the two approaches up until $\frac{h\tau_{\text{coh}}}{\tau_G} = 1$, or equivalently $\tau_G/h = \tau_{\text{coh}}$, the point which is highlighted in the figure. This divergence can be understood as the point where the frequency noise induced by the sampling of the frequency data starts to be converted into phase noise, an effect which gets partially mitigated by the insertion of phase coherent simulated

noise. This shows that the insertion of simulated noise is indeed favorable to the other methods compared here, when evaluating a coherent fiber link where missing data is present. Applying this method does require prior knowledge on the noise behavior of the link under study, as detailed in chapter 3.4 where the generation of the simulation is explained. This is mostly the case of the optical fiber links in the REFIMEVE network, where large amounts of data are gathered continuously.

In this study, I have not included any effects arising from correlations between the forward and backward propagating light in the fiber, which can arise from polarization asymmetry as explained in chapter 2.1. In the case of GNSS comparisons, such a correlation is evaluated in [66]. As such an effect can lead to a frequency shift, this shift would vanish with an increasing amount of missing data, when using the fill-in approach. However, even if such an example highlights the limitations of the fill-in approach, these short-term perturbations are at most of the order of a few 10^{-20} [27], which is well below any practical uses of the fiber links.

4.2.1 Long-term behavior of a fiber link

Link B is the longest operating of the long-haul fiber links in the REFIMEVE network. From the end of April 2015, until the end of June 2020, the link operated with an average uptime between 40 % - 46 %, depending on the required performance level. Unfortunately, the link ceased operation in June 2020 for more than a year. In the following, I will present a study of the noise behavior of the link over these 5 years and 65 days, or 1890 days. With one measurement each second, this corresponds to more than 162 million data points. I have been working with filtering criteria resulting in an uptime of $\sim$ 44 %. This corresponds to 825 days of data, and equivalently 1064 days of missing data. For such a study of the long-term noise behavior of the link, it is evident that the handling of the missing data is crucial to the result of the study. This study is built on an initial study, which is presented in [62].

1890 days of operation

Figure 4.11(a) shows the average uptime of Link B for each of the 63 months. The highest uptime of the link was found in 2018 and 2019 (month 32 to month 56), with a total uptime over the two years of 65 %. An in-depth study of Link A and Link B in this period is presented in [28]. Figure 4.11(b) shows the absolute value of the average frequency shift, indicated by green circles, and

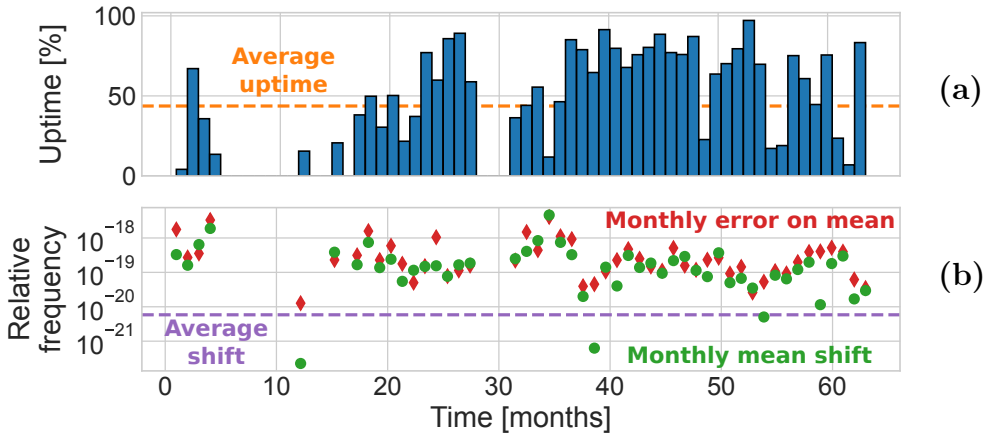

FIGURE 4.11: (a): Uptime of Link B between April 2015 and June 2020. Each bar represents the average uptime over one month. The average uptime of the full period is shown by the orange dashed line. (b): Absolute value of the average relative frequency shift of each month of operation (green circles), and error of the mean (red diamonds). The purple dashed line indicates the total weighted average shift, using the uptime as frequency weights.

error on the average frequency shift, shown by red diamonds, for each of the 63 months. These shifts vary from $4.6 \cdot 10^{-18}$ to $2.2 \cdot 10^{-22}$. The average shift, indicated by the purple line, is calculated as a weighted average of all the shifts, using frequency weights, which are given by the uptime of the link for the given month. The weighted average shift has a value of $5.8 \cdot 10^{-21}$, with a weighted error of $3.4 \cdot 10^{-19}$.

Data preparation

As the full data set consists of 162 million data points, further preparation of the data is needed to perform a statistical analysis. I introduce an extra averaging step, drastically reducing the amount of data points per day. In this study, I have chosen to average every 216 s of data, corresponding to 400 data points each day. This effectively reduces the bandwidth of the data set from 0.5 Hz to $\sim$ 2.3 mHz. From here on, I called these averaged data *stacked data points*. Like in chapter 5.5, I have studied the long-term statistical effects of the link, both where remaining data has been concatenated, and where the missing data has been replaced with simulated noise. In [62], we presented this study but with one main differences: In [62], data was bundled into stacks of 2160 s, which has been decreased with a factor 10 in the study presented in this manuscript. This increases the bandwidth of the data set tenfold, but likewise increases the computation time.

Each new stacked data point will consist of information of the mean value of the relative frequency data, and the uptime of the stacked data point. If the missing data is not replaced, this can lead to some of the stacked data points being an average of very few data points, if the uptime in the 216 s segment was poor. This will lead to an increase in uncertainty of each stacked data point, which will depend on the uptime of the averaged data. As such, an additional filtering criteria can be introduced: to put a threshold on the allowed uptime for each stacked data point.

Statistical properties over 1890 days

As discussed in chapter 3.2, the long-term noise of the fiber link is dominated by white frequency noise, and determined by the white frequency noise parameter b_{-2}. Figure 4.12(a) shows the frequency PSD, $S_{\Delta\nu}(f) = S_\phi(f)f^2$, where the

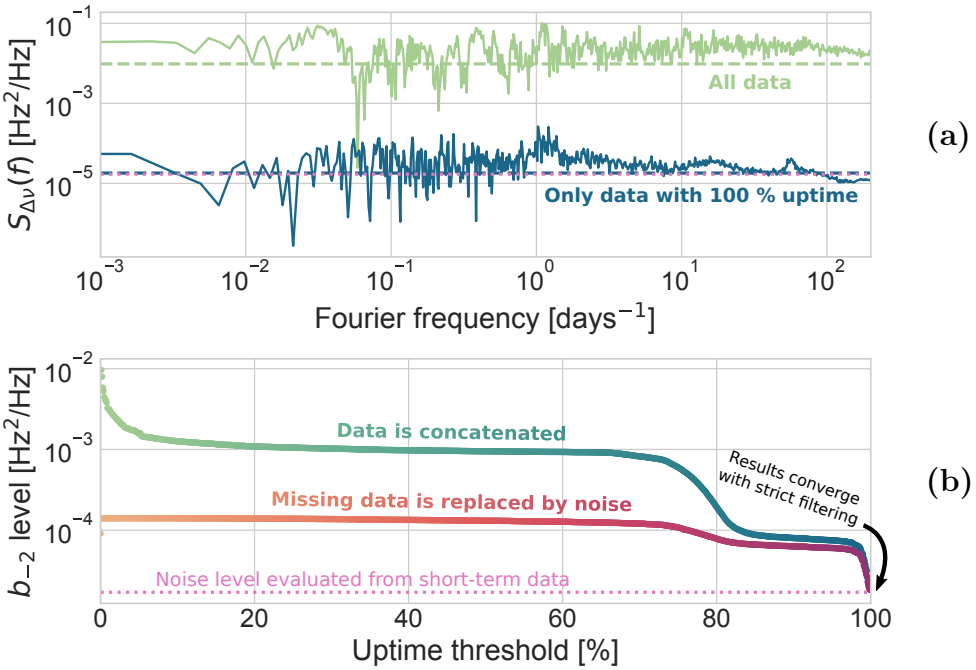

FIGURE 4.12: (a): Frequency PSD of Link B over 1890 days, using all data (green), and only using stacks of data with 100 % uptime (blue). In both curves, data has been concatenated. (b): Noise level of the spectra, after applying an uptime criteria on the stacks of data, when concatenating the remaining data (green to blue gradient), and when replacing the missing data with simulated noise (orange to purple gradient). Both noise levels converge at the short-term evaluation of the link noise, shown in pink, and discussed in chapter 3.2.

data have been concatenated, both before and after being stacked. The light green trace shows the frequency PSD of all stacked data, and the dark blue

trace where only stacked data with an uptime of 100 % is included. We see a white noise behavior of the link, since the "new" gate-time of 216 s is much larger than the coherence time of the link at 87 s. The level of white frequency noise, b_{-2}, can approximately be calculated as the mean PSD level.

Varying the criteria of the uptime of the new data points, I have calculated the b_{-2} parameter for a continuous amount of PSD spectra, i.e. all the spectra between the two traces in figure 4.12(a). These levels are shown in figure 4.12(b), both where data is concatenated (green), and where missing data has been replaced by simulated noise (red). Here, it is clear that the b_{-2} noise level changes in stages: for the concatenated data set, after an initial steep drop-off, the noise level is at $b_{-2} \approx 1 \cdot 10^{-3}$ between an uptime criteria of ~ 10 % to ~ 70 %, and between ~ 85 % to ~ 98 %, the noise level is around $b_{-2} \approx 1 \cdot 10^{-4}$. The data set where missing data has been replaced by simulated noise, has no steep initial drop-off for a low uptime criteria. Between a threshold of 0 % and ~ 70 %, the noise level is at $b_{-2} \approx 1 \cdot 10^{-4}$, and between ~ 80 % and ~ 98 %, it drops to $b_{-2} \approx 5 \cdot 10^{-5}$. Figure 4.12(b) shows that the two different ways of handling missing data gives reasonably consistent results for uptime thresholds above 85 %. This means that, if one is purely interested in knowing the noise level of the long-term data set, by applying an uptime threshold at 85 % or more, one can obtain a consistent evaluation without replacing the missing data with simulated noise.

Applying a threshold of 100 %, both noise levels converge with the value obtained at the short-term evaluation of Link B from chapter 3.2, at $b_{-2} = 1.7 \cdot 10^{-5}$. This is shown by the pink dotted lines in figure 4.12 (a) and (b)[1]. When the data stacks with an uptime of less than 100 % is removed, the uptime of the resulting data set drops with $1/4^{\text{th}}$, to 32 %.

As discussed in chapter 4.2, concatenation of data is not a good approach for the evaluation of the intricacies of a spectrum. In both studies shown in figure 4.12(b), both curves includes a degree of concatenation, which is higher for the "concatenated" curve (green) as even the stacked data is concatenated, which is not the case for the "replaced" curve (red). Here, I use the concatenation to get a sense of the average resulting white frequency noise level. However, with an increasing uptime threshold, only the regions where the link is performing the best is included in the calculation.

To improve on the Fourier analysis, one has to replace the missing data with simulated noise, as this does not bias the Fourier frequency. This is shown in

[1]Notice: the mean noise levels b_{-2} are calculated from the full frequency PSD spectra, and not the averaged version shown in figure 4.12(a). The averaging of the spectra is purely for visual help.

figure 4.13. The light brown trace shows the PSD of all the data, where missing data has been replaced with simulated noise. The purple trace shows the PSD, including only the data stacks with an uptime of 100 %, and with simulated noise replacing the missing data occurring after applying the uptime filter.

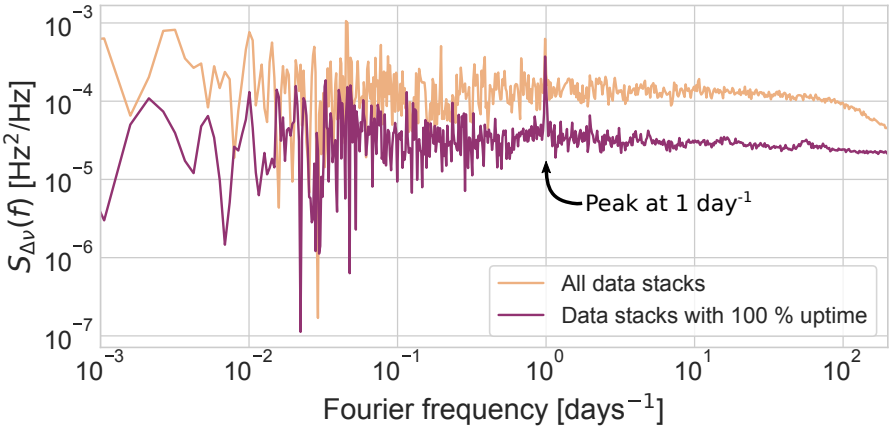

FIGURE 4.13: Frequency PSD when using all stacks of data (orange), and when only using stacks of data with 100 % uptime. Missing data has been replaced with simulated noise for both spectra.

Applying the additional filter, requiring the uptime of the stacked data to be at 100 %, decreases the noise level, in correspondence to the similarly colored trace in figure 4.12(b). Furthermore, the full spectrum becomes closer to consist purely of white frequency noise, whereas the full data set has a drop in the noise level at higher Fourier frequencies. A peak is visible in the PSD around 1 day^{-1}, which is relatively larger for the more filtered data (purple curve). We believe this peak arises from day/night temperature fluctuations in data centers, which induces a low-frequency modulation to the optical phase of the signal, in the short uncompensated arms of the interferometers. At frequencies below 1 day^{-1}, there seems to be no clear peaks arising from the noise.

In figures 4.12(a) and 4.13, four different Frequency PSD traces are shown, which corresponds to the extremes of applying the uptime thresholds for concatenated data, and where missing data are replaced with simulated noise, as shown in the two gradient curves in figure 4.12(b). In figure 4.14 the corresponding phase traces are shown. In figure 4.15, the (a): corresponding relative frequency shifts, and (b): MDEV of the corresponding data sets are shown.

The relative frequency shifts are shown in units of 10^{-19}. For the concatenated data, the shift over the 1890 days is $-0.6(12) \cdot 10^{-19}$ for the full data set, and $-3(5) \cdot 10^{-21}$ when only including the data stacks with 100 % uptime.

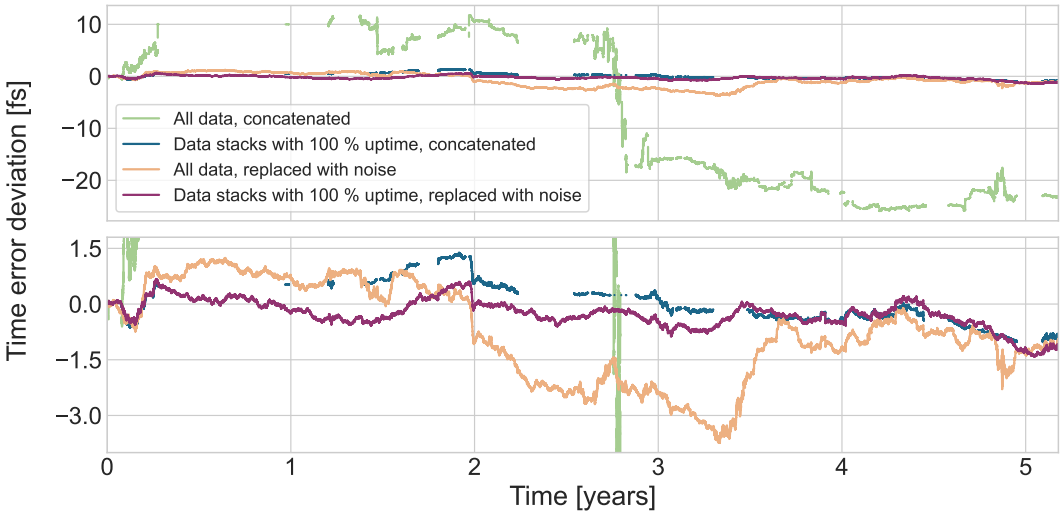

FIGURE 4.14: Phase evolution of Link B over 5 years, calculated in 4 different ways: from all data stacks (green), only data stacks with 100 % uptime (blue), all data stacks where missing data is replaced with simulated noise (light brown), and only data stacks with 100 % uptime where missing data is replaced with simulated noise (purple). Bottom plot is a zoom of the top plot.

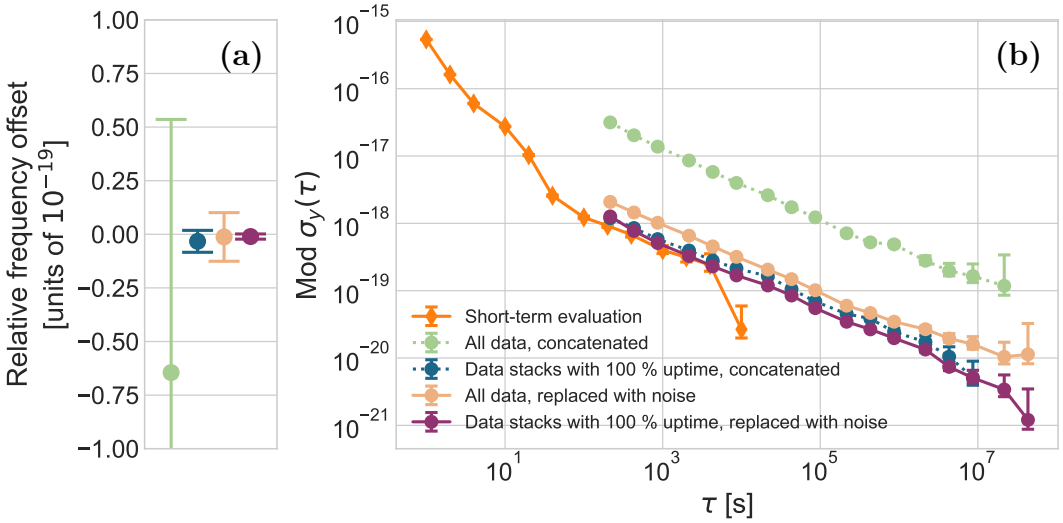

FIGURE 4.15: (a): Relative frequency offsets and (b): modified Allan deviations (MDEVs) of Link B over 5 years, calculated from the four phase traces shows in figure 4.14.

Indeed, since some stacks of data will have a very low uptime, they create a significant bias in the mean frequency shift. The big difference in the uncertainty is likewise clear in the MDEV, between the two curves. Here the difference is almost one order of magnitude at 216 s, and 1.5 orders of magnitude at long term.

A difference is also seen in the data sets, where missing data has been replaced with simulated noise. When the full data set is used, the relative frequency shift is $-0.1(11) \cdot 10^{-21}$, and when only the data stacks with 100 % uptime is used the shift is $0.2(25) \cdot 10^{-22}$. This discrepancy arises from an effect which is also present in the concatenated data, but in that case is not dominating: the filtering criteria applied, which removes all data points if there is just one outlier in a 216 s segment, strictly filters regions where outliers are present. This ensures only the "best behaving" regions are included. Naturally, since this decreases the amount of "real link" data points with 25 %, it can also be seen as a slight bias for already pre-filtered data. These frequency shifts are compatible with zero, as expected for stabilized fiber links, as explained in chapter 3.3. Indeed, as long-term goal of coherent fiber networks are to be operating continuously, potentially ensuring a continuous comparison of optical clocks, it is important that the link does not induce any frequency shifts at long term. This is an important result towards the redefinition of the SI-second.

Figure 4.15(b), shows good correspondence between the short-term and long-term stability of the fiber link, which is visible at integration times between 200 s and 4 000 s. This shows that, even on very long term, the link operates relatively predictable. This means that the link indeed can be considered stationary at a wide sense, on the scale of a few years. Furthermore, it shows that using simulated noise to replace the missing data gives converging results, even on timescales of several years.

Chapter 5

International comparisons with a fiber network

In chapters 3 and 4 I show a model of fiber links, and introduce a methodology to asses their performances with missing data. In this chapter I will show how to use these tools in the frame of optical clock comparisons in Europe.

I will first describe the main components of the European fiber network, enabling comparisons of optical clocks between four European NMIs. I will describe the specifics of the frequency chain used in the comparison in greater details, which enters the uncertainty budget of a comparison. I will focus on the setup between the French NMI SYRTE and the German NMI PTB as a case study.

Showing the general structure of this clock network, I will show how the optical fiber links are used as one among other means for clock comparisons, all of which relies on very different types of paths and technologies. These complex networks require supervision and efficient data processing which, with the upcoming optical time scale(s) generation and their comparison in mind, is a global objective pursued by several laboratories.

For the French REFIMEVE network this is very true, both in the context of clock comparisons, but also in the context of the service delivered by REFIMEVE to the many laboratories, aiming at a high level of uptime of the signal, and quick access to the data. I will then give a brief description of the global server structure of REFIMEVE, illustrating the global context of the studies shown in this manuscript. Here, I will show how the data processing software I have created, is a useful tool for the reliable operation of such a fiber network. I will describe the software, and which opportunities it provides, both in the context of the evaluation of the performance of the fiber network, as well as in the context of fundamental studies using fiber links.

I will then show a case study of an evaluation of an optical clock comparison campaign in March 2022. I will go through different sources of uncertainty from the French network, ranging from remote synchronization with the Network Time Protocol (NTP), remote frequency referencing, and uncompensated fiber noise, enabling the construction of an uncertainty budget contribution of the French network for the clock comparisons.

After, I will discuss a four months long comparison campaign between SYRTE and INRIM, during the winter 2021/2022. This campaign set a new milestone in international optical clock comparisons with fiber links. With the 1716 km long Link E between SYRTE in Paris, and Modane at the French-Italian border, this is the longest operating fiber link for a comparison of optical clocks. For the clock comparisons between SYRTE, NPL and PTB, the signals from two laboratories were disseminated to a mid-point between the two institutes. During the campaign between SYRTE and INRIM, the signal from SYRTE was disseminated all the way to INRIM, where the comparison was performed. This includes 2×869 km fiber link in France, and 2×154 km in Italy. The complexity of such a long dissemination is high, including many EDFAs, one MLS, and seven RLSs. Lastly, the four months of comparison campaign was the longest long-haul optical clock comparison to date, and four times longer than the previous record from 2019. I will compare the performance of Link E during the campaign, with the performance of other French links, during previous and later campaigns.

Lastly, I will show a study of the evaluation of the statistical performance of Link B during a one month long optical comparison campaign, where I consider the link signal sampled by the uptime of the comparison. I present an evaluation of the total uncertainty contribution of the REFIMEVE fiber link to such a comparison.

5.1 An international network of NMIs

For the steering of the TAI by the Bureau International des Poids et Mesures (BIPM), atomic clocks around the world are compared mainly using GNSS satellites with various methods, as common view (CV), precise point positioning (PPP), and integer ambiguity precise point positioning (IPPP) [67, 68]. At long term, the IPPP technique is limited to a fractional instability in the low 10^{-17} within a month [68]. IPPP links is very attractive as an alternative comparison method to the fiber links, as it potentially connects all NMIs [68]. two-way satellite time and frequency transfer (TWSTFT) are also deployed with

specific emitters and receivers, and a dedicated telecommunication channel [69, 70, 71, 66]. At long term, the TWSTFT technique is limited to a fractional instability in the low 10^{-16} within a month. More specific microwave links are developed for the Atomic Clock Ensemble in Space (ACES) mission, linking NMIs to the International Space Station with similar performance levels [58]. More exploratory techniques develop optical links in free space, that can achieve fractional instability of 10^{-19} or lower within a day, but with a limited range of about 100 km for the most recent reports [72, 73, 74, 75, 76, 77]. It was shown recently that a very-long-baseline interferometry (VLBI) observatory connected by a fiber link enables clock comparisons between NMIs in Italy and Japan [78], with a fractional instability of 10^{-16} or lower within tens of days. Such an experiment was also run recently between INRIM and Korea Research Institute of Standards and Science (KRISS) in the Republic of Korea.

The simultaneous use of different means of comparison is a completely novel situation, very interesting for time and frequency (T/F) metrology, in order to eliminate any potential systematic effects of the means of comparison. In the future, any NMI can run at least two of these novel methods. Housing also several optical atomic clocks, this indeed provides a complex system of comparison of a number of different atomic references, from several institutes around the world, using different comparison techniques. Such efforts are already reported. For instance, cross-comparisons of ensembles of atomic fountains and optical clocks, inter-compared with IPPP and TWSTFT, were achieved in Europe to the 10^{-16} level and was recently reported [66]. Such a complex and multi-technique clock comparison infrastructure enables the measurement of the difference in gravitational potentials, between transportable optical clocks and an ensemble of statically operated clocks, enabling so-called chronometric geodesy [79, 80, 81].

Such a resolution is sufficient for the comparison of microwave atomic clocks around the world. However, this is not sufficient for the comparison of state-of-the-art optical clocks, which claims uncertainties in the low 10^{-18} within a day [82, 83]. It is a desired goal in the community to reach an assessment of the uncertainty of optical clocks within a few hours. Currently, only coherent optical fiber links shows this ability for a continental optical clock comparison: On shorter ranges, there is already optical clock comparisons that combines optical fibers and optical link combs, as it was reported in Boulder, Colorado, USA [84].

As detailed in chapter 2.3, the French REFIMEVE network currently includes 5 operational national links. Furthermore, international connections in

Villetaneuse (North of Paris), in Strasbourg, and in Modane, ensures connections to the European partner NMIs NPL, PTB, and INRIM. This is illustrated in the map in figure 5.1.

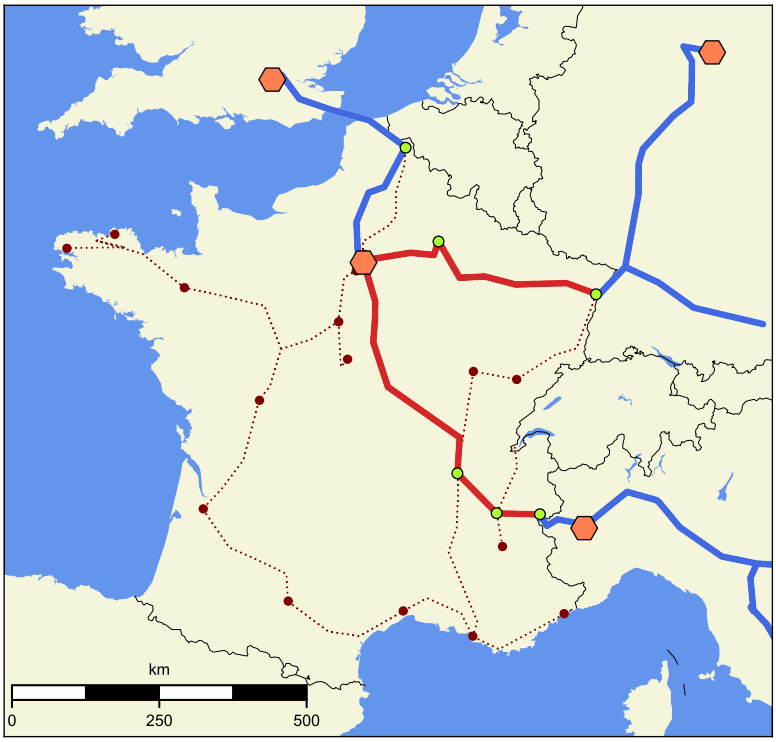

FIGURE 5.1: Map of fiber links operated by the EU consortium ROCIT during international optical clock comparisons, spanning from 2018 to 2022. The relevant REFIMEVE links are highlighted with red continuous lines, and other REFIMEVE links are shown as dashed lines. Blue lines indicate international links, operated by partner NMIs, and orange hexagons shows the locations of the four partner NMIs.

In the frame of the European project Robust optical clocks for international timescales (ROCIT), clock comparisons with IPPP and TWSTFT have been performed between the Paris Observatory, Valtion Teknillinen Tutkimuskeskus (National Technical Research Centre) (VTT) in Finland, NPL in England, and Uniwersytet Mikołaja Kopernika w Toruniu (UMK) and Space Research Centre of Polish Academy of Sciences (SRC PAS) in Poland. Furthermore, a high number of institutes are connected with satellite techniques, for a potentially even more complex comparison network.

5.1.1 Continental clock comparisons

A continental clock comparison is conceptually the same as a world wide comparison, with the sole difference that a comparison through optical fibers are,

so far, only possible continental. As with the specific European connections shown in figure 5.1, this can, and probably will, be more complex in the future, including several other European NMIs or other metrology laboratories. Such a complex network must be able to compare any number of different clocks, oscillators, or lasers, all operating at, in principle, arbitrary frequencies. Naturally, this requires vastly different hardware, as well as different means of comparison, as the fundamental and technical challenges differs greatly depending on the nominal oscillator frequency, stability and accuracy. In that frame a universal formalism was developed and reported [85], enabling clock comparisons of any kind with sufficiently low uncertainty.

In the following I will describe the principles of remote clock comparisons as performed by SYRTE and the European partner NMIs. A case study of a comparison between SYRTE and PTB will be shown. I will describe the setup used in the comparison between the two NMIs at UoS in Strasbourg. The gen-

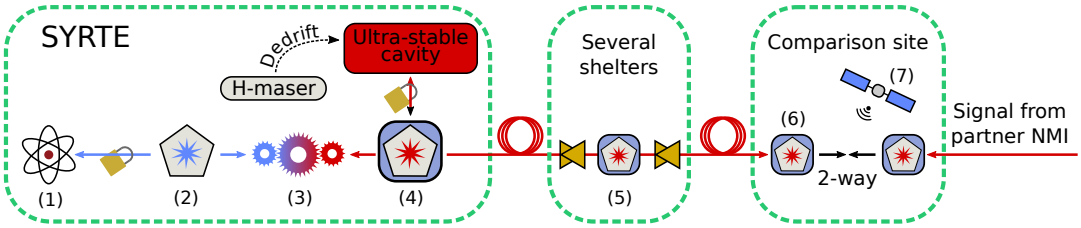

FIGURE 5.2: Optical frequency chain in the French network during an optical clock comparison between SYRTE and PTB. (1): Atomic reference. (2): Clock laser. (3): Frequency comb. (4): Transfer laser, as part of a repeater laser station (RLS). (5): several EDFAs and RLSs along the link. (6): Two RLSs enabling a two-way (TW) comparison, and downlink dissemination. (7): GNSS frequency reference.

eral scheme of the frequency chain of the remote comparison is illustrated in figure 5.2: a clock laser is locked to the atomic reference by an active feedback loop. The clock laser is measured against the transfer laser at 1542 nm using an optical frequency comb. The transfer laser is locked to an ultra-stable cavity, which is actively dedrifted by an H-maser. The ultra-stable signal is disseminated through the REFIMEVE network, being amplified and regenerated as described in chapter 2.2. At the comparison site, the signal from the partner NMI arrives as well. A beat-note between the two transferred signals is generated. The beat-note is amplified and filtered, and its frequency is measured with a remote dead-time free frequency counter. The counter is referenced on short term by an oven-controlled crystal oscillator (OXCO), which is referenced by a GNSS signal, removing the long-term drift, which will be present for the quartz oscillator. This provides an accurate enough 10 MHz reference, which is detailed

in chapter 5.3. For a full comparison between the two atomic references, the full frequency chain is monitored at all times. The frequency differences between each link in the chain is continuously recorded, and is validated by the responsible scientist(s). The validation of each measurement is different between any subsystems.

5.2 Palantír: the software backbone

Historically, a comparison of atomic clocks could only be performed in two ways: either by physically moving a clock from one place to another, or remote comparisons through GNSS links, which are still being used to this day. An ensemble of links connecting several remote clocks is called a clock network, and an illustration of such a clock network is shown in figure 5.3. At the Paris Observatory,

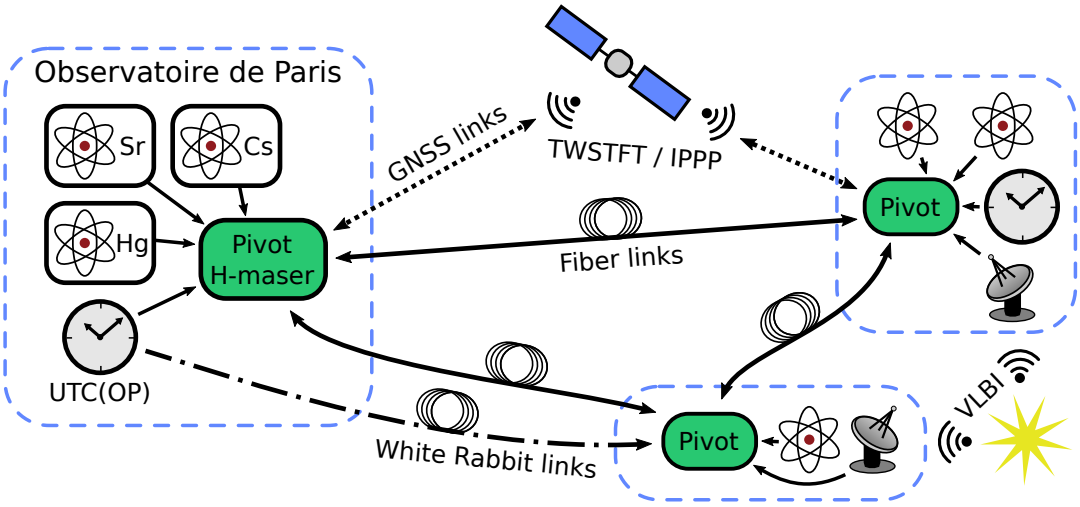

FIGURE 5.3: Illustration of a network of atomic clocks. The representation of the Paris Observatory includes the Cs, Sr, and Hg atomic clocks, as well as the generation of the timescale UTC(OP). The two other laboratories are arbitrary representations, and does not illustrate any specific laboratories. The inter-comparison of the atomic clocks in different laboratories, are illustrated with a number of different means of comparison: GNSS links, fiber links, and VLBI comparisons.

different primary and secondary frequency standards are built and operated, in the form of 3 atomic Cs (and Rb) fountains, including one transportable, and 3 optical lattice clocks, two Sr, and one Hg. In the future, a transportable Yb clock should join the frequency standards ensemble. These atomic clocks contribute to TAI through very regular reports through the circular-T, and to the realization of the French national timescale UTC(OP), that is the basis of the legal time in France. Referenced to a pivot H-maser, these atomic frequency

standards can be compared to similar frequency standards in other NMIs, as illustrated in figure 5.3. Here, the inter-comparison between three different laboratories are illustrated, which can be done through several different means of comparison: TWSTFT, IPPP and GNSS time-calibrated receivers, through VLBI, or using optical fibers, which is the focus of this manuscript. The complexity of modern clock networks can include any number of laboratories, each with different species atomic clocks, and ultra-stable lasers. These can be compared through a number of different means of comparison. This requires a large amount of continuously operating hardware, automation, and supervision, for all parts of the global clocks network.

5.2.1 Requirements of a fiber network

With the still growing complexity of the REFIMEVE network, efficient and powerful supervision is key for an overview of the full network. For the day-to-day managing of the network, different subsystems can be supervised by different companies and people. At SYRTE, we have implemented supervision systems for the laser source and the generation of the REFIMEVE signal, as well as a large part of the instrumentation for remote measurements in-field. The equipment set for the metrological network is communicating with the Network Operating Center of RENATER, that can set any equipment on the network on or off, and issue tickets when an alarm is raised, and when work is on-going on the fiber backbone. An additional layer of the supervision of the network deals with the proper functioning of the equipment in the network. This operational part of the supervision of the optical frequency transfer is largely subcontracted to a company, iXblue, that manufactures the RLSs, and supervises the RLSs and EDFAs. Regarding the White Rabbit (WR) network that provides the reference signal in the central hub, TH2, in Paris, the supervision integrate the supervision tools of SevenSol, that is now part of the company Orolia. The interface between these subsystems is still on-going.REFIMEVE continuously monitors the hardware in the network such as EDFAs, RLSs and MLSs. Dedicated engineers enrolled by the academic or by the subcontractors are able to quickly intervene if any problems arise.

For the monitoring of the heart of the signal and optical frequency chain at SYRTE, I have developed a dedicated software which has been named *Palantír*[1]. This software is build to be a processing engine, capable of processing and making a metrological evaluation of any data in the REFIMEVE network.

[1]Singular form of *Palantíri*, magical crystal balls found in Middle-earth [86].

5.2.2 Global structure

Palantír itself is part of a more global software and computing structure, that was developed with the increased complexity of the network, and the EU design study of CLOck NETwork Services (CLONETS). The system is illustrated in figure 5.4. Here, the content and roles of the three main internal servers are illustrated. These servers are mostly located at SYRTE, but includes also remote machines around the network, which drives frequency counters or other types of hardware, measuring the signals and saving the measurement data files.

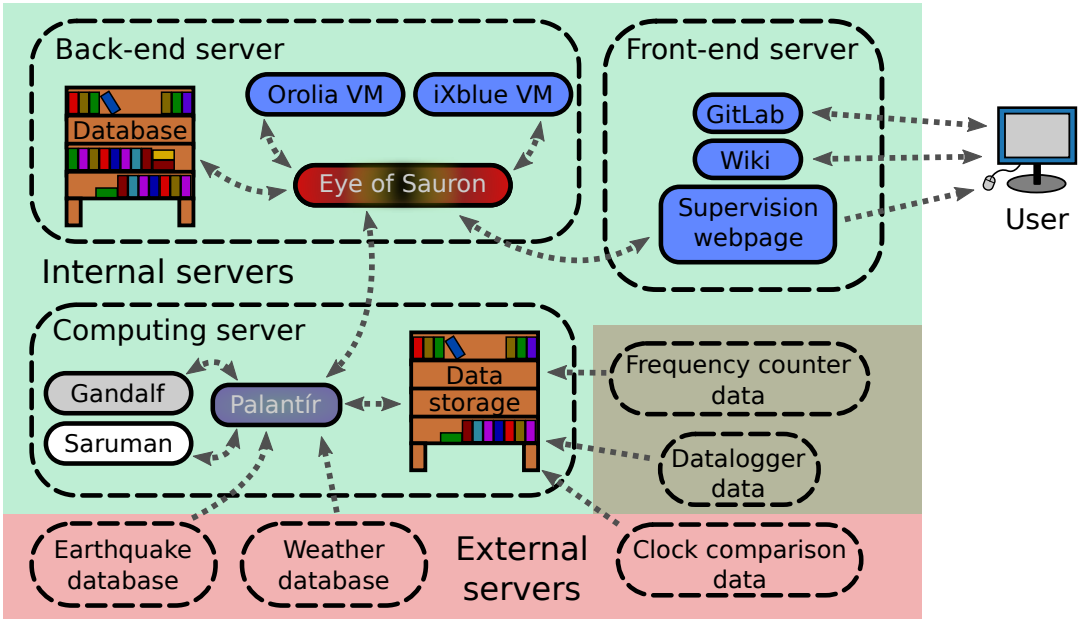

FIGURE 5.4: Illustration of the structure of the internal servers at SYRTE, consisting of a front-end server, a back-end server, and a computing server, shown in the green region. The red region indicates a non-exhaustive list of external servers with data used for computations by the Palantír software. The overlapping region indicates types of data that can be found both on internal and external servers.

The internal servers at SYRTE consists of three main servers:

- **the front-end server**, which host the activities directly interactable by the users of the REFIMEVE network. This includes an open-source GitLab, a wiki with information about structure of the links, interpretations of different types of data, etc, as well as a supervision web page. However, these services are still at their infancy. It is also planned to set up a web page from the supervision, so that users will be able to track the performance of their required link in real-time, as well as having access to the required data and uncertainty evaluations needed for their measurements, after secured authentication.

- **The back-end server**, hosting virtual machines (VMs) and the database. The supervision VM, named the *Eye of Sauron* [87], will be the focal point of the global supervision, interacting with the hardware supervision of subcontractors. This allows it to collect data of the hardware monitored by the industrial partners, while providing them metrologically processed data and status of the network. The Eye of Sauron will take requests from the supervision web page, and process the requests using the Palantír software. The database contains information on parameters used for the data processing, which will depend on the requests from the users. Subcontractors will each have access to a VM, from where they are able to request similar data and uncertainty evaluations from the Eye of Sauron.

- **The computing server**, which contains the Palantír software as well a data storage. Data is gathered from the whole network across France, and is collected to the same server, reducing the computational complexity of the data processing, as well as backing up the data. This includes data generated by partner NMIs during clock comparison campaigns, allowing a real-time processing of the comparison data. Furthermore, the Palantír software connects to external databases to gather information about earthquakes, meteorological temperature measurements, and more. The Palantír software and the two current modules for scientific data analysis, *Gandalf* [88] and *Saruman* [89], are detailed below.

5.2.3 Data processing

The structure and interplay of the servers is still evolving, and the increasing access to different data increases the computational possibilities of the software. The Palantír software, in itself, is able to take requests to process and validate any type of data in the network. This can be done for any desired time and duration. The detection of outliers and bad regions in time series data is done automatically with the general principles described in [90]: the filtering is performed in several stages, applying increasingly narrow and subtle filters. These filters are based on the frequency trace of the data, the rolling mean and rolling standard deviation of the frequency trace, and more when needed. Referencing the database, which stores information on filtering parameters for a given fiber link measurement or other data type, the same filtering procedures can be applied to any time series data recorded in the REFIMEVE network. Depending on the request of the users, the level of the filtering of the data might change. For an optical clock comparison, the tightest filters are required, not

to induce any error into the comparison of the ultra accurate and stable optical clocks. The need of the users of the network is typically more relaxed, with a short-term stability of a few 10^{-14} often being sufficient. With the data of the network being stored on the same machine, data can be loaded and processed fast. This is essential for the supervision of the Eye of Sauron, which requires a real-time status of the network, in order to raise alarms if anything goes wrong.

Palantír enables scientific studies, which are shown and discussed in this manuscript. So far it has been used in two main modules:

- **Saruman**: engine for generating simulated noise, using the principles described in chapter 3.4. This is also used in the fill-in method to mitigate aliasing effects from missing data, as detailed in chapter 4.2.
- **Gandalf**: the machine learning engine developed by Hendrix Montalvan Leyva, Université Paris. This has been used in the identification of seismic events in the fiber network, which is detailed in chapter 6.2.

5.2.4 Palantír for clock comparisons

During an optical clock comparison campaign, the Palantír software plays a central role for the French network. As described above, it allows for a complete view of the many components and links in the network, which is needed for an accurate assessment of the uncertainty induced by the network. Furthermore, it allows for an automatic processing of the data in the network, which ensures an on-the-fly evaluation of the network status. Indeed, it is important for the many colleagues both at SYRTE, LPL and the other partner NMIs, to know whether the network is working and the clocks can be compared at any given time, and if any action is needed upon their responsibility.

The reporting of data for a comparison of optical clocks can be quite complex, as the total frequency chain consists of many different subsystems, which consists of different types of clocks, lasers, cavities, combs and links, which can be operated all at different frequencies. As already mentioned, a universal formalism was proposed [85], which was adopted for the comparison campaign in March 2022. This formalism consists, for each couple of consecutive subsystems in the frequency chain, in a set of customized metadata stored to a *.yaml* format text file. Such a new standard protocol, acting as a small information system for the campaign, allows the automation of the computational data treatment. Therefore, the resulting frequency ratio needs little to no handmade correction. Here, I will give a brief summary of how this formalism is implemented for the fiber links in the French network.

In the French network, we report three different values during a clock comparison campaign:

1. **The time stamp**: each measurement is reported with a gate-time of $\tau_G = 1$ s. The synchronization of the time stamps is done with the NTP, as discussed in chapter 5.3.

2. **The frequency difference between the two stations of the link**: the frequency of the disseminated signal will be slightly shifted at fixed frequencies throughout the network, depending arbitrarily on the settings of the AOMs at the different RLSs, typically at a few tens of MHz. For each span in the network, this frequency difference is reported each second.

3. **The validity of the frequency dissemination**: based on the filtering procedures described above, a validity of the frequency transfer is calculated, filtered to a level sufficient for the comparison of the optical clocks.

Along with the reported status of the frequency dissemination, an extra file is required to be able to properly read and process the reported frequency difference values. The frequency difference between two stations in a link, station A and station B, is calculated as the *reduced frequency ratio*

$$R_{A\to B}(t) = f_B(t) - \frac{\nu_B}{s_B \nu_A} f_A(t). \tag{5.1}$$

Typically, we report the frequency difference in Hz, and report the carrier frequencies as $\nu_A = 194$ THz and $\nu_B = 194$ THz, and the division factor as $s_B = 1$. Furthermore, we need to report the settings of the frequency counter used for the measurements. This is more cautionary, as the formalism needs to be adapted to include any future type of frequency comparison. In the case of the reported frequency values of microwave fountain clocks, measurements are chosen to be averaged and reported every 864 s, with the timestamp given by the middle value of the given duration. In the case of the French network, as well as the rest of the optical clock comparison chain, we report one frequency value every 1 s, with the time stamp being given by the end of the duration. By reporting these settings, it is possible to automatically compare the different oscillators, working at different frequencies and in different intervals, to each other.

5.3 Synchronization and syntonization

For users of the REFIMEVE network, synchronization and syntonization of the network is essential to ensure the accuracy of the comparison and the traceability of the signal. This allows them to access information on the performance of the network in the past and present, helping the users to reliably perform measurements, traceable to UTC(Paris Observatory (OP)), and calculate the uncertainty contribution from the fiber links. Synchronization and syntonization is essential for a clock comparison, as the frequency differences needs to be recorded and compared at the same time intervals. Otherwise, an error in time will be introduced, which with a non-stationary frequency signal will correspond to an error in the frequency comparison. In the following I will calculate the uncertainty contribution of the French network to an optical clock comparison, showing a one month case study of an optical clock comparison campaign between SYRTE, PTB and INRIM in March 2022. In this period the network was properly synchronized and syntonized. I will show a comparison with a previous period where the syntonization was off, illustrating how quickly the error of the remote measurement will increase in the case of problems with the remote references. I will focus the study on the comparison of the SYRTE and PTB ultra-stable cavities, calculating the error induced by the remote desynchronization and frequency references. I will not study the full frequency chain with relation to the optical clocks however, as these results are out of the scope of this manuscript.

5.3.1 Cavity comparisons

The comparison site used for the comparison between SYRTE and PTB is at the UoS in Strasbourg, roughly at the mid-way point between the two institutes. As detailed chapter 2.3, the optical signal from SYRTE is disseminated through an 11 km fiber link to a data center, where it is regenerated by an MLS. From here it is disseminated to Strasbourg through a 700 km long fiber link, being regenerated once in Reims after 223 km. A second fiber to transfer the signal back from Strasbourg to Paris, where the E2E measurement is performed in the MLS. In Strasbourg, the German signal arrives from the north-east, and an RLS regenerates the signal and sends it back to Braunschweig. The user output of these RLSs in Strasbourg is used to perform a two-way measurement: the two beat-notes are amplified, filtered and measured, and the half-sum of the beat notes perform the comparison between the near-infrared lasers operated at PTB and at SYRTE.

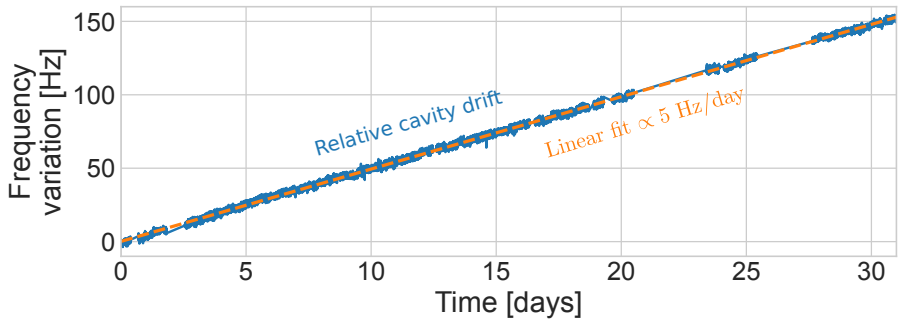

FIGURE 5.5: Variation of the two-way comparison between the ultra-stable cavities as SYRTE and PTB, for the duration of 1 month. Orange dotted line shows a linear fit, with a relative drift of 5 Hz/day.

Figure 5.5 shows the relative frequency drift between the two cavities over the span of the one month of comparison campaign, March 1st - 31st 2022. A frequency offset of 1.886 MHz, corresponding to the frequency difference between the two RLSs at Strasbourg at the beginning of this measurement session, has been removed. In post-processing, the data has been filtered. Since the relative drift of the two cavities is not centered around 0 Hz, a first step is to remove the rolling mean of the data. With a data set then centered around 0 Hz, regular filtering procedures can be applied. These procedures removes outliers and rogue data points from the two-way. In the end, a strongly linear relative drift between the two cavities, of ~ 5 Hz/day is revealed.

This relative drift arises from several reasons, among which the ultra-slow expansion of the optical cavities, that are fundamentally unavoidable but, that can be reduced with technological advancement. For instance, crystalline coatings [91]. Great effort has gone into pursuing low-drift cavities, which has primarily been motivated by the search for the ultimate performance of optical clocks, and for fundamental physical studies such as the search for dark matter. In the context of clock comparisons, the relative drift of the cavities determines the level of required synchronization at the comparison site in Strasbourg: a drift of 5 Hz/day corresponds to a relative frequency drift at one second of

$$\frac{d\Delta_{AB}(t)}{dt}\frac{1}{\nu_0} = \frac{d\left(\nu_B(t) - \nu_A(t)\right)}{dt}\frac{1}{\nu_0} \propto \frac{5 \text{ Hz/day}}{86400 \text{ s/day}}\frac{1}{\nu_0} \approx 3 \cdot 10^{-19} \text{ s}^{-1},$$

with ν_0 being the optical carrier at 194.4 THz. To keep the error below the desired goal of 10^{-18}, this would require the error of the synchronization of the comparison site to be within 3.4 s, a requirement which is well fulfilled as detailed below.

5.3.2 Synchronization of computers

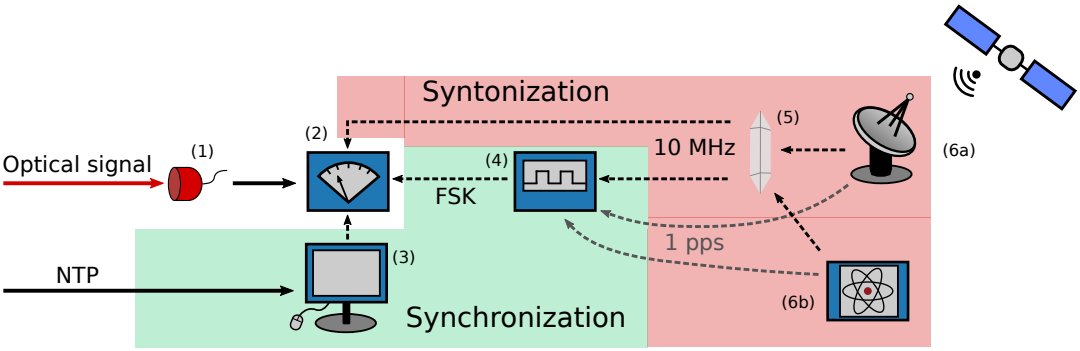

FIGURE 5.6: Synchronization (green area) and syntonization (red area) of a remote frequency counter. (1): Photodiode. (2): Frequency counter. (3): Computer driving the counter, synchronized by the NTP. (4): Frequency-shift keying (FSK) signal. (5): OXCO. (6a): GNSS reference. (6b): Rb clock reference.

The frequency counters used in the REFIMEVE network are controlled by computers. When the data are streamed out to be saved on such a computer, a timestamp given by the time machine of the computer is associated to each data. The time of the remote computers in the network is synchronized using NTP, which is illustrated in the green part of figure 5.6. NTP is a protocol that offers a rough synchronization based on an estimation of the delay of the internet link and the offset between the emitters' and receiver's time machine. The NTP can log the information of the delay and offset. Using the Palantír software, we process the delay and offset of the NTP synchronization, that we set to log every 5 minutes, for the whole network. The Eye of Sauron raises an alarm in case of problems with the synchronization.

Figure 5.7 shows the delay and offset of the NTP engine at the comparison site in Strasbourg for the duration of the campaign. The delay corresponds to the travel time of the signal from the NTP server to the remote computer, and back. This delay correspond to the transit time of the photons, plus the delay for each electric-to-optic and optic-to-electric conversions, plus the processing time of the data routers. The offset describes the time difference between the clock of the remote computer and the clock of the NTP server, corresponding to the uncompensated delay. The mean offset over the one months is 0.0083 ms, which corresponds to an average relative frequency shift of the cavity comparison of

$$\frac{d\Delta_{AB}(t)}{dt} \cdot 8.3 \cdot 10^{-6}\ \mathrm{s} = 2.4 \cdot 10^{-24}. \tag{5.2}$$

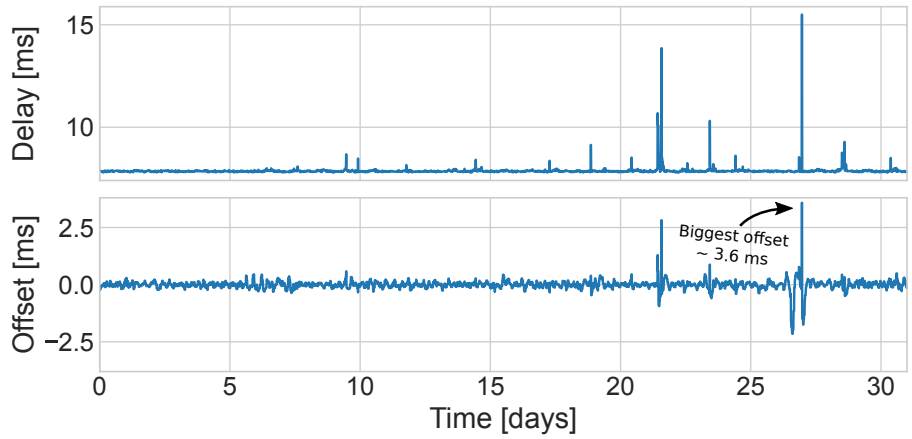

FIGURE 5.7: Delay (top) and offset (bottom) of the NTP synchronization of the computer driving the frequency counter in Strasbourg, over the span of one month.

The largest fluctuation highlighted in figure 5.7 is at $\sim$ 3.6 ms, corresponding to a shift of $1 \cdot 10^{-21}$ for the corresponding data point. Over one month the computer in Strasbourg had a median delay of 7.85 ms, which is compatible with the travel time of the optical signal between SYRTE and Strasbourg of 6.6 ms, as described in chapter 2.3. A total of $7.85 - 6.6 = 1.25$ ms delay is not accounted for, which sets an estimation of a systematic uncertainty contribution of

$$\frac{d\Delta_{AB}(t)}{dt} \cdot 1.25 \cdot 10^{-3}\ \mathrm{s} = 3.7 \cdot 10^{-22}. \tag{5.3}$$

This is almost 4 orders of magnitude lower than the requirements of the network of $1 \cdot 10^{-18}$, and is much lower than the uncertainty contribution from the uncompensated noise from the fiber links.

As the whole REFIMEVE network is synchronized with NTP, there is no ambiguity in the time-of-the-day timestamp associated to a given data. The synchronization of the data relies on the synchronization of the counters, which I describe in the next section. It is possible to compare and correlate events around the network. For instance, efforts have been made to correlate detected cycle slips, which can be measured locally at the stations in the network, with outliers detected in the E2E measurements of the links. To be able to achieve such a network-wide correlation, a synchronization process like NTP is required.

5.3.3 Remote frequency counters

Syntonization

Similarly to ensuring the accuracy of the time stamps reported by the remote frequency counter using the NTP, a stable external frequency reference is required for ensuring the accuracy of the frequency measurement. As shown in the red part of figure 5.6, the 10 MHz external reference of the frequency counter is driven by an OXCO. Normally, the long-term drift of the OXCO is corrected with a GNSS signal, which is transmitted from the receiver at the campus of the UoS to the data room by WR dissemination. For earlier campaigns, the RLSs were placed in a different room, much closer to the Global Positioning System (GPS) antenna. Here, WR dissemination was not necessary, and the antenna was simply connected to the OXCO with a copper cable. During the March 2022 campaign, the OXCO was instead referenced by a local Rb clock. This allowed the additional comparison between the disseminated signal from the GPS, and the Rb clock. Figure 5.8 shows the GNSS signal measured by the

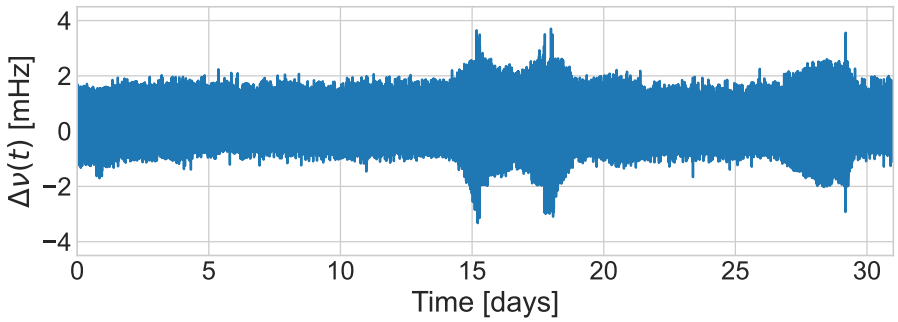

FIGURE 5.8: The GNSS signal measured against the Rb clock reference during the span of the comparison campaign.

frequency counter during the one month of comparison campaign. At long term the GNSS signal will be more stable than the Rb clock, which is dominating the long-term noise behavior of the measurement. The mean relative frequency shift of the remote reference vs GNSS receiver over the one month of the comparison is $1.7 \cdot 10^{-18}$, with an uncertainty of $1 \cdot 10^{-19}$, given by previous studies on this GNSS receiver. That result is consistent with the $1 \cdot 10^{-18}$ goal. This is primarily induced by the long-term instability of the Rb clock, which will not be present for future comparison campaigns. This furthermore emphasizes the need of parallel WR dissemination, as a simultaneous cross-check of remote frequency references would help eliminate any systematic bias.

Synchronization

With the NTP disciplined computer ensuring the accuracy of the time stamps, and the OXCO, and GNSS signal or Rb clock, ensuring a stable and accurate remote frequency reference, the frequency counters additionally need to trigger their windows of acquisition synchronously across the network. The counters we use in the network can be synchronized with a pulse per second (PPS) signal. The problem is then to remotely synchronize the counters, in Strasbourg for instance, and to perform a check of the synchronization of the counters during a clock comparison campaign. Indeed, during a previous campaign, one counter lost the synchronization due to a fault happening in the 10 MHz signal. So, a continuous check has been implemented to ensure that the counters are synchronized with a reference time signal accurately related to a timescale. In practice, we use the timescale UTC(k) of the partnering NMI when available, and GPS time otherwise. The principle of the measurement is illustrated in figure 5.6 and explained below. This technique was introduced by Daniele Nicolodi at SYRTE in 2015, and has been used to check the synchronization of all frequency counters in the REFIMEVE network since the first campaign, as well as by other NMIs like PTB, NPL and INRIM.

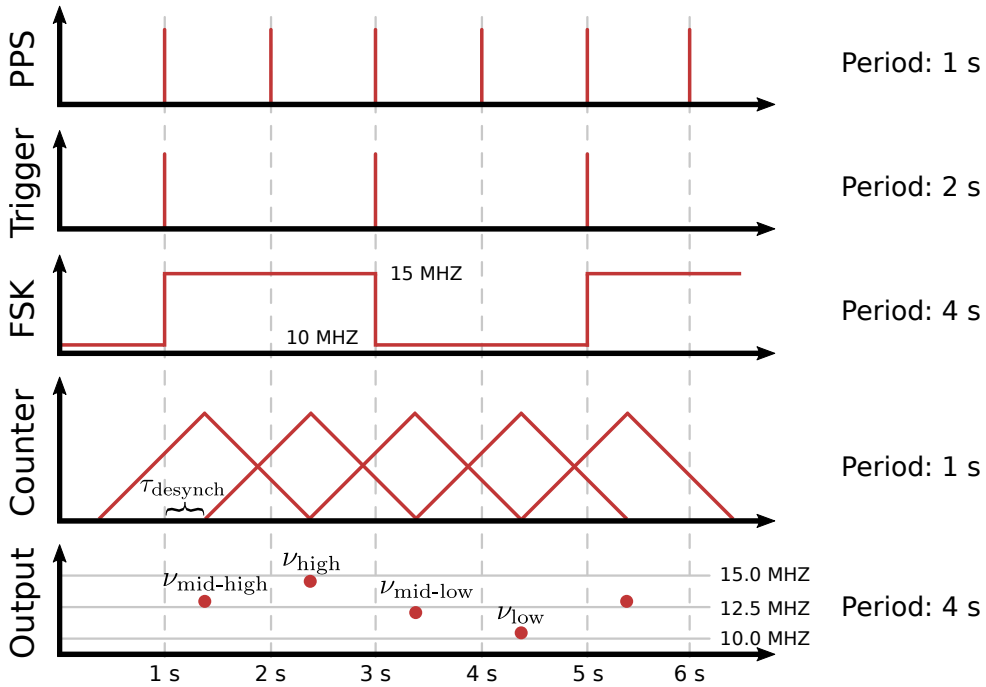

FIGURE 5.9: Scheme used for the measurement of the desynchronization of frequency counters. The synthesizer triggers on a pulse per second (PPS) signal, and creates a frequency-shift keying (FSK) signal, which gets measured by the frequency counter.

A 10 MHz reference signal, given by either a GNSS signal receiver or an

atomic clock (Rb clock for instance), is used after a distribution amplifier as an external frequency reference for a digital frequency synthesizer. Furthermore, the GNSS receiver or the atomic clock provides a PPS signal, which is illustrated in figure 5.9. A fast logic electronic divide the frequency rate of the PPS signal by two, so that the synthesizer every 2^{nd} second can trigger on a modulation input of the digital synthesizer. The synthesizer generates an frequency-shift keying (FSK) signal with a frequency jump of 5 MHz, between 10 MHz and 15 MHz, with a period of 4 s. This signal is counted by the frequency counter, which being set to Λ-mode and a gate time of $\tau_G = 1$ s, measures a triangular signal as illustrated in figure 5.9, and plotted in figure 5.10. If the frequency

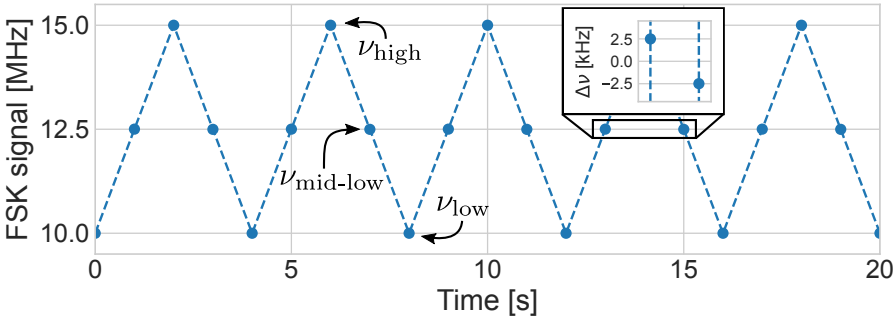

FIGURE 5.10: Frequency-shift keying (FSK) signal measured by the frequency counter in Λ-mode, over the duration of 20 s. Small insert shows the frequency difference between the two central values around 12.5 MHz ± 2.5 kHz.

counter is perfectly synchronized, it will measure the frequencies $\nu_{\text{low}} = 10$ MHz, $\nu_{\text{mid}} = 12.5$ MHz, and $\nu_{\text{high}} = 15$ MHz, with a period of 4 s. When a desynchronization is introduced as illustrated in figure 5.9, these measurement values will be slightly shifted. The closer the measured frequencies are to the 10 MHz, 12.5 MHz, and 15 MHz, the higher is the degree of synchronization. The desynchronization of the frequency counter can as such be calculated as:

$$\tau_{\text{desynch}} = \tau_G \frac{\nu_{\text{high}} - \nu_{\text{low}} - \sqrt{2(\nu_{\text{mid-low}} - \nu_{\text{low}})(\nu_{\text{high}} - \nu_{\text{low}})}}{\nu_{\text{high}} - \nu_{\text{low}}}. \tag{5.4}$$

In such a setup for an accurate time calibration, one has to consider the propagation delay from the receiver, to the 10 MHz and PPS input. However, the objective of the synchronization is to ensure an accuracy at the 10 µs level at worst, so that these delays can be neglected, at least in a first approach. Here, I show the behavior of the synchronization of the counter during the one month of comparison campaign. I found that the desynchronization was steady around 0.5 ms with very good time stability (see figure 5.11).

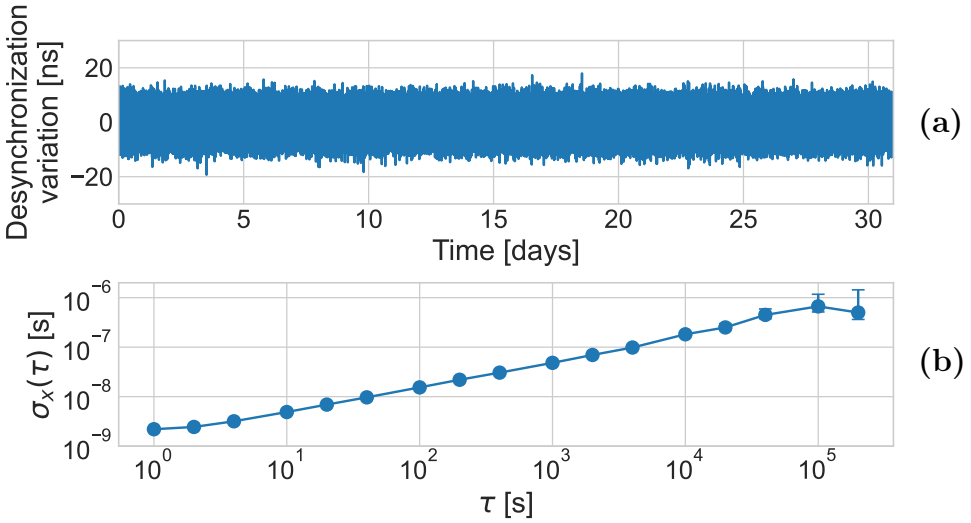

FIGURE 5.11: (a): Variation of the desynchronization of the remote frequency counter in Strasbourg, after the subtraction of the mean value of 0.5 ms. (b): Time deviation (TDEV) of the desynchronization. The desynchronization is calculated from the measurement of an FSK signal as shown in figure 5.10, by equation 5.4.

Figure 5.11(a) shows the variation of the desynchronization of the counter, showing a constant behavior over the one month for this campaign. Figure 5.11(b) shows the time deviation (TDEV) of the desynchronization. The TDEV is elaborated in appendix A. It shows a long-term time stability of 500 ns, which 1 000 times smaller than its mean. It can thereby be concluded that the desynchronization can be considered constant over the one month. Using the same calculation as in equation 5.2, a total worst case desynchronization of 1 ms (0.5 ms for each of the two counters) corresponds to a relative uncertainty contribution of $2.9 \cdot 10^{-22}$ to the cavity comparison shown in figure 5.5, which indeed can be considered negligible. Here, we have assumed the PPS and the counter to be perfectly synchronized. Because of various delays in the laboratory this will not strictly be the case, however, these delays are certainly much lower than the 0.5 ms, and can be considered negligible.

Synchronization vs syntonization - a cross-check

When performing remote measurements, it is not always straightforward to spot bugs and issues in the systems. This can either be related to the synchronization of the computer from the NTP, or any of the frequency references like the OXCO, or the GNSS signal or Rb clock. In the case of an inaccurate

frequency reference, the duration between the time stamps reported by the frequency counter will increase or decrease depending on the error of the frequency reference. The same effect will arise if the computer driving the counter is not properly synchronized with the NTP. This relative drift between the frequency reference and the NTP synchronization is expressed in the reported *decimal value* of the timestamps, which is reported with a resolution of 1 ms. The decimal value of a timestamp should be understood as the reported milliseconds, i.e. 10:43:05.XXX.

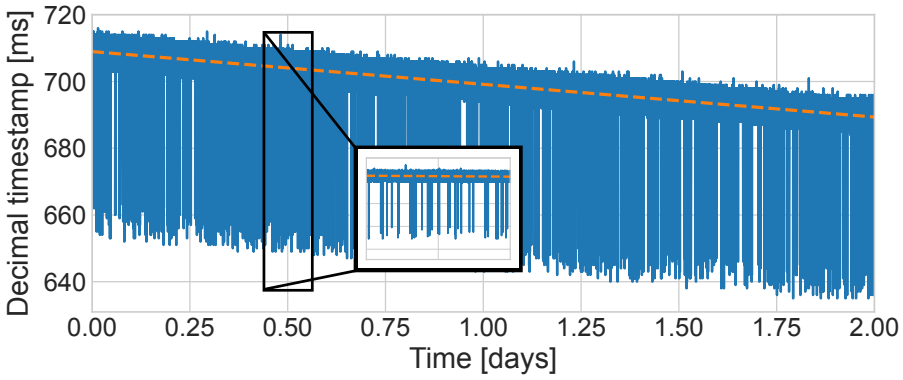

FIGURE 5.12: Decimal part of the timestamps reported by the remote frequency counter, over the duration of 2 days during the preparation of the clock comparison campaign. Insert highlights the nominal drift with anomalous jumps. Dashed orange line shows a linear fit the the nominal drift, with a slope of 9.8 ms/day.

Figure 5.12 shows the reported decimal value of the time stamps of the remote frequency counter over the duration of two days. This data was taken in February 2022, in the preparation for the March 2022 optical clock comparison campaign. The insert shows how the reported time stamps consists of a nominal linear drift, with irregular jumps of ~ 50 ms. We cannot elaborate on the origin of such jumps. It might be due to variation of the data traffic load, or to some processes in the software implementation of the NTP. The orange line shows a linear fit to the nominal drift, which reveals a drift of 9.8 ms/day. As we have simultaneous logs of the NTP synchronization of the computer, which shows no significant offset for the given duration, it can be concluded that the drift arises from an inaccuracy of the frequency reference. This inaccuracy, translated to the 10 MHz at which the OXCO operates, corresponds to an inaccuracy of the frequency reference of

$$\frac{9.8 \cdot 10^{-3}\ \text{s/day}}{86400\ \text{s/day}} \cdot 10\ \text{MHz} = 1.14\ \text{Hz}.$$

This result is consistent with a local measurement performed on site by our colleagues[2] from PTB, who performed a *frequency chirp* measurement following a method introduced in [92]. This technique imprints FSK steps similar to the illustration in figure 5.9 to the disseminated laser, directly enabling a remote measurement of desynchronization. Using this technique, they observed a frequency offset of the OXCO of 1.4 Hz.

The approach presented here to determining the offset of the local frequency reference, using the drift of the decimal time stamps reported by the frequency counter, is limited by the resolution of the time stamps reported of 1 ms, as well as the occurrence of the many irregular jumps of 50 ms, which is not included in this analysis. Nevertheless, this approach proves very convenient to determine problems with either the remote NTP synchronization or frequency references, as it can be performed from afar with decent accuracy. This is important for the supervision of a network like REFIMEVE, where it will not always be trivial to gain access to remote sites quickly, both due to travel times and restricted access of the data centers.

5.3.4 Uncompensated fiber link noise

As explained in chapter 5.1, the optical signal is disseminated from SYRTE in two main steps: first, it gets disseminated through the 11 km long Link C to a data center, which functions as a hub of the REFIMEVE network. From this data center the signal is disseminated through the 700 km long Link B to Strasbourg, where it is compared to the German signal. The German signal is disseminated in one span from PTB to Strasbourg, through a 710 km long fiber link [48]. The total uncertainty contribution the fiber links will, assuming uncorrelated noise between the three spans, be

$$\sigma^2_{\text{total}} \approx \sigma^2_{\text{Link C}} + \sigma^2_{\text{Link B}} + \sigma^2_{\text{German link}}. \tag{5.5}$$

At short timescales, the correlation between the links is most likely very small. At longer timescales of days, there could be correlated noise between the links, as they are located in each others general vicinity. A test of the level of correlation for long-haul fiber links in-field is difficult to carry out. Future extensions of the network, with double connections to a site with different paths, will provide a more robust test of correlations and improve the uncertainty budget. For now, equation 5.5 serves to indicate the upper value of a conservative uncertainty

[2] Sebastian Koke, Erik Benkler, and Alexander Kuhl

estimate, to approximate the total uncertainty contribution of residual fiber link noise to the comparison campaign.

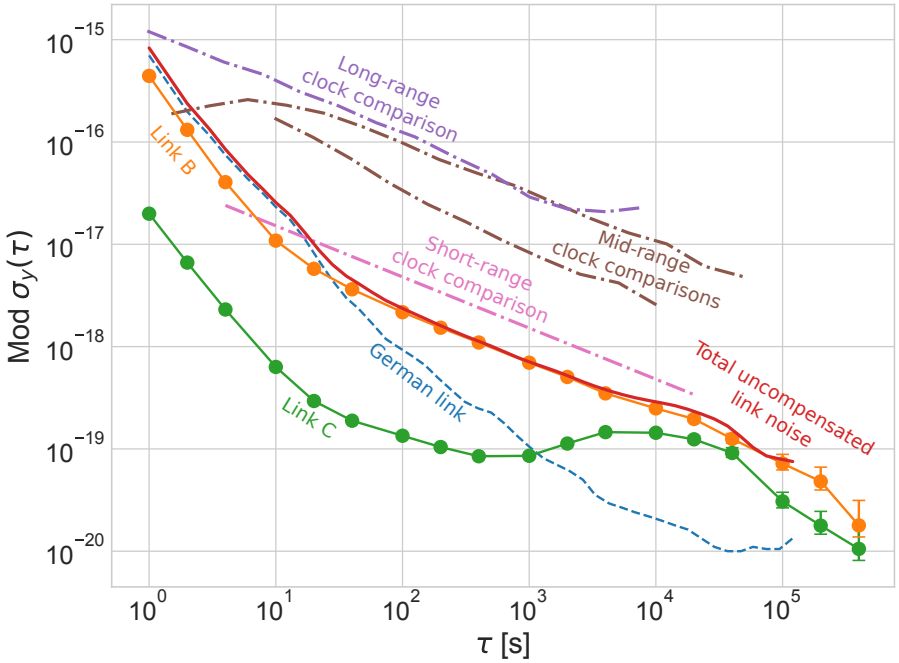

FIGURE 5.13: Modified Allan deviation (MDEV) of the two French links, Link B and Link C, during the one month of comparison campaign. The MDEV of the German link is derived from [48]. Total uncertainty of the links is calculated as a quadratic sum of the MDEV of the three links, as given by equation 5.5. Brown dot-dashed curves shows the stability of remote optical clock comparisons reported in [82] (top, long) and [84] (bottom, short). Pink dot-dashed line shows local optical clock comparison reported in [83]. Purple dot-dashed line shows long-range clock comparison reported in [40].

Figure 5.13 shows the MDEV of the French links during the one month of comparison campaign. Link B (orange) and Link C (green) shows similar behavior as presented and discussed in chapter 3.2. The uptime of the two links were 95.6 % and 99.3 % respectively over the duration of the campaign. The MDEV of the German link presented here is derived from [48], and is not from the same time period as the campaign. Therefore, the total fiber link uncertainty presented in the red curve in figure 5.13 is valid to the degree that the noise of the German link has remained relatively stationary since 2018.

The German link has a slightly higher short-term noise level than Link B in the French network. As such, it is expected to dominate the total link noise at short timescales, as seen in the red curve in figure 5.13 between 1 s and $\sim$ 30 s integration time. However, with a seemingly longer coherence time than Link B, the noise integrates faster than the French links on longer time scales, and is

not limiting the total link noise uncertainty after ~ 40 s integration time. On the longer time scales, the total link noise uncertainty contribution is indeed dominated by the French Link B. The reason for the excellent integration at long time scales for the German link is two-fold. First, there is no in-field interferometer in their setup, which is usually the dominating noise source for our fiber links at longer timescales [3]. Secondly, the servo loop of the gain of the FBAs, despite working around 11 GHz remotely, is excellent.

The dot-dashed pink curve in figure 5.13 corresponds to the most stable local optical atomic clock comparison reported to date [83], which was within the same laboratory. The brown dot-dashed lines shows the two most stable mid-range atomic clock comparisons to date [82, 84] (30 km and 3.6 km apart respectively). The purple dot-dashed curve shows a long-range comparison between SYRTE and PTB in 2015 [40], using Link B and the German link. We see the longest links in the network being potentially limiting on the short-term stability of such a comparison. Due to the phase coherence of the links, resulting in a faster averaging of $\tau^{-3/2}$, the instability contribution of the links after 20 s averaging time becomes smaller than that of even the most stable clocks. This shows indeed the use of long, international fiber links for the comparison of state-of-the-art optical atomic clocks.

The relative frequency shifts induced by the French links is calculated as the mean relative frequency value for the duration, as discussed in chapter 3.3. This shift is $1.7(4.5) \cdot 10^{-20}$ for Link B, and $1.1(1.4) \cdot 10^{-20}$ for Link C over the one month, with the uncertainty given by the long-term stability, as discussed in chapter 3.3. This assessment is made from the E2E measurement, where uncorrelated noise in the uplink and downlink of the fiber is assumed. As shown in [48], the noise is usually not anti-correlated in the uplink and downlink. This in turn induces, that the systematic uncertainty of the uplink is lower that that of the E2E measurement. In case of perfect correlation, it is half that of the E2E measurement. In [27], an uncertainty budget is presented from a local experiment at SYRTE on the optical frequency dissemination through a 50 km long spooled fiber link. Here, a polarization asymmetry of $1.2 \cdot 10^{-20}$ is found for counter-propagating signals in the fiber. Such an effect was not observed yet with in-field fiber, where the expected effect is much lower than in fiber spools, as the birefringence is known to be higher than in deployed fiber. Thus we believe this effect will not be greater than $1 \cdot 10^{-19}$ for the in-field fiber links. However, this can only be an estimate, as this effect needs to be directly measured in the field, which is yet to be done. Other technical effects were

[3] There is only one interferometer at PTB, in the well-controlled laboratory environment.

also evaluated, which were all smaller than the contribution from polarization asymmetry. As such, these effects can be considered to be included in the above evaluation.

5.3.5 Statistical uncertainty contribution

The statistical uncertainty contribution of the French network to the optical clock comparison consists of an evaluation of the performance of fiber links, remote frequency references, NTP synchronization and frequency counter synchronization, as discussed in this chapter. This is shown in the MDEV in figure 5.14, which summarizes the total statistical uncertainty contribution of the French network to the clock comparison between SYRTE and PTB in March 2022. The stabilities of the E2E signals of the two links are shown in figure 5.14, and is the same curves as presented in figure 5.13. Since it will only be the one-way uncompensated noise of the links that will induce uncertainty to the comparison, these curves shows an upper limit of the instability induced by the links. Assuming uncorrelated noise between the uplink and the downlink of the fiber links, the induced uncertainties will in reality be a factor $\sqrt{2}$ smaller than the represented values in figure 5.14. In the case of perfectly correlated

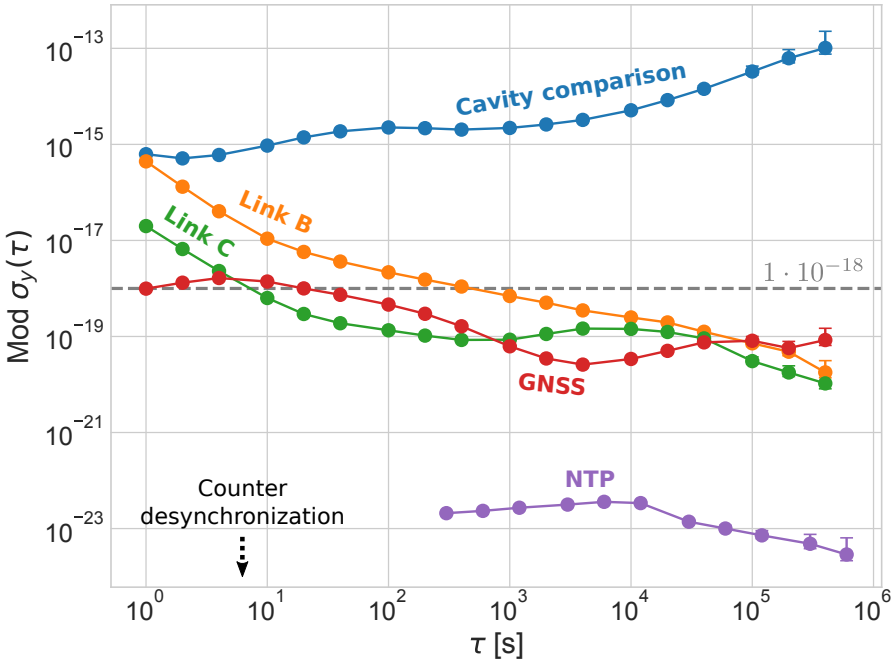

FIGURE 5.14: Instability contribution of the French network to the clock comparison campaign in March 2022 between SYRTE and PTB. The contribution from the NTP and counter desynchronization is calculated in relation to the relative drift of the cavities shown in figure 5.5.

noise between the uplink and the downlink, the induced uncertainties will be a factor 2 smaller. The stabilities of the two links are discussed in detail in chapter 3.2.

The cavity comparison (blue curve) is limited on short term by the stability of Link B (orange curve), which has a 1 s stability of $4.4 \cdot 10^{-16}$. Integrating with a slope of $\tau^{-3/2}$, due to the white phase noise behavior, the instability of the link goes below $1 \cdot 10^{-18}$ after 1000 s integration time. As explained in chapter 3.2, this is the level of the currently most stable optical atomic clocks, and is the goal of a continental optical clock comparison campaign set by the BIPM towards the future redefinition of the SI-second.

The 11 km long Link C (green curve) shows a 1 s instability of $2 \cdot 10^{-17}$, which is almost 2 orders of magnitude from limiting the cavity comparison at short term. The GNSS signal disseminated with WR shows an instability of $1 \cdot 10^{-18}$ between 1 s and 100 s. The long-term stability is limited by the Rb clock used at that time to frequency-discipline the OXCO. The Rb clock has a higher long-term instability and higher systematic uncertainty than the GNSS receiver we used for previous campaigns. An improvement could be made by installing a local Cs clock, or to use parallel WR dissemination, which shows superior performance as compared to the GNSS [93], enabling a cross-check of the references.

The instability of the NTP synchronization is calculated as the resulting error it would induce, in the determination of the frequency of the cavity comparison as shown in figure 5.5. It shows a maximal instability contribution around 12 000 s integration time of $3.6 \cdot 10^{-24}$, which is several orders of magnitudes from the level of the clock comparison. The same is the case for the instability induced by the desynchronization of the frequency counter, which has a short-term instability of $1 \cdot 10^{-27}$, and a long-term instability of $2.6 \cdot 10^{-30}$. For readability, the contribution of the desynchronization of the frequency counter is not shown in figure 5.14.

I show here that the French network potentially limits a comparison between optical atomic clocks for integration times below 50 s, primarily induced by the 700 km long Link B between Paris and Strasbourg, but will not limit such a comparison for integration times longer than 100 s.

5.3.6 Uncertainty budget

Table 5.1 summarizes the relative frequency shifts, statistical and systematic uncertainty contributions from the French network, to a fiber link comparison in Strasbourg. The statistical contributions (type A) are detailed above. The

	Shift	Statistical	Systematic
Remote frequency reference	$1.7 \cdot 10^{-18}$	$1.0 \cdot 10^{-19}$	-
Desynchronization of counters	$2.9 \cdot 10^{-22}$	$2.6 \cdot 10^{-30}$	-
Desynchronization of computers	$2.4 \cdot 10^{-24}$	$3.6 \cdot 10^{-24}$	$3.7 \cdot 10^{-22}$
Uncompensated fiber noise, Link B	$1.7 \cdot 10^{-20}$	$4.5 \cdot 10^{-20}$	$< 1 \cdot 10^{-19}$
Uncompensated fiber noise, Link C	$1.1 \cdot 10^{-20}$	$1.4 \cdot 10^{-20}$	$< 1 \cdot 10^{-19}$
Total	$1.7 \cdot 10^{-18}$	$1.1 \cdot 10^{-19}$	$< 1.4 \cdot 10^{-19}$

TABLE 5.1: Uncertainty budget of the French network for the clock comparison between SYRTE and PTB in March 2022.

remote frequency reference was the most limiting factor of the French network, and the only part of the network with a non-negligible relative frequency shift over the one month. Naturally, such a shift is not limiting the comparison itself when it is known, as one can compensate for it in post-processing. The statistical uncertainty contribution of the frequency reference of $1.0 \cdot 10^{-19}$ is currently not limiting the comparison at long timescales, but will still improve for future campaigns, when the Rb clock will be replaced with the GNSS signal.

The uncertainty contribution arising from the desynchronization of both computers and frequency counters is negligible with a well disciplined NTP server. However, if the NTP engine fails, the error will increase rapidly, as the internal clock of the computer will drift when not being disciplined. Indeed, the supervision of the synchronization of the machines is an important task of the Eye of Sauron, as explained in chapter 5.2

The total statistical uncertainty contribution of the French network to this comparison is $1.1 \cdot 10^{-19}$ over one month, with an estimated systematic uncertainty contribution of less than $1.4 \cdot 10^{-19}$. These results are compatible with the goal set by the BIPM as part of the roadmap towards the redefinition of the second. The goal states that we must be able to compare optical atomic clocks on a continental scale to the level of $1 \cdot 10^{-18}$.

5.4 Long-term clock comparison between SYRTE and INRiM

In February 2020 we established the fiber connection between the French REFIMEVE network and the Italian IQB network [94], allowing the dissemination of an optical signal from SYRTE to INRIM. Starting in the end of October 2021, a four month long comparison campaign between SYRTE and INRIM was held. The primary goal of the campaign was a comparison of Cs, Rb and

Yb atomic clocks, and is presented in [45]. This is the longest comparison campaign with the French network to date, which tested the long-term reliability of the network on an unprecedented scale. Furthermore, it was the first comparison campaign with the 858 km long Link E, which stretches from the data center TH2 in Paris, to Modane on the French-Italian border. From Modane, the signal was disseminated to INRIM, where the signal was compared to a local H-maser pivot. This is a unique approach compared to the previous campaigns between SYRTE, NPL and PTB, where signals from both institutes were disseminated to a comparison site [40].

The comparison campaign comprised of four months of comparison of the three microwave clocks: the Italian primary frequency standard, IT-CsF2 [95], and the two French frequency standards FO2-Cs and FO2-Rb [6, 7]. For one week, the Italian IT-Yb1 optical clock compared to the H-maser at INRIM, enabling a comparison between all four frequency standards. For the computation of the relative frequency ratios, all data were averaged into *stacks* over 864 s, which is the normal procedure of the Cs and Rb clocks, when reporting to Circular T. The uptime of the full frequency chain over the four months was at 57 %, with an uptime as high as 72 % over one month. Data stacks with more than 50 % valid points were used for the relative frequency ratio computations.

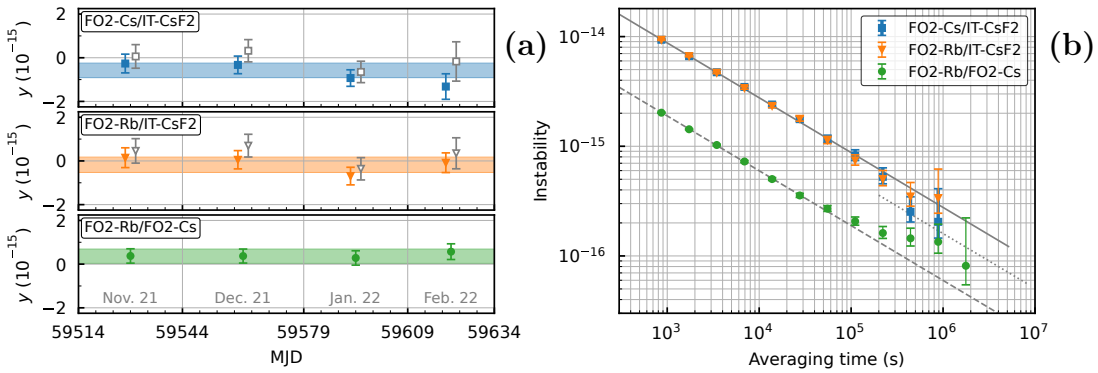

FIGURE 5.15: (a): Relative frequency ratios between the three microwave clocks FO2-CS and FO2-Rb at SYRTE, and IT-CsF2 at INRIM. Colored dots represents one month averages off comparisons with the fiber links, and colored regions shows the relative frequency ratios over the full four months. White dots shown the comparisons with GNSS, as reported to Circular T. (b): Relative frequency stabilities between the three microwave clocks. Plots from [45].

Figure 5.15(a) shows the obtained relative frequency ratios between the three microwave clocks. The figures are published in [45]. The relative frequency ratios were averaged in periods corresponding to Circular T, resulting in one data

point for each month of comparison. The colored points correspond to ratios obtained in the fiber comparison campaign for each of the four periods, and white points correspond to the ratios obtained from Circular T. These are comparisons using GNSS techniques, and have a larger uncertainty, calculated by the BIPM, as seen in the size of the error bars. Naturally, this distinction is not present in the comparison between the two French FO2-Cs and FO2-Rb clocks, as these are computed locally. The relative frequency ratio over the full period is shown by the colored regions. the remote frequency ratios between FO2-Cs and FO2-Rb, and IT-CsF2, are $-5.5(3.7) \cdot 10^{-16}$ and $-1.5(3.8) \cdot 10^{-16}$ respectively. There is agreement between the remote comparisons with fiber, and with GNSS techniques, within 1σ uncertainty. The relative stabilities between the three microwave clocks are shown in figure 5.15(b). Here, the comparison between the two French clocks, and the Italian clock, are almost identical, and only deviated after $\sim 3 \cdot 10^5$ s averaging time. This is because the relative stability is limited by IT-CsF2.

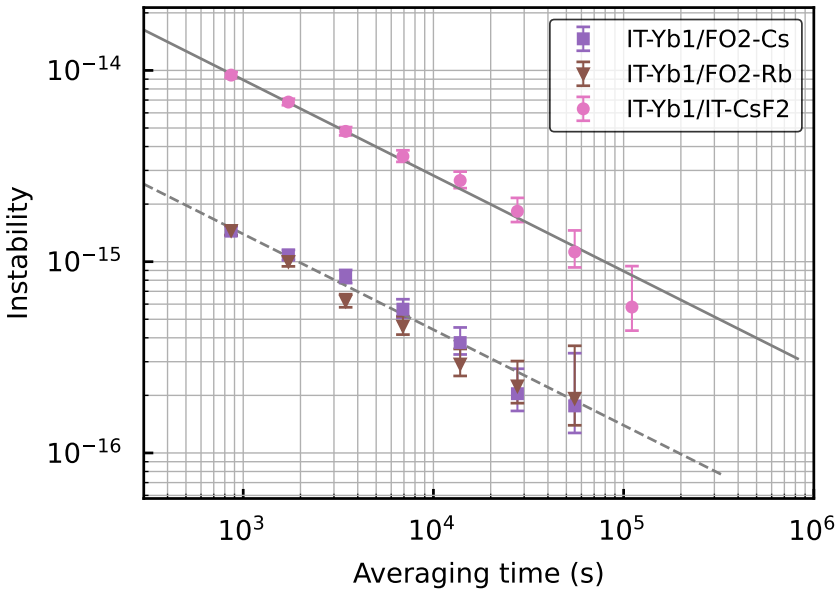

FIGURE 5.16: Relative frequency stabilities between IT-Yb1 and the three microwave clocks. Plot from [45].

Figure 5.16 shows the comparison between the Italian optical Yb clock IT-Yb1, and the three microwave standards. The stability is limited by the microwave clocks, which is seen in the similar stability behavior, as between the microwave inter-comparison. Notably, the 2×858 km long Link E does not impact the stability of the comparison. This is shown and discussed below. The relative frequency ratios between IT-Yb1, and the three microwave clocks FO2-Cs, FO2-Rb, and IT-CsF2, were $-0.4(3.0) \cdot 10^{-16}$, $-4.2(3.2) \cdot 10^{-16}$, and

$-4.9(5.9) \cdot 10^{-16}$ respectively. These measurements are in good agreement with the recommended values, which confirms our actual assessment that no significant systematic uncertainty contribution arised from the fiber links to that level.

This campaign proved a significant result towards using coherent optical fiber links, as a reliable mean, for the comparison of ensembles of atomic clocks. The long-term comparison over four months, is timescales which are necessary to reach, in order to use comparisons with fiber links in the generation of TAI.

5.4.1 Comparison of clock comparison campaigns over 4 years

In the following, I will compare the performance of Link E during this four month long comparison campaign, with the performance of the comparable Link B during five previous comparison campaigns. Link B has been operated for several clock comparison campaigns over the span of several years. Here, I will discuss the performance of the four months long campaign involving Link E, and the performance of Link B for five different campaigns, all between 2018 and 2022, comparing optical clocks at SYRTE to optical clocks at PTB. As the structure of the network has changed during the years, I will give a brief description of the important changes in network between the different campaigns, as well as general information about the six campaigns, from the side of the French network:

1. **2018 #1**: A one month long campaign between 20$^{\text{th}}$ April and 25$^{\text{th}}$ May 2018. This was before the inclusion of the MLS in the data center TH2, which means the E2E signal of Link B included the 11 km stretch between SYRTE and TH2, in addition to the 694 km between TH2 and Strasbourg. The link was working well.

2. **2018 #2**: A 12 days long campaign between 1$^{\text{st}}$ and 12$^{\text{th}}$ December 2018. Link B was operating well, and this campaign was used in the study of the sampling of the uptime of the link by optical clocks, as presented in [62]. After the campaign, the MLS in TH2 was set up, introducing the 11 km long Link C as an intermediary link.

3. **2019**: A one month long campaign between 18$^{\text{th}}$ June and 19$^{\text{th}}$ July 2019. Link B was operating well.

4. **2020**: Between 1$^{\text{st}}$ to 19$^{\text{th}}$ March 2020. A historically problematic campaign where everything that could go wrong went wrong all at once. 1: A

problem occurred with the lock of the short link between the ultra-stable cavity and the MLS at SYRTE, inducing an unusually high number of cycle slips. 2: Being in the early stages of the supervision of the French network, what we thought was a supervision of the remote frequency reference in Strasbourg was not. The OXCO was not well referenced to the GNSS signal, and the comparison data collected was practically invalid. (3): In the middle of the campaign, most European countries shut down, due to the outbreak of the COVID-19 virus, blocking all access to the laboratories. Link B was seemingly operating with a high level of nominal noise. This was due to an issue in the downlink of Link B, which drastically worsened the E2E evaluation of the fiber link. However, as the uplink was not affected, we believe this issue did not lead to a deterioration of the frequency comparison in Strasbourg.

5. **2021**: The four month long campaign between SYRTE and INRIM, between 27$^{\text{th}}$ October 2021 and 24$^{\text{th}}$ February 2022. In the end of 2020, there were a relocation of fibers, leading to a change of the length of Link B to 700 km. During the four month long campaign, Link E was working well.

6. **2022**: The one month long campaign between 1$^{\text{st}}$ and 31$^{\text{st}}$ March 2022. An in-depth study of the French network during this campaign is presented in chapter 5.3. The links were working well.

Figure 5.17(a) shows the duration of all 6 campaigns, stretching from campaign #2 in 2018 with a duration of 12 days, to the campaign between SYRTE and INRIM of 121 days. During these four months, Link E showed an uptime of 75 %. This corresponds to $\approx$ 30 days of downtime during the campaign. Out of these 30 days of downtime, almost 1/3 was due to a crash of a software of the remote frequency counter in the data center TH2, which did not get restarted. During these 9+ days, Link E might have been working, but the traceability of the signal is lost with the crash of the software.

The five campaigns displayed involving Link B includes a total of 123 days of comparisons. Of these the link was down a total of 13 days, resulting in a total uptime of 89 %. This is indeed comparable with the uptime of Link E, which without the software crash might have been as high as 84 %, over a comparable timescale. We believe the uptime will be drastically better for future comparisons, as the supervision services have improved significantly since 2018, and is continuously improving.

Over the four months, Link E showed a relative frequency shift of $-1.4(1.4) \cdot 10^{-19}$, which was not limiting the comparison of the clocks as explained in [45].

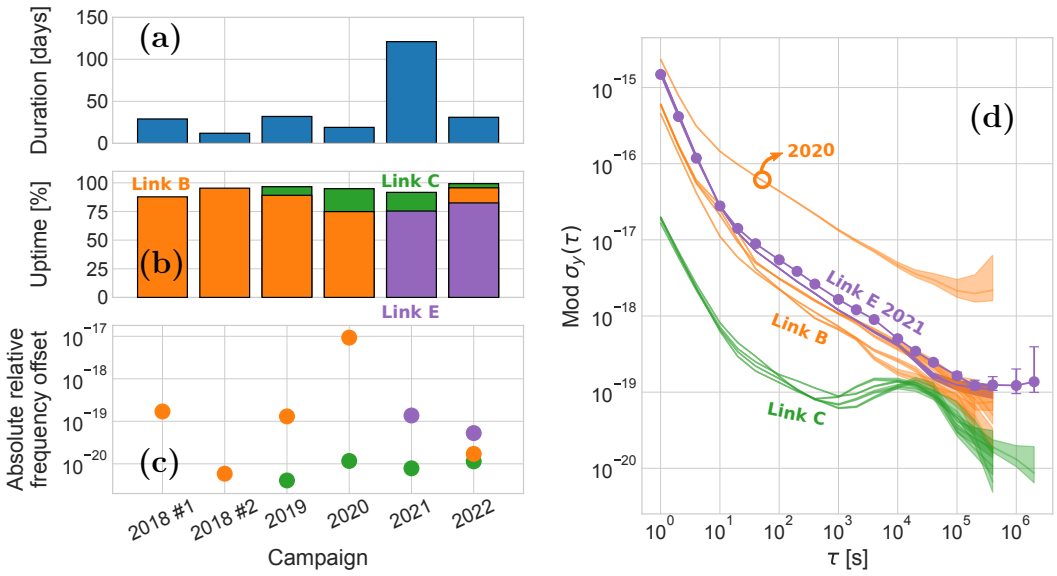

FIGURE 5.17: Comparison of the performance of Link B (orange), Link C (green) and Link E (purple), during 6 different clock comparison campaigns. (a) Duration, (b) uptime, (c) absolute relative frequency shift, and (d) modified Allan deviation of the three links, during the respective campaigns they were used in.

This is shown in figure 5.17(c), with the uncertainty given by the long-term instability as shown in figure 5.17(d). As seen in figure 5.17(c), this shift is comparable with the shift of Link B in the 2019 campaign. I have calculated the average shift of Link B as a weighted average over the four campaigns, excluding the outlier of the 2020 campaign. The weights are chosen as *frequency weights*, i.e. the durations of valid comparison data. This results in a weighted average frequency shift of $-1.2(11.3) \cdot 10^{-20}$, which is below the goal of a $< 1 \cdot 10^{-18}$ uncertainty contribution from the French network. As seen in the MDEV in figure 5.17(d), the stability of Link B showed a reasonably constant behavior between the four campaigns, where the link was working normally. The stability of Link E is comparable with that of the nominal behavior of Link B. With an instability below $1 \cdot 10^{-18}$ after 4 000 s integration time, the instability of Link E did not limit the clock comparison, as shown in [45].

For completeness the short 11 km Link C has been included in figure 5.17 (green). The link was established shortly after the 2$^{\text{nd}}$ campaign in 2018, and has been a part of all subsequent campaigns. During the 203 days of comparison campaigns relying on this link, it had a combined $\sim$ 12 days of downtime, resulting in an effective uptime of 94 %. As seen in figure 5.17(b), the uptime of Link C during the one month long 2022 campaign was as high as 99.3 %,

corresponding to a downtime of $\sim$ 5.5 hours in 31 days. The short link shows a total weighted average relative frequency shift of $1(8) \cdot 10^{-21}$ over the four campaigns, which by far can be considered negligible. As seen in the green stability curves in figure 5.17(d), the instability behavior of Link C changed very little between the four campaigns. The high uptime and low uncertainty of this link is indeed important, as it can practically be ignored as a noise source, even for a comparison of state-of-the-art optical clocks.

5.5 Uncertainty contribution from sampling

When comparing remote optical clocks, the total uncertainty of the comparison will depend on the uncertainties of all the subsystems:

$$\sigma^2_{\text{total}} = \sigma^2_{\text{clocks}} + \sigma^2_{\text{cavities}} + \sigma^2_{\text{combs}} + \sigma^2_{\text{links}}.$$

As such, the uncertainty of the fiber links disseminating the clock signals can not be evaluated independently. In the evaluation of the link signal $y(t)$, the uptime of the whole comparison chain needs to be considered, and not just the uptime of the links. This leads to the effective link signal $y_{\text{eff}}(t)$:

$$y_{\text{eff}}(t) = y(t) \cdot \prod_n g(t)_n,$$

where $\prod_n g_n(t)$ represents the ensemble of annihilation operators from the different subsystems:

$$\prod_n g(t)_n = g(t)_{\text{clocks}} \cdot g(t)_{\text{cavities}} \cdot g(t)_{\text{combs}} \cdot g(t)_{\text{links}},$$

representing the total uptime of the comparison. Following the analysis previously this chapter, I will be focusing on the cavity comparison, and evaluate the effective signal of Link B based on the uptime of the link itself, as well as the uptime of the cavity comparison. I choose to perform this study on Link B, as this long-haul fiber link is the most dominating source of uncompensated fiber noise in the French network, in the comparison between SYRTE and PTB. As shown in chapters 5.3 and 5.4, the uncertainty contribution of the short Link C is much smaller than the uncertainty of state-of-the-art optical clocks. However, with the study shown here, the further inclusion of an expanded set of subsystems is straightforward, if one wishes for future studies.

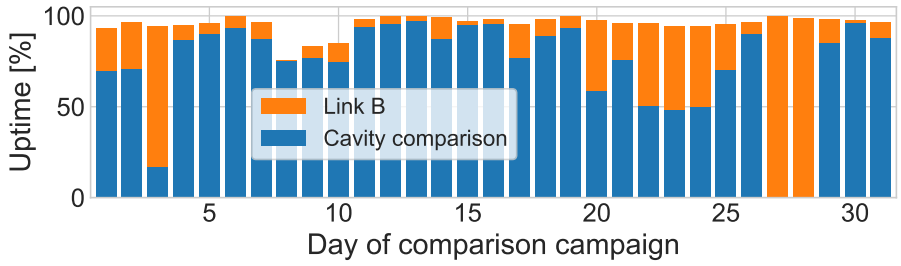

FIGURE 5.18: Uptime of Link B (orange) and the cavity comparison (blue) during the one month of comparison campaign. Each bar represents the average uptime of 1 day.

Figure 5.18 shows a bar chart of the uptime of Link B and the cavity comparison during the one month of comparison campaign. Each bar shows the average uptime of 1 day. The uptime of Link B over the one month was 96 %, and the uptime of the comparison was 74 %. The total uptime of both systems, $g(t)_{\text{comparison}} \cdot g(t)_{\text{link}}$, was only slightly limited by the uptime of Link B, and was at 73 %.

The uncertainty contribution of Link B has been evaluated as explained in chapter 3.3. I have evaluated the uncertainty of the link signal both including and not including the sampling by the uptime of the comparison. In both cases, the uncertainty has been evaluated in the two following cases: using a concatenation of the remaining data, and replacing the missing data with simulated noise, as discussed in chapter 4.2. To remove the statistical fluctuations of the simulated noise, the uncertainty is calculated as an average of 10 iterations of the calculation.

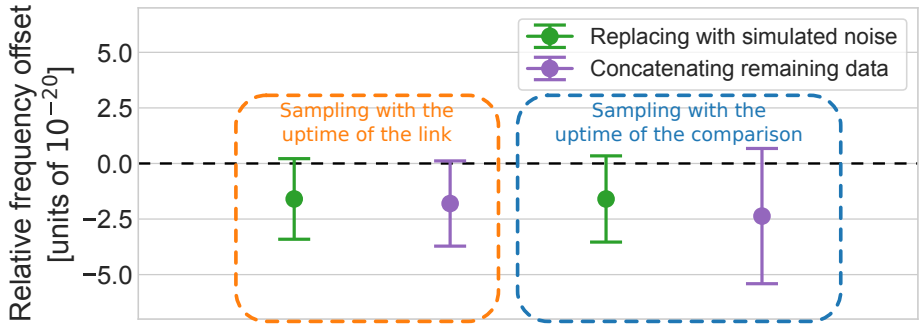

FIGURE 5.19: Uncertainty contribution of the optical fiber link to the cavity comparison, over the one month of comparison campaign when: sampled by the uptime of the link itself (orange box), and when sampled by the full cavity comparison (blue box). Evaluations are made in the two following cases: using a concatenation of the remaining data (purple) and replacing the missing data with simulated noise (green).

The data points in the orange box in figure 5.19 shows the relative frequency shift of the fiber link when considering solely the uptime of the link itself. Over the one month, the uncertainty contribution of the link is evaluated to be $-1.8(\pm 1.9) \cdot 10^{-20}$ when the remaining data is concatenated (purple), and $-1.6(\pm 1.8) \cdot 10^{-20}$ when missing data has been replaced with simulated noise (green). The similarity between the two results is due to the low density of missing data of ~ 4.4 %, corresponding to a mean duration between missing data points of $\tau_G/h \sim 23$ s. With a coherence time of Link B of $\tau_{\text{coh}} = 87$ s, this is indeed well in the regime of $\tau_G/h < \tau_{\text{coh}}$, where the two approaches should give converging results, as shown in chapter 4.2.

The data points in the blue area in figure 5.19 shows the evaluation of the uncertainty of the link when sampled by the uptime of the comparison. When concatenating the remaining data set, a relative frequency shift of $-2.4(\pm 3.0) \cdot 10^{-20}$ is found. Most notably, this result is not satisfying, as it implies that the performance of the links depends on the performance of the other subsystems. On the other hand, a total relative frequency shift of $-1.6(\pm 1.9) \cdot 10^{-20}$ is found when replacing missing data with simulated noise, which is almost the same as found in the case of only sampling with the uptime of the link itself.

These results show that the increase in uncertainty brought by the long link to the comparison is almost 2 orders of magnitude from being limiting for a comparison of most accurate optical clocks [82], even when sampled by the uptime of the comparison. This is compatible with the goal of the fiber links, inducing an error smaller than $1 \cdot 10^{-18}$ for an international comparison.

5.5.1 Uncertainty contribution over several campaigns

Above, I have evaluated the uncertainty contribution of Link B to the one month long comparison campaign, when sampled by the uptime of the cavity comparison. This is important in the determination of the uncertainty contribution of the fiber link to the specific campaign in March 2022. Such comparisons with optical fibers will only become more widespread in the future, as fiber links are currently the most mature technology for the comparison of remote optical clocks. Ideally, the links will be comparing optical clocks continuously in the future, allowing long-term and ultra-precise frequency ratio measurements. Furthermore, current primary microwave frequency standards averages measurements of one month for the calibration of the TAI. This is a convenient time scale, as this is the same duration as the comparison campaign investigated in this chapter.

In the context of using the optical clocks as either secondary or primary frequency standards, I have calculated the expected total uncertainty contribution if a similar campaign gets repeated 400 times. This calculation is done by "simulating" campaigns, with the same duration and uptime as the one discussed previously in this chapter. This calculation is done in the following steps:

1. The uptime of the comparison of 73 % has a given distribution of missing data, as seen in the regions of missing data in figure 5.5, and in the bar chart in figure 5.18. Using the same one month of data from Link B, I have, for each simulated campaign, redistributed the missing data using the binomial annihilation operator $g(t)$, as discussed in chapter 4.1.

2. The uncertainty of the effective fiber link data set, $y_{\text{eff}} = y(t)g(t)$, is then evaluated in the same two ways: where the effective data set is concatenated, and where the missing data is replaced with simulated noise.

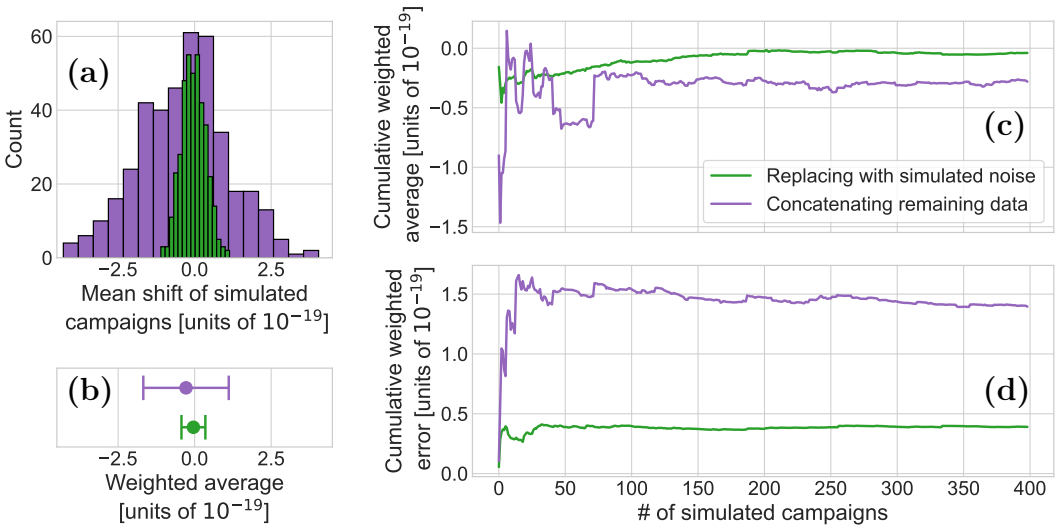

FIGURE 5.20: Evaluation of uncertainty induced by Link B to optical comparison campaigns, when sampled by the uptime of the comparison, with durations and uptimes similar to that shown in figure 5.18. (a): Distribution of the mean relative frequency shifts of 400 simulated campaigns, (b): total weighted relative frequency shift, (c): cumulative weighted average, and (d): cumulative weighted uncertainty, where the remaining data is concatenated (purple), and where missing data is replaced with simulated noise (green).

Figure 5.20(a) shows the distribution of the average relative frequency shift of 400 simulated campaigns. The spread in the relative frequency shifts is bigger when concatenating the remaining data (purple), compared to when replacing missing data with simulated noise: the standard deviation of the 400

simulations is 3.7 times higher when concatenating the remaining data. The largest frequency shift when concatenating the remaining data is found to be $4.3 \cdot 10^{-19}$, and $1.1 \cdot 10^{-19}$ when replacing the missing data with simulated noise. These "worst case scenarios" are still well below the goal of $1 \cdot 10^{-18}$, which indeed confirms the reliability of the use of long-haul fiber links for optical clock comparisons.

Figure 5.20 (c) and (d) shows the *cumulative weighted average* and *cumulative weighted uncertainty* of this average. This means a weighted average and weighted standard deviation, calculated on an increasing number of simulated campaigns. The weights used to calculated the weighted average is $1/\sigma^2$, with σ indicates the long-term instability as described in chapter 3.3. Averaging over less than 50 campaigns, the evaluation of the weighted uncertainty stays within $0.5 \cdot 10^{-19}$ when missing data replaced with simulated noise. When concatenating the data set, uncertainties can fluctuate up to $1.5 \cdot 10^{-19}$. After ~ 70 campaigns, both evaluations has mostly converged, with only very subtle changes in the uncertainty evaluation with an increasing number of campaigns. After 400 simulated campaigns, the weighted average of the concatenated data converges to $-3(\pm 14)10^{-20}$, which is the shown in the purple data point in figure 5.20(b). When replacing the missing data with simulated noise, the total weighted average frequency shift of the 400 simulated campaigns is $-4(\pm 40) \cdot 10^{-21}$. Such an average frequency shift, which is compatible with zero, is more than two orders of magnitude from bringing a noticeable frequency shift to a comparison of optical clocks.

This shows that the link is indeed eligible for the use of future long-term optical clock comparisons, where the uncertainty induced by the links should not be noticeable in the relative frequency ratio measurements of the optical clocks. This conclusion holds under the assumption that the behavior of the link over the one month is representative for the general behavior of the link. This will only be true to a certain degree, as the noise of the links is not strictly stationary, as discussed in chapter 3. However, as a one month long data set was used, the day/night fluctuations will be averaged out, and this error will mostly be due to seasonal variations, which we believe to be significantly smaller than the day/night fluctuations.

In this chapter, I have discussed the complexity in the operation of the French REFIMEVE network, both in the context of ensuring a reliable frequency dissemination to users of the network, as well as in the context of optical clock comparisons. I have described how the network is monitored at all

times, and how the Palantír software ensures reliable and efficient data processing. I have described how the internal servers are structured, which enables the data processing software to have an overview of the complete network at all times. I have discussed how the Palantír software is used during an optical clock comparison campaign, and the importance of remote synchronization and syntonization. In this context, I have used the software to demonstrate a case study of a one month long comparison campaign. From the comparison signal between two ultra-stable cavities at Strasbourg, I have analyzed the uncertainty contribution of the French network to the comparison. I found that the most limiting uncertainty contribution is brought by the remote frequency reference, with a total uncertainty contribution of $1.7 \cdot 10^{-18}$. This can potentially be limiting for the best performing optical clocks, where the goal is an uncertainty contribution from the network of $< 1 \cdot 10^{-18}$. We expect this uncertainty contribution to be significantly lower for future comparison campaigns, where the long-term remote frequency reference will be improved.

Lastly, I have considered the sampling of the optical fiber link by the uptime of the cavity comparison. I have found an uncertainty induced by the sampled fiber link signal of $-1.6(\pm 1.9) \cdot 10^{-20}$ to the comparison campaign, which is not limiting for the uncertainty contribution of the network. Assuming 400 campaigns similar to the one under study in this chapter, I found a total expected weighted uncertainty contribution of the sampled fiber link to be $-4(\pm 40) \cdot 10^{-21}$. These results shows that even very long-haul fiber links are indeed viable for long-term optical clock comparisons to the level of $1 \cdot 10^{-18}$, which is the goal set by the BIPM on the road-map towards the future redefinition of the SI-second.

Chapter 6

Earth science with optical fiber links

In this thesis, I have so far been describing fundamental noise processes of the links themselves. I have mostly assumed reciprocal noise processes, which leads to straightforward modeling of the links, and evaluations of their statistical properties. This has been exploited to create an uncertainty budget of the French fiber network for optical clock comparisons.

In this chapter, I will present studies on external noise processes affecting the fiber links. These noise processes are induced by Earth itself, in which the fiber links have their home. I will be investigating two very different noise processes induced by the Earth: first, in chapter 6.1, I will discuss an experiment which I performed to be able to measure fundamental physical effects arising from the rotation of the Earth around itself. Afterwards, in chapter 6.2, I will present an analysis of the interaction between seismic waves released from the Earth, and the optical fiber links which also inhabits it. These acoustic perturbations are seen by the optical fiber links, which are acting like long one-dimensional seismometers. I will show a study of a parametrization of this interaction, and discuss the prospects of using the fiber links for seismological assessments.

6.1 Sagnac detection

In 1913 Georges Sagnac reported his experiment, which had been realized the year before, *The Luminiferous Ether is Detected as a Wind Effect Relative to the Ether Using a Uniformly Rotating Interferometer*[1] at the Sorbonne Université in Paris [96, 97]. He reported the effect which became known as the *Sagnac effect*. The Sagnac effect arises from interference between counter-propagating

[1] Originally: L'éther lumineux démontré par l'effet du vent relatif d'éther dans un interféromètre en rotation uniforme

light signals, which travels the same path, in a system that undergoes an inertial rotation.

One thrilling question for the community of fiber links is to determine whether a fiber link forming a ring topology can serve as such a gyrometer. With the fiber networks currently under study in Europe [98] and China, there are potentials to create the biggest gyrometers yet, by many orders of magnitudes. In the applications of using in-field fiber links as gyroscopes, a theoretical prediction [99], and one experimental test [100], performed on the Italian fiber network, have been reported so far. Here, 110 years since the original experiment of Georges Sagnac, I present a study of, to the best of my knowledge, one of the worlds largest gyroscopes to date. This is very comparable in size to a study performed almost ten years ago by C. Clivati and collaborators at INRIM with a fiber loop around Torino [100]. This gyroscope is realized on a topology on the regional REFIMEVE network in Paris[2]. The originality of this study is to compare the situation with a fiber spool, with nearly equivalent length and order of magnitudes smaller area. For any setup with two counter-propagating beams circulating in a loop encompassing an enclosed area, the phase difference between the two counter-propagating signals is called the Sagnac phase, and can be expressed as [96]

$$\Delta\phi_s = \frac{8\pi\nu_0}{c^2}\mathbf{\Omega}\cdot\mathbf{A},$$

where $\nu_0 = 194.4$ THz is the carrier frequency, c the speed of light in vacuum, $\mathbf{\Omega}$ the rotation rate of the system, and $\mathbf{A}$ the enclosed area. This equation highlights the intrigue of a continental-scale gyrometer: since the variation of the Sagnac phase scales with the enclosed area, the sensitivity of such a topology seems to be able to detect even the smallest changes in the rotation rate of the Earth.

As our measurement is sensitive to the *time variations* of the phase, the measured Sagnac phase variation of a fiber link gyrometer is

$$\frac{d\Delta\phi_s}{dt} = \frac{8\pi\nu_0}{c^2}\left(\frac{d\Omega}{dt}A\sin(\theta_{\text{lat}}) + \Omega\frac{dA}{dt}\sin(\theta_{\text{lat}}) + \Omega A\frac{d\sin(\theta_{\text{lat}})}{dt}\right), \tag{6.1}$$

with $\theta_{\text{lat}} \approx 48.8°$ being the latitude of Paris, and thereby the gyrometer. The rotation rate of the Earth Ω is ≈ 1 day^{-1}, or equivalently ≈ 11.6 µHz. The area A depends on the enclosed area of the fiber link. For any of the five links in the REFIMEVE network, as discussed throughout this manuscript, the enclosed area will be very small, not to say zero, as the two parallel fibers are

[2] I believe the gyroscope encircles the very location of the first ring gyroscope of Georges Sagnac, but I have not been able to confirm this.

part of the same cable bundle. However, if the generalized Sagnac effect [101, 102] is considered, such effects could be relevant on longer time scales. The third term, containing the change in latitude with time, corresponds to changes in the Earths rotation axis, including effects like the Chandler wobble [103].

A difficulty in measuring such a Sagnac phase in a fiber link, is the very nature of the effect: it is non-reciprocal, and will therefore not be compensated, neither actively nor passively, as it violates the fundamental hypothesis of noise compensation. This is explained in chapter 2.1. The Sagnac effect is not the only non-reciprocal effect acting on a fiber link: in [27], the non-reciprocal effect of polarization mode dispersion is reported for a 25 km spooled fiber link. Such an effect is, unlike the Sagnac effect, not known to scale with the enclosed area of the fiber link. As such, by documenting a non-reciprocal processes which scales with the enclosed area, one of the only effects such could be due to is the Sagnac effect. Furthermore, equation 6.1 highlights difficulties in such an experiment, if a Sagnac phase is successfully measured: all three terms, which are all non-reciprocal, changes with time. They are indistinguishable from each other, which makes the measurement and determination of any single term difficult.

In the following, I will present an experimental study of the effects of the enclosed area on the Sagnac phase. I will give a brief introduction to the experimental setup, after which I will discuss the obtained results.

6.1.1 Experimental setup

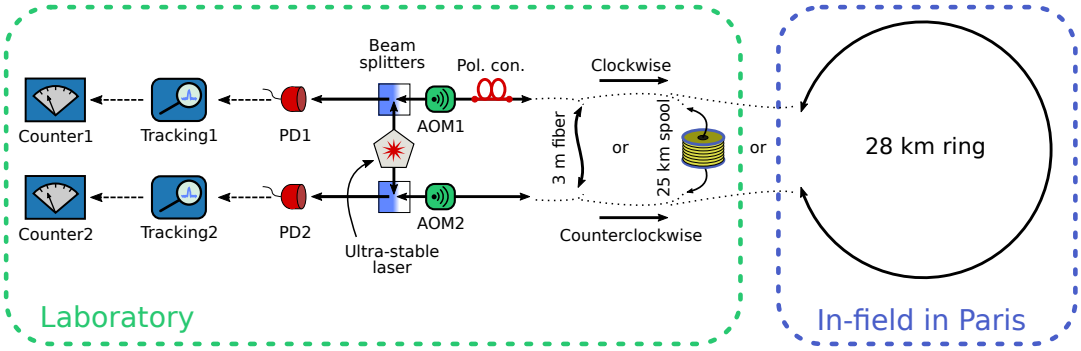

FIGURE 6.1: Experimental scheme used for non-reciprocal fiber noise detection. PD1 and PD2: Photodiodes. AOM: Acousto-optical modulator. Pol. con.: Polarization controller. Beam splitters are the ones of the multi-branch laser station (MLS). For a sake of clarity in the sketch, only their functionalities is represented. On PD1 and PD2, optical beats between the ultra-stable laser light, and the light that experiences the trip in the device under test are generated.

The basic experimental principle of this study, is to measure a TW beat note, of two signal enclosing an area. Figure 6.1 shows the experimental setup used for this realization. This scheme is similar to the one introduced in chapter 2.1, but instead of performing a TW comparison between two different lasers in two different laboratories, there is only one laboratory, and only one ultra-stable laser.

The ultra-stable signal gets split up by two beamsplitters in an interferometer. Part of the signals are used for the self-heterodyne beat note detection, and part of the signals are sent in what I will call the *clockwise* and the *counter-clockwise* paths, in the same fiber link. The fiber link can be in either of three different configurations:

1. A 3 m long fiber, with enclosed area ≈ 0.7 m^2, used as a measure of the noise floor of the system.
2. 25 km of spooled fiber, with an enclosed area ≈ 1580 m^2.
3. A 28 km in-the-field fiber link around the central-Eastern part of Paris, with enclosed area ≈ 23 km^2.

Figure 6.2 illustrates the path of the in-field loop. From the Paris Observatory, the 28 km long fiber stretches around the central/eastern part of Paris, in a path very close to the depiction in the figure.

After traveling the length of the link, the two signals are measured against the local light in the photodiode. The RF signals are filtered, amplified, tracked, and measured by a dead-time free frequency counter. The two measured beat notes are

$$\nu_{CW}(t) = \frac{1}{2\pi}\frac{d\phi_{CW}(t)}{dt} \text{ and}$$
$$\nu_{CCW}(t) = \frac{1}{2\pi}\frac{d\phi_{CCW}(t)}{dt},$$

for the clockwise (CW) and counterclockwise (CCW) signals respectively. The fiber noise, $\phi_{CW}(t)$ and $\phi_{CCW}(t)$, consists of a reciprocal part (rec), and a non-reciprocal part (n-rec):

$$\phi_{(C)CW}(t) = \phi^{\text{rec}}_{(C)CW}(t) + \phi^{\text{n-rec}}_{(C)CW}(t).$$

By the definition of reciprocity, it is evident that

$$\phi^{\text{rec}}_{CW}(t) = \phi^{\text{rec}}_{CCW}(t) = \phi^{\text{rec}}(t)$$
$$\phi^{\text{n-rec}}_{CW}(t) \neq \phi^{\text{n-rec}}_{CCW}(t).$$

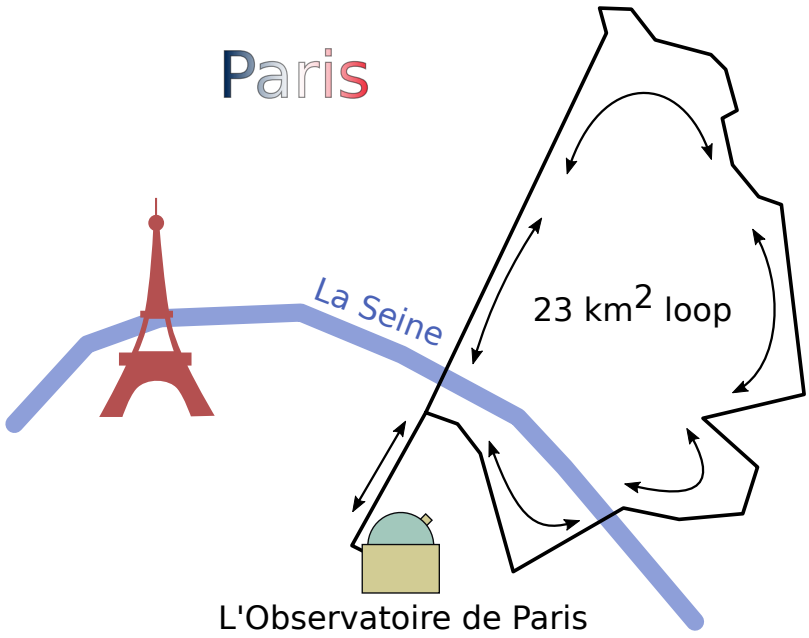

FIGURE 6.2: Depiction of the fiber loop used for Sagnac sensitivity determination. Two signals propagate from the Paris Observatory around the 28 km long fiber, which going around the central/eastern part of Paris encloses a 23 km^2 area, before being combined back at the Paris Observatory.

This allows for the construction of two TW observables, by either adding or subtracting the two signal from the beat notes:

$$\nu_{CW}(t) - \nu_{CCW}(t) = \frac{1}{2\pi}\frac{d\phi^{\text{n-rec}}_{CW}(t)}{dt} - \frac{1}{2\pi}\frac{d\phi^{\text{n-rec}}_{CCW}(t)}{dt}. \tag{6.2}$$

$$\nu_{CW}(t) + \nu_{CCW}(t) = \frac{1}{\pi}\frac{d\phi^{\text{rec}}(t)}{dt} + \frac{1}{2\pi}\frac{d\phi^{\text{n-rec}}_{CW}(t)}{dt} + \frac{1}{2\pi}\frac{d\phi^{\text{n-rec}}_{CCW}(t)}{dt} \tag{6.3}$$

The difference in the beat notes, according to equation 6.2, removes the reciprocal fiber noise. The sum of the two beat notes, equation 6.3, contains twice the reciprocal fiber noise, $\phi^{\text{rec}}(t)$, as well as the clockwise and counterclockwise non-reciprocal terms, $d\phi^{\text{n-rec}}_{CW}(t)$, and $d\phi^{\text{n-rec}}_{CCW}(t)$ respectively. Normally in the fiber links in the REFIMEVE network, the reciprocal fiber noise is orders of magnitudes larger than the non-reciprocal noise, which can be considered negligible in equation 6.3.

The experiment was run in the three different configurations. The 3 m fiber configuration was used to get a measurement of the noise floor of the experiment. A second noise floor of the frequency counter was recorded, which was found to be negligible for this experiment. The experiment was run with the in-field configuration, and the fiber spool configuration, switching back and forth several times. In the in-field loop, the signal experiences a much larger

attenuation than in a fiber spool. Therefore, each time the configuration was switched back and forth, the attenuation of the signal in the spool experiment was set to match the attenuation of the in-field experiment. This was done in order to, to the highest degree possible, only change one variable between the two experiments: the enclosed area.

6.1.2 Results

During the many runs of the experiment, a clear tendency appeared: the tracking system could follow the fiber spool configuration well, and it was possible to get runs of days in a row without cycle slips. This was not possible with the in-field experiment, which is shown in figure 6.3. Here, the differential TW,

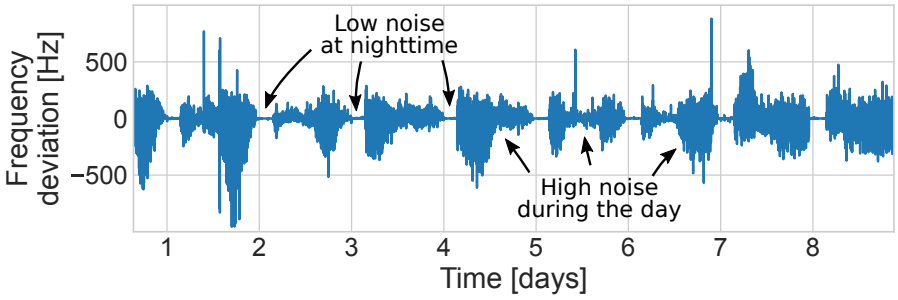

FIGURE 6.3: Frequency deviation of the in-field experiment over the span of 8 days. The noise is low for a few hours during the night, and the tracking mostly fails during the day.

corresponding to equation 6.2, of the in-field experiment is shown over the span of 8 days. Usually, the experiment could run for a few hours during the night, with just $\sim$ 11 cycle slips per hour. However, during the day, the measurements consists almost entirely of cycle slips. Figure 6.4(a) shows the phase PSD of the in-field loop configuration for the whole measurement period, filtered to remove the cycle slips, in light green. The PSD of the signal during the night is shown in dark green. Using equation 2.8, predicting the mean time between cycle slips $\bar{T}$ for a given SNR, I can get an estimate of the SNR of the in-field loop during the night. 11 cycle slips per hour corresponds to a SNR of 9.7 dB at the tracking bandwidth of 300 kHz. Adding the increase in noise, which is highlighted in figure 6.4(a), to the SNR, drastically decreases the expected mean time between cycle slips, illustrated in figure 6.4(b). Here, $\bar{T}$ is plotted in purple as a function of SNR, at a bandwidth of the tracking at 300 kHz. The decrease in the mean time between cycle slips between the two periods is illustrated, dropping far below the "limit" of 1 s, shown in black. So, the increase in cycle slips seems roughly consistent with the increase in noise.

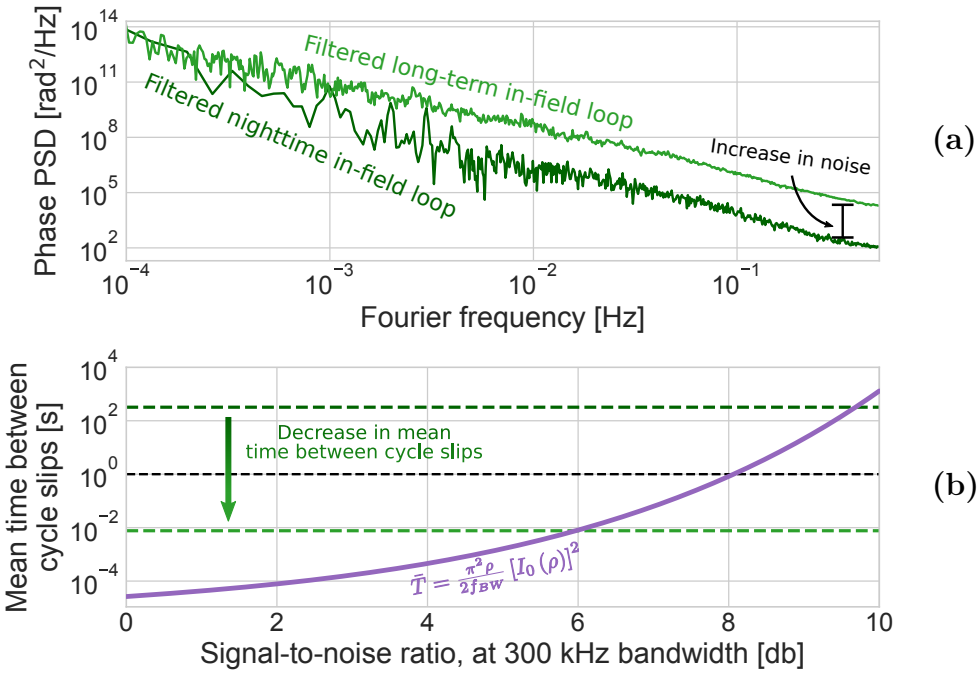

FIGURE 6.4: (a): Increase in noise between the measurement during nighttime (dark green), and the full measurement (light green). Both have been filtered to remove cycle slips. (b): Mean time between cycle slips $\bar{T}$ for a tracking bandwidth of 300 kHz, calculated with equation 2.8 (purple), as a function of the signal-to-noise ratio (SNR). The decrease in $\bar{T}$ is shown in dashed lines. The limit of operation at $\bar{T} = 1$ s is illustrated by a black dashed line.

A question is then what the increase in noise arises from. Considering the expression of the change in Sagnac phase variation in equation 6.1, the three terms consists of a change in rotation speed, a change in area, and a change in the latitude. We know from the operation of the fiber network, that there is an increase in noise during the day, compared to during the night, as shown in chapter 3.1. There is no evidence for a different change of the Earths rotation rate variations, or in the wobble of the rotation of the Earth, between the Parisian night and day. Therefore, the increase in noise is most likely due to the change in the enclosed area, induced by the increased human-induced noise, which is primarily present during the day

Of the three terms in the Sagnac phase variation, two of them are linearly dependent on the enclosed area. As the fiber spool has an enclosed area of ≈ 1580 m^2, which is ≈ 23 km^2 for the in-field loop, the difference in the scaling factor of the two terms, between the two configurations is ~ 40 dB. Figure 6.5

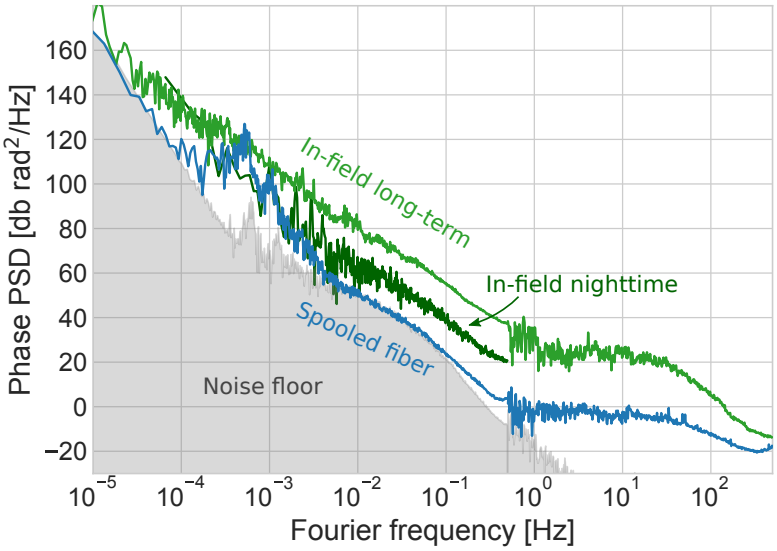

FIGURE 6.5: Sum of the two beat notes, according to equation 6.3, of the two configurations: the 25 km, 1580 m^2 fiber spool (blue), and the 28 km, 23 km^2 in-field loop (green). Light-green shows the long-term behavior of the in-field configuration, and dark green shows the behavior during the night.

shows the phase PSD of the sum of the beat notes, according to equation 6.3. A run of the in-field loop configuration is shown in green, and the fiber spool configuration in blue. Notice that the phase PSD has been plotted in dB, which is a differently chosen scale from the rest of the manuscript. This is meant for visual help, to compare with the 40 dB difference a linear scaling with the area would correspond to. Between ~ 5 mHz and ~ 30 Hz, which consists of most of the spectra, the noise level difference between the two configurations

is $\sim$ 30 dB. They seem to converge to the noise floor measurement, shown by the gray shaded area, at very low frequencies. As discussed in chapter 2.2, the reciprocal link noise roughly scales with the length of the fiber link. With a length difference between the two experiments of $\sim$ 3 km, corresponding to just 10 %, it seems unlikely that the factor of 30 dB can be explained purely from the relatively small increase in fiber length. On the other hand, the difference in noise of 30 dB is 10 dB less than the 40 dB scaling factor, which would be our expectation for a linear scaling with the area. A likely explanation is the correlation between the counter-propagating signals: as shown in [27], such correlations are typically somewhere in between zero correlation, and a maximal correlation. Such correlations have not been evaluated for this experiment, which could be good to include in a future study. Furthermore, there is likely also a noise contribution from the change in area. As discussed above, these distinctions are very difficult with this experimental setup, since the three terms of the Sagnac phase variation are indistinguishable in this realization, with only two observables (the difference and the sum of the frequencies, according to equations 6.2 and 6.3).

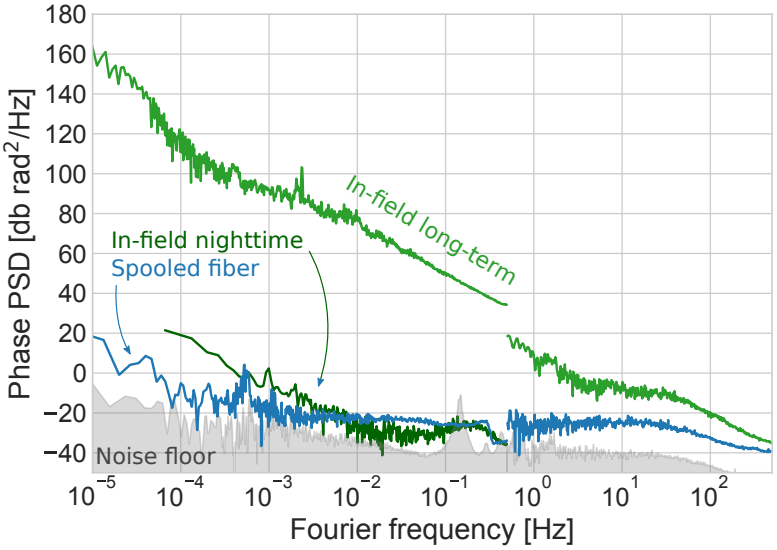

FIGURE 6.6: Difference between the two beat notes, according to equation 6.2, of the two configurations: the 25 km, 1580 m^2 fiber spool (blue), and the 28 km, 23 km^2 in-field loop (green). Light-green shows the long-term behavior of the in-field configuration, and dark green shows the behavior during the night.

Figure 6.6 shows the phase PSD of the differential beat notes, corresponding to equation 6.2, of the two configurations of the experiment. Here, the reciprocal noise is removed from the observable. In the fiber spool configuration, the spectrum is mostly flat for Fourier frequencies below $\sim$ 30 Hz, indicating a

dominatingly white phase noise behavior. In the noise floor measurement, a strong periodic perturbation is visible at 150 mHz, which is not present in the fiber spool measurement.

The long-term in-field configuration shows no white phase noise behavior below ~ 4 Hz. This is due to the increase in noise, which makes the tracking fail, resulting in little compensation of the noise. There is a discontinuity between the short-term (above 0.5 Hz) and long-term measurements (below 0.5 Hz). I believe this is due to non-stationarity of the noise in the loop: the short-term measurement only consists of 3 minutes of data, whereas the long-term data is averaged over several days. If the short-term measurement gets recorded in a period with lower noise than the average, a discontinuity will occur between the spectra. This is less the case for the spooled configuration, which indicates a higher degree of stationarity. The nighttime data of the in-field configuration shows a comparable noise level to the spooled fiber. However, it does not show white phase noise behavior at lower Fourier frequencies. This could be due to the excess of noise from the variation of the area, which likely is an effect that is mostly present at longer timescales. As demonstrated in [27], the non reciprocal effect due to polarization noise should be higher in the fiber spools. Thus, since the noise during nighttime is much lower, it can be concluded that the reciprocal noise does not arrive from polarization noise.

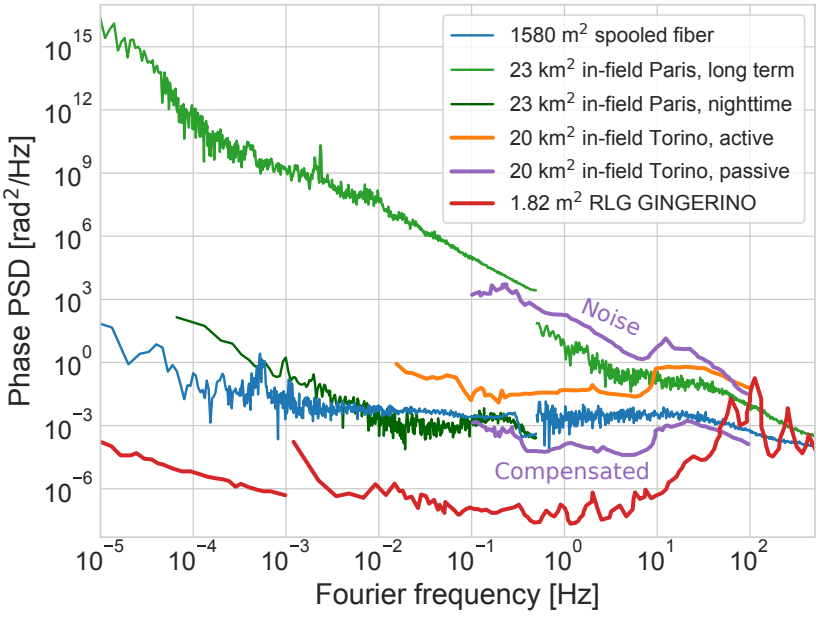

FIGURE 6.7: Comparison between the two configurations in Paris, with an active [100] and passive [19] experiment on a 20 km^2 loop in Torino, Italy, and the 1.82 m^2 ring laser gyroscope (RLG) GINGERINO in Italy [104, 105].

Figure 6.7 shows a comparison of the PSD between the in-field and spool configurations, with other comparable experiments. In purple in seen a similar experiment, with a passive TW configuration on a loop in Torino, Italy [19]. An active ring laser gyroscope (RLG) configuration of the same loop is shown in orange [100], both experiments by our colleagues from INRIM. This experiment had an enclosed area of 20 km^2, which is comparable to the 23 km^2 Paris loop presented here. The phase noise was similar to our realization, as seen in figure 6.7.

In red is shown the sensitivity of the RLG GINGERINO [104, 105] in Pisa, Italy[3]. We see an increase in noise from the $1.6 \cdot 10^{-3}$ km^2 fiber spool, to the 20 km^2 loop in Torino, which is similar to the long-term 23 km^2 loop in Paris. With an increasing enclosed area, it seems likely that we will see an even higher amount of noise. This potentially results in a design difficulty in using fiber links for the purposes of Sagnac measurements: too small an enclosed area, and the fiber link will not be sensitive enough to the change in Sagnac phase. Too high an enclosed area, and the link will be *too* sensitive, which will result in an excess amount of noise. Figure 6.7 compares the frequency sensitivity of the four systems, but this is not directly translated to a comparable sensitivity of the rotation of the Earth. The RLG of GINGERINO and the active loop in Torino both measure the Sagnac phase directly, whereas our system measures the change in the Sagnac phase.

Finally, if the increase in noise in the system is due to the increased enclosed area, this could have consequences in fiber link design. Indeed for national or sup-national networks, the enclosed area may be of the order of 100 000 km^2. In such large-scale ring topologies, the Sagnac noise will largely dominate the propagation noise. That would obviously not be a desirable trait for fiber networks aiming at ultra-stable frequency dissemination.

In this study, we tried to repeat the experiment over months, achieving the same results. It can be that we have a special situation in Paris for the fiber link we used, and for that particular time, or that a technical issue was not spotted despite our best efforts. Here I report on our observations, that are calling to more studies and in-field trials, which would very much be welcomed before drawing any final conclusions.

[3]The phase PSD of GINGERINO is calculated for low Fourier frequencies from [104], and for high frequencies from [104], by using equation (1) in [106], and the technical parameters reported therein.

6.2 Acoustic detection of earthquakes

As optical fiber links usually are placed in the ground, the Doppler-shift induced to the optical signal will mostly be due to acoustic vibrations in the Earth. These usually arise from nearby human traffic from cars, trains or metro, or seismic events like earthquakes. Terrestrial fiber links [107], and to a larger degree submarine fiber links [107, 108], have the last couple of years been studied in Italian and English fiber networks. Here, there has been work towards the investigation of the use of a coherent optical fiber link as a seismometer on the seafloor. This is seemingly an easy option, compared to the complexity of the ensemble of seismometers placed in the ocean [109] that are used nowadays, as optical fibers already are placed on the ocean seafloors. Furthermore, the metrological techniques developed for Frequency transfer on commercial telecommunication networks, are working in parallel with data traffic [110, 34], so it seems like an attractive prospect. A central question discussed in the use of fiber links for seismic detection is towards using fiber links for localization of seismic events [108, 111]. Currently, techniques providing a localization of events, or more generally, time-resolved information like optical frequency-domain reflectometry (OFDR), optical time-domain reflectometer (OTDR) [112] and Distributed Acoustic Sensing (DAS) [113] can be used. Furthermore, it is currently being investigated, if measurements of the status of polarization of the telecommunication signals can prove a future solution to such localization [111]. Here, I will show an analysis of the prospect of using the REFIMEVE fiber network for the detection and localization of seismic events, using the currently implemented technology of the network.

6.2.1 Principles of seismic detection

During seismic events like earthquakes, a huge amount of energy gets released in an instant. The *magnitude* of the event can be measured in many different scales, but in this study I will be referring to the *moment magnitude*, denoted Mw, of the earthquakes. The moment magnitude is related to the amount of energy released (in Joule) by the event as [114]

$$E_s = 10^{1.5Mw+4.8}. \tag{6.4}$$

A large part of the released energy propagates through the Earth, in the form of acoustic waves called *seismic waves*. Two types of body waves are released: longitudinal/compressional primary (P) waves, and transverse/shear secondary

(S) waves. P waves arrive first at detection sites, and travels with $\sim 6-14$ km/s, depending on the layer of the Earth [115]. The S wave is stronger than the P wave, and travels with velocities of $3-7$ km/s, but can not propagate through the liquid core of the Earth [115]. When an acoustic wave hits a fiber cable, it will induce a strain in the fiber, modulating the index of refraction. This will correspond to a Doppler shift of the light, which is measured in the interferometer. For such a study, of the interaction between acoustic waves and the optical fiber links, I will exclusively be discussing the *noise of the fiber link*, at not the compensated E2E signal, which has otherwise been discussed throughout this manuscript.

The phase noise experienced by the uncompensated round-trip fiber signal, can be expressed as a sum of the experienced noise traveling up and down the fiber [21]:

$$\phi(t) = \phi_{\rightarrow}(t) + \phi_{\leftarrow}(t) = \int_0^L \delta\phi\left(z, t - \tau_D + \frac{z}{v}\right)\, dz + \int_0^L \delta\phi\left(z, t + \frac{z}{v}\right)\, dz,$$

where z is the location along the fiber, and v is the speed of the light in the fiber. $\delta\phi$ is the *phase noise per unit length*, which is difficult to model and will depend on a number of parameters. Noticeably, the medium in which the fiber cables are placed can heavily affect its sensitivity to seismic events. Cables placed in concrete will for example be less sensitive compared to a cable placed in earth. The length of the fiber, L, is a critical parameter for the detection of seismic events: for too short a link, the integrated acoustic noise will be too small, resulting in a limited seismic detection. However, as discussed in chapter 3.2, the nominal noise level of a fiber link scales with the length of the link. As such, the acoustic noise from seismic events detected by very long fiber links can easily be hidden in the nominal noise level.

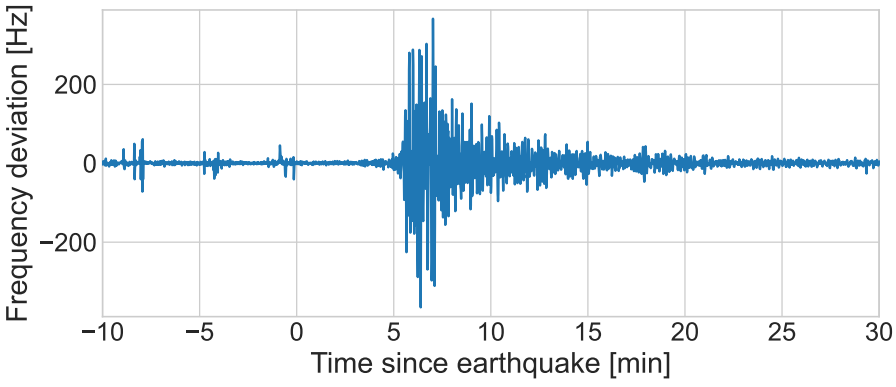

FIGURE 6.8: Example of the detection of an Mw 6.4 earthquake in Croatia, by Link A in the REFIMEVE network.

Figure 6.8 shows an example of a seismic detection in the 2×43 km long Link A, of an Mw 6.4 earthquake in Croatia. The time axis corresponds to the time elapsed since the earthquake, which will be used for all illustrations throughout this study. The arrival of the seismic wave around the 6^{th} minute is visible in the significant increase in noise, which slowly decreases afterwards to once again reach the nominal noise level. Depending on various factors like the size of the earthquake and the distance away, the detection of the seismic waves can last between a few minutes, to several 10s of minutes. It usually consists of a big envelope, which can be 10 minutes long, consisting of smaller oscillations with periods $\sim 5 - 30$ seconds. For an S wave, traveling with ~ 3 km/s at the crust of the Earth, this corresponds to wavelengths of $15 - 1\,800$ km.

The signature of the detection in fiber links is very reminiscent of the one seen in seismometers. In this study, I will be comparing the detection of earthquakes by the fiber links, with the detection of the same earthquakes by nearby seismometers. Figure 6.9 shows in green triangles all seismometers in the French reseau sismologique et géodésique français (RESIF) network. The highest densities of seismometers are found near the Alps and Pyrenees, where the seismic activity is the highest. However, most of France is relatively well covered, which allows the comparison of the detection of REFIMEVE links with nearby seismometers. All time-series data of the seismometers shown in this study are gathered from the database of RESIF[4]. All of this data is available freely, and is easily accessible, from several infrastructures. Indeed, the studies presented here have been made possible due to the huge work and open access policy from the seismological community, whom I will give my sincerest thanks.

An approximation of the path of the fiber links is used throughout this study, which I will call the *linear approximation of the path*. As shown by the blue lines in figure 6.9, the fiber links are approximated to be a straight line from A to B. This approximation is shown with the actual path of the link, shown in red. Currently, the fiber noise is not recorded throughout the whole network. Therefore, it is only the first spans of the long-haul fiber links, as shown in figure 6.9, which will be considered for this study.

Figure 6.10(a) shows a detection of a different earthquake in the noise of Link A. The top, blue trace shows the fiber noise of Link A, over the duration of 1.5 hours. Three brown traces show the signal of a local seismometer in Paris[5], close to the link. The three brown traces shows the three individual components of the seismometer, recording the East, North and the radial Z components of

[4] All seismometer data shown are measured with TRILLIUM-120PH broadband triaxial sensors by Nanometrics.

[5] Named CURIE in the RESIF network.

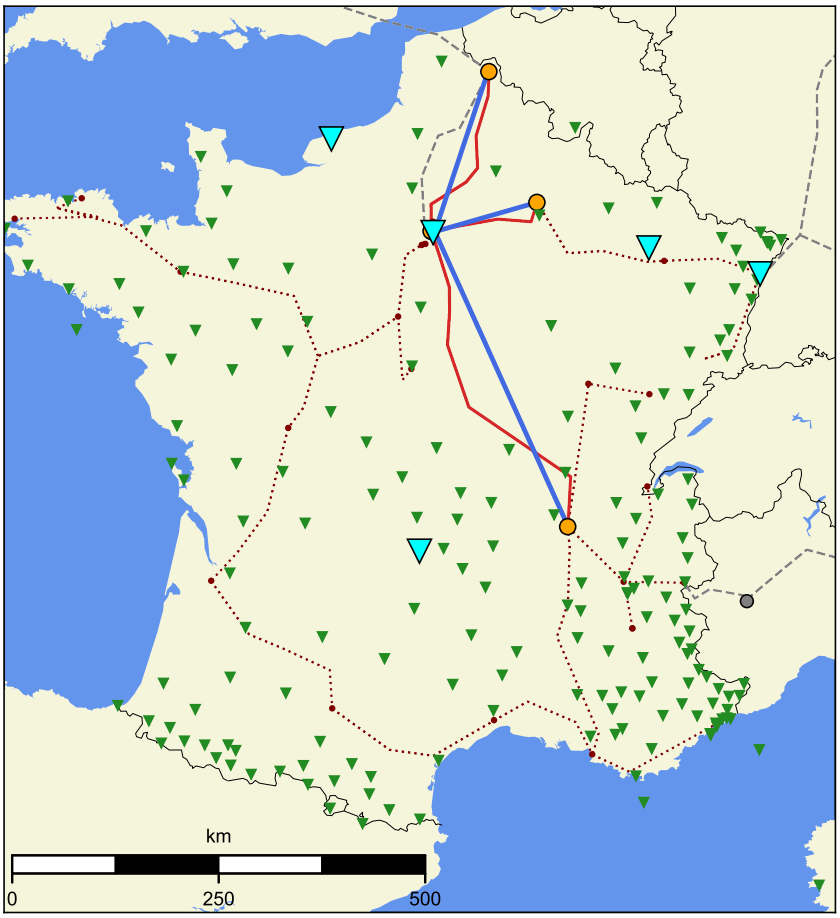

FIGURE 6.9: Map of all seismometers in the French RESIF network (small green triangles), and the seismometers which data is used in this chapter (big cyan triangles). The paths of the first span of the fiber links are shown in red, and the linear approximations of the paths are shown in blue.

the seismic waves, from top to bottom respectively. The acoustic perturbation of the earthquake is seen in all signals, with the highest correlation between Link A, and the North and Z components of the seismometer.

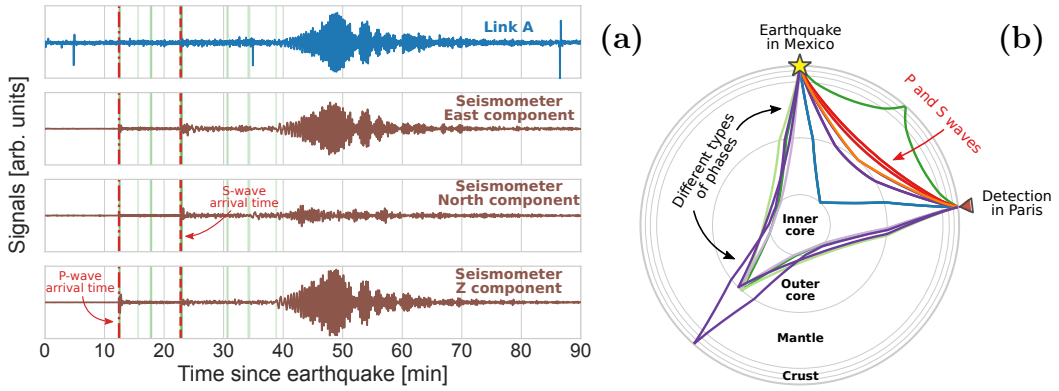

FIGURE 6.10: Detection of an Mw 7.4 earthquake in Mexico. (a): Frequency trace of the noise of Link A (blue, in arbitrary units), and trace of the three different components of a local seismometer (brown, arbitrary units): East, North and Z components, from the top to bottom respectively. Green and red horizontal lines shows arrival times of different phases of the earthquake, with the primary (P) and secondary (S) waves shown in red. (b): Travel paths on a spherical Earth, of the phases shown in (a), from the epicenter in Mexico to the detection in Paris. Plot realized with ObsPy [116].

Due to refractions and reflections with the different layers of the Earth, the same type of seismic wave can propagate through different paths in the Earth, and arrive at different times at a given location. These many different potential paths of the seismic waves of an earthquake is called *phases*, and is illustrated in figure 6.10 (a) and (b), for an earthquake under study. The arrival times of these different phases is shown in green in figure 6.10(a). The arrival of the P and S waves (without any refractions or reflections) are shown by the vertical red lines, which coincide with the increase in noise, most prominently noticeable in the East and Z components of the seismometer, around minute 12 and 23. As there is a correlation between the increase in noise and the predicted arrival times, it can be concluded that it is very likely the earthquake under study that is detected by the link and the seismometer. Here, the arrival of the phases are calculated from an earthquake of magnitude Mw 7.4 at the Mexican Southwestern coast, more than 9 000 km from Paris. The arrival times are calculated using the *ObsPy* Python package [116], from the *iasp91* model [115].

Figure 6.10(b) shows the corresponding travel paths of the different phases from the earthquake, similarly made possible by ObsPy, calculated with the

same model. The figure illustrates the Earth, approximated as a sphere. The earthquake in Mexico in indicated by the yellow star, and the detection site in Paris by the red triangle at the right. The travel paths of the different phases are indicated by differently colored lines, illustrating how they get reflected and refracted at the inner core, the outer core, the mantle, and the crust of the Earth. The P and S waves are shown as red lines.

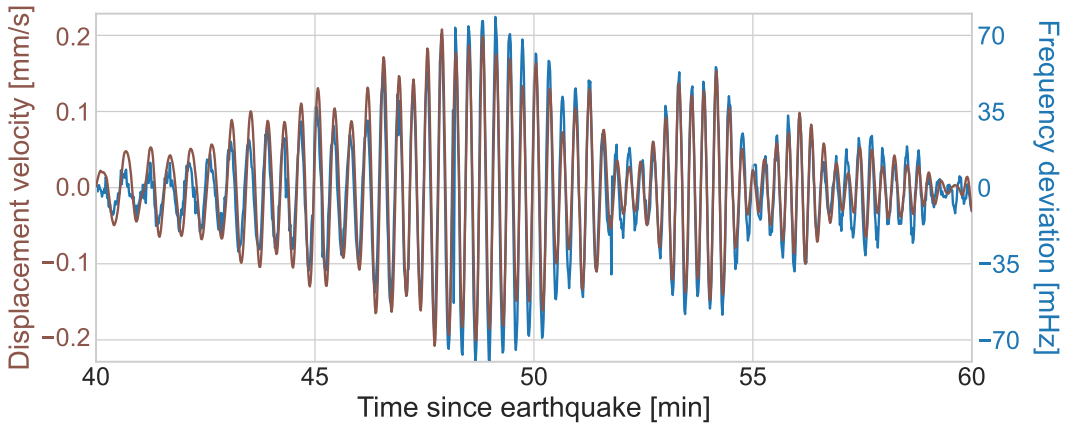

FIGURE 6.11: Overlap of the detection of an earthquake by Link A (blue), and the East component of a nearby seismometer (brown), over the duration of 20 minutes. The time trace of Link A and the seismometer are both a cut-out of the traces shown in figure 6.10.

Figure 6.11 shows the frequency trace of Link A and the East component of the seismometer, as shown figure 6.10(a), focused on the duration 40-60 minutes after the time of the event. Since the wave arrived ~ 2 s before at Link A than at the seismometer, the time axis of Link A has been shifted with 2 s, in order to illustrate the similar structure of the wave. Accounting for the 2 s delay, the correlation between the noise of Link A and the East component of the seismometer in the shown duration is at 0.94. The correlations between the North and Z components are 0.43 and 0.90 respectively. The linear approximation of Link A stretches almost perfectly in a North/South direction, which indicates that the link is more sensitive to wave components orthogonal to the direction of the link itself, as expected.

I have manually investigated a number of seismic events from around the Earth, and identified if they correlate with seismic waves detected by the noise of the links in the REFIMEVE network. Figure 6.12 shows earthquakes, which I have found was detected by the REFIMEVE network. The closest event is in France, ~ 500 km from Link A in which it was detected, and the furthest away event is in Fiji, on the very opposite site of Earth. Detected events ranges from

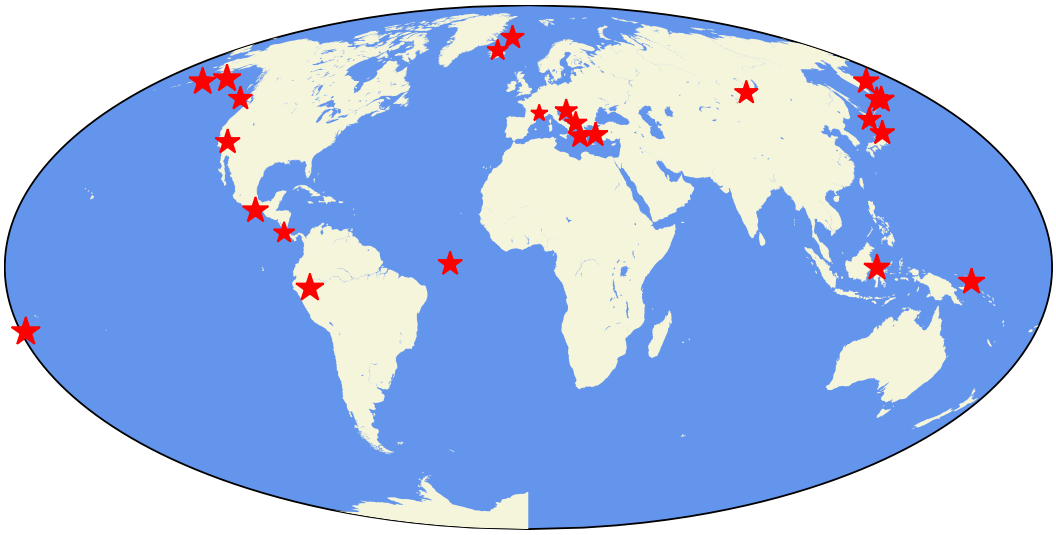

FIGURE 6.12: Location of the 24 detected seismic events with the REFIMEVE network, shown by red stars.

magnitudes of Mw 4.8, to Mw 8.2. A more detailed study of the earthquakes detected by Link A is shown in the next part of this chapter.

6.2.2 Prospects of seismic detection with coherent optical fiber links

Modern seismometers are widespread around the world. They are easily deployable, reliable, very sensitive to acoustic vibrations, and can detect all components of the seismic wave in its three measurement axes. Therefore, the use of optical fiber links for seismology must meet some criteria to be considered as a supplementary technology for seismometers. This can either be:

1. To provide the same information as modern seismometers, but more reliably or with a higher sensitivity.

2. To provide new information about seismic events, where the nature of a fiber link is exploited: they can be hundreds of kilometers long, which means they can easily cover a great distance. Depending on how the seismic wave hits a fiber network, new information about the earthquake or the seismic waves, or at least same information but more easily derived, could potentially be exploited.

In the following, I will investigate these prospects of using terrestrial coherent optical fiber links for detection of seismic events. First, I will show a study of the first point from above, investigating the sensitivity of fiber links to seismic

events, and compare it to modern seismometers. Afterwards, I will show a study of the second point, and discuss the prospects of using a network of fiber links for seismic detection.

6.2.3 Detection range of a mid-haul fiber link

Since 2015, the REFIMEVE network has included five different links, which have operated at different times, as explained in chapter 2.3. Of the five links, Link A seems to have the highest sensitivity to seismic events. With a total length of 86 km, this low-noise link is long enough to integrate a significant amount of seismic noise. Furthermore, as discussed in chapter 3.2, the environments of the MLSs in SYRTE and LPL are significantly better isolated than the other stations around the network, resulting in few and small periodic perturbations, which can otherwise disturb the measurement. Lastly, the link is not placed in concrete, which could otherwise damp the seismic oscillations.

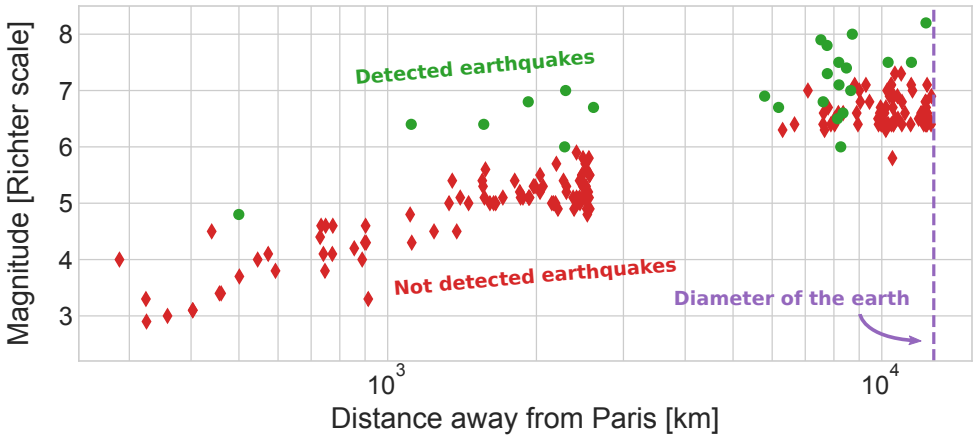

FIGURE 6.13: Detection range of Link A, of 186 manually screened earthquakes. Detected earthquakes, which are the same as shown in figure 6.12, are shown in green, and earthquakes which are not seen by the link is shown in red. The diameter of the Earth is indicated by the vertical purple line.

Figure 6.13 shows the detection range of Link A, of more than 180 manually scanned events. Earthquakes which are detected are shown in green, and earthquakes which are not detected by the link are shown in red. The magnitude of the events is plotted as a function of distance away from Paris, where the purple line indicates the diameter of the Earth. Paris is located in an interesting spot on the Earth, which can be inferred by the plot: in central/Northern Europe, only few and small earthquakes occur. The further away one goes from Paris, the bigger the earthquakes become, both in number and magnitude. As such, it is mostly tele-seismic events that gets detected by the fiber network, which

are more than 1 000 km away. Lastly, there seems to be what looks like a somewhat linear tendency on the double-logarithmic plot, whether an earthquake can be detected, based on its magnitude and distance away. However, a larger data ensemble would be needed to draw any final conclusions. Modern seismometers can normally detect seismic events larger than a magnitude of Mw 5 from anywhere in the world [117]. As such, figure 6.13 shows that even the most sensitive fiber link in the REFIMEVE network, seemingly shows a significantly worse detection range than modern seismometers.

6.2.4 Sensitivity of a fiber link

I have investigated the sensitivity, which is given by the SNR, of 18 detected events in Link A. The amplitude of the detection signal is given by the amplitude of the detected wave, and the noise is given by the standard deviation of the signal before the occurrence of the earthquake. I have worked with three different parameters, which all are affecting the sensitivity: the distance from the epicenter to the link, the magnitude of the earthquake, and the incident angle between the acoustic wave and the fiber link. This angle is calculated as a 3-dimensional angle, where first the incident angle between the acoustic wave and the surface of the detection site is found, which can be calculated with ObsPy in similar ways as explained above. Then, accounting for the directional vector of the fiber link, an effective angle between the Poynting vector of the wave and the link is derived. Because of the nature of the path of seismic waves from far away in the Earth, the effective angle will mostly be close to 90°

Figure 6.14 shows a 3D plot of the SNR of the detection of Link A, as a function of the distance and incident angle, with the magnitude of the earthquake given by an increasingly purple color. From this, albeit small sample size, some observations can be seen: the biggest SNRs are seen for events which are close by, with orthogonal incident angles. This is consistent with the detection shown in figure 6.11, which indicated a higher sensitivity for the East/West traveling components for Link A, which stretches from South to North. This is opposite of the sensitivity of DAS, which is virtually blind to waves traveling perpendicular to the fiber [118].

An orthogonal sensitivity of the phase of the signal is proportional to $\sim \sin(\theta)$, thus it seems likely that the sensitivity of the SNR of the fiber link has an angle dependence of $\sim \sin^2(\theta)$. The relation between the released energy and the moment magnitude is given by equation 6.4, and with an energy dispersion proportional to L^{-2}, a first guess for a dependence of the sensitivity of a fiber

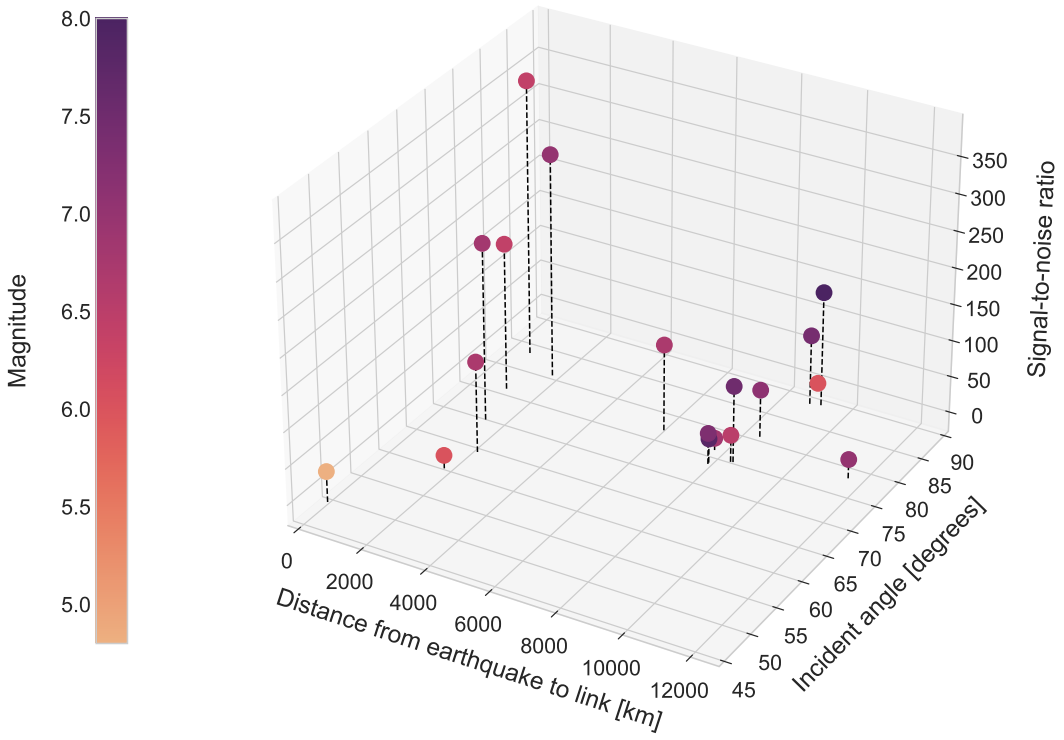

FIGURE 6.14: Signal-to-noise ratio of detected earthquakes by Link A, as a function of distance away, and incident angle to the direction of the fiber. The magnitude of the earthquakes is shown by increasingly purple color.

link to seismic events could be similar to

$$\mathrm{SNR}_{\mathrm{link}} \propto \frac{10^{1.5Mw+4.8}}{L^2} \sin^2(\theta). \tag{6.5}$$

Figure 6.15 shows the SNR of the detected events by Link A, as a function of

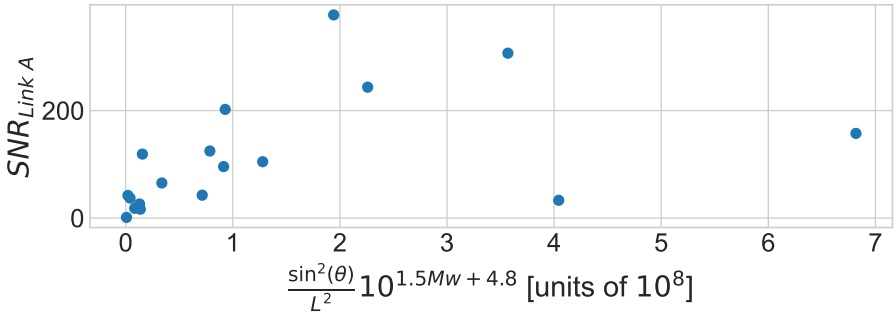

FIGURE 6.15: Signal-to-noise ratio (SNR) of detected earthquakes by Link A, as a function of equation 6.5.

equation 6.5. It seems to show a tendency for a first model, with a few outliers. A larger sample size would be necessary for a future determination of an actual law, describing the sensitivity of fiber links to seismic perturbations.

Modern seismometers shows a high sensitivity to seismic waves, and the ability to correlate detections of the fiber network with detections of seismometers, has been an invaluable tool in the studies presented here. The relative sensitivity between the optical fiber link and a seismometer is calculated as

$$\mathrm{SNR}_{\mathrm{relative}} = \frac{\mathrm{SNR}_{\mathrm{link}}}{\mathrm{SNR}_{\mathrm{seismometer}}}. \tag{6.6}$$

The relative sensitivity of 20 identified events with Link A, and the closest seismometer, is shown in figure 6.16.

The three components of the seismometer will have three different SNRs. This is illustrated by the error bars: the lowest error bar corresponds to the lowest value of $\mathrm{SNR}_{\mathrm{relative}}$ for any of the three components, the highest error bar for the highest value of $\mathrm{SNR}_{\mathrm{relative}}$, and the circle indicates the ratio between the SNR of Link A and the mean SNR of the three seismometer components. For all detected events, the sensitivity of the fiber link was significantly lower than that of the seismometer. Only in one case, event #3, the sensitivity of the link was higher than that of *one* of the three components of the seismometer. Keeping the small sample size in mind, this result indicates that the use of coherent optical fiber links, with the current technological setup employed in the REFIMEVE network, for seismology, seems to not use the link as classical

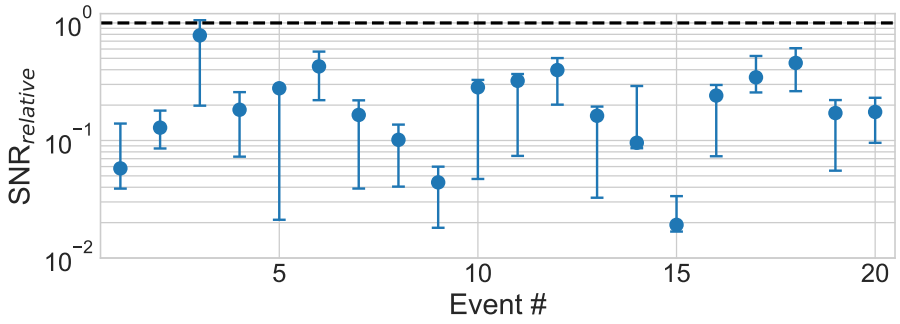

FIGURE 6.16: Relative signal-to-noise ratio (SNR), $SNR_{relative}$, between detected earthquakes by Link A and the three detection axes of a nearby seismometer, as given by equation 6.6. Top of the error bars corresponds to the highest value of $SNR_{relative}$ for any of the axes, the lowest error bars corresponds to the lowest value of $SNR_{relative}$ for any of the axes, and blue circles corresponds to the mean $SNR_{relative}$ between the link and all three axes. Black dotted line indicates where the SNR of the link is the same as the SNR of the seismometer, $SNR_{relative} = 1$.

seismometers. For this, the sensitivity seems not nearly as high as modern seismometers, as it does not seem to provide any obvious advantages.

6.2.5 Network detection of earthquakes

One prospect of using optical fiber links for seismology, is to use them in relation to one another, which potentially enables a seismic detection of a fiber network, as discussed above. In the following, I will show an analysis on the prospects of such an approach.

An illustration of the potential use of a fiber network for such studies is shown in figure 6.17. Here, the first section of the two long-haul fiber links, Link B and Link E, are shown in their linear approximations in green.

A given seismic wave, arising from a seismic event, will be detected in both the long links. If one is able to deduce the location of the detection along each of the two links, it will in theory be possible to extrapolate a corresponding trajectory of the earthquake. This concept is similarly used in VLBI, with radio antennas. This is illustrated by the gradient in figure 6.17. As an example, the white part corresponds to the longest possible distance between the first sections of Link B and Link E, of 390 km. In that case, if it would be possible to infer that a seismic wave was detected by the two links with a corresponding detection distance of 390 km, the corresponding trajectory of the event could be determined to correspond to the whitest part of the gradient on the map.

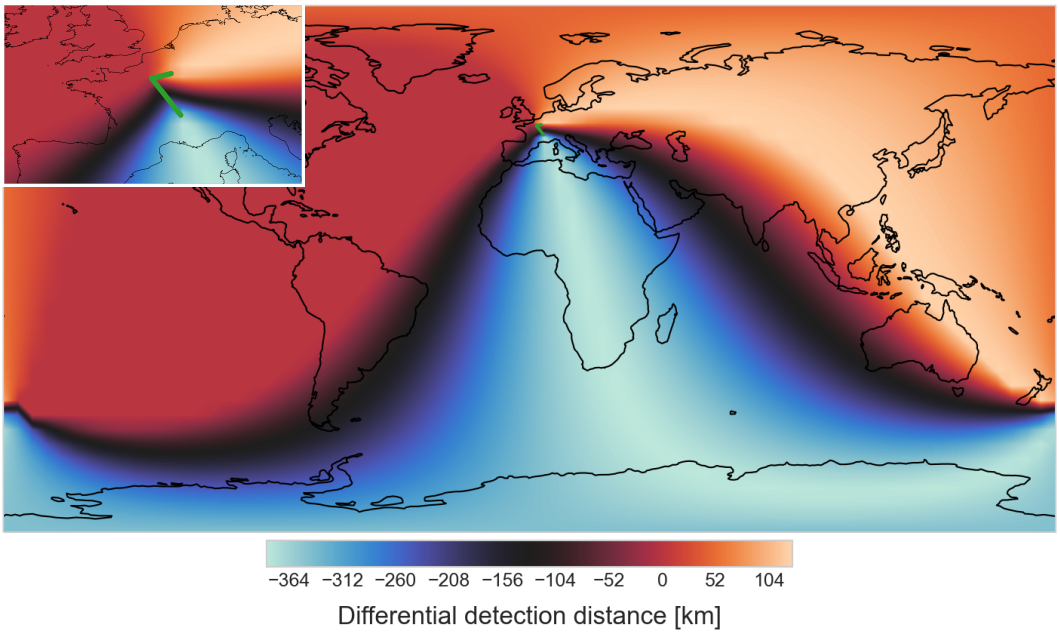

FIGURE 6.17: Map showing a potential use of the detection of a seismic wave by the two links, Link B and Link E, shown as green straight lines. If it is possible to infer a distance between the detection point in each of the two links, illustrated by the color gradient, it would be possible to infer the trajectory of the seismic wave. Insert shows a zoom in the region around France. Concept of the illustration derived by Hendrix Montalvan Leyva.

Including a third link, a three dimensional pinpoint of the earthquake would be possible.

This concept does not depend on the detection time or velocity of the wave, as only a space coordinate difference is computed. However, such a study is very complex. The resolution of the technique depends on the length of the fiber links involved: the longer links, the higher achievable resolution. On the other hand, long-haul fiber links have a much lower sensitivity to seismic waves than shorter links. Lastly, it must be possible to reliably determine where along the link the wave is detected. This last point is investigated below.

Propagation of seismic waves in a fiber network

Figure 6.18 shows an example of a network detection of an Mw 5.7 earthquake in Bosnia and Herzegovina by the REFIMEVE network. The predicted P and

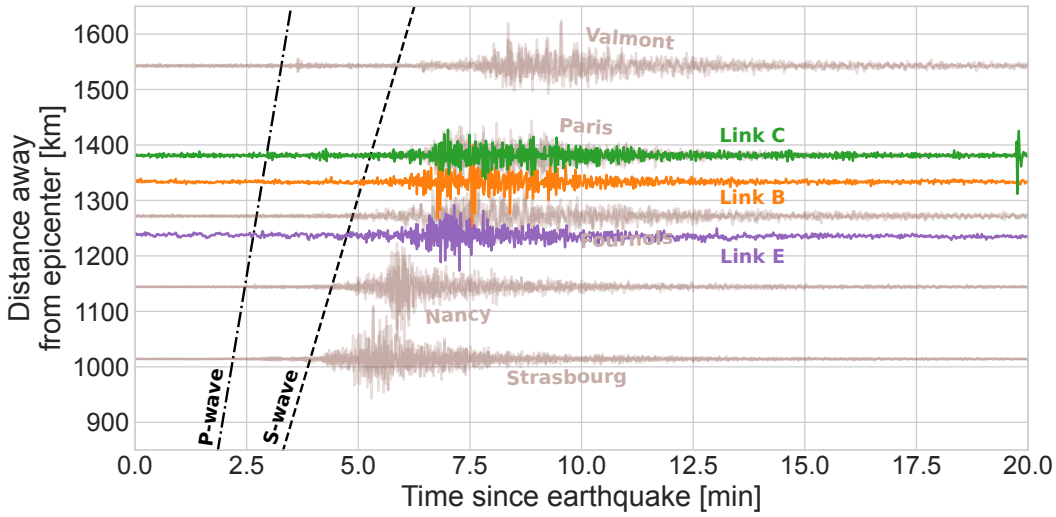

FIGURE 6.18: Detection of an Mw 5.7 earthquake in Bosnia and Herzegovina by the fiber network. Three links detects the earthquake, which are shown in green, orange and purple. Data of five seismometers are shown in brown. The locations of the five seismometers are shown by the cyan triangles in figure 6.9. Y-axis represents distance away from the earthquake, which for the fiber links are calculated from the midpoint of the link. Data traces are scaled in amplitude for purely visual help.

S waves are shown in black lines. Signals from five different seismometers are shown in brown traces, plotted with a y-scale corresponding to the distance away from the event. The location of the five seismometers are shown as cyan triangles in figure 6.9. The three fiber links which detected the event, Link B, C and E, are shown with the usual color code. Here, the distance away is

calculated from the center of the fiber link. We call this the *barycenter*[6] of the fiber link. In the following, I will show a study of the determination of the barycenter of the link.

The barycenter of a fiber link

To calculate the barycenter of a fiber link for a given seismological event, the detection of the link is compared to the detection of nearby seismometers, as illustrated in figure 6.18. A first step is to find events, where the precise arrival time of the P wave can be determined in the fiber link under study. This can be difficult with the low SNR of the fiber links, which is usually not sensitive to such a high degree, and it narrows the opportunities of the study considerably down. As shown in figure 6.10(a) and figure 6.18, the arrival time of the P wave can be calculated with the ObsPy Python package. As this approach takes some general assumptions on the speed of the wave in the different layer of the Earth, the most reliable approach is to correlate the predicted arrival time of the P wave, with the measured arrival time of the seismometers.

When the arrival times of the P-wave at the seismometer and at the link is determined, the apparent distance between the earthquake and the link can be approximated as

$$d_{\mathrm{EQ}\to\mathrm{link}} \approx d_{\mathrm{EQ}\to\mathrm{seismo}} \left(\frac{T_{\mathrm{link}} - T_{\mathrm{seismo}}}{T_{\mathrm{seismo}}} + 1 \right), \tag{6.7}$$

where $d_{\mathrm{EQ}\to\mathrm{seismo}}$ is the distance between the epicenter and the seismometer, and T_{seismo} and T_{link} is the arrival time of the P wave at the seismometer, and at the link respectively. From this, the barycenter can be approximated as the part of the linear approximation of the link which has a distance of $d_{\mathrm{EQ}\to\mathrm{link}}$ to the epicenter. This approximation gets better, the closer the earthquake is to the fiber link. Assuming reasonably synchronized measurements for both the seismometers and the links, the biggest source of error is in the determination of the arrival time of the P wave at the link, T_{link}. As the P wave travels with a speed of ~ 6 km/s in the crust of the Earth [115], a one second shift on the determination of the arrival time of the earthquake will lead to a *minimum* 6 km shift in the determination of the barycenter. As such, this determination is very difficult to do for short links, where the relative error can get very big. As described above, Link A is the most sensitive of the links in the REFIMEVE network, and therefore the one which is easiest to determine the arrival time

[6] The term arises from the center of mass between astronomical bodies in orbit. It seems fitting to describe the "center of mass" of the detection of a fiber link.

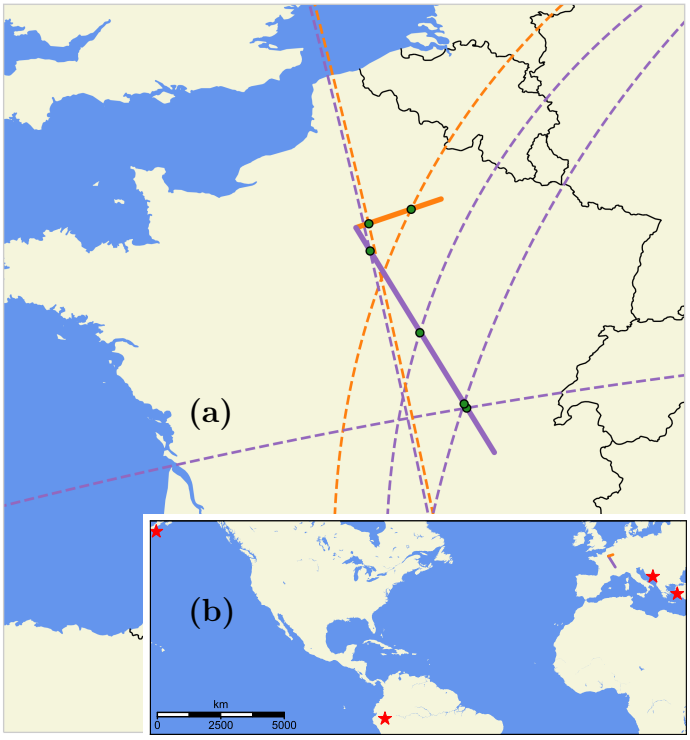

FIGURE 6.19: (a): Determined barycenters of Link B (orange) and Link E (purple), for four different earthquakes. Barycenters are shown as green dots, and the circles indicate the distances calculated from the epicenters to the links, as calculated by equation 6.7. (b): a map of the location of the earthquakes, shown as red stars.

of P waves. Even though the link is 43 km long one way, the physical distance between its start and end point, SYRTE and LPL, is just 10 km. An error of just a few seconds can quickly lead to a determination of a barycenter much longer away than the location of the link itself.

Indeed, using long-haul fiber links, the calculation of the barycenter becomes relatively much more precise, assuming the SNR of the detection is high enough. I have calculated the barycenter of the two longest links in the REFIMEVE network, Link B and Link E, from four different earthquakes, of magnitudes ranging from Mw 5.7 to Mw 8.2. Of these four events, a reasonably precise arrival time could be determined for all four events for Link E, and for two of the events for Link B. This is shown in figure 6.19. Figure 6.19(b) shows the four earthquakes under study. Figure 6.19(a) shows the linear approximation of the links, with similarly colored circles indicating the calculated distance between the epicenter and the link, $d_{\mathrm{EQ}\to\mathrm{link}}$, from equation 6.7. The point at which the circles crosses the respective link is shown by green dots. These green dots indicate the barycenter of the link, for the corresponding earthquake. The

barycenters of the two links span most of the length of the links themselves. This shows that the links, unlike seismometers, most likely cannot be considered to detect the seismic waves at a given point in space.

This study is made from an even smaller sample size than the sensitivity study above. This is because the nature of fiber links, which by construction makes such a study difficult: short fiber links, like Link A discussed above, shows the highest sensitivity to seismic events. However, the shorter the link, the less the nature of the links can be exploited in the detection: that they span large distances. Furthermore, the determination of the barycenter for such a short link will be very difficult, because of the uncertainties involved as discussed above. On the other hand, as discussed in chapter 2.2, the noise of the link scales with its length. Long-haul fiber links seems to have too low a sensitivity, to currently be considered a supplementary technology to seismometers. As the prediction of the barycenter of a link for a given seismic event is very complex and, so far, unknown, the huge uncertainty in *where* the earthquake is detected means if it difficult to provide additional information about the waves.

All studies presented here have been made with earthquakes which are relatively far away form the fiber links. I have not investigated Earthquakes occurring close to the fiber links, which are very sparse in France. Indeed, future studies on the sensitivity of the fiber links to local earthquakes compared to seismometers could be interesting.

Some future prospects of using coherent optical fiber links for seismic detection, could be to implement time-dependent measurement techniques, as is currently seen in OFDR, OTDR [112] and DAS [113]. These techniques could resolve the localization issue, by introducing a time dependence. Lastly, measuring the status of polarization of the telecommunication signals is also currently being investigated, as a cheaper and more easily implementable option for future localization solutions [111]

Work has gone towards an automatic detection of seismic events in the noise of the links in the REFIMEVE network, which has been carried out by Hendrix Montalvan Leyva. He has developed a machine learning algorithm, which is able to recognize noise induced by seismic perturbations, to other types of outliers and rogue data points in the links. Still being in its early stages, it is able to recognize the noise behavior of the seismic waves, but it is not yet able to predict which earthquake the noise arises from. With more extensive studies on the response of the links to seismic waves, like presented in this chapter, it might be possible to expand the algorithm to include the prediction of which earthquake is detected in the link.

Chapter 7

Conclusion

This manuscript starts with a brief introduction to time and frequency metrology, and key concepts to understand the physics of fiber links. I end chapter 1 with an explanation of the different links in the French REFIMEVE fiber network, which are studied throughout the thesis. I showed in chapter 3 the theoretical limits and noise modelization of the fiber links, in the presence of continuous measurements. I demonstrated the ability to simulate the fiber links. In chapter 4, I presented a study of the impact of missing data to the statistical evaluation of a coherent optical fiber link, and discussed ways to mitigate these effects. Here, I end with a case study where missing data is inevitable: an evaluation of the statistical properties of a long-haul fiber link, over the span of more than 5 years. These studies have all been possible due to the data processing software that I have built, which enables a quick and reliable data analysis. Furthermore, the statistical tools developed in chapter 3 and 4 enables the evaluation of the French fiber network in applied studies, which are presented in chapter 5 and 6.

In chapter 5, I discussed the complexity of modern fiber networks, in the context of comparing optical clocks. Here, I explained the data processing software that I have created, which ensures reliable and efficient processing of the large ensemble of data generated in the REFIMEVE network. I presented case studies from two different campaigns: in the context of a one month long comparison campaign between European NMIs, I evaluated the uncertainty budget from the French network. Afterwards, I discussed the results from a four month long comparison campaign between atomic clocks at SYRTE and INRIM. Here, I compared the performance of the French fiber network to previous and future campaigns. I ended with a study of the aliasing effects arising in a fiber link during a clock comparison, where it is necessary to not only account for the uptime of the link itself, but the uptime of other subsystems in the frequency

chain.

Chapter 6 steps out of the field of pure metrology, where I evaluated two studies of the use of fiber links for sensing effects induced by the Earth itself: first, I investigated an experiment I performed with a fiber link with a ring topology around Paris. Here, I discussed the prospects of using such fiber links as a gyrometer. Afterwards, I showed a study of the acoustic detection of seismic waves, which can be visible in the noise of a fiber link. Here, I compared the sensitivity of fiber links to modern seismometers. Furthermore, I discussed the prospects of using network detection of multiple fiber links, in order to derive information about earthquakes.

The work of this thesis shows several analyses of the use of coherent optical fiber links for the comparison of optical clocks. It shows reliable operation of the links over many years, and that the uncertainty contribution induced by the links is compatible with the goal set by the CCTF towards the future redefinition of the SI second. In the future, similar studies can be performed for more links, both in France as well as around the world. Here, the comparison of the long-term behavior of several fiber links would be very interesting, in order to test the ergodicity of links around the world. In the context of using the fiber links as sensors, it raises potential issues with future fiber link design, where the results presented here suggests that ring topologies could be desirable to avoid. This has been studied very little previously, and future similar studies would be desirable to verify these results. For the use of fiber links as seismic sensors, I find that localization can be difficult with the current experimental setup implemented in the REFIMEVE network. Here, future time-dependent measurements will likely be necessary, in order to fully exploit the fiber network for seismic detection and localization. Implementation of parallel measurement techniques could be interesting, in order to gain increased knowledge on the response of seismic waves on the optical fibers.

Appendix A

Statistical tools

Assuming an ergodic and stationary frequency signal $\nu(t)$, the relative frequency fluctuations $y(t)$, frequency fluctuations $\Delta\nu(t)$, phase evolution $\phi(t)$, and time error evolution $x(t)$, are defined as [15]

$$y(t) = \frac{\nu(t) - \nu_0}{\nu_0} = \frac{\Delta\nu(t)}{\nu_0} = \frac{1}{2\pi\nu_0}\frac{d\phi(t)}{dt} = \frac{dx(t)}{dt}.$$

A.1 Power spectrum densities and autocorrelation function

The phase power spectral density (PSD) $S_\phi(f)$ is often used to describe the spectral properties of the signal. Assuming wide-sense stationarity, this is found as the Fourier transform of its autocorrelation function:

$$S_\phi(f) = \mathcal{F}\{R_\phi(\tau)\},$$
$$R_\phi(\tau) = \mathcal{F}^{-1}\{S_\phi(f)\}.$$

This is known as the Wiener–Khinchin theorem. The autocorrelation can be found as the time average of the product between the phase, and a time-lagged version of itself:

$$R_\phi(\tau) = \overline{\phi(t)\phi(t-\tau)},$$

where τ represents the time-lag. The autocorrelation can be a useful tool in order to highlight periodic behaviors in the signal.

The PSD describes the power of the different frequency components of the signal at any Fourier frequency (or equivalently timescale). The relation between the phase PSD, the frequency PSD $S_{\Delta\nu}(f)$, and the relative frequency

PSD $S_y(f)$, is given by:

$$S_{\Delta\nu}(f) = f^2 S_\phi(f) = \frac{f^2}{\nu_0} S_\phi(f),$$

where ν_0 is the nominal frequency of the signal. The units of $S_\phi(f)$ is rad^2/Hz, the units of $S_{\Delta\nu}(f)$ is Hz^2/Hz, and the units of $S_y(f)$ is Hz^{-1}. These can also be described in dB, as $10\log_{10}(S_\phi(f))$, which has the units $\text{dB}\,\text{rad}^2/\text{Hz}$.

The phase PSD can be modeled by the power law:

$$S_\phi(f) = b_\beta f^\beta,$$

where b_β describes the amplitude of the given noise component, which has a frequency dependence of f^β, and β takes an integer value between -4 and 0. This power law is illustrated in figure A.1, where the corresponding noise type

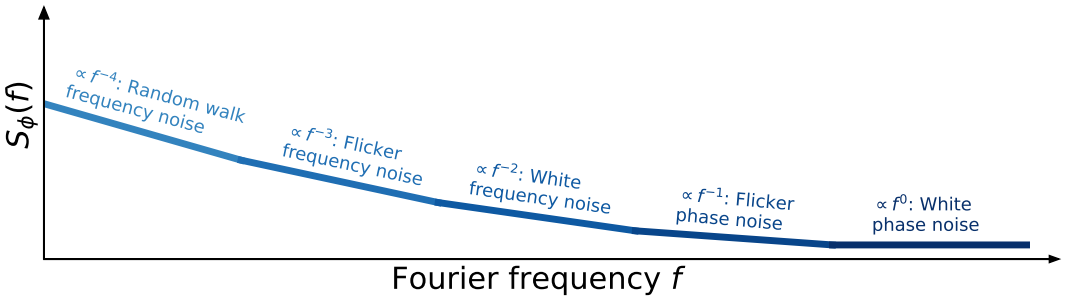

FIGURE A.1: The power law of the phase PSD.

for a given value of β is highlighted. The overlapping Allan deviation (ADEV) describes the stability of the signal as a function of integration time, and can be calculated from the phase PSD by [119]

$$\sigma_y^2(\tau) = 2\int_0^\infty S_\phi(f)\frac{\sin^4(\pi f\tau)}{(\nu_0\pi\tau)^2}\,df. \tag{A.1}$$

The overlapping Allan deviation (ADEV) can, like the PSD, be described by a similar power law, as a function of integration time τ. It does however not differentiate between white phase noise and white frequency noise, which both integrates with τ^{-1}. To differentiate these noise processes, which are dominating the fiber link noise at short timescales, the modified Allan deviation (MDEV) is often often used [50]:

$$\text{Mod}\ \sigma_y^2(\tau) = 2\int_0^\infty S_\phi(f)\left[\frac{\tau_G\sin^3(\pi f\tau)}{\nu_0\pi\tau^2\sin(\pi f\tau_G)}\right]^2 df, \tag{A.2}$$

where τ_G is the spacing between consecutive measurements. The power law of ADEV and MDEV is illustrated in figure A.2.

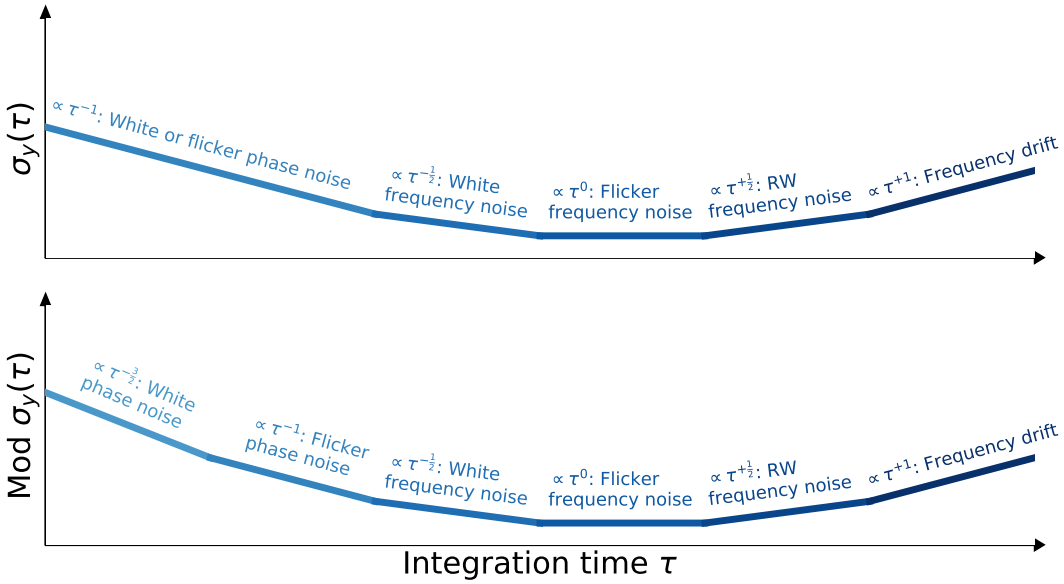

FIGURE A.2: The power law of the ADEV and MDEV.

Finally, the time deviation (TDEV) shows the corresponding desynchronization, and can be calculated from the MDEV as

$$\sigma_x^2(\tau) = \frac{\tau^2}{3}\text{Mod } \sigma_y^2(\tau).$$

A.2 Periodic perturbations in MDEV and ADEV

A relative frequency signal with a periodic perturbation can be written as

$$y(t) = y_{\text{stochastic}}(t) + A\sin(2\pi f_m t),$$

where $y_{\text{stochastic}}(t)$ are any stochastic noise processes, which can be described by the power law, A is the amplitude of modulation, and f_m is the modulation frequency. The corresponding relative frequency PSD is

$$S_y(f) = S_y(f)_{\text{stochastic}} + \frac{A^2}{4}\left(\delta\left(f - f_m\right) + \delta\left(f + f_m\right)\right)$$

ADEV By applying equation A.1, the corresponding ADEV can be found to be

$$\sigma_y^2(\tau) = \sigma_y^2(\tau)_{\text{stochastic}} + \frac{A^2}{2}\left[\frac{\sin^4(\pi f_m \tau)}{(\pi f_m \tau)^2}\right]$$

Assuming the periodic perturbation to be dominating around the top of its oscillation, we can isolate the periodic term:

$$\sigma_y^2(\tau)_{\text{periodic}} = \frac{A^2}{2}\left[\frac{\sin^4(\pi f_m \tau)}{(\pi f_m \tau)^2}\right].$$

In the ADEV curve, this is visible as a "bump". The top of the "bump" can be found by differentiation:

$$\frac{d\ \sigma_y(\tau)_{\text{periodic}}}{d\tau} = \frac{A}{\sqrt{2}\pi f_m \tau^2}\sin^2(\pi f_m \tau)\left(\pi f_m \tau \cot(\pi f_m \tau) - 1\right) = 0$$

from which

$$\tan(\pi f_m \tau) = 2\pi f_m \tau.$$

This has solutions at $\tau = \{0.37\,T_m,\ 1.46\,T_m,\ 2.48\,T_m,\ ...\}$, where $T_m = f_m^{-1}$ is the modulation period. The solution at $\tau = 0$ has been omitted, since such an integration time is not physically interesting.

MDEV Following the same approach, the MDEV of the periodic perturbation is

$$\text{Mod}\ \sigma_y^2(\tau) = \frac{A^2}{2}\left[\frac{\tau_G \sin^3(\pi f_m \tau)}{\pi f_m \tau^2 \sin(\pi f_m \tau_G)}\right]^2,$$

which has its maximum at

$$\frac{d\ \text{Mod}\ \sigma_y(\tau)_{\text{periodic}}}{d\tau} = \frac{A}{\sqrt{2}}\sin^2(\pi f_m \tau)\left(3\pi f_m \tau \cos(\pi f_m \tau) - 2\sin(\pi f_m \tau)\right) = 0.$$

This can be written as

$$\tan(\pi f_m \tau) = \frac{3}{2}\pi f_m \tau,$$

which has solutions at $\tau = \{0.31\,T_m,\ 1.46\,T_m,\ 2.48\,T_m,\ ...\}$.

Finally, it will mostly be the first period which will be visible in the stability curves, which gives the two conversion factors

$$\tau_m = 0.37\,T_m \text{ for ADEV}$$
$$\tau_m = 0.31\,T_m \text{ for MDEV},$$

between the integration time identified by the top of a periodic perturbation in the stability plot, τ_m, and the modulation period of the periodic perturbation T_m.

Appendix B

More details on the Sagnac experiment

The in-field measurement shows a very high level of noise outside a few hours during the night. Figure B.1(a) shows the long-term phase power spectral density (PSD) of the full length of the data set, where a very selective filter has been applied, accepting only relative frequency fluctuations below 10^{-16}. Doing such, all outliers and excess of noise are filtered out, and remains the data where the trackers were healthy. Such a treatment also destroys any potential periodic signal, as explained in chapter 4.1.

It shows the PSD calculated with two different ways of treating the missing data: by concatenation (red), and by keeping the phase a constant value across the gap left by the missing data (purple). In the latter case, the high-frequency noise level have been corrected, as a bias otherwise would be present.

One observes that the PSD of phase noise is more comparable in orders of magnitude. The in-field configuration at nighttime shows an excess of noise of about 10 dB for Fourier frequencies below 10 mHz. An excess of noise for nighttime measurement as compared to the long-term measurement is seen at a Fourier frequencies around 500 mHz.

The coherence time during the night is ~ 60 s, whereas it shows ~ 20 s for the long-term data, when the phase is kept constant. This is reduced to ~ 10 s, where the data has been concatenated, since the time-axis of the data set gets shortened.

For completion of the study presented in chapter 6.1, I present here the corresponding modified Allan deviation (MDEV) for the two configurations explored in this manuscript, the fiber spool and in-field looped fiber, with a distinction for the later one between nighttime and long-term data, including daytime.

Figure B.1(b) shows the MDEV of the same data sets as shown in figure 6.6, corresponding to the differential beat note observable, given by equation 6.2.

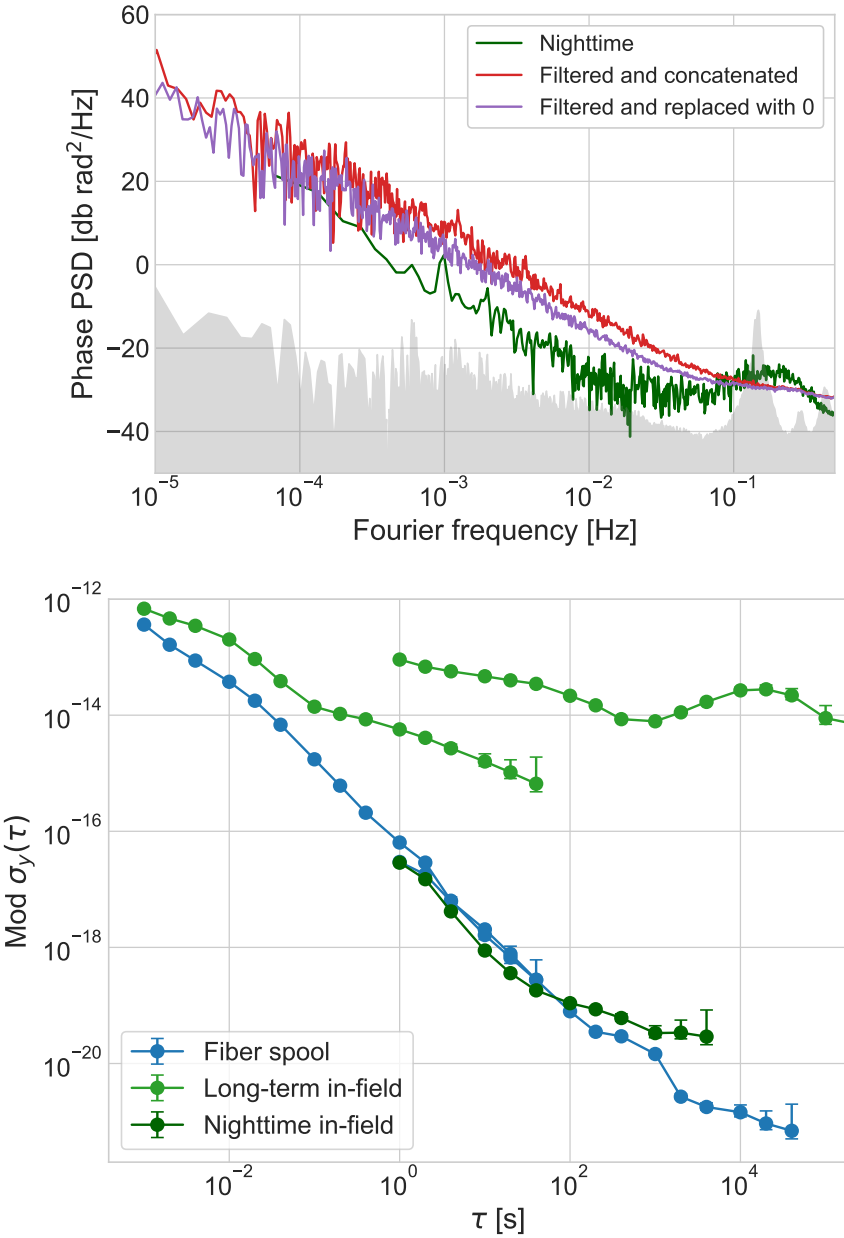

FIGURE B.1: (a): Phase power spectral density (PSD) of the of the in-filed configuration during nighttime (green), filtered long-term where data is concatenated (red), and filtered long-term where the phase is kept constant across the gap left by the missing data (purple). (b): modified Allan deviation (MDEV) of the long-term in-field configuration (light green), nighttime in-field (dark green), and fiber spool configuration (blue).

Appendix C

Article in New Journal of Physics

An article on the operation of Link A and Link B over 2 years, in 2018 and 2019. Furthermore, there are technical details on the multi-branch laser station (MLS).

PAPER • OPEN ACCESS

An accurate and robust metrological network for coherent optical frequency dissemination

To cite this article: Etienne Cantin *et al* 2021 *New J. Phys.* **23** 053027

New Journal of Physics
The open access journal at the forefront of physics

Deutsche Physikalische Gesellschaft DPG
IOP Institute of Physics

Published in partnership with: Deutsche Physikalische Gesellschaft and the Institute of Physics

OPEN ACCESS

RECEIVED
8 November 2020

REVISED
5 February 2021

ACCEPTED FOR PUBLICATION
18 February 2021

PUBLISHED
18 May 2021

PAPER

An accurate and robust metrological network for coherent optical frequency dissemination

Etienne Cantin[1,2,*], Mads Tønnes[1], Rodolphe Le Targat[1], Anne Amy-Klein[2], Olivier Lopez[2] and Paul-Eric Pottie[1]

[1] LNE-SYRTE, Observatoire de Paris, Université PSL, CNRS, Sorbonne Université, 61 av. de l'Observatoire, 75014 Paris, France
[2] Laboratoire de Physique des Lasers, Université Sorbonne Paris Nord, CNRS, 99 av. J.B. Clément, 93430 Villetaneuse, France
[*] Author to whom any correspondence should be addressed.

E-mail: etienne.cantin@univ-paris13.fr

Keywords: frequency transfer, metrology, fiber optic links, laser optics, interferometer

Supplementary material for this article is available online

Abstract

We introduce multi-branch repeater laser stations (MLSs) for the dissemination of an ultra-stable signal from one point to multiple users and the simultaneous evaluation of the stability and accuracy of multiple links. We perform the study of the noise floor of this new instrument. We present then an optical fiber network of 4800 km built with three MLSs and 13 repeater laser stations (RLSs). We show the multi-user optical frequency dissemination on four links totalizing 2198 km with uncertainties below 1.1×10^{-19}. The robustness of the network over two years is presented and stability and accuracy at 10^7 seconds integration time are finally showed.

1. Introduction

Optical fiber links enable the accurate and ultra-stable transfer of an optical frequency reference on distances of more than 1000 km [1–5]. They include an active or passive correction of the noise added through the fiber propagation leading to uncertainties in the range of 10^{-20} or even below [3, 6]. It is thus an unavoidable technique for the accurate comparison of distant optical clocks [7, 8] and their applications to chronometric geodesy [9] and search for new physics [10]. Moreover it provides an input reference frequency signal for a wide range of precision measurements from spectroscopy [11–15] to geophysics [16–18] and syntonisation in astrophysics [5, 19].

Since a few years, the number and length of optical links increased in order to connect national metrological institutes (NMIs) or laboratory users and extend the possible applications. These links are mainly point-to-point links connecting two NMIs or an NMI and a user. However, comparison of multiple clocks in multiple NMIs requires the development of an NMI network, with the possibility of coherent dissemination between all the NMIs. It will enable not only to make significant advances in fundamental metrology but also to search for dark matter [20] or test new physics. Moreover, the development of fiber networks will provide ultra-stable frequency dissemination to many labs and institutes, and thus broaden the range and number of precision experiments.

For that purpose in-line extraction has first been proposed [21] and demonstrated in 2014 [21–23]. It is mainly suitable for dissemination to users along a main link, e.g. using a ring topology in an urban area. Nevertheless, building a fiber link network also requires some hub in order to transfer the signal from an NMI to multiple users and to develop a star, a tree or a mesh network topology.

Here we demonstrate a fiber network operated with multi-branch laser stations (MLSs) which enable coherent dissemination of an ultra-stable signal from one point to multiple users and simultaneously assess the stability and accuracy of the multiple links. It is part of a national metrological network called REFIMEVE+ [24] which aims to disseminate an ultra-stable and accurate signal generated at LNE-SYRTE to around twenty labs across France and to connection points to European NMIs. Fields of study of REFIMEVE+ concern high-resolution spectroscopy, measurements of fundamental constants, remote laser

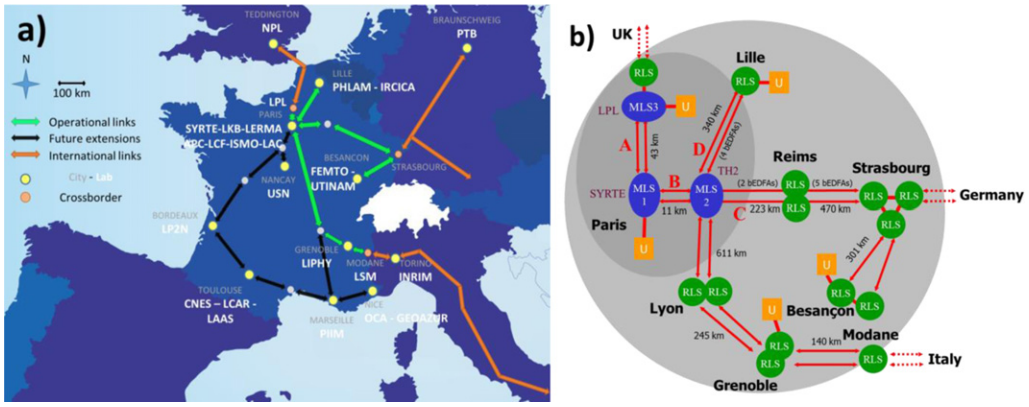

Figure 1. (a) REFIMEVE+ metrological network in France with laboratories currently benefiting from the signal. (b) Sketch of the network architecture, MLS: multi-branch laser station, RLS: repeater laser station, bEDFA: bidirectional erbium doped fiber amplifier, U: user.

stabilization or stability assessment and more generally high-precision atomic and molecular spectroscopic measurements. Together with the repeater lasers stations (RLSs) [25] already demonstrated and used for ten years, the MLS allows us to build a robust metrological network of twice 2400 km with state-of-the-art accuracy and stability.

In this paper, we first present the metrological network we are implementing on the fiber network of RENATER, the French National Research and Education Network (NREN) and the various equipment required for the signal dissemination. Then we describe the principle of the MLS, its design and the functions it provides, from the noise compensation to the assessment of the residual instability of a link. Next, we give the resulting performance of optical links driven by such MLSs, in terms of stability, accuracy and robustness and uptime. In conclusion, we give some perspectives of new applications opened by this work.

2. Implementation of an ultra-stable optical link network on the RENATER fiber network

Figure 1(a) displays the current status of the REFIMEVE+ metrological network and its European connections. Besides regional dissemination inside the Paris area and especially to LPL [6], it includes four optical links to Lille [25], Strasbourg [2], Besançon and Modane. It totalizes 4802 km of coherent optical frequency links. The link lengths range from 11 to 1000 km with attenuation up to 262 dB. Connections with European links to PTB in Germany, NPL in the UK and INRIM in Italy happen respectively at Strasbourg [4, 7], LPL [10] and Modane. Operation of the whole network will be reported elsewhere. We will restrict this paper to the study of the MLSs and the links to LPL, Lille and Strasbourg.

Figure 1(b) shows the network design with three nodes including an MLS at LNE-SYRTE, LPL and TH2 (a data center in Paris). The network is fed with an ultra-stable laser, with a linewidth about 200 mHz. The drift of the ultra-stable laser is measured against an active H-Maser using an optical frequency comb. This drift is actively suppressed applying a correction via a programmable radio peripheral platform (ETTUS), which slope is updated every 30 s, resulting in a residual drift smaller than 10 mHz s^{-1} at all times [26]. The whole network is based on cascaded links using remote control of servo loops, gain parameters and measuring devices. This gives the possibility to compensate for the large noise and attenuation, and, moreover, to improve the short-term noise rejection, which is limited by the round-trip propagation time in each segment [25, 27].

Active noise compensation (ANC) is implemented on each link using the Doppler noise compensation technique [27]. Both the bandwidth and the amplitude of the correction are limited by the roundtrip propagation delay [27], giving rise to typical residual instabilities around 10^{-15}–10^{-17} at 1 s averaging time. This residual noise is evaluated using a second parallel link, denoted as down-link, in order to send back the signal transferred with the first optical link, denoted as up-link, to the input lab as depicted in figure 2 (see supplementary material for detailed explanation (https://stacks.iop.org/NJP/23/053027/mmedia)). One can thus detect the so-called end-to-end beat-note between the input signal and the signal transferred by the up-link and down-link successively. The frequency of this beat-note is counted and it gives an upper value of the stability and accuracy of each link [4].

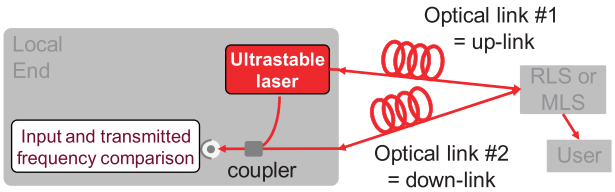

Figure 2. Principle of an optical link with simultaneous assessment of the residual noise and accuracy. The input and transmitted frequency comparison, so-called end-to-end measurement, gives an upper value of the up-link and down-link stabilities and accuracies (see supplementary for details).

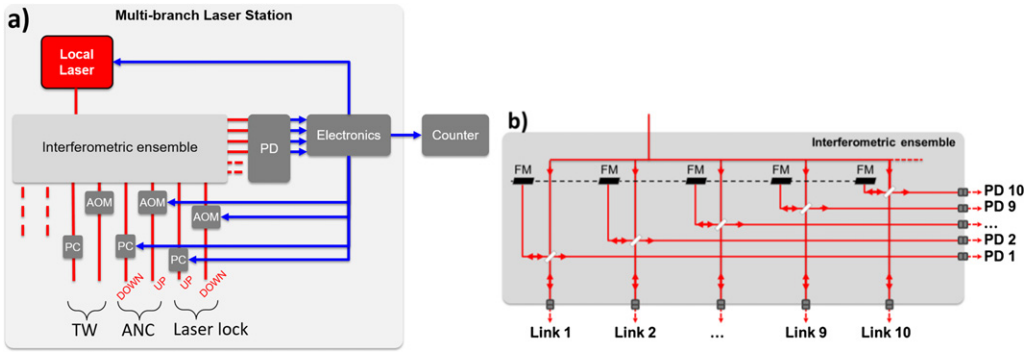

Figure 3. (a) Schematic of a multi-branch laser station (PD = photodiode, PC = polarization controller, AOM = acousto-optic modulator, TW = two-way, ANC = active noise compensation). (b) Schematic of the interferometric ensemble (FM = Faraday mirror, PD = photodiode).

The optical links are implemented on the fiber network of RENATER. The metrological signal is transferred on a dedicated frequency channel of bandwidth 100 GHz centered at wavelength 1542.14 nm (channel #44 of the International Telecommunication Union Grid). It is multiplexed with the data traffic using optical add-drop multiplexer. The propagation of the metrological signal is fully bidirectional using dedicated bidirectional optical erbium-doped fiber amplifiers (bi-EDFAs), and RLSs [2, 4, 25]. At the network output ends, a user module can be connected to an RLS and enables any user to get an ultra-stable signal with noise correction up to this module. MLS, RLS and bi-EDFAs are remotely controlled. Their supervision is integrated into the network operating center of RENATER. Bidirectional amplifiers, RLSs and user modules are now commercially available [25].

3. The multi-branch laser station

3.1. Principle and description

In order to transfer the signal to several points, the network includes three MLSs. These stations are based on the RLS principle [2, 25] and includes new functionalities which are mainly multiple link coherent dissemination and residual noise measurement (figure 3(a)). It provides several coherent outputs which are all copying the ultra-stable input signal. In addition, this device can compensate for up-link noise, controls polarization and verifies in real time the performance of each down-link independently.

An MLS includes a laser, a multi-branch optical interferometric ensemble, electronic boards to lock the laser and the up-links and a control rack to control the down-links and to assess the locking performance. The local laser is divided in the interferometric ensemble (gray part) into 8 to 12 coherent ports which feed several fiber links (bottom of the figure). The multi-branch low-noise interferometric ensemble (figure 3(b)) is designed to detect the beat-notes of the same optical phase of the laser with several external optical signals. It includes several reference arms of similar optical length, each combined with an external optical port that corresponds to the second arm of a highly unbalanced Michelson interferometer, thus providing several phase-coherent two-arm interferometers. Such an interferometric ensemble is also suitable for multi-branch optical frequency comb.

The dissemination configuration is fully versatile. It can be achieved either by ANC of the fiber noise, or by a two-way technique, or by a combination of the above techniques (as illustrated in [6]).

The local laser is phase-locked on the incoming metrological signal using one of the two-arm interferometers. The other interferometers are used in pairs to establish up and down-links to transfer the

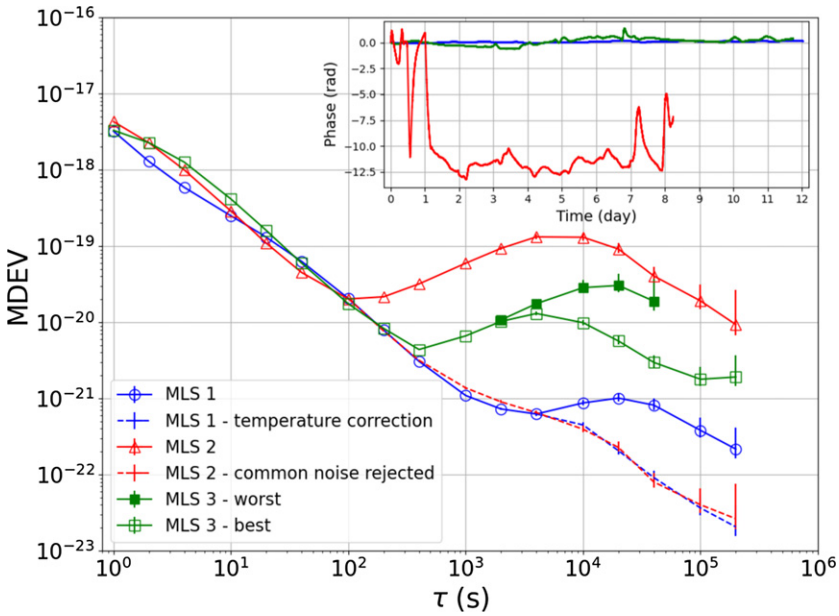

Figure 4. Characterization of the noise floor of the multi-branch interferometric ensemble of the different MLSs. Fractional stability versus averaging time of the free space interferometer from MLS1 (blue circles) and from ML2 (red triangles) without (continuous line) and with (dashed line) correction or common noise rejection and of the free space interferometer from MLS3 (green squares). Inset: phase fluctuations of the three measurements (one optical cycle lasts 5 fs).

signal to a remote location (up-link) and check the quality of the transfer using the second link (down-link). The beat-note between the local laser and the signal received after the round-trip propagation through the up and down-link gives a measurement of the out-of-loop end-to-end residual noise. It is filtered and sent to an external counter (electronics part on the right of figure 3(a)). For the up-link, it includes an AOM for noise correction. For the down-link, it includes a polarization controller, which is required for the automatic maximization of the beat-note amplitude. The beat-notes are detected, filtered and used for either a servo-loop, noise measurement or frequency counting. It uses the multifunction electronic board developed for commercial RLSs [25] for the laser and link stabilization. For the detection and polarization optimization of the measurement system, it uses specifically designed homemade electronic boards.

The MLS can be designed in order for the noise compensation to be insensitive to the frequency fluctuations of the local RF oscillator [2, 25, 28]. In that case, an acousto-optic modulator with a proper frequency shift is inserted in the multi-arm interferometer. Such MLS can be used outside a lab, for instance in a telecommunication node, without the need for accurate atomic clocks or a GNSS signal.

We benefit from the development performed for the RLS to supervise the operation of the MLS [2, 25]. Notably every lock, or relock, is automatic and can be controlled remotely. Detailed description of the electronic processing and control can be found in [25]. Moreover, the robustness and reliability of the link stabilization system of the MLS is insured by industrial-grade components, tested and validated in the field, and by the availability of spares for fast replacement. The result is a plug and play equipment, which was operational the day after it was installed in the network and shows very high uptime (see section 4).

As shown in figure 1, we built and set up three MLSs (see supplementary material for technical details). The first two MLSs, denoted MLS1 and MLS2 on figure 1, include a free space interferometric ensemble for optimal noise floor. They are set up at the input end of the REFIMEVE network at LNE-SYRTE and at TH2 respectively, and are used as nodes of a star national network. MLS2 includes an acousto-optic modulator in order to reject the noise of the local RF oscillator.

The last MLS is set up at LPL (MLS3 in figure 1) and is used for local dissemination inside the lab [13, 15] and for frequency comparison with the signal arriving with another fiber link from NPL [29]. It includes a fibered interferometer ensemble.

3.2. Performance

Figure 4 shows the noise floors of the multi-branch interferometric ensembles of the MLSs, which give the best possible performance of any ultra-stable frequency transfer or comparison.

This noise floor was measured by connecting two optical ports of the same multi-branch interferometric ensemble, thus being an out-of-loop measurement. This way we connect two interferometers with a short

fiber, sharing then the same external arm and we realize a two-way frequency comparison using the same laser source [30, 31]. The beat-note signal of both interferometers were counted with a dead-time free frequency counter in lambda-mode [32, 33] and post-processed to obtain their half difference. It is free from laser noise and from the noise of the shared fiber and exhibits the residual noise of the interferometers, known as interferometric noise [34, 35]. This noise is expected to arise from the mismatch of the optical lengths between the laser output and each interferometer, including the paths to the interferometer couplers and the short reference arms.

The free space interferometers of MLS1 exhibits the lower noise floor, as shown with blue circles in figure 4. The stability is 3.2×10^{-18} at 1 s averaging time, it decreases to 6.2×10^{-22} at 4000 s before increasing to 1×10^{-21} at 20 000 s averaging time. The corresponding phase fluctuations are shown in the inset in blue. To the best of our knowledge, this is a record noise floor for optical link noise detection. The thermo-optic sensitivity is almost completely suppressed. Moreover, the long-term stability can be reduced to 2.5×10^{-23} by post-processing the data taking into account the temperature variations [6]. In addition, we have tested this MLS1 on a dedicated test-bench and we have demonstrated that all the outputs of the interferometric ensemble show the same performance in a simulated link and can then be used independently.

The noise floor of the interferometric ensemble of MLS2, which is free space and includes an AOM, is displayed as red triangles in figure 4. This measurement has been realized in the field at TH2 data center. The stability starts at 4.3×10^{-18} at 1 s averaging time and reaches a noise floor of 2×10^{-20} at 100 s averaging time before increasing to 1.2×10^{-19} at 10 000 s averaging time. We have determined that it is limited by the phase fluctuations occurring in the AOM [36]. The corresponding phase fluctuations are shown in the inset in red. By correlating those phase fluctuations with an additional simultaneous measurement between a pair of other outputs, we can reject the common fluctuation sources of the two measurements, including the ones from the AOM, as shown with the dashed red line. This result by post-processing is consistent with the blue dashed line as expected.

The green squares in figure 4 show the modified Allan deviation (MDEV) for the fibered interferometric ensemble of MLS3 in two different cases. Open squares correspond to a measurement using two ports of the last coupler of the interferometric ensemble, thus showing the maximum noise correlation between outputs and giving the best stability limit of the noise floor of this MLS. The corresponding phase fluctuations are shown in the inset in green. Full squares correspond to a measurement between two different branches after the first coupler of the interferometric ensemble, thus showing the minimum correlation between outputs, thus giving the worst stability limit of the noise floor. The stability starts at 3.3×10^{-18} at 1 s averaging time and reaches a minimum of 4.4×10^{-21} at 400 s averaging time. Then it increases due to the temperature fluctuations of the interferometric ensemble. For the worst case, it shows a maximum of 3×10^{-20} at 20 000 s averaging time, whereas the bump is reduced to 1.3×10^{-20} at 4000 s averaging time for the better case, and the long-term stability reaches 2×10^{-21} at 200 000 s averaging time. Note that the noise arising from local temperature variation can be partially compensated in post-processing [6].

We can notice that the MLS3's interferometric noise limitation occurs one order of magnitude higher than that of the MLS1 interferometer, emphasizing the fact that fibered interferometers are more sensitive to thermal fluctuations than free space ones.

For all three MLSs, the interferometric noise is low enough for long-haul frequency dissemination and comparison, as shown in section 4. The ultra-low noise interferometric ensemble of MLS1 is especially suitable for relatively short fiber links where the noise rejection is very high. Alternatively, fibered interferometers are easier to realize and can be used for long-haul fiber links or frequency transfer at the 10^{-19} level. The noise floor of MLS2's interferometric ensemble is dominated by the phase fluctuations induced by the AOM. Its design could be improved in the future.

4. Results

We present the experimental end-to-end data acquired with the REFIMEVE+ network at LNE-SYRTE and at the central node of the network, located at the TH2 data center. The ultra-stable optical reference signal is transferred with four optical links to the remote ends, located at the TH2 data center, LPL, Lille and Strasbourg. The RLS or MLS transfers the signal back to the input end with a second fiber link. We record the end-to-end frequency fluctuations of the beat note between the returned signal and the original signal of the MLS. Table 1 displays the main characteristics of each fiber link, ranging from 22 to 1410 km, and denoted as A to D on figure 1(b). The A, B and D links are two segment fiber links (for instance SYRTE–LPL and LPL–SYRTE for link A) whereas the C link is a cascaded link of four segments (Paris–Reims, Reims–Strasbourg, Strasbourg–Reims and Reims–Paris). Link C uses home-made RLSs [2] whereas link D uses commercial RLSs [25].These links are operated simultaneously.

Table 1. Length, number of segments, number of amplifiers and losses for the four links using MLSs and sketched on figure 1(b).

	Distance (km)	Number of segments	Number of EDFAs	Total fiber losses (dB)
A: SYRTE–LPL–SYRTE	2×43	2	0	45
B: SYRTE–Paris–SYRTE	2×11	2	0	16
C: Paris–Strasbourg–Paris	2×705	4	2×7	410
D: Paris–Lille–Paris	2×340	2	2×4	160

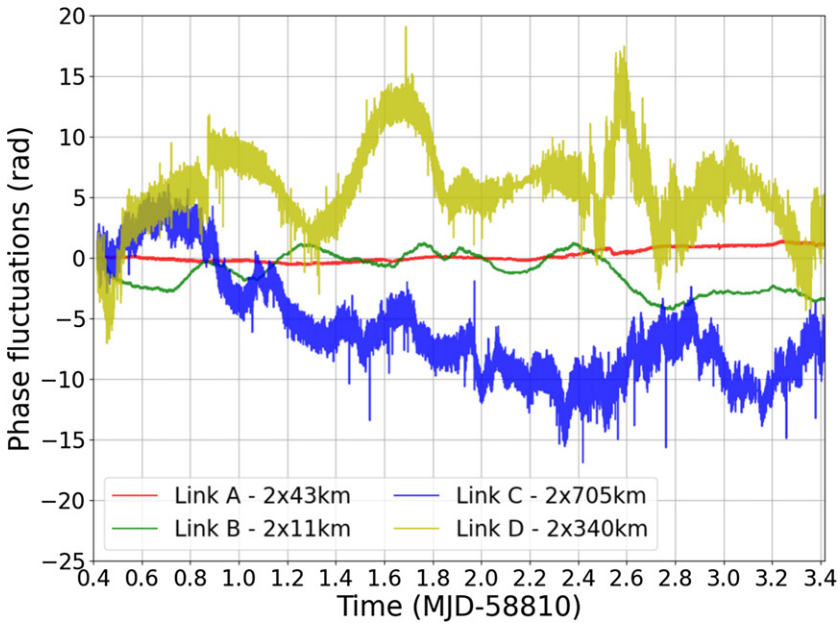

Figure 5. End-to end phase fluctuations of the four links using MLSs during 3 days. Data are recorded with 1 s gate time.

4.1. Experimental data at a few days

We discuss first the situation of data recorded during a period of almost continuous operation of the four links. We process the end-to-end data with similar procedure described in [37]. The residual phase fluctuation is calculated from the integration of the frequency fluctuations over the time. Figure 5 displays the phase variations of a 3 days measurement duration without significant missing data. The uptimes for the links A to D are respectively 97.3%, 97.9%, 98.1% and 93.0%. Note that better uptime and lower uncertainty can be achieved after dedicated optimization of the links and extensive data analysis [25].

We observe much lower noise for the shortest links (red, 86 km and green, 22 km), as expected. For this period, the phase wanderings over 3 days for the links A to D are respectively 1.1 rad, 3.4 rad, 7.0 rad and 3.2 rad (one optical cycle lasts 5 fs).

Figure 6 shows the corresponding relative frequency stability, with the same color code. All the links integrate with a slope of $\tau^{-3/2}$ until about 20–100 s integration time, showing the coherent regime. The 1 s MDEV are 2.0×10^{-17}, 1.7×10^{-17}, 5.9×10^{-16} and 5.4×10^{-16} for the links A to D respectively. The free running noise of the first span of each of the links are reported on figure 6, as dashed lines, with the same color code. We observe that it differs from one link to the other and does not simply scale with the length. In particular, one notices that for the two short links (A and B, red squares and green bottom triangles), although A is four times longer than B, it is ten times less noisy. The link B is particularly noisy between 10 and 1000 s integration time. Except for link B, the short term noise is limited by the finite propagation time of the light in the fiber [27].

The 705 km link (link C, blue circles) is affected by a pseudo-periodic perturbation of 10–100 s that degrades the MDEV. This perturbation may be due to the air conditioning and acoustic noise at the departing node in Paris, at mid-point and/or at the remote end of the cascaded link. For the three other links, we do not observe such perturbations.

At 40 000 s integration time the MDEV are 6×10^{-21}, 2×10^{-20}, 5×10^{-20}, 6×10^{-20} for the links A to D respectively. At one day, all four links show a bump, due to the diurnal variation of temperature affecting the Michelson interferometers of the RLSs and MLS2 or MLS3 [2, 35]. The excess of long-term noise on

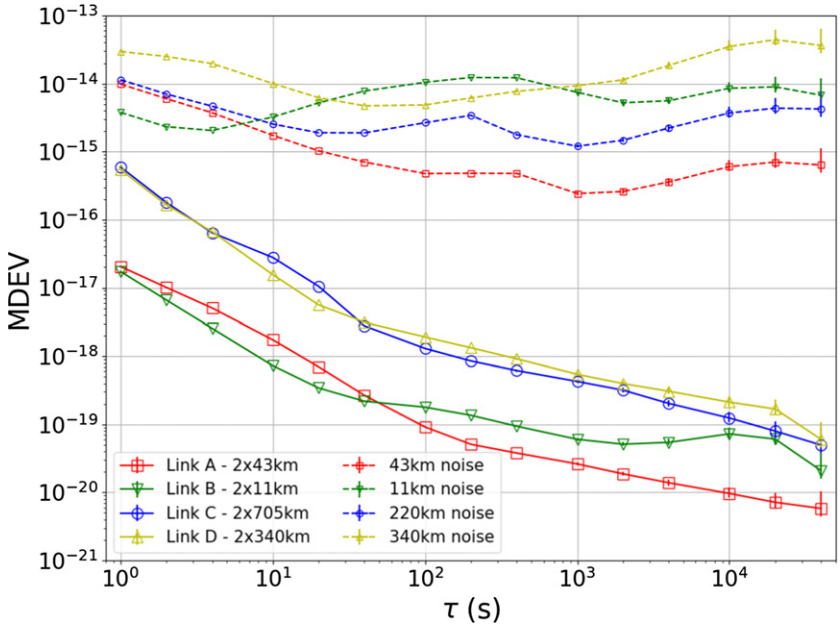

Figure 6. Stability (MDEV) of the four links using MLSs, for the data displayed on figure 5, together with the free-running stability of the first span of each links.

Table 2. Uptime (see section 4.3) and uncertainty of the four links using MLSs for the data displayed on figures 5 and 6. OADEV and MDEV are given at 40 000 s integration time.

	Uptime (%)	Mean ($\times 10^{-20}$)	OADEV ($\times 10^{-20}$)	MDEV ($\times 10^{-20}$)
A: SYRTE–LPL–SYRTE	97.3	0.4	0.9	0.6
B: SYRTE–Paris–SYRTE	97.9	−1.1	5.0	2.1
C: Paris–Strasbourg–Paris	98.1	−2.3	10.2	5.0
D: Paris–Lille–Paris	93.0	1.1	10.9	6.0

link B is due to the imperfect balance of the non-common paths and to the thermal sensitivity of the acousto-optic modulator set inside the TH2 interferometric ensemble. It copies the noise floor shown in figure 4 with a factor 2 amplification due to the double sensitivity to interferometric noise of a cascaded link, compared to a two-way measurement.

We can note a significant variation of the short-term phase noise of the 340 km link (link D, yellow) which reduces generally during the night (here observed between 1:30 and 6:00 UTC). As the data were acquired simultaneously with those of the three other links we can exclude instrumental effects related to the lasers or the electronics used in the MLS. It possibly comes from a diminution of the traffic along the highway near the path of the fibers or from any interruption of a noise source along the fiber. If the origin of the noise cannot yet be elucidated in our fiber network, this is a striking example of the non-stationarity of the short-term noise that affects ultra-stable fiber links.

4.2. Accuracy

In order to evaluate the fractional frequency offset of the frequency transfer, we calculate the mean relative frequency for these data sets, no corrections being applied to the data. By varying the frequency of the local oscillator of MLS2, we first verified that the transferred frequency is not affected by this local RF oscillator, which is thus not a limit for the uncertainty of the frequency transfer.

The uncertainty budget is therefore given by the statistical uncertainty, estimated by using the overlapping Allan deviation (OADEV) at 40 000 s. The values are reported in table 2. We evaluate the residual offset of the frequency transfer of the above data set as $(0.4 \pm 0.9) \times 10^{-20}$, $(-1.1 \pm 5) \times 10^{-20}$, $(-2.3 \pm 10.2) \times 10^{-20}$, $(1.1 \pm 10.9) \times 10^{-20}$, for links A to D respectively. No significant deviation of the mean is observed. Lower residual offsets can be obtained after extensive data analysis and dedicated link optimization.

This accuracy fully satisfies the requirements of the REFIMEVE project, and complies with the roadmap defined by the CCTF of BIPM for the future redefinition of the SI second at the level of 10^{-18}.

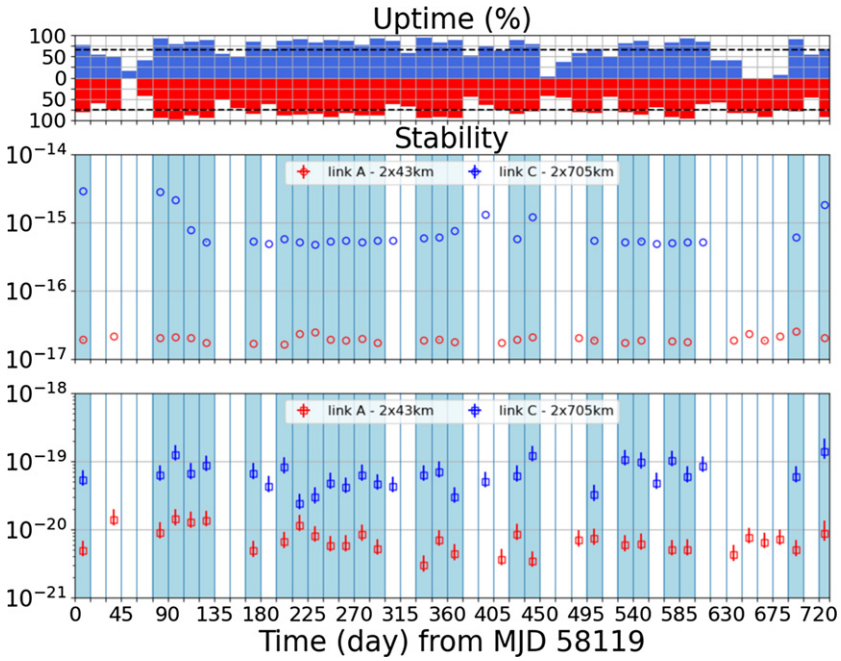

Figure 7. Uptime and stabilities over 2 years of two links departing from an MLS. The period is divided into bins of 15 days. Data concerning the Paris–Strasbourg–Paris link (link C) are in blue, and the ones concerning the SYRTE–LPL–SYRTE link (link A) in red. The circles correspond to stabilities at 1 s averaging time and the squares at 100 000 s. These stabilities are calculated for bins with uptime greater than the mean uptime, 75% and 66% for links A and C respectively (black dotted lines on upper graph). Data meeting these criteria are highlighted in sky blue in the lower graphs.

4.3. Network operation at a yearly scale

We now show the results of the operation of the links A (2×43 km) and C (2×705 km) during two years after the in-field set-up, from 2018-01-01 to 2019-12-31 using the three MLSs introduced above Over such a long period, there is missing data that are due to technical failure and to interruption of the service for maintenance, fiber operation or upgrade.

We first define the uptime of a link as the ratio between validated data points, estimated as a successful optical frequency transfer, and the total number of data points. This observable is therefore dependent on the criteria chosen to validate data. The uptime shown here is for the entire system composed of the ultra-stable cavity, the comb and the fiber link. The uptimes for the data shown in figure 5 are displayed in table 2. They are significantly above 90% since we chose a good functioning period of the four links.

For the two-year period, we process the end-to-end data with the three steps procedure described in [37]. First, we reject outliers, for which the norm of the relative frequency is 20 to 100 times larger than the short-term stability of the link. Then we process the data by calculating the rolling mean and rolling standard deviation over a time window of 10 s and 2800 s respectively. The parameters of the filters are tuned for each of the two links. We check that short-term stability and coherence of the links are kept, so that the frequency delivered to the remote end of the network can be used effectively by the users. For the two-year period, the uptime of the 86 km link (A, red) and 1410 km link (C, blue) are presented in figure 7. One bar of the histogram is the uptime calculated over 15 days, in red for link A and in blue for link C.

For the link A (SYRTE–LPL–SYRTE), the total uptime over the two years reaches 75%. It is more than 47 million seconds of frequency comparison. It is mainly limited by two regions of non-operation, from modified Julian day (MJD) 58161 to 58185, where the power supply of the MLS1 at LNE-SYRTE broke down and from MJD 58569 to 58599, where some upgrades of the optical reference were performed. The 6 months from MJD 58314 to 58494 presents an impressive uptime of 85%.

For the link C (Paris–Strasbourg–Paris), the total uptime over the two years is 66%. It is more than 41 million seconds of frequency comparison. The downtime periods of this link often coincide with that of the link A, except for the region between MJD 58764 and MJD 58809 where an upgrade of the link C' amplifiers has been realized. The uptime of the 6 months between MJD 58314 to 58494 is 85%. This last value is similar to that of the other link, emphasizing the fact the links are mostly limited by common sources of interruption.

The contributions of the downtime were investigated in details for the period between MJD 58119 and 58468, thanks to the remote control and logs of all the equipment in the network. The replacement of the electrical supply of the electronic boards of MLS1 in LNE-SYRTE is the main contributions of the

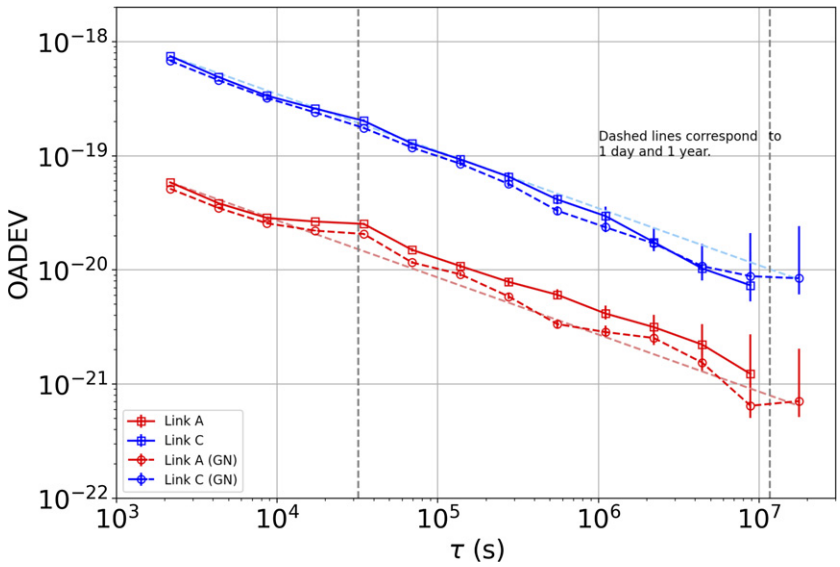

Figure 8. Long-term stability (OADEV) of the SYRTE–Strasbourg–SYRTE link (C, solid line and blue squares) and the SYRTE–LPL–SYRTE link (A, solid line and red squares) calculated from the averaged frequencies on periods spanning 2160 s. 31% and 47% of the data have been removed for links A and C respectively. Dotted lines follow a slope of $\tau^{-1/2}$ (represented by the dashed lines in light blue and red). Dotted lines and circles show the long-term stability when removed data were replaced by Gaussian noise. Dashed vertical lines correspond to the position of the bump expected for sinusoidal frequency fluctuations with periods 1 day and 1 year respectively.

downtime for both links. It represents 47% and 35% of the downtime of this period for the links A and C respectively. The second contribution comes from the interruptions of the phase/frequency counters that give the end-to-end measurement. This contributes to 30% and 25% of the downtime of this period for the links A and C respectively. The remainder of 23% and 40% for the links A and C respectively comes from several different contributions: the availability of the ultra-stable cavity, the network installation and maintenance, the adjustment of the polarization and interruptions of the 10 MHz reference. We are confident that the uptime can reach up to 90% and even close to 99% for the upcoming years.

Figure 7 shows the corresponding stabilities at 1 s and at 100 000 s integration time. We observe that the short-term stability of the 1410 km link (C) varies over months and is higher during winter, whereas it is approximately stationary for the 86 km link (A). At long term we observe repeatable results for both links, from 2×10^{-20} to 14×10^{-20} for the longest link and 3×10^{-21} to 14×10^{-21} for the shortest link.

4.4. Long term stability at a yearly scale

Finally, we use the 63 million points to calculate the long-term stabilities of the links A and C. After filtering the data with the procedure described above [37], we add a test condition on the mean value at 1000 s integration time to be below 10^{-18}. Then, we subdivide the data set in subsets of 2160 s, leading to 40 subsets per day. At 2160 s measurement time, the links are no longer in the coherent regime. The dominant noise is white frequency noise.

For each subset, we then calculate the mean frequency and the associated uptime. We consider any subset with an uptime higher than 90% as validated data. With this criterion, we keep 69% and 53% of the data for links A and C respectively. We then associate the resulting mean to a 2160 s measurement time. With this procedure, the missing data with small durations compared to 2160 s are handled with equivalent noise present in the given subset. For larger gaps, the subsets are simply handled as missing data or filled with a Gaussian noise model, not to perturb the stability at short integration time.

We check that the optical phase behaves steadily over the 2 years integration period and that the behavior does not depend critically on the uptime criteria of 90%. When processing the data with an uptime criterion of 99%, we remove only 34% and 53% of the data for links A and C respectively and obtain similar stabilities as shown in the supplementary material.

We then calculate the OADEV of the resulting collection of mean frequencies. It is displayed in figure 8, with red and blue squares for the A and C links respectively, together with the stabilities obtained when replacing the removed data with Gaussian noise (red and blue circles respectively).

As expected, we observed that the latter stability follows a slope of $\tau^{-1/2}$ as underlined by the light dashed lines. It is also approximately the case for the stability of the filtered collection of mean frequencies. We obtain long-term stabilities of 1.2×10^{-21} and 7×10^{-21} for the links A and C respectively. We also

calculate the mean of the mean frequencies. Despite the amplitudes of those means and stabilities should be taken carefully with such methodology, we thus estimate the fractional offset of the frequency transfer to $(-3 \pm 2) \times 10^{-21}$ $(-0.5 \pm 1) \times 10^{-20}$ for the links A and C respectively. This accuracy shows the robustness of the two links operated simultaneously with our MLS. Note that residual offset of link A is not significant because it is only 1.5 times the $1-\sigma$ uncertainty, and could be due to non reciprocal effects or to residual effects of the data processing.

We observe one small bump, at integration time around 30 000 s in the OADEV of the shorter link A. On the longer link C, no clear bump is observed.

By comparing with a simulation, we found that the bump corresponds to a periodic noise of period approximately 1 day. In order to confirm this time period, we calculated the autocorrelation of the mean frequency. In that stage, there is no filtering on the uptime to preserve the time coherence of the data, giving more reliability to this method. We obtained a similar result of a periodic perturbation at 1 day. The detailed study of the long-term behavior and corresponding methods is beyond the scope of the paper.

5. Conclusion and perspectives

We present in this article MLSs that enable the building of fiber networks with excellent phase stability between the branches.

Three models were built. We presented the performances of the inner branches and branches-to-branches optical phase stability. We show that a simple temperature correction can improve the results by a factor of 30 and finally reach the 2.5×10^{-23} relative frequency stability. These results are state of the art.

The three MLSs were set up in the network. We present the simultaneous operation of the core of the REFIMEVE+ network with four branches. It demonstrates the viability of our approach for building coherent fiber networks.

The reliability of the network is studied in details, and thanks to the supervision of our network, causes for dysfunction are analyzed. We show an uptime of 85% over 6 months for a cascaded link of 1410 km. We conclude that 90% uptime over 1 year can be reached in the near future.

We report for the first time the operation of a metrological network, with four branches and a record range of 2198 km in total. We report frequency dissemination capabilities that matches the accuracy and stability specification of REFIMEVE+ and of the comparisons of any clock built to date. For the first time, to the best of our knowledge, relative frequency stability of a frequency network at long term is presented, until an integration time of 10^7 s. This integration time is two orders of magnitude larger than any other experimental results reported so far, and comparable to studies reported with satellite means. This work is a major step towards reliable optical frequency dissemination over fiber networks, and gives important credit for such new research infrastructures, enabling new scientific opportunities for precise spectroscopy and for a wide scope of research laboratories and research communities, concerned by chronometric geodesy, dark matter hunt, gravitational wave detection and very long baseline interferometry.

Funding

Program 'Investissements d'Avenir' launched by the French Government and implemented by Agence Nationale de la Recherche with references Labex First-TF ANR-10-LABX-48-01, Equipex REFIMEVE+ ANR-11-EQPX-0039, ANR-10-IDEX-0001-002 PSL, Conseil Régional Bourgogne-Franche-Comté, Conseil Régional Ile de-France (DIM IFRAF), the European Metrology Program for Innovation and Research (EMPIR) in Project 15SIB05 (OFTEN). The EMPIR is jointly funded by the EMPIR participating countries within EURAMET and the European Union.

Data availability statement

The data that support the findings of this study are available upon reasonable request from the authors.

Acknowledgments

We acknowledge unfailing and continuing support of the network and engineering team of RENATER, and especially Nicolas Quintin, Xavier Misseri, Laurent Gydé and Emilie Camisard. We also acknowledge Michel Abgrall and Hector Alvarez for providing us with the ultra-stable and accurate optical signal generated at

LNE-SYRTE. We also acknowledge support of Fabrice Wiotte and Albert Kaladjian for the building of the MLS. We acknowledge Yann Kersalé for providing us with RIO diode lasers. Finally, we acknowledge Giorgio Santarelli for fruitful discussions and Christian Chardonnet for continuing support.

ORCID iDs

Etienne Cantin https://orcid.org/0000-0001-9362-0628
Mads Tønnes https://orcid.org/0000-0002-3630-3121
Rodolphe Le Targat https://orcid.org/0000-0002-8740-1709
Anne Amy-Klein https://orcid.org/0000-0002-5122-7868
Olivier Lopez https://orcid.org/0000-0003-3171-2863
Paul-Eric Pottie https://orcid.org/0000-0003-3677-2208

References

[1] Calonico D *et al* 2014 High-accuracy coherent optical frequency transfer over a doubled 642 km fiber link *Appl. Phys.* B **117** 979–86
[2] Chiodo N *et al* 2015 Cascaded optical fiber link using the internet network for remote clocks comparison *Opt. Express* **23** 33927–37
[3] Raupach S M F, Koczwara A and Grosche G 2015 Brillouin amplification supports 1×10^{-20} uncertainty in optical frequency transfer over 1400 km of underground fiber *Phys. Rev.* A **92** 021801
[4] Koke S *et al* 2019 Combining fiber Brillouin amplification with a repeater laser station for fiber-based optical frequency dissemination over 1400 km *New J. Phys.* **21** 123017
[5] Clivati C *et al* 2020 Common-clock very long baseline interferometry using a coherent optical fiber link *Optica* **7** 1031–7
[6] Xu D, Delva P, Lopez O, Amy-Klein A and Pottie P-E 2019 Reciprocity of propagation in optical fiber links demonstrated to 10^{-21} *Opt. Express* **27** 36965–75
[7] Lisdat C *et al* 2016 A clock network for geodesy and fundamental science *Nat. Commun.* **7** 12443
[8] Takano T *et al* 2016 Geopotential measurements with synchronously linked optical lattice clocks *Nat. Photon.* **10** 662–6
[9] McGrew W F *et al* 2018 Atomic clock performance enabling geodesy below the centimetre level *Nature* **564** 87
[10] Delva P *et al* 2017 Test of special relativity using a fiber network of optical clocks *Phys. Rev. Lett.* **118** 221102
[11] Friebe J *et al* 2011 Remote frequency measurement of the $^1S_0 \rightarrow {}^3P_1$ transition in laser-cooled ^{24}Mg *New J. Phys.* **13** 125010
[12] Matveev A *et al* 2013 Precision measurement of the hydrogen 1S − 2S frequency via a 920 km fiber link *Phys. Rev. Lett.* **110** 230801
[13] Argence B *et al* 2015 Quantum cascade laser frequency stabilization at the sub-Hz level *Nat. Photon.* **9** 456–60
[14] Insero G *et al* 2017 Measuring molecular frequencies in the 1–10 μm range at 11-digits accuracy *Sci. Rep.* **7** 12780
[15] Santagata R *et al* 2019 High-precision methanol spectroscopy with a widely tunable SI-traceable frequency-comb-based mid-infrared QCL *Optica* **6** 411–23
[16] Clivati C, Calonico D, Costanzo G A, Mura A, Pizzocaro M and Levi F 2013 Large-area fiber-optic gyroscope on a multiplexed fiber network *Opt. Lett.* **38** 1092–4
[17] Clivati C, Tampellini A, Mura A, Levi F, Marra G, Galea P, Xuereb A and Calonico D 2018 Optical frequency transfer over submarine fiber links *Optica* **5** 893–901
[18] Marra G *et al* 2018 Ultrastable laser interferometry for earthquake detection with terrestrial and submarine cables *Science* **361** 4458
[19] Clivati C *et al* 2017 A VLBI experiment using a remote atomic clock via a coherent fibre link *Sci. Rep.* **7** 40992
[20] Roberts B M *et al* 2020 Search for transient variations of the fine structure constant and dark matter using fiber-linked optical atomic clocks *New J. Phys.* **22** 093010
[21] Grosche G 2014 Eavesdropping time and frequency: phase noise cancellation along a time-varying path, such as an optical fiber *Opt. Lett.* **39** 2545
[22] Bercy A, Guellati-Khelifa S, Stefani F, Santarelli G, Chardonnet C, Pottie P-E, Lopez O and Amy-Klein A 2014 In-line extraction of an ultrastable frequency signal over an optical fiber link *J. Opt. Soc. Am.* B **31** 678–85
[23] Bercy A, Lopez O, Pottie P-E and Amy-Klein A 2016 Ultrastable optical frequency dissemination on a multi-access fibre network *Appl. Phys.* B **122** 189
[24] REFIMEVE+ project, http://refimeve.fr/index.php/en/
[25] Guillou-Camargo F *et al* 2018 First industrial-grade coherent fiber link for optical frequency standard dissemination *Appl. Opt.* **57** 7203–10
[26] Lodewyck J *et al* 2016 Optical to microwave clock frequency ratios with a nearly continuous strontium optical lattice clock *Metrologia* **53** 1123–30
[27] Newbury N R, Williams P A and Swann W C 2007 Coherent transfer of an optical carrier over 251 km *Opt. Lett.* **32** 3056
[28] Lopez O, Haboucha A, Kéfélian F, Jiang H, Chanteau B, Roncin V, Chardonnet C, Amy-Klein A and Santarelli G 2010 Cascaded multiplexed optical link on a telecommunication network for frequency dissemination *Opt. Express* **18** 16849–57
[29] Delva P *et al* 2017 Test of special relativity using a fiber network of optical clocks *Phys. Rev. Lett.* **118** 221102
[30] Hanson D W 1989 Fundamentals of two-way time transfers by satellite *Proc. of the 43rd Annual Symp. on Frequency Control* pp 174–8
[31] Calosso C E, Bertacco E, Calonico D, Clivati C, Costanzo G A, Frittelli M, Levi F, Mura A and Godone A 2014 Frequency transfer via a two-way optical phase comparison on a multiplexed fiber network *Opt. Lett.* **39** 1177–80
[32] Rubiola E 2005 On the measurement of frequency and of its sample variance with high-resolution counters *Rev. Sci. Instrum.* **76** 054703
[33] Dawkins S T, McFerran J J and Luiten A N 2007 Considerations on the measurement of the stability of oscillators with frequency counters *IEEE Trans. Ultrason. Ferroelectr. Freq. Control* **54** 918–25

[34] Williams P A, Swann W C and Newbury N R 2008 High-stability transfer of an optical frequency over long fiber-optic links *J. Opt. Soc. Am.* B **25** 1284–93
[35] Stefani F, Lopez O, Bercy A, Lee W-K, Chardonnet C, Santarelli G, Pottie P-E and Amy-Klein A 2015 Tackling the limits of optical fiber links *J. Opt. Soc. Am.* B **32** 787–97
[36] Wada M, Okubo S, Kashiwagi K, Hong F, Hosaka K and Inaba H 2018 Evaluation of fiber noise induced in ultrastable environments *IEEE Trans. Instrum. Meas.* **68** 2246–52
[37] Xu D, Cantin E, Frank F, Quintin N, Meynadier F, Tuckey P, Amy-Klein A, Lopez O and Pottie P-E 2019 Two-branch fiber link for international clock networks *IEEE Trans. Instrum. Meas.* **68** 2195–200

Appendix D

Article in Radio Science Letters

An article published in URSI Radio Science Letters. This is in continuation of a talk I gave at the URSI-GASS 2021 conference, on the subject of missing data.

Scientific Data Processing of a Fiber Network for Optical Frequency Transfer: Methods and Studies

Mads Tønnes, Etienne Cantin, Dan Xu, Olivier Lopez, Anne Amy-Klein, and Paul-Éric Pottie

Abstract — In recent years, the use of optical frequency dissemination through telecommunication fibers has steadily grown both in the context of state-of-the-art metrology like optical clocks and in the use of ultrastable reference signals for precision measurements in other fields of physics or earth science. Evaluating the performance of the fiber link can be difficult, as outliers and dysfunctioning regions lead to missing data. In this article, we discuss these challenges and investigate three different approaches to dealing with the missing data of a 1410-km-long optical link. We find a benefit in replacing the missing data with simulated noise with a statistical behavior similar to that of the original signal.

1. Introduction

Coherent optical fiber links is a rapidly emerging technology, enabling ultrastable optical frequency transfer over thousands of kilometers. Compared to the traditional methods of frequency transfer through the Global Navigation and Satellite Services (GNSS), it operates with orders-of-magnitude lower noise. This makes it suitable for the comparison of optical clocks and cavities [1], very long baseline interferometry (VLBI) [2], spectroscopy [3], along with many other applications. In France in particular, the research infrastructure Réseau fibré métrologique à vocation européenne aims at providing an ultrastable frequency reference to more than 32 partner laboratories throughout France [4]. It is evident that such a network will consist of many branches and have several simultaneous users. Supervision and data processing of the full network are therefore of the utmost importance. In the following, we will consider problems occurring when evaluating the stability of the frequency dissemination in the case of missing data. Similar concerns have been considered for GNSS [5–7], where the main difference to this work is that the fiber links tend to operate in the phase-coherent regime, leading to complexities in the evaluation of the phase of the signal in the case of missing data. In [8], a method of applying a correction to the Allan variance of a data set with missing data is presented.

Manuscript received 6 December 2021.

Mads Tønnes is with LNE-SYRTE, Observatoire de Paris, Université PSL, CNRS, Sorbonne Université, 61 Avenue de l'Observatoire, 75014 Paris, France; e-mail: mads.tonnes@obspm.fr.

Etienne Cantin is with Laboratoire de Physique des Lasers, Université Sorbonne Paris Nord, CNRS, 99 Avenue Jean-Baptiste Clément, 93430 Villetaneuse, France; e-mail: etienne.cantin@univ-paris13.fr.

Dan Xu is with LNE-SYRTE, Observatoire de Paris, Université PSL, CNRS, Sorbonne Université, 61 Avenue de l'Observatoire, 75014 Paris, France; e-mail: dan.xu@obspm.fr.

Olivier Lopez is with Laboratoire de Physique des Lasers, Université Sorbonne Paris Nord, CNRS, 99 Avenue Jean-Baptiste Clément, 93430 Villetaneuse, France; e-mail: olivier.lopez@univ-paris13.fr.

Anne Amy-Klein is with Laboratoire de Physique des Lasers, Université Sorbonne Paris Nord, CNRS, 99 Avenue Jean-Baptiste Clément, 93430 Villetaneuse, France; e-mail: amy@univ-paris13.fr.

Paul-Éric Pottie is with LNE-SYRTE, Observatoire de Paris, Université PSL, CNRS, Sorbonne Université, 61 Avenue de l'Observatoire, 75014 Paris, France; e-mail: paul-eric.pottie@obspm.fr.

2. The Challenge of Missing Data

In this article, we show a case study of a 2×705-km-long optical fiber link between the two French cities of Paris and Strasbourg. The link is actively compensated, and the optical signal is regenerated three times along the way [9]. We measure the end-to-end signal of the 1410-km link, which is the frequency difference between the original signal and the disseminated light. This is the only data we are discussing in this article.

The end-to-end frequency is measured using a dead-time free frequency counter. This measures the optical beat $f(t)$ continuously. However, due to technical challenges, not all the recorded data will be valid in the end, leading to gaps in the frequency data [4]. When calculating the phase evolution of the signal in postprocessing, we usually express the phase in terms of the *time error*, $x(t)$, which has the unit of seconds. The time error is calculated from the relative frequency fluctuations $y(t) = \frac{f(t)-\nu_0}{\nu_0}$, with ν_0 being the nominal frequency, by the integral

$$x(t) = \int_{t_1}^{t_2} y(t)\, dt, \tag{1}$$

with $t_2 - t_1$ being the time interval of the integration. As this integral assumes a continuous frequency measurement, the periods of missing data will lead to unknown phase evolution, impairing the phase coherence of the link. This is problematic for the postprocessing of the data. Therefore, we need to have an evaluation of the effects of missing data and the bias it introduces in the statistical evaluation of the fiber link. If we want to be able to evaluate the long-term behavior of the link, we will need to deal with the missing data in a way that biases the evaluation of the link as little as possible.

3. Comparison of Methods Dealing With Missing Data

We investigated three different methods of dealing with missing data in the link signal. To analyze the effects of each method, we use a reference data set that is perfectly continuous. In a controlled way, we remove data points at random, deal with the missing data each of three different ways, analyze the statistical consequences, and compare the results. In the following, we discuss three different approaches: concatenation of the resulting data set, keeping the phase constant across the gap left by the missing data, and the more novel approach of replacing the missing data with simulated data, which follows a simple noise model of the link.

The most important criterion on which we are evaluating each method is how well they are able to keep the statistical behavior as close as possible to the reference. To make this assessment, we use two different tools to analyze the signals. The first is the phase power spectral density, which is calculated from the Fourier transform of the autocorrelation function of the time error, $S_\phi(f)$. This is used to analyze the amount of phase noise at a given Fourier frequency and is a good method of determining periodic perturbations to the signal. The second tool we use is the modified Allan deviation, Mod $\sigma_y(\tau)$, calculating the stability of the signal as a function of integration time τ [10]. This is a tool commonly used in time and frequency metrology, and in this context, we will use it to evaluate the phase coherence of the link both with and without missing data.

3.1 Concatenating the Remaining Data

One can choose to ignore the problem altogether. This effectively concatenates the data set, creating a length mismatch as compared to the reference. This creates a bias in the Fourier domain, where it becomes difficult to identify periodic perturbations to the signal. This is illustrated in Figure 1, where we show the phase noise of the reference signal (blue) with the phase noise of the three different methods. It is clear that many periodic peaks have either vanished or are blue-shifted (red curve) after removing 10% of the data.

Finally, this method does not address the problem of the deterioration of the phase coherence, which can be seen in the deterioration of the stability for an increasing amount of removed data, as shown in Figure 2.

3.2 Keeping the Phase Constant

A second method is to keep the phase constant across the gap left by the missing data. From a conceptual point of view, this is more reasonable, as it keeps the length of the data set intact, which makes for a more reasonable Fourier analysis, as seen by the peaks in the yellow trace in Figure 1. However, it still has the problem of not addressing the deterioration of the coherence, and having periods of a constant phase

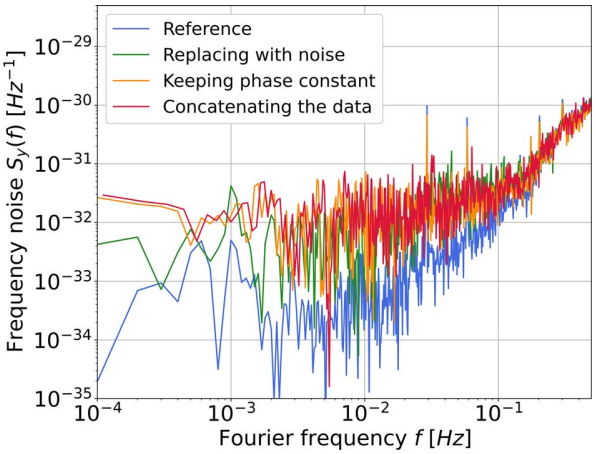

Figure 1. Phase noise of the reference signal (blue) and the three different methods of dealing with missing data. Ten percent of the data has been removed, and the data set has been concatenated (red), the phase has been kept constant across the missing data (orange), and the missing data have been replaced with statistically similar simulated data (green).

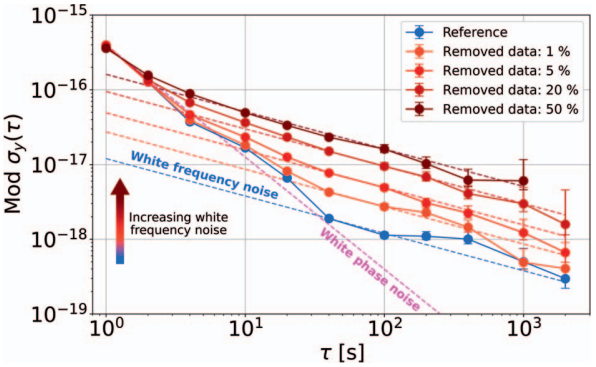

Figure 2. Modified Allan deviation of the reference signal without missing data (blue) and the concatenated signal of an increasing amount of removed data (increasingly dark red).

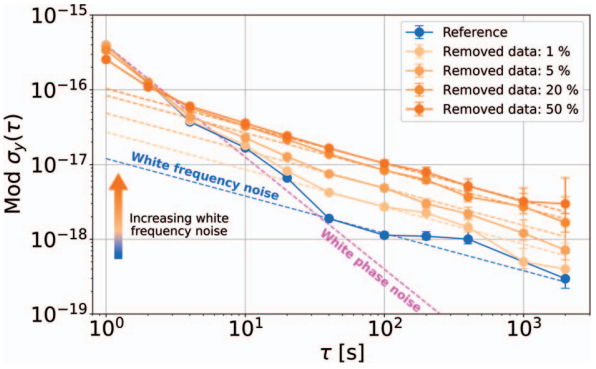

Figure 3. Modified Allan deviation of the reference signal without missing data (blue) and with an increasing amount of removed data, where the phase is kept constant across the gap of the missing data (increasingly dark orange).

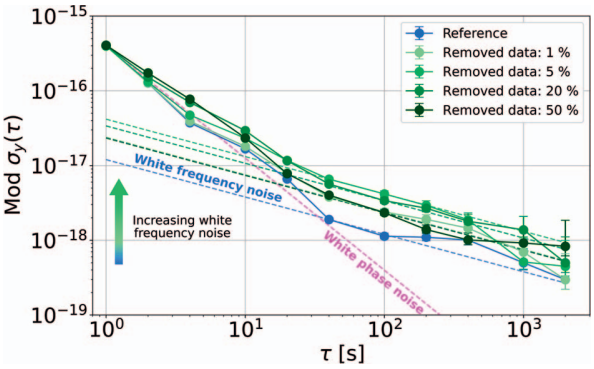

Figure 4. Modified Allan deviation of the reference signal without missing data (blue) and with an increasing amount of removed data, where removed data are replaced with simulated noise (increasingly dark green).

will bias the short-term noise level, which is seen in the stability curves in Figure 3.

3.3 Replacing With a Noise Model

The last method we investigated is a more novel approach: we made a simple method to produce noise with statistical behavior largely comparable to that of the link, consisting of white phase noise and white frequency noise. A more detailed model will be described in a future publication. We used this model to simulate noise that we could place instead of the missing data, effectively "filling" up the gaps in the data set. In this way, we kept the original length of the data set, and we avoided the bias in the short-term noise level. We furthermore observed a decrease in the deterioration of the coherence of the link, which is seen in the modified Allan deviation in Figure 4: the increase in white frequency noise with an increased amount of missing data is lower. This directly corresponds to a lower effective decoherence of the data as compared to the two previous cases shown in Figures 2 and 3.

4. Conclusion

We have discussed the challenges with missing data in the data analysis of coherent optical fiber links. We have compared different approaches of handling the missing data and found that it is possible to reduce the aliasing effects by replacing the missing data with a simple noise model with similar statistical behavior as that of the fiber link itself. This is an important step for exploring long-term effects on fiber links, where missing data are inevitable, and finding line identifications in their Fourier analysis at very low frequency. We believe that this work may find its application in earth science and fundamental science, like the exploration of the Sagnac effect and other tests of relativity [11] or the search for dark matter.

5. References

1. C. Lisdat, G. Grosche, N. Quintin, C. Shi, S. M. F. Raupach et al., "A Clock Network for Geodesy and Fundamental Science," *Nature Communications*, **7**, August 2016, pp. 12443.
2. C. Clivati, R. Aiello, G. Bianco, C. Bortolotti, P. De Natale, et al., "Common-Clock Very Long Baseline Interferometry Using a Coherent Optical Fiber Link," *Optica*, **7**, 2020, pp. 1031-1037.
3. R. Santagata, D. B. A. Tran, B. Argence, O. Lopez, S. K. Tokunaga, et al., "High-Precision Methanol Spectroscopy With a Widely Tunable SI-Traceable Frequency-Comb-Based Mid-Infrared QCL," *Optica*, **6**, 2019, pp. 411-423.
4. E. Cantin, M. Tønnes, R. Le Targat, A. Amy-Klein, O. Lopez, et al., "An Accurate and Robust Metrological Network for Coherent Optical Frequency Dissemination," *New Journal of Physics*, **23**, March 2021, pp. 053027.
5. I. Sesia and P. Tavella, "Estimating the Allan Variance in the Presence of Long Periods of Missing Data and Outliers," *Metrologia*, **45**, December 2008, pp. S134-S142.
6. I. Sesia, E. Cantoni, A. Cernigliaro, G. Signorile, G. Fantino, et al., "An Efficient and Configurable Preprocessing Algorithm to Improve Stability Analysis," *IEEE Transactions on Ultrasonics, Ferroelectrics, and Frequency Control*, **63**, October 2015, pp. 575-581.
7. C. Xu, "Reconstruction of Gappy GPS Coordinate Time Series Using Empirical Orthogonal Functions," *Journal of Geophysical Research: Solid Earth*, **121**, December 2016, pp. 9020-9033.
8. L. Galleani and I. Sesia, "The Corrected Allan Variance: Stability Analysis of Frequency Measurements With Missing Data," *IEEE Transactions on Ultrasonics, Ferroelectrics, and Frequency Control*, **66**, July 2019, pp. 1667-1683.
9. N. Chiodo, N. Quintin, F. Stefani, F. Wiotte, E. Camisard, et al., "Cascaded Optical Fiber Link Using the Internet Network for Remote Clocks Comparison," *Optics Express*, **23**, 2015, pp. 33927-33937.
10. D. W. Allan and J. A. Barnes, "A Modified 'Allan Variance' with Increased Oscillator Characterization Ability," *Thirty Fifth Annual Frequency Control Symposium*, May 1981, pp. 470-475.
11. P. Delva, J. Lodewyck, S. Bilicki, E. Bookjans, G. Vallet et al., "Test of Special Relativity Using a Fiber Network of Optical Clocks," *Physical Review Letters*, **118**, June 2017, 221102.

Appendix E

Article in Metrologia

An article which is published in Metrologia. This is a study of the noise modelization of fiber links, and the fill-in approach for missing data. Large parts of chapters 3 and 4 are shown in this article.

Coherent fiber links operated for years: effect of missing data

OPEN ACCESS
IOP Publishing | Bureau International des Poids et Mesures Metrologia
Metrologia **59** (2022) 065004 (15pp) https://doi.org/10.1088/1681-7575/ac938e

Coherent fiber links operated for years: effect of missing data

Mads Bebe Krog Tønnes[1,*], Frédéric Schuller[1,3], Etienne Cantin[1,4], Olivier Lopez[2], Rodolphe Le Targat[1], Anne Amy-Klein[2] and Paul-Éric Pottie[1]

[1] LNE-SYRTE, Observatoire de Paris, Université PSL, CNRS, Sorbonne Université, 61 Avenue de l'Observatoire, 75014 Paris, France
[2] Laboratoire de Physique des Lasers, Université Sorbonne Paris Nord, CNRS, 99 Avenue Jean-Baptiste Clément, 93430 Villetaneuse, France

E-mail: mads.tonnes@obspm.fr

Received 21 June 2022, revised 4 September 2022
Accepted for publication 21 September 2022
Published 18 October 2022

Abstract

Aiming at delivering a highly available service, the French national optical fiber link network is run mostly unmanned and automatically, with the help of a global supervision. However, at a year scale, missing data are seemingly unavoidable. Here, we present a first study of the uncertainty of coherent fiber links with missing data. We present the tools to assess statistical properties for processes which are not strictly stationary, and a simulation of optical fiber links depending only on a handful of parameters. We show how missing data affects the phase-coherent optical fiber links, and how to mitigate the issue with a fill-in procedure that preserves the statistical properties. We apply the method for a 5 years-long data set of a 1410 km long fiber link. Second, we apply the method to the case of optical clock comparisons, where the downtimes of the optical clocks degrade the coherence of the links. We show that our methodology of processing the missing data is robust and converges to consistent mean values, even with very low uptimes. We present an offset and uncertainty contribution from the French fiber network of $2.4(9.0) \times 10^{-20}$, that is an improvement by a factor 5 as compared to a processing without taking the effect of missing data into account.

Keywords: fiber links, statistics, clock comparisons

(Some figures may appear in colour only in the online journal)

1. Introduction

Optical clocks are a new generation of atomic clocks, with superior frequency stability and accuracy as compared to clocks based on microwave transitions. However, the comparison of these optical clocks over large distances is very challenging, since traditional means of comparison of the clocks through the global navigation satellite system (GNSS) are no longer viable. Reliable and long-term comparison of optical clocks at 10^{-18} fractional frequency uncertainty is among the mandatory criteria set on the roadmap for a new definition of the SI-second [1, 2]. The operation of optical clocks in a network is a very exciting prospect, as it enables stringent tests of special and general relativity [3–6], search for dark matter [7], and direct measurement of the differential redshift between frequency standards at different geopotentials [8–11]. Coherent optical fiber links have shown great promise, allowing the comparison of optical clocks on a continental scale [10]. This has led to the development of coherent optical networks around the world [12]. In France, the Réseau Fibré

* Author to whom any correspondence should be addressed.
3 Now affiliated at Leibniz-Institut für Astrophysik Potsdam (AIP) An der Sternwarte 16, D-14482 Potsdam, Germany.
4 Now affiliated at 2.

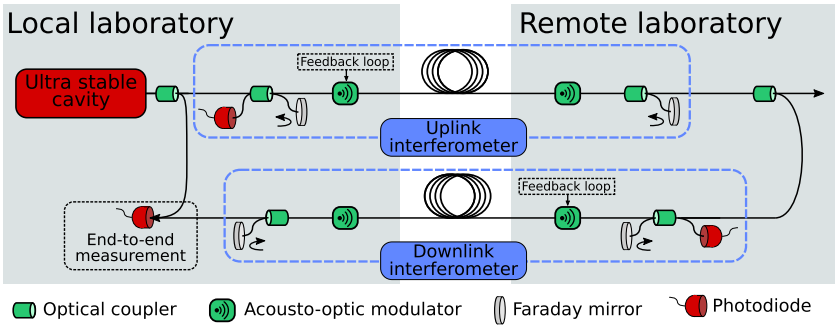

Figure 1. Illustration of the active noise compensation scheme (ANC) used for long distance fiber links. The end-to-end measurement is recorded as the beat node between the local ultra-stable cavity and the light disseminated first in the uplink, and afterward in the downlink interferometer.

Métrologique à Vocation Européenne (REFIMEVE) [13] network disseminates an ultra-stable optical frequency over large distances to multiple users, aiming at more than 30 laboratories all over the country [14]. Applications range from atomic and molecular spectroscopy [15–20], radio-astronomy [21], laser frequency control [22, 23], tests of fundamental physics [5, 7, 24–26], as well as particle and high energy physics [27, 28]. Aiming at delivering a highly available service, the links are run mostly unmanned and automatically, with the help of a global supervision. A large amount of data is gathered continuously over the years from all the links across the network. The data sets of two of the links of this network are used in this study.

Beyond the need for the redefinition of the SI unit 'second', ultra-precise frequency comparisons with an uncertainty below 10^{-18} relies either on continuous optical frequency dissemination or on a rigorous evaluation of the effect of the missing data. Interruptions do however occur in the form of unlocks of the link, cycle slips, polarization adjustments, and general maintenance on the network. A rigorous evaluation of the performance and statistical behavior of the fiber links is needed to handle the issues from missing data. Similar evaluations have been performed in the case of frequency transfer through the GNSS and two-way satellite time and frequency transfer [29–37], but were never performed in the frame of coherent fiber links, which raises novel challenges.

Indeed, the strength of optical fiber links is that they operate in the phase coherent regime, which ensures that their instability decreases with time with a larger slope. This phase coherence, however, is the origin of aliasing effects [38], and adds complexity to the post-processing in the case of missing data, which can cause deterioration of the evaluation of the frequency transfer due to aliasing effects.

The second difficulty with fiber links arises from the fact that the noise is not strictly stationary [39, 40]. The performance of a link depends on external conditions that are imperfectly under control. The comparison of performances varying only one parameter is not always obvious.

A first approach for optical fiber links was introduced and discussed in [14, 41]. Here we provide a concise and consistent evaluation of the fiber links reduced to a handful of parameters, both on short/medium term (on the scale of seconds to hours) and very long term (on the scale of years). As the former case operates in the phase-coherent regime, which is not the case of the latter, we will split up their analyses: we first evaluate the short/medium term behavior of the fiber links, followed by an analysis of the aliasing effects arising from the sampling of missing data. Afterward, we analyze the long-term behavior of the links, using a data set of 1890 days from the REFIMEVE network. We apply the study to the case of optical clock comparisons and evaluate the effect of the downtime of the clocks on the uncertainty budget of the contribution of the link.

2. The experiment

In this paper, we will show studies of two links in the REFIMEVE network, which we will call *Link A* and *Link B*. Link A stretches from Systèmes de Référence Temps-Espace (SYRTE) in Paris to Laboratoire de Physique des Lasers (LPL) in the city of Villetaneuse north of Paris, where it is looped back to SYRTE. It has a total length of 86 km and is a two-span cascaded link.

Link B is 1410 km long and stretches from SYRTE to the University of Strasbourg, where it is looped back to SYRTE. This link is used in the clock comparisons between SYRTE and Physikalisch-Technische Bundesanstalt (PTB, Braunschweig, Germany). This link is a four-span cascaded link, which enables us to compensate more noise in each segment and reach a higher correction bandwidth and noise rejection [42]. It uses repeater laser stations (RLSs) and since 2018 multi-branch laser stations (MLSs) [14, 43]. This link is optically amplified in 16 bidirectional erbium-doped fiber amplifiers (EDFAs).

Each segment of the fiber links consists of a strongly imbalanced Michelson interferometer, where an acousto-optic modulator (AOM) is used as an actuator on the outgoing light, compensating the noise of the reflected signal in the fiber [44]. In this paper, we will focus on the properties of the end-to-end (E2E) signal of the fiber link, which is an out-of-loop assessment of the frequency transfer measured by comparing the outgoing light with the looped back signal. This scheme is illustrated in figure 1. The E2E signal of the fiber link is counted by dead-time free frequency counters. Our experiments are using K + K counters [45] with a fundamental sampling interval of 1 ms, operated in Λ mode with a gate time

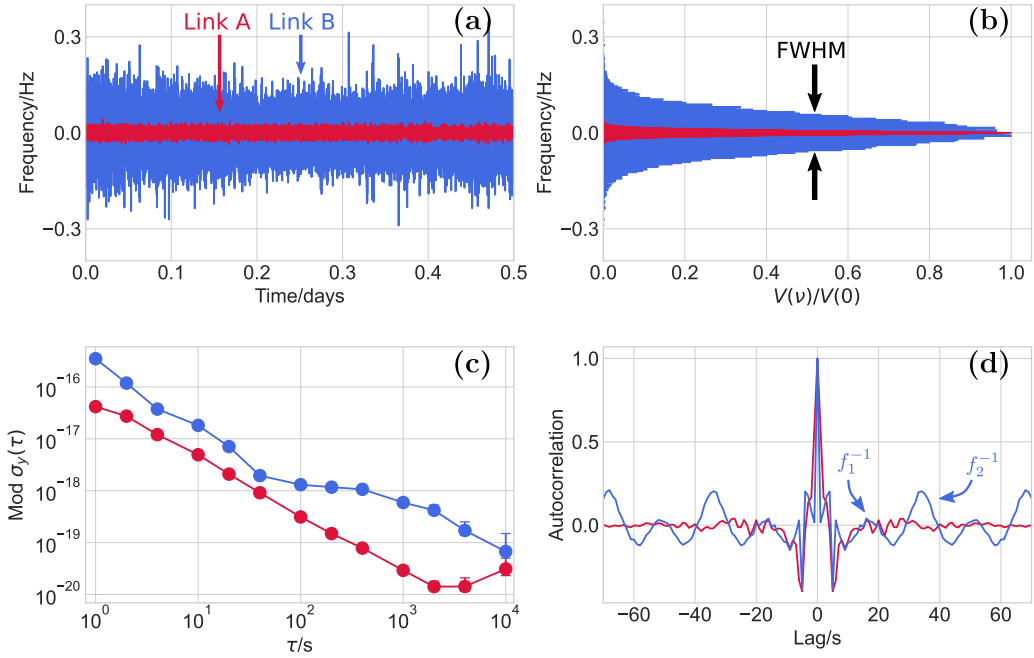

Figure 2. Behavior of the noise of Link A (red) and Link B (blue) for half a day of measurement time, with a gate time of $\tau_G = 1$ s. (a) Frequency fluctuations. (b) Normalized distribution of frequency fluctuations. (c) MDEV of the fractional frequency fluctuations. (d) Auto-correlation of the frequency fluctuations. Arrows point out two of the periodic perturbations in Link B.

of $\tau_G = 1$ s, corresponding to a bandwidth of 0.5 Hz [46]. The reference clock is provided by an active H-Maser disseminated by fiber links across the campus and has negligible contribution to the uncertainty [47]. Further information on the links and technical details can be found in [14, 43].

3. Modeling fiber links

The phase of a continuous E2E signal without any missing data can be expressed as

$$\phi(t) = 2\pi\nu_0 \int y(t)\mathrm{d}t + \sum_n \phi_n(t), \qquad (1)$$

with $y(t)$ being the relative stochastic frequency fluctuations of the link. The terms $\phi_n(t) = A_n \sin(2\pi f_n t)$ sum up any periodic perturbations to the phase affecting the fiber link, where A_n is the modulation amplitude and f_n the modulation frequency. Pseudo-periodic perturbations are expected, since the optical length of the short arm of the interferometers is sensitive to temperature variations that cannot be compensated from the interferometric measurement [44, 48, 49]. On top of day-night fluctuations, several groups report observations of the effects of air conditioning systems that impose much shorter time periods, like 400 s–2000 s. More recently, humidity variations were also found to play a similar role [47]. The global mathematical frame of the study is given in appendix A.

3.1. Case study with mid-haul and long-haul fiber links

We show in figure 2 four representations of the end-to-end measurement for a duration of half a day, showing a red trace for the mid-haul (Link A) and a blue trace for the long-haul (Link B) fiber link. Figure 2(a) shows the fractional frequency fluctuations over the acquisition period, that we chose conveniently without any missing data. Figure 2(b) shows the distribution of the data. We fit this distribution with a pseudo-Voigt profile, and extract from the fit the full width at half maximum (FWHM), and the weight of the Gaussian and Lorentzian parts (see equation (A.8) and details in appendix A). Figures 2(c) and (d) show respectively the modified Allan deviation (MDEV) and the auto-correlation plots. The auto-correlation is calculated on a moving average of the frequency

Table 1. Noise parameters for the 2 links. Parameters are found from the plots in figures 2 and 3, using the formulas described in appendix A. Coherence time of Link B is calculated using equation (2), and of Link A using the '+' solution of equation (A.6).

	Link A	Link B
Lorentzian weight	0.44	0.11
FWHM/mHz	15.8	122
b_0/rad^2/Hz	4.0×10^{-2}	5.9×10^{-2}
b_{-1}/rad^2	1.4×10^{-4}	0
b_{-2}/rad^2 Hz	1.8×10^{-7}	1.9×10^{-5}
τ_{coh}/s	214	55
n	A_n/rad	f_n/mHz
#1	7×10^{-3}	285
#2	9×10^{-3}	234
#1	0.11	59
#2	0.15	29
#3	0.03	5
#4	0.05	3
#5	0.08	2
#6	0.24	1

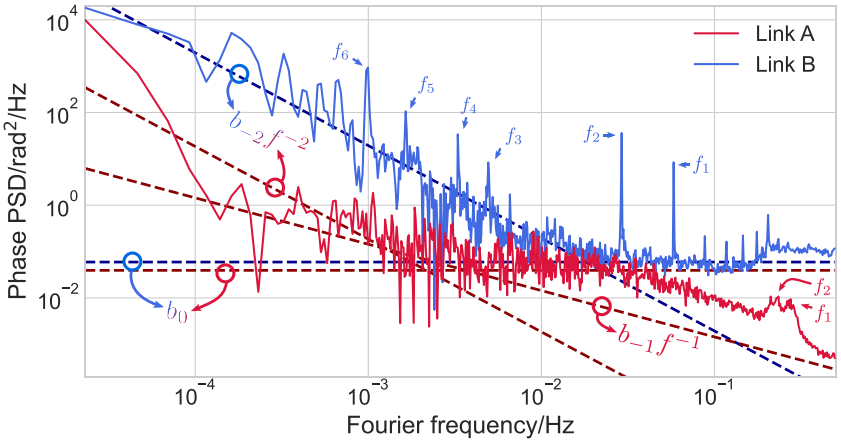

Figure 3. PSD of the phase noise, for Link A (red) and Link B (blue), with a linear density of points per decade. The noise coefficients b_n are indicated from equation (A.3) and are listed in table 1.

data, with a window of 5 s. Using this approach, the short-term periodic perturbations of Link B become clearly visible.

As displayed in table 1, the FWHM of Link A is as low as 16 mHz, and is 122 mHz for Link B, showing that the degradation of the transmitted laser is very low and can be neglected. Although an extensive study of the line width of the distributed signal is beyond the scope of this paper, we can notice that these line-widths are much lower than that of lasers usually used for precision spectroscopy, and thus the transmitted signals are worth to be used at the user end to reduce the line-width of local lasers [12, 18, 22]. We also notice that the weight of the Lorentzian part is lower for Link B than for Link A, showing that the contribution of white frequency noise is higher than that of white phase noise, as expected for a longer link. Similarly, the MDEV of 4×10^{-17} at 1 s averaging time for Link A is typically ten times lower than for Link B.

To identify the periods and amplitudes of the pseudo oscillations, there are elaborated methods reported in the literature applied to GNSS and geodetic surveys, as principal component analysis (PCA), independent component analysis (PCA) and wavelets [50–52]. Here, we use a simple peak identification procedure of the auto-correlation plot to extract their amplitude and their frequency. It appears to be sufficient for the case of fiber links where the number of components generally are only a few, the signal-to-noise ratio is greater than 1, and there is no phase ambiguity. Periodic perturbations are clearly visible for Link B and are discussed below.

Power spectral densities. Figure 3 shows the power spectral density (PSD) of the phase noise for the two links with the same color code. As expected, we observe that the longest link has a higher amount of noise across the whole spectrum. First, we identified periodic perturbations of Links A and B, highlighted with arrows in figure 3. In total, 2 components are identified for Link A and 6 components for Link B. Then, we fit the rolling median of the PSDs with a window size of 35 data points (in order to remove the contribution of the peaks) and determine the noise coefficients b_n for the two links (see equation (A.3) in appendix A). The obtained coefficients are indicated by dashed lines in figure 3. It is noticeable that for Link A, a non-zero flicker phase component with a power of law as f^{-1} at low Fourier frequencies is found, whereas Link B exhibits only white phase noise and white frequency noise components. For Link A, at frequencies higher than a few 10 mHz, the phase PSD is limited by the bandwidth of the detection system.

For Link B, by contrast, the white phase noise behavior below 1 Hz is due to the active phase stabilization of the link delay. The white frequency noise at lower Fourier frequencies can arise from various phenomena breaking the coherence, as for instance the spontaneous emission of the optical amplifiers.

Coherence time. The coherence time of the fiber link is defined here as the time at which the PSD of the phase noise changes its slope from white phase noise to white frequency noise. When flicker phase noise is negligible and when b_{-2} is not zero, this is simply given by the relation

$$\tau_{\mathrm{coh}} = \sqrt{\frac{b_0}{b_{-2}}}, \tag{2}$$

where b_0 and b_{-2} are respectively the white phase noise and white frequency noise coefficients. This ratio should determine the slope change in the overlapping Allan deviation, that is the same for flicker phase noise and white phase noise.

When flicker phase noise is not zero, a generalization of equation (2), as well as the relation between these noise coefficients and the two statistical estimators, phase PSD and MDEV, can be derived and is given in appendix A. Three poles can be found as detailed in appendix A and in the following we will consider the coherence time of Link A to be defined by the crossing of the terms b_0 and $b_{-1} + b_{-2}$.

The coherence time of Link B is 55 s, whereas that of Link A is as long as 214 s, due to its shorter length and thus lower noise. The coherence time of Link A, being longer than that of Link B, is less clear from the plot in figure 3. This is due to the reduced resolution at lower frequencies, which increases the uncertainty of the b_{-2} noise parameter.

Reduction to a few parameters. With the outcome of the analysis of the auto-correlations, phase noise PSDs, and frequency noise distributions, one can draw a complete picture

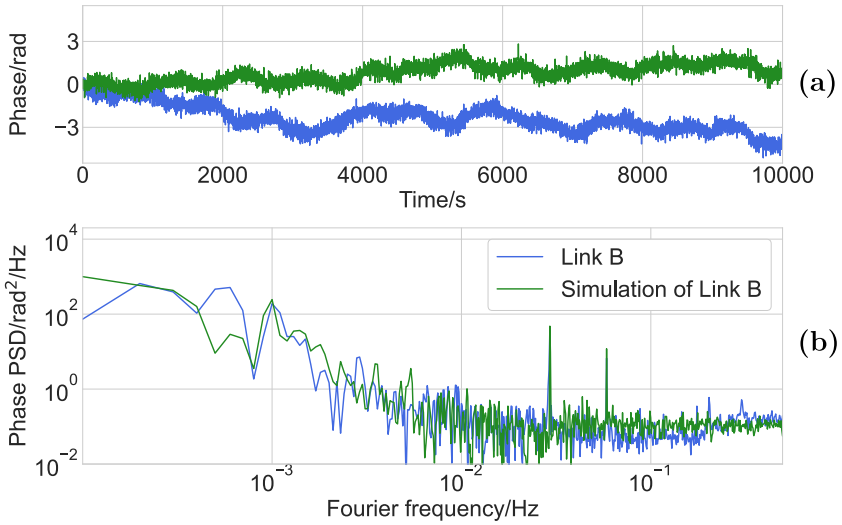

Figure 4. Link B (blue) and a simulation of the link (green). (a) Evolution of the phase over 10 000 s. (b) Phase PSD of the phase shown in (a).

of the physical characteristics of a link, reduced to just a few parameters. We present in table 1 the parameters describing the two links introduced above, enabling a straightforward comparison between them. One observes that the shorter Link A has fewer and smaller periodic perturbations. We believe that it is due to its simpler architecture and shorter length, which expose the fiber to fewer noise sources. Furthermore, this should lead to a lower amplitude of the noise, since the level of fiber noise is typically proportional to the fiber length.

3.2. Fiber link simulation

With the link parameters identified in table 1, which are stable over typically months, we can appropriately simulate the behavior of fiber links. We can generate data sets at will, with a similar statistical behavior as that of the link, with no missing data, and thus study the effects of missing data within these data sets. We ran Monte-Carlo simulations, repeating calculations on any number of identically simulated data sets.

In figure 4 we show a comparison between a case of continuous experimental data from Link B (blue trace), and a simulation of the link (green trace). Both traces show a data set without any missing data. We show the end-to-end phase variations and phase PSD of Link B and the simulation in figures 4(a) and (b) respectively. We observe a very good correspondence between the two, which shows that the simulated link can be used to study the behavior of the real link. Taking advantage of the flexibility offered by the control of the various parameters, we are able to look for the impact of missing data on the link performance, as shown in the next part.

4. Links with missing data

Missing data in frequency comparisons have been studied for several applications, mainly using GNSS frequency transfer, for the comparison of microwave fountain clocks [30], or tests of fundamental physics [53]. A common conclusion is that the handling of, and the uncertainty introduced by, the missing data is dependent on the noise model of the data. Here we study missing data in coherent optical fiber links, both in relation to the fundamental behavior of the links themselves, and in their applications to the comparison of optical clocks.

In figure 5 we have illustrated an extreme case of missing data. We show the (a) systematic and (b) statistical uncertainty of the same continuous frequency measurement of Link B. Removing every second data point in post-processing is introducing an artificial frequency shift to either lower (green) or higher (orange) values, changing the relative frequency offset from $-5(6) \times 10^{-20}$ to $\sim \pm 1(2) \times 10^{-18}$. We expect that it is related to a technical limitation of the dead-time free counters, even with their very good resolution. The decreased stability performance in figure 5(b) is a consequence of the aliasing arising from the Dick effect [54], which is detailed below.

At each run of our simulation of the fiber links, we can likewise generate missing data. With the same tools, and following the same general formalism, we can control the density of missing data and their statistical properties. This is indeed a necessity in the study of external noise sources to the fiber links like missing data, as the noise of the links is not strictly stationary. This is also intended to avoid effects that would arise from a peculiar arrangement of data and missing data, that would not be reproducible. First, we describe here our noise model for the missing data. We then present a study on the effects of missing data on the statistical and systematic evaluation of the fiber link on reproducible data sets, i.e. with a steady and controlled statistical behavior. As for the data represented by equation (1), it can be split into a stochastic component and a systematic component expressed as a sum of pseudo-periodic components, which we study individually.

4.1. Noise model of missing data

To represent missing data, we use the annihilation operator $g(t)$. At any point in time $t = t_k$, this is defined to be either representing valid data ($g(t_k) = 1$) or missing data ($g(t_k) = 0$).

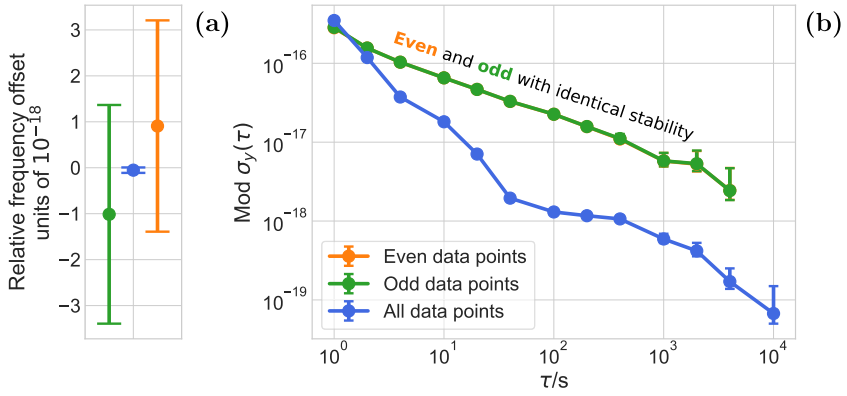

Figure 5. Systematic (a) and statistical (b) uncertainty of a continuous fiber link end-to-end signal (blue) split up in even (green) and odd (orange) data points.

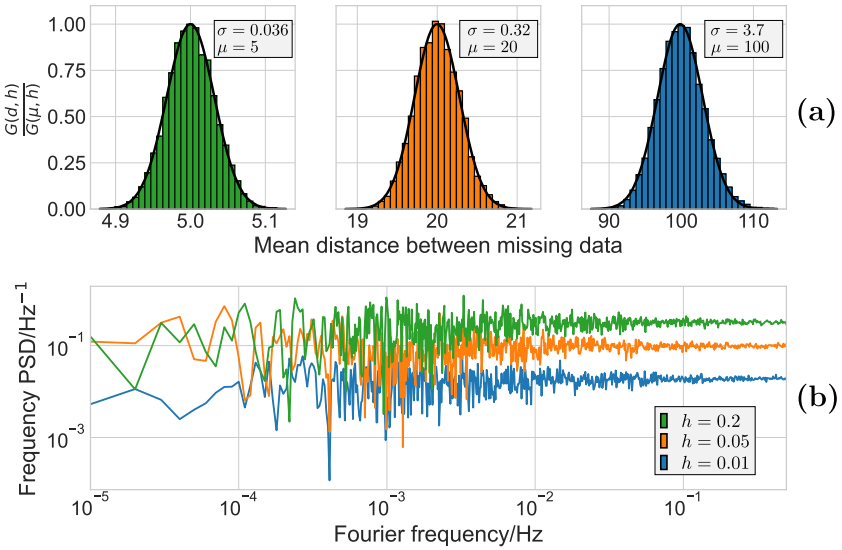

Figure 6. Statistical properties of the annihilation operator for 3 values of h: 0.2 (green), 0.05 (orange), and 0.01 (red). (a) The mean distance between missing data, simulated from 10 000 iterations of $g(t)$. Black lines indicate Gaussian fits. (b) The Fourier spectrum of the annihilation operator. The properties of the Gaussian distributions $G(d, h)$ and the noise level of the frequency spectrum is described in appendix B.

The *density of missing data* is given by

$$h = 1 - \frac{\tau_G}{T} \sum_{k=1}^{T/\tau_G} g(t_k), \tag{3}$$

with T being the total duration of the data sample and τ_G the time gap between consecutive measurements. By this definition the two extreme cases are given by $h = 0$, corresponding to a complete data set without missing data, and $h = 1$ describing the case of an empty data set. This allows us to represent the effective relative frequency of a sample data set as

$$\tilde{y}(t_k) = g(t_k) \cdot y(t_k). \tag{4}$$

4.2. Gaussian distribution of missing data

In this study, we first assume that missing data are incoherent, follows a Gaussian distribution, and exhibits a white frequency noise spectrum. The noise density h is the only parameter and has an equivalent role of b_{-2}. This is illustrated first in figure 6(a), where we have calculated the distribution $G(d, h)$ of the mean distance d between missing data for 3 densities of missing data h. The mean of the three Gaussian distributions is given by the inverse of the density, and their width is given by around $h^{-3/2}$, as expected (see appendix B). In figure 6(b) we show the Fourier spectrum of the annihilation operator $g(t)$ for the same values of h. It shows a white frequency noise behavior, which can be described analytically, and is given in appendix B.

4.3. Periodic effects

We will now consider the simple case of periodic sampling, where 1 measurement value is removed every τ_G/h seconds. This is a well known case, found for instruments with 'dead time', radars and lidars, and particularly well known in metrology for clocks with non-continuous operation. The latter case was introduced by John G Dick in the late 80s to describe

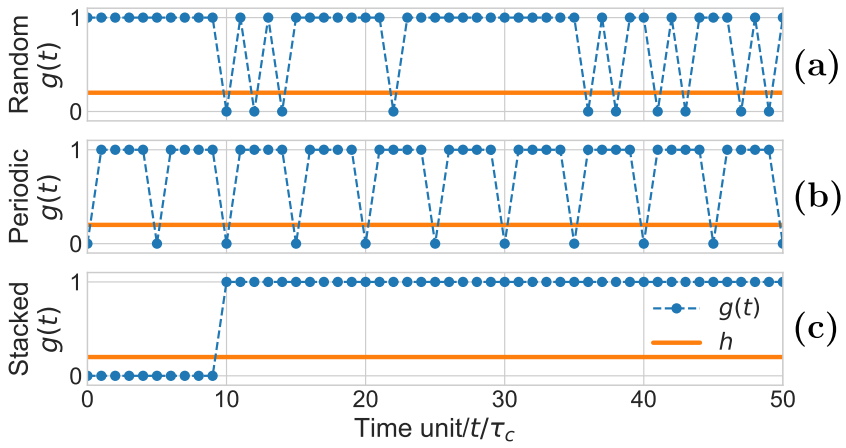

Figure 7. Illustration of three different representations of the annihilation operator $g(t)$, showing examples of (a) random, (b) periodic, and (c) stacked missing data. The density of missing data, $h = 0.2 = 20\%$, is the same in all 3 cases.

the periodic sampling of low-noise oscillators with periodic sampling from atomic response [54].

The increase in frequency noise due to the Dick effect as a function of the density of missing data h can be written, following [55], as

$$S_{\phi'}^{\mathrm{Dick}}(f,h) \approx \frac{2h}{(\tau_G f)^2}\sum_{n=1}^{\infty}\mathrm{sinc}(n\pi(1-h))^2 n^2 S_\phi\left(\frac{nh}{\tau_G}\right), \quad (5)$$

with $S_\phi(f)$ being the nominal phase noise of the signal without missing data. Applying an upper limit of the summation of $n \leqslant \lfloor \frac{1}{2h} \rfloor$, with $\lfloor\cdot\rfloor$ denoting the 'floor' function, and evaluating the function in the case of a nominal signal of pure white phase noise $S_\phi(f) = b_0$, we find the following expression for the effective phase noise $S_{\phi'}(f,h) \approx S_\phi(f) + S_{\phi'}^{\mathrm{Dick}}(f,h)$:

$$S_{\phi'}(f,h) \approx b_0 + b_0 h^2 \frac{2\lfloor\frac{1}{2h}\rfloor - \frac{1}{\sin(\pi h)}\sin\left(2\pi h\lfloor\frac{1}{2h}\rfloor + \pi h\right) + 1}{\tau_G^2 f^2 2\pi^2 (h-1)^2}$$

$$= b_0\left(1 + \frac{\mathbb{D}(h)}{f^2}\right). \quad (6)$$

The second term corresponds to the Dick noise, and is a white frequency noise term due to the aliasing of the original white phase noise. We introduce the notation $\mathbb{D}(h)$ to express the sensitivity of the phase noise PSD to the density of missing data.

4.4. Sensitivity function approach

The sensitivity approach was developed in the frame of cold atom clocks (atomic fountains) to simplify the modeling of the sensitivity of the phase noise power spectrum density of the servo-looped oscillator (the clock output), as a function of the ratio of the interrogation time of the atomic clock transition over the clock cycle time [56]. The sensitivity function formalism is very convenient to describe periodic perturbations, as shown in the previous part. Here, we adapt this formalism to show the convergence between the white frequency noise model and the periodic model for the missing data. Illustrated in figure 7, the missing data for a given density can be distributed with (a) no preferred order, or with a specific order:

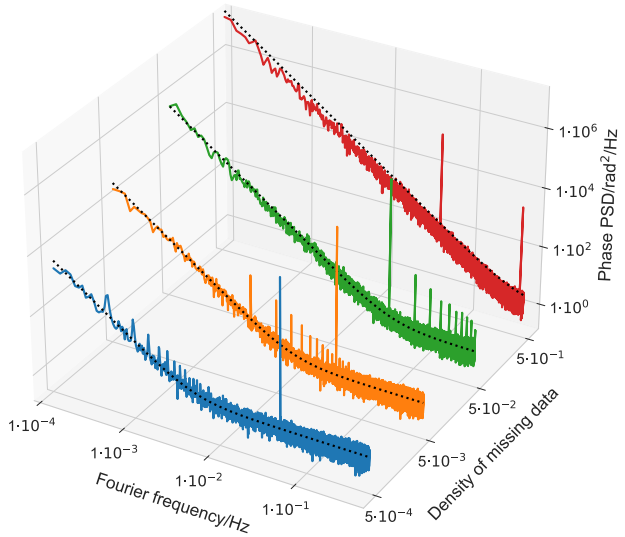

Figure 8. Phase noise PSD of a carrier signal with white phase noise for 4 different densities of periodically missing data. Both the aliasing due to the Dick effect and due to the sampling of the modulation are clearly seen. The black dotted lines represent equation (6).

(b) the missing data is periodically spaced, or (c) all the missing data can be at the beginning or the end. For a periodic spacing between the missing data, equation (5) can be applied. We thus simulate missing data with various density of missing data, using a Gaussian distribution or a periodic distribution, and will compare the resulting phase noise with expression (6) of the Dick effect.

4.5. Results

Aliasing effects. We first consider a simulated link signal with a white phase noise component and a strong periodic modulation $\phi_p(t) = A\sin(2\pi f_m t)$ around 50 mHz. The four different curves shown in figure 8 correspond to the same signal with a varying amount of periodically missing data. The phase noise using equation (6) is shown as a dotted line and predicts very well the simulated noise, except for at very high

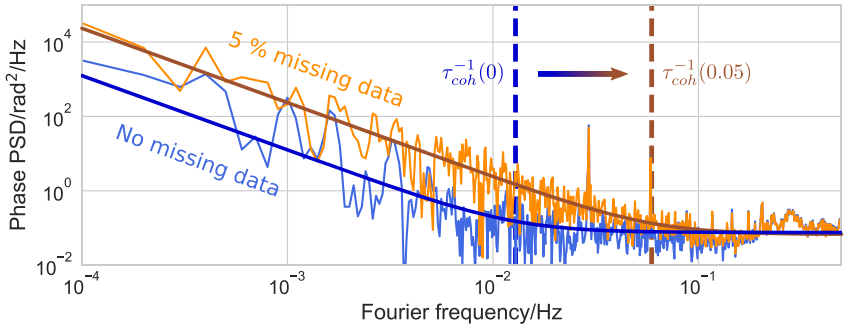

Figure 9. Phase PSD of Link B without missing data (blue) and where 5% of the data is removed. Thick solid lines corresponds to a fit to equation (A.3), and dashed lines to τ_{coh}^{-1}.

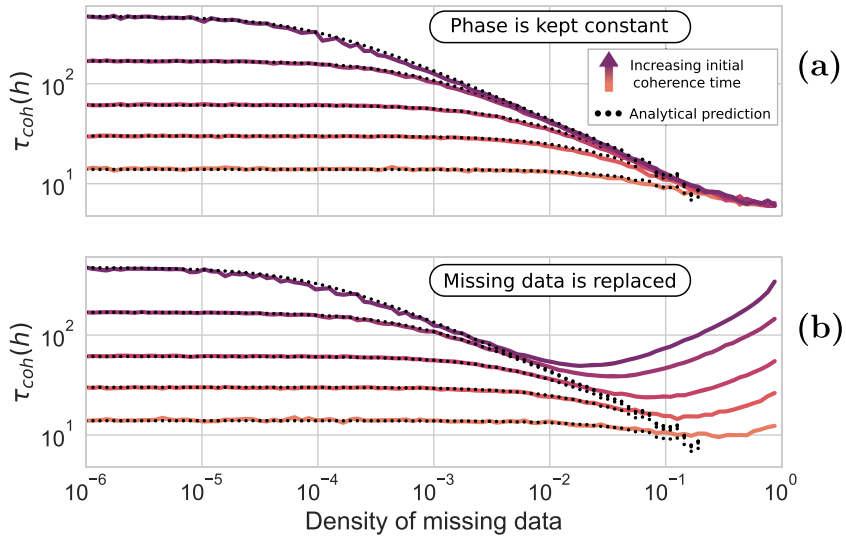

Figure 10. Effective coherence time of a simulation of a link as a function of density of missing data. Solid lines indicate the numerically calculated coherence time, with an increasing initial coherence time (increasingly purple). (a) When the phase is kept constant over the missing data, and (b) when missing data is replaced by simulated noise with a similar behavior of that of the link. Equation (7) is shown by black dotted lines.

densities of missing data (red curve). In that last case indeed the assumptions of quite low density of missing data leading to equation (6) are no longer fulfilled. We can see that the frequency noise is increasing with the amount of missing data, as expected from equation (5). Furthermore, the sampling of the strong carrier signal can be seen, resulting in an additional aliasing effect.

Coherence time. The increase in white frequency noise according to equation (6) directly corresponds to a decrease in coherence time, as described by equation (2). For a signal consisting of white phase noise and white frequency noise, we can find the following expression for the effective coherence time as a function of the density of missing data:

$$\tau_{\text{coh}}^{\text{eff}}(h) \approx \left(\mathbb{D}(h) + \tau_{\text{coh}}(0)^{-2}\right)^{-\frac{1}{2}}, \tag{7}$$

with $\tau_{\text{coh}}(0)$ being the nominal coherence time without missing data.

Figure 9 illustrates how missing data leads to increased frequency noise, and thereby a decrease in effective coherence time. The blue trace shows the short term phase noise of Link B without any missing data, which serves as a reference. In orange, we have removed 5% ($h = 0.05$) of the data points, using a Gaussian distribution of the missing data (with a white frequency noise spectra). This leads to an increase in frequency noise, and a decrease in effective coherence time. Repeating the simulation with a varying density of missing data (h), the aliasing effects of the missing data is shown in figure 10(a). Here we have calculated the effective coherence time as a function of the density of missing data for five nominal coherence times, ranging from 10 s–300 s. The dotted line corresponds to equation (7) and perfectly predicts the simulated data, although there is no free parameter for the simulation. This shows that the sensitivity function of equation (5), even though derived for periodically spaced missing data, can be applied for a Gaussian distribution of missing data as well. This is possible for any distribution of missing data as long as the mean of the data is unaltered, which is the most important assumption for applying equation (6) [37, 57].

4.6. Mitigating the effects of missing data

Up to here, we discuss the effect of missing data, and kept the phase constant across the missing data, which conserves the length of the data set. However, such an approach biases the short-term noise level. Here, we test a second approach of dealing with the missing data, and simulated how it affects the effective coherence time. This second approach is to replace the missing data with simulated noise (according to equation (A.3)), with the same statistical parameters as the 'original' data. Our method relies on inserting the new data point as a stochastically generated point into the phase. For this part, for simplicity, we consider a link without periodic perturbations to the phase, as described in the derivation of equation (7). The mean of the distribution is determined by the mean of phase data points just before the missing data, where the number of points to be considered depends on the coherence time of the data. An initial comparison between the two approaches, as well as the option of concatenating the effective data set, can be found in [41].

We observe that there is no significant difference in the two approaches for small densities of missing data, $h < \tau_G/\tau_{\mathrm{coh}}(0)$. However, for densities $h > \tau_G/\tau_{\mathrm{coh}}(0)$ we start to see divergence between the two models: when the phase is kept constant, the effective coherence time is limited by equation (7). This limit does not apply when the missing data are replaced with simulated data. In this case, we observe that the link coherence is increasing toward its nominal value without missing data. Thus, by treating missing data and replacing them with simulated data, we can have a better estimation of the link behavior without missing data.

5. Long term behavior of fiber links

In section 3.1 we analyzed the behavior of the short-term noise of the links, with up to half a day of data. At these timescales it is possible to acquire continuous data, and the assessment of the links' statistical behavior becomes straightforward. Assessing the long term behavior, on the scale of years, of a fiber network presents many challenges, however, from both an operational and a computational point of view.

Here we present the analysis of the long term behavior of Link B, starting in April 2015, and ending in June 2020. The total period lasts 5 years and 64 days, with a total uptime of 41.6%. As the frequency data is recorded with a gate time of 1 s, 1890 days corresponds to more than 163 million data points. This is more than twice the duration in [14].

First, we processed data over subsets of 3 months using similar filtering procedures as in [58]. For data sets longer than 3 months, our data filtering procedures starts to become critically slow, so that we have to reduce the number of data points. We used an additional filtering stage to check that the mean fractional frequency over subsets of 1000 points is below 9×10^{-18}, so that each reduced data point is not critically depending on the uptime of the subset. Then, we reduced the data to 40 data points per day, i.e. averaging over 2160 s. For our statistical analysis, we remove all the subsets with an uptime less than 100%, resulting in an uptime of 17% for further analysis. Then, missing data are replaced with data containing the statistical properties as analyzed in section 3, in a similar way as illustrated in figure 4.

The phase coherence has no effect due to averaging of the data over 2160 s intervals, which is much longer than the coherence time of the link. In figure 11 we plot (a) the frequency noise PSD, given by $S_{\delta\nu}(f) = f^2 S_\phi(f)$, and (b) the auto-correlation of the rolling mean of the frequency fluctuations, for the reduced data. We observe a white frequency noise behavior, consistent with the white frequency noise behavior observed with the data of shorter duration (see table 1), which is highlighted with the dashed green line.

Furthermore, we observe a peak with a period of one day, highlighted by the orange shaded area. This one-day period is confirmed by the auto-correlation plot in the region of a few days. This peak is not represented by the simulated data computed using the noise model, and is revealing information contained solely in the experimental data. This result is revealed when repeatably replacing the missing data, and averaging the resulting phase PSD. This approach averages out all sporadic peaks caused by chance by single iterations, and leaves solely the peaks hidden in the data. We believe that the one-day periodic perturbation is due to daily temperature variations, which affects the reference arms of the interferometer set in the RLSs at data centers in Paris and in Strasbourg.

The analysis of the pseudo-periodic perturbation beyond one day is beyond the scope of this article. Indeed, such an analysis would rely on a good knowledge of the long term behavior without missing data, or a more elaborated statistical analysis.

We show the resulting MDEV and associated means and uncertainty in figure 12. The stability plot spans from 1 s integration time to 4×10^7 s. The short/medium term stability of Link B is shown in light blue, for the same period without any missing data as analyzed in section 3.1. The stability of the 5+ years of data, where the missing data have been replaced with simulated noise, is shown in dark blue, and where the missing data have been concatenated in orange.

We see an excellent agreement between the three stabilities in the region $\tau = 2000$ s to $\tau = 10\,000$ s. The dashed lines show the noise terms of the link: $\sqrt{\frac{0.038}{\nu_0^2\tau^3}b_0}$ corresponding to white phase noise, and $\sqrt{\frac{1}{4\nu_0^2\tau}b_{-2}}$ corresponding to white frequency noise. They cross at the expected value of $0.39\tau_{\mathrm{coh}}$, indicated by the vertical line on the plot [59]. These noise terms and the coherence time translated to integration time is discussed in appendix A.

The coherence time as revealed by the spectrum of Link B (in figure 3) is shorter than what could be deduced from the inflection point of the MDEV. This is due to the two periodic perturbations f_1 and f_2, which have periods shorter than the coherence time of the link, and induce a small bump in the stability around 10 s.

Finally, the accuracy of the frequency transfer was evaluated by calculating the mean value of the reduced end-to-end beat-note frequency offset. Although the data were acquired with a dead-time free counter in Λ-mode, one expects an excellent convergence at long term with an evaluation for data

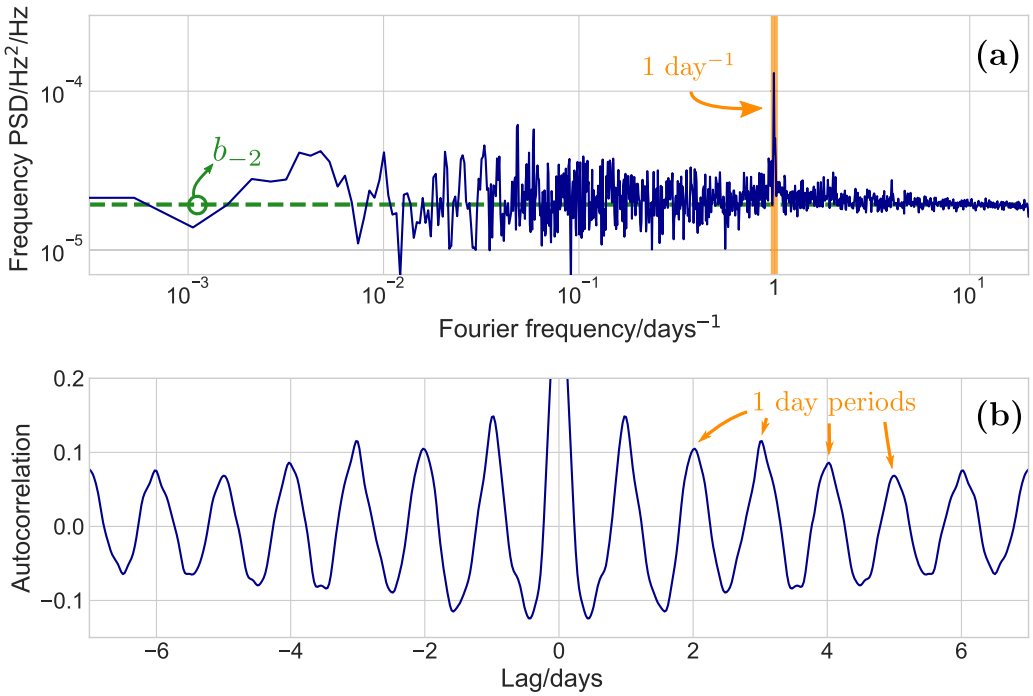

Figure 11. (a) Long term frequency PSD and (b) autocorrelation of Link B. The green dashed line shows the b_{-2} noise parameter from table 1. 1 day fluctuations are noted with orange arrows and writing in both the Fourier frequency (a) and time (b) domain.

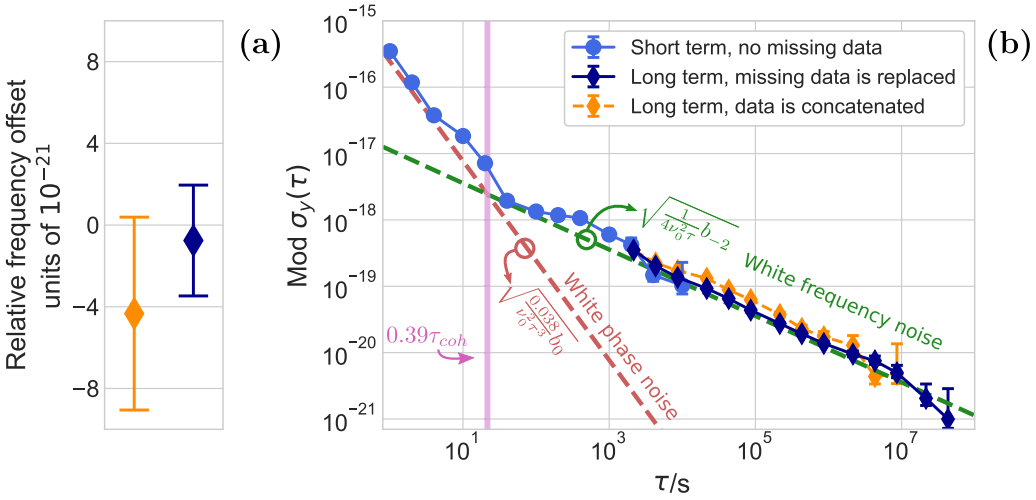

Figure 12. (a) Systematic and (b) statistical uncertainty of the long-term noise behavior of Link B. In (b), both the short-term (without any missing data, light blue) and the long-term (dark blue and orange) MDEV of Link B is shown. The dark blue stability curve is obtained when missing data have been replaced by simulated noise, and the orange curve when the resulting data have been concatenated. Green and red dashed lines show the white frequency noise and white phase noise model respectively, for values as reported in table 1. The pink shaded area corresponds to the expectation of the coherence time derived in appendix A.

acquired in Π-mode [60]. Following [61, 62], we estimate its statistical fractional uncertainty as the long-term overlapping Allan deviation at 864 000 s or 4320 000 s of the data set without and with a treatment of the missing data respectively. The results are plotted in figure 12(a). The mean is $-1(2) \times 10^{-21}$ when the missing data were treated using the noise model, and $-4(5) \times 10^{-21}$ when the missing data are not treated. For both cases we obtain a mean which is consistent with zero within the statistical 1 σ uncertainty. However the uncertainty obtained with the missing data treatment is reduced by a factor 2 compared to the case of concatenated data, highlighting the role of data treatment.

6. Uncertainty contribution to clock comparisons

When comparing distant optical clocks, both the clocks and the links between them must be running at the same time. If we consider the simple case of the comparison of two clocks, called C_1 and C_2, they will at any given time either be considered to be valid or not (up or down), indicated by their

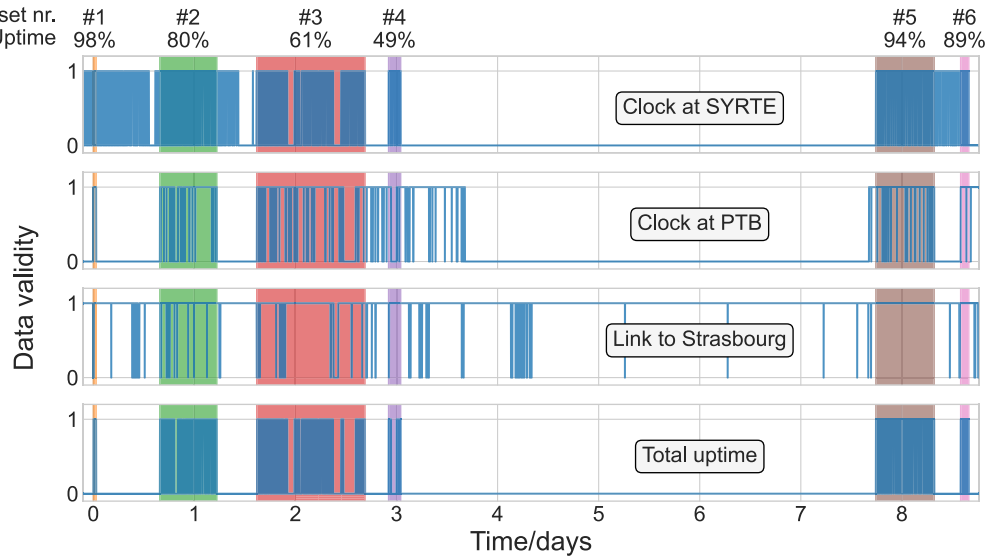

Figure 13. Illustration of the operation time of the two clocks, Link B, which is used in their comparison, as well as the total uptime of the comparison. From the total uptime, 6 subsets are chosen and analyzed individually.

respective annihilation operators $g_{C_1}(t)$ and $g_{C_2}(t)$. We denote the annihilation operator of the comparison chain between them $g_\rho(t)$, which consists of optical frequency combs, ultra stable cavities, as well as the optical fiber link connecting them. The total uptime of the comparison can be written as the product

$$g_{\text{tot}}(t) = g_{C_1}(t)g_\rho(t)g_{C_2}(t). \tag{8}$$

In the following we will evaluate the links' contribution to the uncertainty of the comparison in the case of missing data, evaluating the effective relative frequency fluctuations of the link

$$y_{\text{eff}}(t) = g_{\text{tot}}(t)y(t), \tag{9}$$

where $y(t)$ represents the link without any missing data[5].

In figure 13 we show the uptime of the comparison of two optical clocks during a comparison campaign in December 2018. The two clocks are located at SYRTE in Paris [63] and at PTB in Braunschweig [64]. Each laboratory compares their respective clocks to an ultra-stable cavity, from which an ultra-stable frequency is disseminated to the city of Strasbourg, conveniently placed in the mid-point between the two laboratories at the French–German border [10]. There a local two-way comparison of the disseminated signals of the cavities is performed, from which we have an indirect comparison of the optical clocks.

During the 9 days of comparison, we observed several periods of simultaneous operation of the two clocks. This is shown in figure 13, where we show the individual uptime of each of the two clocks, the uptime of the link from Paris to Strasbourg, as well as the total uptime of all three systems $g_{\text{tot}}(t)$. Here we did not take the link between Strasbourg and PTB nor the combs into account. We have chosen to break up the periods of simultaneous operation in 6 different subsets with varying duration and uptime, which we have analyzed individually.

For each subset of data, we have calculated the systematic and statistical uncertainty of the effective link signal $y_{\text{eff}}(t)$ contributing to the comparison, and compared it to the direct link signal $\tilde{y}(t) = g_\rho(t)y(t)$. As seen in figure 13, the main contribution of the downtime of $y_{\text{eff}}(t)$ comes from the two atomic clocks.

For each of the 6 subsets, calculating both $y_{\text{eff}}(t)$ and $\tilde{y}(t)$, we have replaced the missing data due to the clocks by simulated noise. We have shuffled the distribution of missing data in each subset, and repeated this simulation 1000 times, keeping the total uptime of the subset the same. We have thus found a mean frequency shift, with a mean error, which would be expected from each period. The error of the mean offset is calculated by the long term overlapping Allan deviation.

In the two top plots in figure 14 we show the mean relative frequency offset of the effective link signal, when sampled by the uptime of the clocks, in two different cases: (a) where the effective data have been concatenated, and (b) where the missing data have been replaced by simulated noise. A weighted average of all 6 subsets yields a total systematic offset of $1.2(3.5) \times 10^{-19}$ for the concatenated data set, and $-2.4(9.0) \times 10^{-20}$ for the data set where the missing data is replaced with the noise model. For comparison, figures 14(c) and (d) shows the fractional frequency offsets when only considering the link uptime, both showing comparable shifts of $-7.1(14.7) \times 10^{-20}$ and $-9.4(9.4) \times 10^{-20}$ respectively. For the clock comparisons (cases (a) and (b)), the estimated uncertainty when replacing the missing data is a better representation of the uncertainty contribution of the link. It is consistent with the uncertainty obtained with the direct link signal $\tilde{y}(t)$ (case (d)), showing the reliance of this approach.

[5] $g_{\text{tot}}(t)$ can easily be generalized to include any number of spans in the comparison $g_{\text{tot}}(t) = \prod_n g_n(t)$, as a real clock comparison can have an arbitrary number of components, like optical frequency combs, and several links cascaded in several spans. In the end it is not important for this demonstration, as $g_{\text{tot}}(t)$ in equation (9) does not distinguish from where the downtime is introduced.

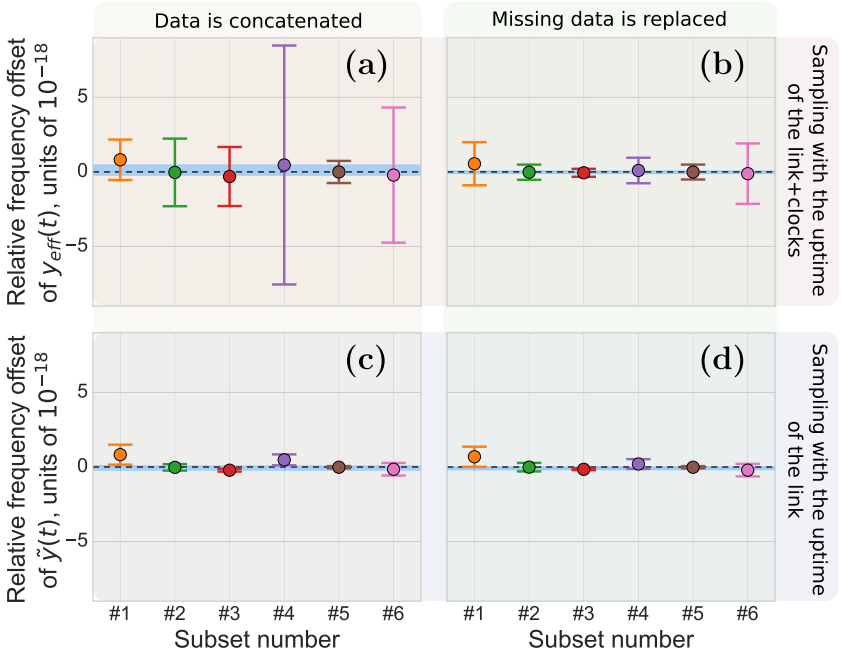

Figure 14. Fractional frequency offset of the E2E signal of Link B, for the 6 different subsets of data (from figure 13), when ((a) and (b)): sampled by the uptime of the clocks $y_{\text{eff}}(t)$, and ((c) and (d)): when sampled only by the uptime of the link itself $\tilde{y}(t)$. In ((a) and (c)) the data have been concatenated, and in ((b) and (d)) the missing data have been replaced by simulated noise. The blue shaded areas indicates the weighted average of each ensemble of subsets.

This method ensures reproducible results, and it implies that the performance of the fiber link does not depend on the uptime of the other subsystems in the comparison. These results are compatible with the scientific goal set by the BIPM of comparing remote optical clocks at least to the order of a few 10^{-18} [1, 2], as a part of the road-map of redefining the SI second to one or more optical transitions [1, 2, 65] in the coming years.

7. Conclusion

In this paper, we have discussed the noise behavior of coherent optical fiber links. Using a study of two French links of very different lengths, we have shown how the links can be described with just a few parameters, making the intercomparison of the links more straightforward. We have used this knowledge to develop a simulation of one of the links, enabling us to generate data with realistic simulated noise and oscillatory contributions on-demand. This method has been used to study the effects that missing data have on the statistical evaluation of the links, in particular the decrease in the coherence time of the links. We have shown that this decrease in coherence time can be reduced by replacing the missing data with simulated noise.

We then investigated two different applications where missing data is unavoidable: first, we have studied the long-term noise behavior of a fiber link, analyzing more than 5 years of data. Using the method of replacing the missing data with simulated noise, we have presented the resulting MDEV, frequency noise spectrum and auto-correlation, where we see periodic perturbations with a period of 1 day. We furthermore see a good agreement between the short-term and long-term evaluation of the links, further enhancing our trust in the results.

Lastly, we have investigated the uncertainty contributions of the links when using them to connect and compare two optical atomic clocks. By replacing missing link data with simulated noise, we have evaluated the uncertainty contribution of the links to be $2(9) \times 10^{-20}$, which is compatible with the goal set by the BIPM of comparing optical atomic clocks to the level of at least 10^{-18}.

Funding

Agence Nationale de la Recherche (Equipex REFIMEVE+ ANR-11-EQPX-0039, Labex First-TF ANR-10-LABX-48-01); *Domaine d'intérêt majeur* SIRTEQ ATH-2019 (ONSEPA). European Metrology Program for Innovation and Research (EMPIR) projects 15SIB05 OFTEN. This project has received funding from the EMPIR program co-financed by the Participating States and from the European Union's Horizon 2020 Research and Innovation Program. Laboratoire National d'Essai (LNE), projects LICORNE, SAMIROFF and TORTUE.

Authors contributions and responsibility

Software: MT, FS, P-EP; formal analysis: MT, FS, AA-K, P-EP; Data curation, Vizualisation; MT; Investigation: MT, FS, EC, OL, RLT, EC, AA-K, P-EP; Methodology, AA-K, P-EP; validation, project administration, funding acquisition: AA-K, P-EP; Writing: MT, AA-K, P-EP; Conceptualization, Supervision: P-EP.

Acknowledgments

The authors thank Christian Chardonnet for his major contribution to the steering and development of REFIMEVE. The authors thank Nicolas Quintin, Émilie Camisard, Laurent Gydé (RENATER) for the very fruitful collaboration, building the REFIMEVE metrological network. The authors are very grateful to Sebastian Koke, Alexander Kuhl, Thomas Waltherholter, Erik Benkler, Sebastian Raupach, Harald Schnatz and Gesine Grosche (PTB) who build and operate the fiber link Braunschweig-Strasbourg, and to Jérôme Lodewyck and co-workers operating the Sr clock at SYRTE, Rodolphe Le Targat and Héctor Álvarez-Martínez, operating the near-infrared source at SYRTE, Christian Lisdat, Uwe Sterr, Erik Benkler and Nils Huntemann and co-workers operating ultra-stable lasers, combs and optical clocks at PTB, and Nils Huntemann for sharing the processed uptime data of the clocks. Lastly, the authors thank Philip Tuckey for fruitful discussions. The clock comparison by December 2018 was partly funded by the European Metrology Program for Innovation and Research (EMPIR) Projects 15SIB03 OC18, 18SIB05 ROCIT, 18SIB06 TiFOON.

Appendix A. Mathematical formulation of noise processes in fiber links

A.1. Autocorrelation and Fourier analysis

The auto-correlation function is a useful tool for studying periodic behaviors of the time trace. The auto-correlation function of the phase can be calculated by

$$R_\phi(\tau) = \langle \phi(t)\phi(t-\tau)\rangle, \tag{A.1}$$

where $\langle\cdot\rangle$ denotes the expectation value over a given integration time, and τ the time lag.

The phase PSD can be calculated by the Fourier transform of the auto-correlation function of the phase using the Wiener–Khinchin theorem:

$$S_\phi(f) = 2\int_0^\infty R_\phi(\tau)\cos(2\pi f\tau)\mathrm{d}\tau. \tag{A.2}$$

The noise of a stabilized fiber link can generally be modeled by the power law:

$$S_\phi(f) = b_0 + b_{-1}f^{-1} + b_{-2}f^{-2} + \frac{1}{2}\sum_n A_n^2\delta(f-f_n), \tag{A.3}$$

consisting of a white phase noise term (b_0), a flicker phase noise term ($b_{-1}f^{-1}$), a white frequency noise term ($b_{-2}f^{-2}$), and any periodic perturbations ($\frac{1}{2}A_n^2\delta(f-f_n)$).

A.2. Frequency stability

The MDEV is usually preferred over the Allan deviation when assessing the frequency stability of fiber links, as it allows distinction between flicker phase noise and white phase noise. The MDEV can be calculated from the phase PSD using the relation

$$\mathrm{Mod}\,\sigma_y^2(\tau) = \int_{\mathrm{BW}} 2S_\phi(f)\left[\frac{\tau_0\sin^3(\pi f\tau)}{\pi\nu_0\tau^2\,\sin(\pi f\tau_0)}\right]^2\mathrm{d}f. \tag{A.4}$$

Using the phase PSD from equation (A.3) we get [66]:

$$\mathrm{Mod}\,\sigma_y^2(\tau) = \frac{0.0380}{\nu_0^2\tau^3}b_0 + \frac{0.0855}{\nu_0^2\tau^2}b_{-1} + \frac{1}{4\nu_0^2\tau}b_{-2} + \sum_n A_n^2\left[\frac{\tau_0\sin^3(\pi f_n\tau)}{\pi\nu_0\tau^2\,\sin(\pi f_n\tau_0)}\right]^2. \tag{A.5}$$

A.3. Coherence time

The coherence time, as introduced by equation (2), is a little more complicated when flicker phase noise is not negligible and/or when $b_{-2} = 0$, as equation (2) is not defined anymore. In that case, one can use

$$\tau_{\mathrm{coh}} = \frac{2b_0}{\pm b_{-1} + \sqrt{b_{-1}^2 + 4b_0b_{-2}}}, \tag{A.6}$$

where the '+' solution corresponds to the crossing between b_0 and $b_{-1}+b_{-2}$, and the '−' solution corresponds to the crossing between the b_0+b_{-1} and b_{-2}.

A.3.1. Translation of the coherence time in MDEV. The coherence time defined from the phase PSD by equation (2) can be translated to the corresponding integration time in MDEV. This is straightforward from equation (A.5):

$$\tau_{\mathrm{coh}}^\sigma = \sqrt{4\cdot 0.038\frac{b_0}{b_{-2}}} = 0.39\tau_{\mathrm{coh}}. \tag{A.7}$$

A.4. Frequency distribution and line-width

A simple approximation to model the optical spectrum of the link is the pseudo-Voigt profile. This is defined as a sum of a Gaussian profile, arising from inhomogeneous broadening (as for instance by external acoustic noise sources), and a Lorentzian profile, describing the homogeneous broadening from the fundamental white phase noise of the link.

$$V_p(\nu,\delta\nu) = wL(\nu,\delta\nu) + (1-w)G(\nu,\delta\nu), \tag{A.8}$$

where the profile is a function of the full width at half maximum (FWHM) $\delta\nu$, and the *weight* parameter w determining the weight of the Gaussian and Lorentzian functions. Writing these as a function of the FWHM they can respectively be written as

$$G(\nu,\delta\nu) = \frac{2\sqrt{\ln(2)}}{\sqrt{\pi}\delta\nu}\,\mathrm{e}^{-4\,\ln(2)(\frac{\nu}{\delta\nu})^2} \tag{A.9}$$

and

$$L(\nu,\delta\nu) = \frac{1}{2\pi}\frac{\delta\nu}{\nu^2+\frac{1}{4}\delta\nu^2}. \tag{A.10}$$

Here the profiles have been assumed to be centered around zero, which will be the case for an actively compensated fiber link.

Appendix B. Properties of the annihilation operator

B.1. Fourier spectrum of the annihilation operator

Assuming the annihilation operator to represent randomly distributed missing data with a density of h, it will have variance $\sigma^2 = h(1-h)$ and a frequency noise level

$$S(f) = \frac{\sigma^2}{f_{\mathrm{BW}}} = \frac{h(1-h)}{f_{\mathrm{BW}}}, \tag{B.1}$$

with f_{BW} being the measurement bandwidth.

B.2. Mean distance between missing data

For a data set consisting of N data points, we can write the probability of the mean distance between missing data, d, with the Gaussian distribution:

$$G(d,h) = \frac{1}{\sigma\sqrt{2\pi}}\,\mathrm{e}^{-\frac{1}{2}\frac{(d-\mu(h))^2}{\sigma^2(h)}}, \tag{B.2}$$

with mean and variance respectively:

$$\mu(h) = h^{-1} \tag{B.3}$$

$$\sigma^2(h) = \frac{1-h}{h^3 N}. \tag{B.4}$$

ORCID iDs

Mads Bebe Krog Tønnes https://orcid.org/0000-0002-3630-3121
Frédéric Schuller https://orcid.org/0000-0002-2609-1604
Etienne Cantin https://orcid.org/0000-0001-9362-0628
Olivier Lopez https://orcid.org/0000-0003-3171-2863
Rodolphe Le Targat https://orcid.org/0000-0002-8740-1709
Anne Amy-Klein https://orcid.org/0000-0002-5122-7868
Paul-Éric Pottie https://orcid.org/0000-0003-3677-2208

References

[1] Fritz R 2015 Towards a redefinition of the second based on optical atomic clocks *C. R. Phys.* **16** 506–15
[2] Working Group on Advanced Time and Frequency Transfer 2016 CCTF strategy document https://bipm.org/documents/20126/2071143/CCTF+Strategy.pdf/7cf0f648-2afe-d15c-0909-1f03406bbb8f (accessed 06 July 2022) p 43
[3] Reynaud S, Salomon C and Wolf P 2009 Testing general relativity with atomic clocks *Space Sci. Rev.* **148** 233–47
[4] Berceau P, Taylor M, Kahn J and Hollberg L 2016 Space-time reference with an optical link *Class. Quantum Grav.* **33** 135007
[5] Delva P *et al* 2017 Test of special relativity using a fiber network of optical clocks *Phys. Rev. Lett.* **118** 221102
[6] Takamoto M *et al* 2020 Test of general relativity by a pair of transportable optical lattice clocks *Nat. Photon.* **14** 411–5
[7] Roberts B M *et al* 2020 Search for transient variations of the fine structure constant and dark matter using fiber-linked optical atomic clocks *New J. Phys.* **22** 093010
[8] Bjerhammar A 1985 On a relativistic geodesy *Bull. Geod.* **59** 207–20
[9] Takano T *et al* 2016 Geopotential measurements with synchronously linked optical lattice clocks *Nat. Photon.* **10** 662–6
[10] Lisdat C *et al* 2016 A clock network for geodesy and fundamental science *Nat. Commun.* **7** 12443
[11] Grotti J *et al* 2018 Geodesy and metrology with a transportable optical clock *Nat. Phys.* **14** 437–41
[12] Schioppo M *et al* 2022 Comparing ultrastable lasers at 7×10^{-17} fractional frequency instability through a 2220 km optical fibre network *Nat. Commun.* **13** 212
[13] REFIMEVE 2022 Réseau Fibré Métrologique à Vocation Européenne https://refimeve.fr/index.php/en/
[14] Cantin E *et al* 2021 An accurate and robust metrological network for coherent optical frequency dissemination *New J. Phys.* **23** 053027
[15] Friebe J *et al* 2011 Remote frequency measurement of the $^1S_0$–$^3P_1$ transition in laser-cooled ^{24}Mg *New J. Phys.* **13** 125010
[16] Thomas T, Fleurbaey H, Galtier S, Julien L, Biraben F and Nez F 2019 High-resolution hydrogen spectroscopy and the proton radius puzzle *Ann. Phys., Lpz.* **531** 1800363
[17] Insero G *et al* 2017 Measuring molecular frequencies in the 1–10 μm range at 11-digits accuracy *Sci. Rep.* **7** 12780
[18] Santagata R *et al* 2019 High-precision methanol spectroscopy with a widely tunable SI-traceable frequency-comb-based mid-infrared QCL *Optica* **6** 411–23
[19] Votava O *et al* 2022 Comb coherence-transfer and cavity ring-down saturation spectroscopy around 1.65 μm: kHz-accurate frequencies of transitions in the $2\nu_3$ band of $^{12}CH_4$ *Phys. Chem. Chem. Phys.* **24** 4157–73
[20] Matveev A *et al* 2013 Precision measurement of the hydrogen ^1S–^2S frequency via a 920 km fiber link *Phys. Rev. Lett.* **110** 230801
[21] Clivati C *et al* 2020 Common-clock very long baseline interferometry using a coherent optical fiber link *Optica* **7** 1031
[22] Argence B *et al* 2015 Quantum cascade laser frequency stabilization at the sub-Hz level *Nat. Photon.* **9** 456–60
[23] Manamanni K *et al* 2022 Limitations due to residual interference in a fiber-based optical frequency reference at 1.55 μm *J. Opt. Soc. Am.* B **39** 438
[24] Uzan J-P 2011 Varying constants, gravitation and cosmology *Living Rev. Relativ.* **14** 2
[25] Morel L, Yao Z, Cladé P and Guellati-Khélifa S 2020 Determination of the fine-structure constant with an accuracy of 81 parts per trillion *Nature* **588** 61–5
[26] Patra S *et al* 2020 Proton-electron mass ratio from laser spectroscopy of HD+ at the part-per-trillion level *Science* **369** 1238–41
[27] Izumiyama S 2020 Development of timing synchronization system for hyper-kamiokande *J. Phys.: Conf. Ser.* **1468** 012159
[28] Baker C J *et al* 2021 Laser cooling of antihydrogen atoms *Nature* **592** 35–42
[29] Hackman C and Parker T E 1996 Noise analysis of unevenly spaced time series data *Metrologia* **33** 457–66
[30] Yu D-H, Weiss M and Parker T E 2007 Uncertainty of a frequency comparison with distributed dead time and measurement interval offset *Metrologia* **44** 91–6
[31] Sesia I and Tavella P 2008 Estimating the Allan variance in the presence of long periods of missing data and outliers *Metrologia* **45** S134–42

[32] Banville S *et al* 2010 Handling cycle slips in GPS data during ionospheric plasma bubble events *Radio Sci.* **45** 1–14

[33] Sesia I, Cantoni E, Cernigliaro A, Signorile G, Fantino G and Tavella P 2016 An efficient and configurable preprocessing algorithm to improve stability analysis *IEEE Trans. Ultrason. Ferroelectr. Freq. Control* **63** 575–81

[34] Leute J *et al* 2016 Frequency comparison of $^{171}Yb^{+}$ ion optical clocks at PTB and NPL via GPS PPP *IEEE Trans. Ultrason. Ferroelectr. Freq. Control* **63** 981–5

[35] Xu C 2016 Reconstruction of gappy GPS coordinate time series using empirical orthogonal functions *J. Geophys. Res. Solid Earth* **121** 9020–33

[36] Galleani L and Sesia I 2019 The corrected Allan variance: stability analysis of frequency measurements with missing data *IEEE Trans. Ultrason. Ferroelectr. Freq. Control* **66** 1667–83

[37] Riedel F *et al* 2020 Direct comparisons of European primary and secondary frequency standards via satellite techniques *Metrologia* **57** 045005

[38] Calosso C E, Clivati C and Micalizio S 2016 Avoiding aliasing in Allan variance: an application to fiber link data analysis *IEEE Trans. Ultrason. Ferroelectr. Freq. Control* **63** 646–55

[39] Galleani L 2014 Characterizing changes in the noise statistics of gnss space clocks with the dynamic Allan variance *22nd European Signal Processing Conference (EUSIPCO)* (Lisbon, Portugal 1–5 September 2014) pp 426–30

[40] Levy C, Pinchas M and Yosef P 2018 A new approach for the characterization of nonstationary oscillators using the Wigner–Ville distribution *Math. Probl. Eng.* **2018** 1–14

[41] Tønnes M *et al* 2021 Scientific data processing of a fiber network for optical frequency transfer: methods and studies *URSI Radio Science Letters* **3** 3

[42] Koke S *et al* 2019 Combining fiber Brillouin amplification with a repeater laser station for fiber-based optical frequency dissemination over 1400 km *New J. Phys.* **21** 123017

[43] Chiodo *et al* 2015 Cascaded optical fiber link using the internet network for remote clocks comparison *Opt. Express* **23** 33927–37

[44] Williams P A, Swann W C and Newbury N R 2008 High-stability transfer of an optical frequency over long fiber-optic links *J. Opt. Soc. Am.* B **25** 1284–93

[45] Kramers G and Klische W 2001 Multi-channel synchronous digital phase recorder *Int. Freq. Control Symp.* 35th Annual Frequency Control Symp. (IEEE) pp 144–51

[46] Rubiola E 2005 On the measurement of frequency and of its sample variance with high-resolution counters *Rev. Sci. Instrum.* **76** 054703

[47] Xu D, Lopez D, Amy-Klein A and Pottie P-E 2021 Non-reciprocity in optical fiber links: experimental evidence *Opt. Express* **29** 17476–90

[48] Cohen L G and Fleming J W 1979 Effect of temperature on transmission in lightguides *Bell Syst. Tech. J.* **58** 945–51

[49] Stefani F *et al* 2014 Tackling the limits of optical fiber links *J. Opt. Soc. Am.* B **32** 787–97

[50] Le Bail K 2006 Estimating the noise in space-geodetic positioning: the case of DORIS *J. Geod.* **80** 541–65

[51] Ji K H and Herring T A 2013 A method for detecting transient signals in GPS position time-series: smoothing and principal component analysis *Geophys. J. Int.* **193** 171–86

[52] Mallat S G 1989 A theory for multiresolution signal decomposition: the wavelet representation *IEEE Trans. Pattern Anal. Mach. Intell.* **11** 674–93

[53] Savalle E, Guerlin C, Delva P, Meynadier F, le Poncin-Lafitte C and Wolf P 2019 Gravitational redshift test with the future ACES mission *Class. Quantum Grav.* **36** 245004

[54] Dick G J 1987 Local oscillator induced instabilities in trapped ion frequency standards *Proceedings of the Nineteenth Annual Precise Time and Time Interval (PTTI) Applications and Planning Meeting* (Redondo Beach, CA 1–3 December 1987) p 16

[55] Lo Presti L, Rovera D and De Marchi A 1998 A simple analysis of the Dick effect in terms of phase noise spectral densities *IEEE Trans. Ultrason. Ferroelectr. Freq. Control* **45** 899–905

[56] Lemonde P *et al* 1998 The sensitivity function: a new tool for the evaluation of frequency shifts in atomic spectroscopy *Proc. 1998 IEEE Int. Frequency Control Symp. (Cat. No. 98CH36165)* pp 110–5

[57] Leute J 2018 Characterization and evaluation of GPS PPP techniques for optical clock comparisons *PhD Thesis* Gottfried Wilhelm Leibniz Universität Hannover

[58] Xu D *et al* 2019 Two-branch fiber link for international clock networks *IEEE Trans. Instrum. Meas.* **68** 1–6

[59] Howe D A 2002 Interpreting oscillatory frequency stability plots *Proc. 2002 IEEE Int. Frequency Control Symp. PDA Exhibition (Cat. No. 02CH37234)* pp 725–32

[60] Raupach S M F, Koczwara A and Grosche G 2015 Brillouin amplification supports 1 10–20 uncertainty in optical frequency transfer over 1400 km of underground fiber *Phys. Rev.* A **92** 021801

[61] Benkler E, Lisdat C and Sterr U 2015 On the relation between uncertainties of weighted frequency averages and the various types of Allan deviations *Metrologia* **52** 565–74

[62] Lee W-K, Yu D-H, Park C Y and Mun J 2010 The uncertainty associated with the weighted mean frequency of a phase-stabilized signal with white phase noise *Metrologia* **47** 24–32

[63] Lodewyck J *et al* 2016 Optical to microwave clock frequency ratios with a nearly continuous strontium optical lattice clock *Metrologia* **53** 1123–30

[64] Huntemann N *et al* 2016 Single-ion atomic clock with 3×10^{-18} systematic uncertainty *Phys. Rev. Lett.* **116** 063001

[65] Lodewyck J 2019 On a definition of the SI second with a set of optical clock transitions *Metrologia* **56** 055009

[66] Allan D W and Barnes J A 1981 A modified 'Allan variance' with increased oscillator characterization ability *35th Annual Frequency Control Symp.* (IEEE) pp 470–5

Appendix F

Article in Physical Review Applied

An article describing the results of the four months long comparison campaign between SYRTE and INRIM, the results of which is discussed in this thesis.

Coherent Optical-Fiber Link Across Italy and France

C. Clivati,[1] M. Pizzocaro,[1,*] E.K. Bertacco,[1] S. Condio,[1,†] G.A. Costanzo,[1,†] S. Donadello,[1] I. Goti,[1,†] M. Gozzelino,[1] F. Levi,[1] A. Mura,[1] M. Risaro,[1] D. Calonico,[1] M. Tønnes,[2] B. Pointard,[2] M. Mazouth-Laurol,[2] R. Le Targat,[2] M. Abgrall,[2] M. Lours,[2] H. Le Goff,[2] L. Lorini,[2] P.-E. Pottie,[2] E. Cantin,[3] O. Lopez,[3] C. Chardonnet,[3] and A. Amy-Klein[3]

[1] *Istituto Nazionale di Ricerca Metrologica (INRIM), Strada delle cacce 91, Torino 10135, Italy*

[2] *LNE-SYRTE, Observatoire de Paris—Université PSL, CNRS, Sorbonne Université Paris, France*

[3] *Laboratoire de Physique des Lasers (LPL), Université Sorbonne Paris Nord, CNRS, Villetaneuse, France*

(Received 21 June 2022; accepted 13 September 2022; published 3 November 2022)

The dissemination of atomic clocks with fiber-based techniques finds application in the fields of metrology, fundamental physics, navigation, and spectroscopy but is a challenge in terms of reliability, maintenance, and performance. Here, we describe the realization of a 1023-km-long fiber link between the metrological institutes of Italy and France that shares the infrastructure with the Internet traffic and exploits segmentation in shorter, cascaded spans to fight optical losses exceeding 280 dB. With four months of quasicontinuous operation of this link, we compared the Cs, Rb, and Yb atomic clocks at our laboratories, highlighting the potential of this tool to assess the clock uncertainty budgets, characterize advanced satellite techniques, and develop optical timescales. The integration of the metrological, fiber-based infrastructures in the two countries, connecting photonics and spectroscopy laboratories as well as telescope facilities, provides the research community with a physical layer over which applications can be built on.

DOI: 10.1103/PhysRevApplied.18.054009

I. INTRODUCTION

Precision spectroscopy of atoms or ions is an important resource for timekeeping, navigation, and fundamental science. The second, unit of time in the International System, is defined upon the ground-state hyperfine transition of the ^{133}Cs atom, and its best realizations achieve an uncertainty in the low 10^{-16} [1–11]. For a few years now, atomic clocks based on optical transitions of neutral atoms or ions demonstrated an even lower uncertainty in the 10^{-18} range [12–15]. The comparison of different atomic clocks led to the recommendation of secondary representations of the second, in view of a future redefinition on a single or a set of optical transitions [16–18]. Before this redefinition becomes possible, independent interlaboratory comparisons of optical clocks both against other optical and primary clocks must be demonstrated. Interspecies atomic clock comparisons, particularly those involving microwave and optical transitions, are also at the heart of physics measurements that constrain the possible variations of fundamental constants [19,20].

In this frame, a network comprising clocks developed by different teams at different institutions leverages the scientific opportunities beyond those of the single laboratory [21,22], but until recently, the instability of satellite-based time-and-frequency transfer techniques was a significant limitation. For instance, the Bureau International des Poids et Mesures (BIPM) maintains the coordinated universal time (UTC), which is the current standard for global timekeeping, from data including both primary and secondary frequency standards and satellite comparisons [23]. Atomic clocks contributing to UTC are routinely compared using the data that appear in the BIPM Circular T bulletin. However, only a few bilateral fountain [24] and optical clock [25–29] comparisons have been performed. The coherent transfer of optical signals across phase-stabilized fibers [30–37], now covering distances of up to thousands of kilometers, represented a breakthrough in this respect, enabling clock comparisons where the space separation no longer contributes to the final uncertainty [5,12,32,38–40].

In this work, we present the permanent 1023-km phase-stabilized fiber link that connects the French and Italian National Metrology Institutes LNE-SYRTE in Paris and INRIM in Torino. We report on the comparisons between three species of atomic clocks among those available at the

*m.pizzocaro@inrim.it

†Also with Politecnico di Torino, corso Duca degli Abruzzi 24, 10124 Torino, Italy.

two institutes, namely two Cs fountain clocks [8,10], a Rb fountain clock [9,10], and an optical Yb lattice clock [41]. Our clock comparison covered four months, demonstrating the degree of maturity achieved by long-haul optical-fiber links in terms of maintenance and uptime. This link is among the few examples of thousand-kilometer-scale optical connections [32–35] and is intended as a tool for scientific tasks that require the regular and long-term comparison of atomic clocks, among which are the periodical assessment of frequency standards, the validation of advanced satellite techniques [28,42,43], the generation of optical timescales [44–48], and tests of relativity [22].

This paper is organized as follows. Section II presents the description of the optical link and its characterization. Section III discusses the result of the clock comparison between the two Cs fountain clocks, the Rb fountain clock, and the optical Yb lattice clock. A conclusion is given in Sec. IV.

II. THE OPTICAL LINK

A. Setup description

The present link connects the Italian Quantum Backbone (IQB) [34] and the French National Research Infrastructure REFIMEVE [49,50], both of which provide frequency references to scientific users in the two countries, serving high-precision atomic and molecular spectroscopy, quantum physics and photonics laboratories [51–54], radio telescopes [25,55], and the national space agencies campuses [34]. Time and rf-frequency transfer to companies and satellite navigation facilities is also being developed, using the White Rabbit technique [56,57]. In addition, via the REFIMEVE network, cross-border connections to the National Metrology Institutes of Germany (PTB) and UK (NPL) are possible [35]. A sketch of the Paris to Torino network is shown in Fig. 1(a). It is composed of a 1023-km cascaded link, in which the optical length of the fibers is actively stabilized using the Doppler noise cancelation technique [58]. An ultrastable radiation at 1542.14 nm is generated at SYRTE by frequency locking a diode laser to a high-finesse optical cavity. Its frequency is constantly measured and steered to a local H maser by an optical frequency comb, thus providing a connection to the local frequency standards. This optical signal is distributed via a stabilized fiber to INRIM, where it is frequency measured against the local H maser using another optical comb.

The link is established using installed telecom fibers provided by the French academic network RENATER and the regional network AMPLIVIA on the French side, and by Consortium TOPIX on the Italian side. These fibers implement dense- and coarse-wavelength-division multiplexing, where channel 44 of the International Telecommunication Union grid, corresponding to a central wavelength of 1542.14 nm, is reserved for frequency dissemination, and the others are used for data traffic. The coherent radiation is periodically extracted from the shared fiber to bypass the standard network equipment that does not sustain the bidirectional operation required for the Doppler noise cancelation, and then injected back. The link is split into six segments with intermediate terminals located in Paris (datacenter TH2), Lyon, Grenoble, Modane, and Frejus tunnel (across the Alps on the Italy-France border) and lengths of 11, 597, 118, 143, 7, and 147 km respectively. Each terminal hosts a repeater laser station (RLS) or a multibranch laser station (MLS), where the metrological signal is regenerated by phase locking a diode laser to the incoming radiation, and phase stabilization of the subsequent segments is performed. MLSs implement star connections that allow the simultaneous stabilization of links to multiple terminals [59]. RLSs and MLSs are engineered in such a way that the transmitted signal is independent of the local rf oscillator, relaxing the need for an accurate and stable rf reference. In addition, 11 bidirectional erbium-doped fiber amplifiers are utilized to partly recover from the signal attenuation on more lossy segments. The segmentation approach, described in detail in Refs. [30,34,37,49,59], is necessary to support the link operation, as the overall one-way power loss exceeding 280 dB could not be compensated using fiber amplifiers only. It also improves the link phase noise suppression by reducing the radiation round-trip delay as compared to a nonsegmented link. The amplifiers and intermediate terminals are operated remotely.

B. Characterization

The noise affecting the distributed frequency signal results from a partially unsuppressed fiber noise, whose cancelation is limited by the link delay that reduces the control bandwidth [58], as well as temporary loss of coherence due to failures of the stabilization electronics (cycle slips), and other uncontrolled effects causing long-term instability or a potential deviation from the nominal frequency. While the instability due to the delay-unsuppressed noise averages down as the inverse of the measurement time, the other effects result in significant frequency bias if affected points are included in the measurement. Synchronously to the link operation it is hence important to validate its performances, detect and remove invalid points. To this end, we established independent phase-stabilized links using the second fiber of the pair, which is always provided by the network operators. By phase comparing the disseminated light on a suitable combination of the two links, it is possible to derive an upper limit for the frequency dissemination uncertainty contributed by each one. In detail, we adopted the scheme shown in Fig. 1(b) to separately characterize the segments SYRTE-TH2, TH2-Modane, and Modane-INRIM.

The SYRTE-Modane link is built by delivering the ultrastable radiation from SYRTE to TH2, where a MLS

FIG. 1. Geographical layout of the infrastructure, with the link between SYRTE, Paris (France) and INRIM, Torino (Italy) characterized in this work highlighted as a thick line. The map also shows the other branches of the REFIMEVE network in blue and the Italian Quantum Backbone (IQB) in red. Cross-border connections of this infrastructure to the National Metrology Institutes NPL in the UK and PTB in Germany are indicated in orange and green. Repeater laser stations (RLS or MLS) and link terminals are represented with open circles. (b) The scheme used for the link characterization: blue paths indicate phase-stabilized links on the two fibers. At SYRTE, local reference light is sent to a photodiode together with the light disseminated through the loop SYRTE-TH2-SYRTE and phase compared to a local rf reference, to evaluate the overall uncertainty of the SYRTE-TH2-SYRTE link (similarly for the path to Modane). The green arrow represents a free-running link whose noise is removed offline. This is detected by heterodyning local radiation at INRIM with light traveling the path INRIM-Modane-INRIM (orange line). The Modane-INRIM link is evaluated by comparing light disseminated through the two fibers.

distributes it further to Modane through cascaded RLSs located in Lyon and Grenoble. A part of the regenerated signal in TH2 is instead sent back to SYRTE using the second fiber of the pair, independently stabilized in the MLS, and here compared to the reference input light (actively stabilized paths are indicated by blue arrows in the figure). This provides a measurement of the frequency distributed along the whole SYRTE-TH2-SYRTE loop, and allows deriving an upper limit to the SYRTE-TH2 dissemination uncertainty. Similarly, from TH2, the regenerated light is sent to Modane via phase-stabilized fiber segments also including intermediate RLSs in Lyon and Grenoble. In Modane, the radiation is regenerated, partly sent back to TH2 using the second fiber, and there compared to the

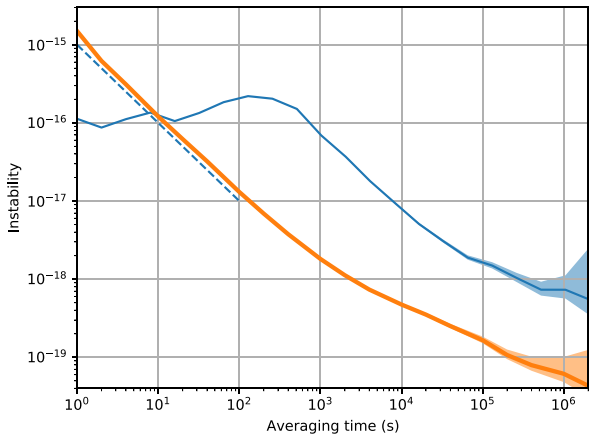

FIG. 2. Measured and expected instability of the link: the orange continuous line corresponds to the end-to-end link instability of the SYRTE-Modane-SYRTE link; the blue solid line shows the measured instability of the INRIM-Modane segment, dominated by that of the validation link (see the text); these instabilities are calculated from four months of data as overlapping Allan deviation and shaded regions denote the uncertainty; the blue dashed line represents the expected instability of the Modane-INRIM link from delay-unsuppressed noise.

reference light to characterize the TH2-Modane segment. The resulting end-to-end instabilities of the SYRTE-TH2-SYRTE and TH2-Modane-TH2 links are quadratically summed to derive the overall instability of the SYRTE-Modane-SYRTE link, as shown in Fig. 2 (orange line). In the short term, it is limited by the delay-unsuppressed noise of the forward and return links. Short optical paths whose length cannot be fully stabilized, mainly contained in the TH2 multibranch station [59], contribute an additional instability that emerges at averaging times of a few thousand seconds and is at the level of 1×10^{-19}. No deviation from the nominal frequency is observed at this level, and we assume this value as the ultimate uncertainty contribution for the SYRTE-Modane segment.

The characterization of the Modane-INRIM segment follows a different scheme, as it is not possible to install any counting equipment in Modane. In Modane, the local regenerated light is split into two parallel links to INRIM, one of them being actively noise canceled to disseminate the signal to INRIM, the second one being used for the uncertainty and instability assessment. The first exploits two RLSs in Modane and the Frejus tunnel [actively stabilized paths are indicated by blue arrows in Fig. 1(b)]. At INRIM the incoming radiation is regenerated and distributed locally. The noise of the second link [green arrow in Fig. 1(b)] is instead continuously recorded and removed offline [60,61]. This is achieved by sending local ultrastable radiation from INRIM to Modane and back, comparing it with the reference light at INRIM [orange arrow in Fig. 1(b)]. The residual noise of the Modane-INRIM segment is then computed by comparing the light distributed through the two independent links.

The instability of the processed signal is shown in Fig. 2 (blue line). Unlike the end-to-end characterization, this scheme partly rejects the delay-unsuppressed noise because the two links are established between the same starting and ending points and because the two fibers are housed in the same cable, so their noise is mostly correlated [62,63]. The short-term instability is thus lower than the instability expected for this link from delay-unsuppressed noise (dashed line in Fig. 2) [64]. For integration times longer than 10 s, the measured instability is higher than the SYRTE-Modane segment and the delay-unsuppressed noise contribution for this span. This is due to about 3 m of uncompensated fibers exposed to temperature variations in Modane, which could not be avoided due to space constraints at this terminal. This contribution will be reduced in the future by modifying the interferometer design inside the RLS in Modane. Uncompensated fibers are present only on the link used for validation and not on the one used for the actual dissemination: we thus expect the dissemination link to exhibit a lower instability, comparable to that observed on the SYRTE-Modane span. Overall, this configuration enables us to spot long-term effects, frequency bias, and cycle slips both in the optical phase-locked loops and in the noise-cancelation loops. Even considering the reported results as an upper limit to the dissemination on the Modane-INRIM segment, the instability reaches 6×10^{-19} and no deviation from the nominal frequency is observed at this level. We assume this value as the ultimate uncertainty for this link. The uncertainty of the optical link between SYRTE and INRIM is thus $< 1 \times 10^{-18}$, which is suitable for the comparison of state-of-the-art optical clocks.

This setup has been operated almost continuously for four months. To ensure a high level of uptime and autonomous operation, all terminals are equipped with automated control of the polarization of incoming radiation, relock algorithms to recover from failures, and operator alert systems. Figure 3 shows the link uptime as a function of the modified Julian date (MJD), calculated daily, over the period from MJD 59514 (October 27, 2021) to MJD 59634 (February 24, 2022). The figure shows the uptime of each stage, including the transfer laser frequency measurements at the two combs and local distribution links between laboratories at SYRTE and INRIM. Downtimes are mostly due to unlocks caused by nonstationary events on the long deployed fiber, such as fast polarization changes or human interventions along the link, or temporary interruptions of end-to-end measurements. The combined uptime of the full chain, shown in the lowermost panel, is 57% on average over the full period, including winter holidays, and reaches 72% on the month between MJD 59583 and 59614 (January

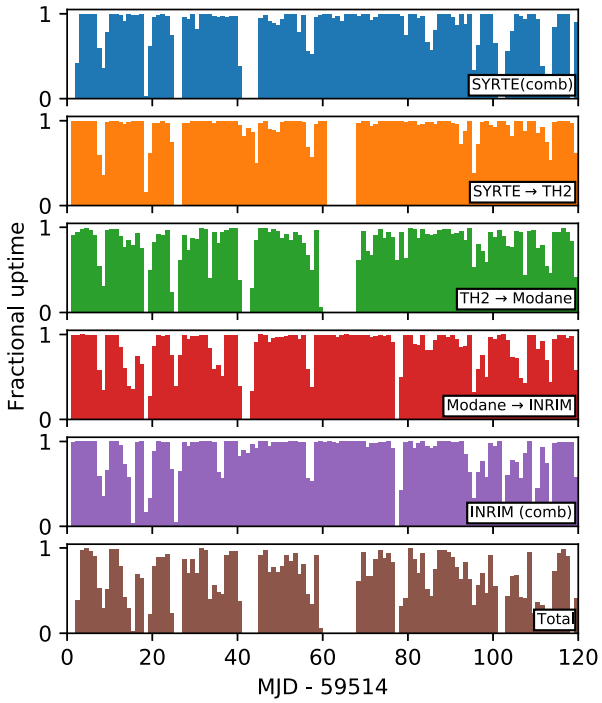

FIG. 3. The daily uptime of individual segments and the combined uptime of the whole link over the four months from October 27, 2021 to February 24, 2022.

4 to February 4, 2022), highlighting the remarkable level of reliability achieved for this infrastructure, also thanks to the automated supervision of the fiber network and terminals.

III. CLOCK COMPARISONS

A. Cs and Rb fountain clocks

As an application, we performed a comparison of the microwave fountain clocks SYRTE FO2 and INRIM IT-CsF2. SYRTE FO2 is a dual fountain that operates with Cs and Rb atoms simultaneously [9,10]. The two parts of FO2, named FO2-Cs and FO2-Rb, are independent frequency standards: FO2-Cs is a primary frequency standard and FO2-Rb, based on the hyperfine transition of ^{87}Rb, is a secondary representation of the second [18,65]. The systematic uncertainty of these two fountains is between 2×10^{-16} and 3×10^{-16}. Their local oscillator is a cryogenic sapphire oscillator, phase locked to a H maser: it grants a stability of $3.2\times10^{-14}/\sqrt{\tau/\mathrm{s}}$ for FO2-Cs and $2.9\times10^{-14}/\sqrt{\tau/\mathrm{s}}$ for FO2-Rb, τ being the measurement time, in full density mode. The density shift is evaluated in real time by alternating full and half density modes: with this measurement protocol, most of the uncertainty due to zero-density extrapolation averages down as $\sqrt{\tau}$ and contributes to the statistical uncertainty [66]. After density correction, systematic uncertainty becomes dominant after 3–4 d.

IT-CsF2 is the Italian primary frequency standard [8]. It is a cryogenic Cs fountain clock with a 2×10^{-16} stated uncertainty. The local oscillator for this clock is a BVA quartz phase locked to a H maser, contributing a short-term instability of $2\times10^{-13}/\sqrt{\tau/\mathrm{s}}$.

Typically, a measurement time of one month is necessary to reduce the statistical uncertainty of IT-CsF2 below the level of systematic. Here we extended the comparison to four months, since all the blocks of the measurement chain can be operated with only minor human intervention. The data processing was performed in two steps. In the first step, following the procedure explained in Ref. [67], the frequency ratio between the two remote H masers was obtained by combining the transfer oscillator frequency measurements on the two remote combs with the link data, excluding points where any of the measurements showed anomalous values or cycle slips. To this end, acquisitions at the counting terminals (SYRTE, TH2, and INRIM) were synchronized to better than 1 s. The synchronization signal was based on local realizations of UTC [UTC(IT) and UTC(OP) at INRIM and SYRTE], while in TH2 it was delivered via a White Rabbit link [56]. In the second step, validated data were averaged in bins with nominal duration of 864 s. Only bins with more than 50% valid data were considered. Fountain data, representing measurements of the H masers with the local microwave clocks, were sampled to the same 864-s grid and combined with the former. Data were processed as fractional frequency ratios $y = r/r_0 - 1$, where r is the physical frequency ratio (or absolute frequency) and r_0 is an arbitrary reference ratio (or reference absolute frequency). This is a common technique to avoid computational problems with numbers with many digits and to linearize equations [67].

Figure 4(a) shows the fractional frequency deviations of FO2-Cs/IT-CsF2 and FO2-Rb/IT-CsF2 obtained via the link, as well as the local measurement FO2-Rb/FO2-Cs at SYRTE, averaged over 864 s. For Rb, we chose the reference frequency to be consistent with the secondary representation of the second for the Rb transition of 6 834 682 610.904 312 6 Hz, which has an uncertainty of 3.4×10^{-16}, as established by the Consultative Committee for Time and Frequency, CCTF, in 2021 [65]. Figure 4(b) shows in full-color symbols the same data averaged in the periods corresponding to the Circular T bulletins n. 407 to n. 410 (from November 2021 to February 2022) [68]. The averages are for 30, 35, 30, and 25 d respectively. The shaded areas represent the $\pm1\sigma$ confidence region for the average fractional frequency ratios over the entire campaign. Open symbols represent the remote comparisons FO2-Cs/IT-CsF2 and FO2-Rb/IT-CsF2 obtained from data that appeared in the Circular T bulletins, which are consistent but have a larger uncertainty coming from the satellite comparison as calculated by the BIPM. All uncertainties

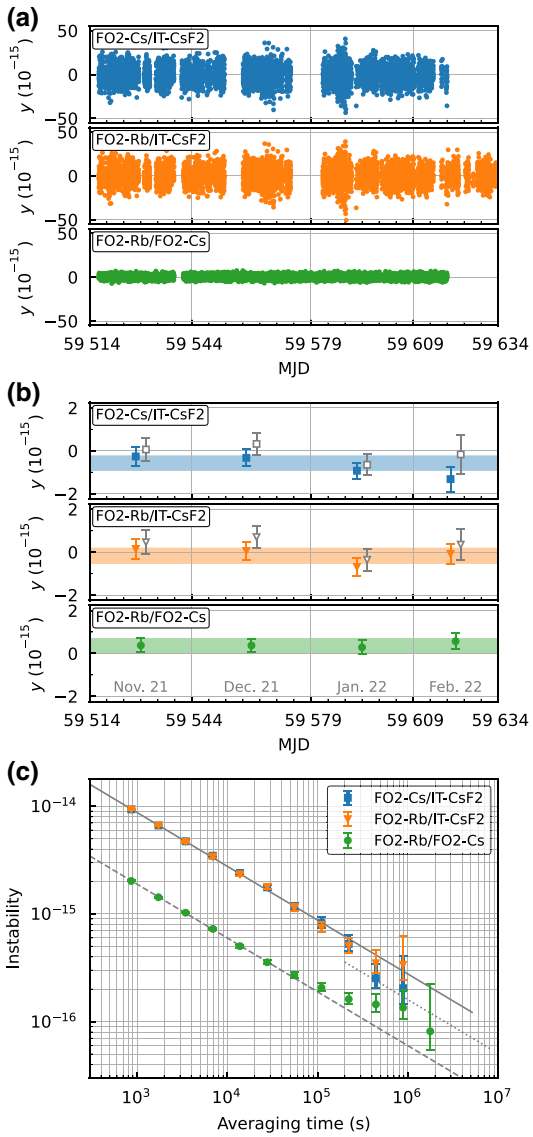

FIG. 4. (a) The fractional frequency ratios FO2-Cs/IT-CsF2, FO2-Rb/IT-CsF2 obtained via the link, as well as the local FO2-Rb/FO2-Cs at SYRTE as a function of the modified Julian date (MJD); each point represents an average over 864 s. (b) Colored points represent the average of the remote and local ratios in the periods of four Circular T bulletins (30, 35, 30, and 25 d, respectively); the colored shaded regions represent the averages over the entire campaign; open gray points show the remote ratios as deduced from data in the Circular T bulletins. All uncertainties correspond to $\pm 1\sigma$ and include the systematic uncertainty of the fountains. (c) Corresponding instabilities of the three ratios as overlapping Allan deviations; the solid gray line represents the white noise contribution of IT-CsF2 (2.8×10^{-13} at 1 s); the dashed gray line represents the short term combined white noise contribution of FO2-Rb/FO2-Cs (6×10^{-14} at 1 s). For FO2-Rb and FO2-Cs, the contribution due to zero-density extrapolation shows up in the Allan deviation for averaging times longer than the period used to calculate the density shift (gray dotted line) and is expected to be $1.6 \times 10^{-13}/\sqrt{\tau/\mathrm{s}}$ from historical data.

include the systematic uncertainties of the fountains. The instabilities of the fiber comparisons are shown in Fig. 4(c) as overlapping Allan deviations. The remote comparison is limited by the instability of IT-CsF2 ($2.3 \times 10^{-13}/\sqrt{\tau/\mathrm{s}}$). The instability of the local comparison at SYRTE is $6 \times 10^{-14}/\sqrt{\tau/\mathrm{s}}$ in the short term. For averaging times $\tau >$ 1 d, the instability is expected to be $1.6 \times 10^{-13}/\sqrt{\tau/\mathrm{s}}$ because of the protocol used to extrapolate data at zero density, as calculated from historical data (ten-years-long dataset). The comparison results are summarized in Table I. The average frequency deviation between FO2-Cs and IT-CsF2 is $y(\text{FO2-Cs/IT-CsF2}) = -5.5(3.7) \times 10^{-16}$. Here the statistical uncertainty is 1.3×10^{-16} with 56.1 d of measurement time derived from the instabilities shown in Fig. 4(c). The result for FO2-Rb/IT-CsF2 is $y(\text{FO2-Rb/IT-CsF2}) = -1.5(3.8) \times 10^{-16}$ where the statistical uncertainty is 1.3×10^{-16} with 60.1 d of measurement time. This corresponds to an absolute frequency of Rb of 6 834 682 610.904 311 4(26) Hz. In these comparisons, the uncertainty of the link contributes negligibly with an uncertainty lower than 6×10^{-19}. The local comparison at SYRTE FO2-Rb/FO2-Cs in the same period results in an average of $y(\text{FO2-Rb/FO2-Cs}) = 3.7(3.5) \times 10^{-16}$, which corresponds to an absolute frequency of Rb of 6 834 682 610.904 315 1(24) Hz. The interlaboratory comparison confirms and validates the stated uncertainties of the clocks.

B. Measurements with IT-Yb1

During the campaign, INRIM operated the optical clock IT-Yb1 [41,69] for 7 d from MJD 59563 to 59570 (December 15–21, 2021). IT-Yb1 is a neutral-Yb lattice clock with instability of $2 \times 10^{-15}/\sqrt{\tau/\mathrm{s}}$ and uncertainty 2.1×10^{-17}. For this measurement, the 1156.84-nm ultrastable laser, subharmonic of the 578.42-nm clock-transition wavelength, was sent to the optical comb at INRIM and compared to the 1542.14-nm laser signal received from the fiber link, using the comb as a transfer oscillator [70]. The comb contribution to the measurement uncertainty was brought to $<1\times10^{-18}$ by operating in a single branch configuration, where both the 1156- and 1542.14-nm laser beams were compared to the same, broadband comb output spanning the full 1- to 2-μm spectrum. The analysis followed the same procedure as in Sec. III A. Figure 5 shows the measured instability for the two remote ratios IT-Yb1/FO2-Cs and IT-Yb1/FO2-Rb and the local ratio IT-Yb1/IT-CsF2. The instabilities are dominated by the contribution of the fountains: $4 \times 10^{-14}/\sqrt{\tau/\mathrm{s}}$ for FO2-Cs and FO2-Rb and $3.2 \times 10^{-13}/\sqrt{\tau/\mathrm{s}}$ for IT-CsF2. For this measurement, the instability of IT-CsF2 was slightly higher than for the entire campaign.

For this analysis, we take as reference the secondary representation of the second for the Yb transition of 518 295 836 590 863.63 Hz, which has an uncertainty

TABLE I. Summary of the remote and local comparisons between INRIM and SYRTE. Here y is the fractional frequency deviation of the ratio (for Rb and Yb relative to the CCTF 2021 recommendations;); u is the total combined uncertainty; u_A is the statistical uncertainty of the measurement, derived from the measured instability and including the contribution from density shift uncertainty for FO2-Cs and FO2-Rb; and u_{B1} and u_{B2} are the systematic uncertainties of each standard. The last column reports the total measurement time.

	y ($\times 10^{-16}$)	u ($\times 10^{-16}$)	u_A ($\times 10^{-16}$)	u_{B1} ($\times 10^{-16}$)	u_{B2} ($\times 10^{-16}$)	Meas. time (d)
Remote comparisons						
FO2-Cs/IT-CsF2	−5.5	3.7	1.3	2.1	2.4	56.1
FO2-Rb/IT-CsF2	−1.5	3.8	1.3	2.5	2.4	60.1
IT-Yb1/FO2-Cs	−0.4	3.0	2.1	0.2	2.1	3.9
IT-Yb1/FO2-Rb	−4.2	3.2	1.9	0.2	2.5	4.0
Local comparisons						
FO2-Rb/FO2-Cs	3.7	3.5	0.6	2.5	2.1	99.7
IT-Yb1/IT-CsF2	−4.9	5.9	5.3	0.2	2.4	4.3

of 1.9×10^{-16}, as established by CCTF in 2021. The result for the comparison between IT-Yb1 and FO2-Cs is y(IT-Yb1/FO2-Cs) $= -0.4(3.0)\times10^{-16}$ with a statistical uncertainty of 2.1×10^{-16} for a total measurement time of 95 h, including the contribution from the zero-density extrapolation of FO2-Cs. Accordingly, the absolute frequency of Yb is 518 295 836 590 863.61(17) Hz. The result for IT-Yb1/FO2-Rb is y(IT-Yb1/FO2-Rb) $= -4.2(3.2)\times10^{-16}$ with a statistical uncertainty of 1.9×10^{-16} for a total measurement time of 95 h, including the contribution from the density extrapolation of FO2-Rb. The corresponding ratio between Yb and Rb frequencies is 75 833 197.545 114 168(24). The local comparison at INRIM between IT-Yb1 and IT-CsF2 in the same period results in an average of y(IT-Yb1/IT-CsF2) $= -4.9(5.9)\times10^{-16}$, corresponding to an absolute frequency of Yb of 518 295 836 590 863.38(31) Hz. The results are summarized in Table I. It should be noted that these measurements, as well as the measurements between fountains, are calculated only on the common uptime. Alternatively, it would be possible to extrapolate over dead time by using the H masers as flywheels [41,71,72] increasing the measurement time at the expense of an extra contribution of uncertainty. Our measurements are in good agreement with the recommendations of secondary representations of the second and previous measurements of the absolute frequency of Yb and Rb [9,41,69,73] and their ratios [74,75].

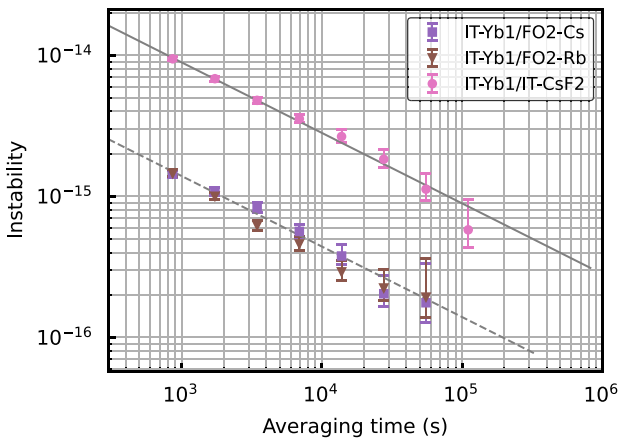

FIG. 5. Instabilities of the ratios between IT-Yb1 and FO2-Cs, FO2-Rb and IT-CsF2 as overlapping Allan deviation. The solid gray line represents the white noise contribution of IT-CsF2 (3.2×10^{-13} at 1 s for this shorter measurement); the dashed gray line represents the short-term instability of FO2-Rb and FO2-Cs (4.3×10^{-14} at 1 s).

IV. CONCLUSIONS AND PERSPECTIVES

We describe the operation and long-term characterization of the optical link between INRIM in Italy and SYRTE in France, which also represents a cross-border connection between the national facilities REFIMEVE and Italian Quantum Backbone. The present connection showed robust operation over the past four months and has been used to compare the Cs and Rb microwave frequency standards at the two Institutes, confirming their uncertainties at the 10^{-16} level. It allowed independent evaluations of the IT-Yb1/FO2-Cs and IT-Yb1/FO2-Rb ratios with uncertainties at the 3×10^{-16} level, limited by the microwave clocks. These measurements contribute to the milestones towards the redefinition of the second. Notably, the direct measurement of the Yb/Rb ratio performed in this work is consistent with the CCTF recommendation and improves the preceding measurement performed using data in the Circular T [74,75]. The link is planned to continue in the next years, with periodical comparison campaigns also involving other optical clocks at the two institutes, i.e., a Hg and Sr neutral lattice clocks at SYRTE [76,77], as well as a neutral lattice Sr clock under development at INRIM [78,79].

The interconnection between the infrastructures REFIMEVE and Italian Quantum Backbone demonstrates the integrability of national networks for frequency distribution at a European scale. Together with two other fiber links to NPL (UK) and PTB (Germany) [35], it opens the possibility of more composite clock comparison campaigns, including optical clocks based on different atomic species, neutral atoms, and ions, from four national metrology institutes. The richness of this network is an important resource for metrology and could support the computation of more accurate regional and global geodetic models [80–83] by providing centimeter-level precision estimates of the gravitational potential using optical clocks as probes [14,39,84], and the search for variations in fundamental constants and dark matter [21,22]. A prominent feature of this infrastructure is the optical continuity of the radiation between the two remote metrological institutes, which can be further exploited to investigate combined interrogation schemes of remote clocks [35] and support other research fields, such as long-distance quantum communication [85] and frequency distribution to telescope facilities [34]. The Italian Quantum Backbone reaches the Medicina radio telescope, which is part of the International Very Long Baseline Interferometry Network, the Matera Space Geodesy Centre and Satellite Laser Ranging facility, and the ground-based control station of Galileo, the European Global Navigation Satellite System. Beyond reaching the Laboratoire Souterrain de Modane in Modane, REFIMEVE is planned to connect the French Space Agency quarters in Toulouse, the lunar ranging and geodetic station of Observatoire de la Côte d'Azur, and the radiotelescopes of Observatoire de Paris-Nançay and Institut de Radioastronomie Millimétrique in the French Alps. The interconnection of such large facilities between them and to European Metrological Institutes is relevant to support Galileo itself and future European satellite missions such as ACES, and in perspective could stimulate a more extended exploitation of high-accuracy time-and-frequency references in geodesy, radio astronomy, and navigation.

ACKNOWLEDGMENTS

We acknowledge unfailing and continuing support from the network and engineering team of RENATER, and especially N. Quintin, X. Misseri, L. Gydé, and E. Camisard. We are grateful to Région Auvergne-Rhone-Alpes, Amplivia, Université Grenoble-Alpes (UGA) and Laboratoire Souterrain de Modane (LSM, UMR 6417 CNRS and UGA) and especially to O. Charrier (AMPLIVIA), R. Dorge, G. Enderlé (UGA), T. Zampieri (LSM), and J. Bernier (CNRS/IN2P3) for their great help in establishing the link Grenoble-Modane. We also thank Consortium TOPIX, especially M. Frittelli and A. Galardini, for access to the fibers on the Italian side. The Yb clock group is grateful to G. Cappellini, M. Takamoto, and H. Katori for assistance with the atomic source and to T. Legero for assistance with the optical cavity. The operation of the Yb clock is enabled by their help.

This work is supported by: the European Metrology Program for Innovation and Research (EMPIR) Projects 18SIB05 ROCIT, 18SIB06 TIFOON, 20FUN08 Next-Lasers, which received funding from the EMPIR programme cofinanced by the Participating States and from the European Union's Horizon 2020 research and innovation programme; the European Union's Horizon 2020 research and innovation programme under Grant Agreement No. 951886 (CLONETS-DS); Program "Investissements d'Avenir" launched by the French Government and implemented by Agence Nationale de la Recherche with references ANR-10-LABX-48-01 (Labex First-TF), ANR-21-ESRE-0029 (ESR/Equipex T-REFIMEVE), ANR-11-EQPX-0039 (Equipex REFIMEVE+), ANR-10-IDEX-0001-002 (Idex PSL); Conseil Régional Bourgogne-Franche-Comté; Domaine d'Intérêt Majeur Science et Ingénierie en Région Île-de-France pour les Technologies Quantiques (DIM SIRTEQ).

A.A.K., D.C., C.Ch., P.-E.P. coordinated the realization of the optical links in Italy and France, their interconnection, and coordinated this project. C.Cl., A.A.K., D.C., E.C., O.L., and P.-E.P. conceived and elaborated the architecture of the link. S.D., M.R., A.M., C.Cl. realized, characterized, and operated the optical-fiber link on the Italian side. M.R., M.P., and C.Cl. operated the INRIM comb and related frequency measurements. I.G., S.C., M.P. realized, characterized, and operated the Yb clock IT-Yb1. M.G., G.A.C., F.L. realized, characterized, and operated the Italian Cs fountain clock IT-CsF2. E.K.B. designed and realized the electronics used to operate the INRIM link and atomic clocks. E.C., O.L., M.T., M.M.L., and P.-E.P. realized, characterized, and operated the optical-fiber link on the French side. B.P. and R.L.T. operated the SYRTE comb and related frequency measurements. M.A. and L.L. realized, characterized, and operated the French Cs and Rb fountains and the oscillators required for their operation. M.L. and H.L.G. contributed to the operation and maintenance of the French Cs and Rb fountains during the comparison campaign. M.P. and C.Cl. analyzed the data produced and processed by the teams and wrote the paper, with relevant input and discussions with all the authors.

[1] A. Takamizawa, S. Yanagimachi, and K. Hagimoto, First uncertainty evaluation of the cesium fountain primary frequency standard NMIJ-F2, Metrologia **59**, 035004 (2022).

[2] S. Beattie, B. Jian, J. Alcock, M. Gertsvolf, R. Hendricks, K. Szymaniec, and K. Gibble, First accuracy evaluation of the NRC-FCs2 primary frequency standard, Metrologia **57**, 035010 (2020).

[3] S. Weyers, V. Gerginov, M. Kazda, J. Rahm, B. Lipphardt, G. Dobrev, and K. Gibble, Advances in the accuracy, stability, and reliability of the PTB primary fountain clocks, Metrologia **55**, 789 (2018).

[4] A. Jallageas, L. Devenoges, M. Petersen, J. Morel, L. G. Bernier, D. Schenker, P. Thomann, and T. Südmeyer, First uncertainty evaluation of the FoCS-2 primary frequency standard, Metrologia **55**, 366 (2018).

[5] J. Guéna, *et al.*, First international comparison of fountain primary frequency standards via a long distance optical fiber link, Metrologia **54**, 348 (2017).

[6] I. Y. Blinov, A. I. Boiko, Y. S. Domnin, V. P. Kostromin, O. V. Kupalova, and D. S. Kupalov, Budget of uncertainties in the cesium frequency frame of fountain type, Meas. Tech. **60**, 30 (2017).

[7] F. Fang, M. Li, P. Lin, W. Chen, N. Liu, Y. Lin, P. Wang, K. Liu, R. Suo, and T. Li, NIM5 Cs fountain clock and its evaluation, Metrologia **52**, 454 (2015).

[8] F. Levi, D. Calonico, C. E. Calosso, A. Godone, S. Micalizio, and G. A. Costanzo, Accuracy evaluation of ITCsF2: A nitrogen cooled caesium fountain, Metrologia **51**, 270 (2014).

[9] J. Guéna, M. Abgrall, A. Clairon, and S. Bize, Contributing to TAI with a secondary representation of the SI second, Metrologia **51**, 108 (2014).

[10] J. Guena, M. Abgrall, D. Rovera, P. Laurent, B. Chupin, M. Lours, G. Santarelli, P. Rosenbusch, M. E. Tobar, R. Li, K. Gibble, A. Clairon, and S. Bize, Progress in atomic fountains at LNE-SYRTE, IEEE Trans. Ultrason. Ferroelectr. Freq. Control **59**, 391 (2012).

[11] R. Li, K. Gibble, and K. Szymaniec, Improved accuracy of the NPL-CsF2 primary frequency standard: Evaluation of distributed cavity phase and microwave lensing frequency shifts, Metrologia **48**, 283 (2011).

[12] K. Beloy, *et al.*, Boulder Atomic Clock Optical Network (BACON) Collaboration, Frequency ratio measurements at 18-digit accuracy using an optical clock network, Nature **591**, 564 (2021).

[13] S. M. Brewer, J.-S. Chen, A. M. Hankin, E. R. Clements, C. W. Chou, D. J. Wineland, D. B. Hume, and D. R. Leibrandt, $^{27}Al^{+}$ Quantum-Logic Clock with a Systematic Uncertainty below 10^{-18}, Phys. Rev. Lett. **123**, 033201 (2019).

[14] W. F. McGrew, X. Zhang, R. J. Fasano, S. A. Schäffer, K. Beloy, D. Nicolodi, R. C. Brown, N. Hinkley, G. Milani, M. Schioppo, T. H. Yoon, and A. D. Ludlow, Atomic clock performance enabling geodesy below the centimetre level, Nature **564**, 87 (2018).

[15] I. Ushijima, M. Takamoto, M. Das, T. Ohkubo, and H. Katori, Cryogenic optical lattice clocks, Nat. Photonics **9**, 185 (2015).

[16] P. Gill, Is the time right for a redefinition of the second by optical atomic clocks?, J. Phys.: Conf. Ser. **723**, 012053 (2016).

[17] J. Lodewyck, On a definition of the SI second with a set of optical clock transitions, Metrologia **56**, 055009 (2019).

[18] F. Riehle, P. Gill, F. Arias, and L. Robertsson, The CIPM list of recommended frequency standard values: Guidelines and procedures, Metrologia **55**, 188 (2018).

[19] C. Sanner, N. Huntemann, R. Lange, C. Tamm, E. Peik, M. S. Safronova, and S. G. Porsev, Optical clock comparison for Lorentz symmetry testing, Nature **567**, 204 (2019).

[20] R. Lange, N. Huntemann, J. M. Rahm, C. Sanner, H. Shao, B. Lipphardt, C. Tamm, S. Weyers, and E. Peik, Improved Limits for Violations of Local Position Invariance from Atomic Clock Comparisons, Phys. Rev. Lett. **126**, 011102 (2021).

[21] B. M. Roberts, *et al.*, Search for transient variations of the fine structure constant and dark matter using fiber-linked optical atomic clocks, New J. Phys. **22**, 093010 (2020).

[22] P. Delva, *et al.*, Test of Special Relativity Using a Fiber Network of Optical Clocks, Phys. Rev. Lett. **118**, 221102 (2017).

[23] G. Panfilo and F. Arias, The coordinated universal time (UTC), Metrologia **56**, 042001 (2019).

[24] A. Bauch, J. Achkar, S. Bize, D. Calonico, R. Dach, R. Hlavać, L. Lorini, T. Parker, G. Petit, D. Piester, K. Szymaniec, and P. Uhrich, Comparison between frequency standards in Europe and the USA at the 10–15 uncertainty level, Metrologia **43**, 109 (2005).

[25] M. Pizzocaro, *et al.*, Intercontinental comparison of optical atomic clocks through very long baseline interferometry, Nat. Phys. **17**, 223 (2021).

[26] F. Riedel, *et al.*, Direct comparisons of European primary and secondary frequency standards via satellite techniques, Metrologia **57**, 045005 (2020).

[27] J. Leute, N. Huntemann, B. Lipphardt, C. Tamm, P. B. R. Nisbet-Jones, S. A. King, R. M. Godun, J. M. Jones, H. S. Margolis, P. B. Whibberley, A. Wallin, M. Merimaa, P. Gill, and E. Peik, Frequency comparison of $^{171}Yb^{+}$ ion optical clocks at PTB and NPL via GPS PPP, IEEE Trans. Ultrason. Ferroelectr. Freq. Control. **63**, 981 (2016).

[28] M. Fujieda, D. Piester, T. Gotoh, J. Becker, M. Aida, and A. Bauch, Carrier-phase two-way satellite frequency transfer over a very long baseline, Metrologia **51**, 253 (2014).

[29] H. Hachisu, M. Fujieda, S. Nagano, T. Gotoh, A. Nogami, T. Ido, S. Falke, N. Huntemann, C. Grebing, B. Lipphardt, C. Lisdat, and D. Piester, Direct comparison of optical lattice clocks with an intercontinental baseline of 9000 km, Opt. Lett. **39**, 4072 (2014).

[30] M. Musha, F.-L. Hong, K. Nakagawa, and K.-i. Ueda, Coherent optical frequency transfer over 50-km physical distance using a 120-km-long installed telecom fiber network, Opt. Express **16**, 16459 (2008).

[31] T. Akatsuka, T. Goh, H. Imai, K. Oguri, A. Ishizawa, I. Ushijima, N. Ohmae, M. Takamoto, H. Katori, T. Hashimoto, H. Gotoh, and T. Sogawa, Optical frequency distribution using laser repeater stations with planar lightwave circuits, Opt. Express **28**, 9186 (2020).

[32] C. Lisdat, *et al.*, A clock network for geodesy and fundamental science, Nat. Commun. **7**, 12443 (2016).

[33] S. Droste, F. Ozimek, T. Udem, K. Predehl, T. W. Hänsch, H. Schnatz, G. Grosche, and R. Holzwarth, Optical-Frequency Transfer over a Single-Span 1840 km Fiber Link, Phys. Rev. Lett. **111**, 110801 (2013).

[34] C. Clivati, R. Aiello, G. Bianco, C. Bortolotti, P. De Natale, V. Di Sarno, P. Maddaloni, G. Maccaferri, A. Mura, M. Negusini, F. Levi, F. Perini, R. Ricci, M. Roma, L. Santamaria Amato, M. Siciliani de Cumis, M. Stagni, A. Tuozzi,

and D. Calonico, Common-clock very long baseline interferometry using a coherent optical fiber link, Optica **7**, 1031 (2020).

[35] M. Schioppo, *et al.*, Comparing ultrastable lasers at 7×10^{-17} fractional frequency instability through a 2220 km optical fibre network, Nat. Commun. **13**, 212 (2022).

[36] D. Husmann, *et al.*, SI-traceable frequency dissemination at 1572.06 nm in a stabilized fiber network with ring topology, Opt. Express **29**, 24592 (2021).

[37] N. Chiodo, N. Quintin, F. Stefani, F. Wiotte, E. Camisard, C. Chardonnet, G. Santarelli, A. Amy-Klein, P.-E. Pottie, and O. Lopez, Cascaded optical fiber link using the internet network for remote clocks comparison, Opt. Express **23**, 33927 (2015).

[38] T. Takano, M. Takamoto, I. Ushijima, N. Ohmae, T. Akatsuka, A. Yamaguchi, Y. Kuroishi, H. Munekane, B. Miyahara, and H. Katori, Geopotential measurements with synchronously linked optical lattice clocks, Nat. Photonics **10**, 662 (2016).

[39] J. Grotti, *et al.*, Geodesy and metrology with a transportable optical clock, Nat. Phys. **14**, 437 (2018).

[40] A. Yamaguchi, M. Fujieda, M. Kumagai, H. Hachisu, S. Nagano, Y. Li, T. Ido, T. Takano, M. Takamoto, and H. Katori, Direct comparison of distant optical lattice clocks at the 10^{-16} uncertainty, Appl. Phys. Express **4**, 082203 (2011).

[41] M. Pizzocaro, F. Bregolin, P. Barbieri, B. Rauf, F. Levi, and D. Calonico, Absolute frequency measurement of the $^1S_0$—$^3P_0$ transition of ^{171}Yb with a link to international atomic time, Metrologia **57**, 035007 (2020).

[42] G. Petit, A. Kanj, S. Loyer, J. Delporte, F. Mercier, and F. Perosanz, 1×10^{-16} frequency transfer by GPS PPP with integer ambiguity resolution, Metrologia **52**, 301 (2015).

[43] G. Petit, Sub-10^{-16} accuracy GNSS frequency transfer with IPPP, GPS Solut. **25**, 22 (2021).

[44] V. Formichella, L. Galleani, G. Signorile, and I. Sesia, Robustness tests for an optical time scale, Metrologia **59**, 015002 (2022).

[45] J. Yao, J. A. Sherman, T. Fortier, H. Leopardi, T. Parker, W. McGrew, X. Zhang, D. Nicolodi, R. Fasano, S. Schäffer, K. Beloy, J. Savory, S. Romisch, C. Oates, S. Diddams, A. Ludlow, and J. Levine, Optical-Clock-Based Time Scale, Phys. Rev. Appl. **12**, 044069 (2019).

[46] W. R. Milner, J. M. Robinson, C. J. Kennedy, T. Bothwell, D. Kedar, D. G. Matei, T. Legero, U. Sterr, F. Riehle, H. Leopardi, T. M. Fortier, J. A. Sherman, J. Levine, J. Yao, J. Ye, and E. Oelker, Demonstration of a Timescale Based on a Stable Optical Carrier, Phys. Rev. Lett. **123**, 173201 (2019).

[47] H. Hachisu, F. Nakagawa, Y. Hanado, and T. Ido, Months-long real-time generation of a time scale based on an optical clock, Sci. Rep. **8**, 4243 (2018).

[48] D. Herman, S. Droste, E. Baumann, J. Roslund, D. Churin, A. Cingoz, J.-D. Deschênes, I. H. Khader, W. C. Swann, C. Nelson, N. R. Newbury, and I. Coddington, Femtosecond Timekeeping: Slip-Free Clockwork for Optical Timescales, Phys. Rev. Appl. **9**, 044002 (2018).

[49] F. Guillou-Camargo, V. Ménoret, E. Cantin, O. Lopez, N. Quintin, E. Camisard, V. Salmon, J.-M. Le Merdy, G. Santarelli, A. Amy-Klein, P.-E. Pottie, B. Desruelle, and C. Chardonnet, First industrial-grade coherent fiber link for optical frequency standard dissemination, Appl. Opt. **57**, 7203 (2018).

[50] https://www.refimeve.fr/index.php/en/.

[51] C. Clivati, G. Cappellini, L. F. Livi, F. Poggiali, M. S. de Cumis, M. Mancini, G. Pagano, M. Frittelli, A. Mura, G. A. Costanzo, F. Levi, D. Calonico, L. Fallani, J. Catani, and M. Inguscio, Measuring absolute frequencies beyond the GPS limit via long-haul optical frequency dissemination, Opt. Express **24**, 11865 (2016).

[52] B. Argence, B. Chanteau, O. Lopez, D. Nicolodi, M. Abgrall, C. Chardonnet, C. Daussy, B. Darquié, Y. Le Coq, and A. Amy-Klein, Quantum cascade laser frequency stabilization at the sub-Hz level, Nat. Photonics **9**, 456 (2015).

[53] O. Votava, S. Kassi, A. Campargue, and D. Romanini, Comb coherence-transfer and cavity ring-down saturation spectroscopy around 1.65 μm: kHz-accurate frequencies of transitions in the $2\nu3$ band of $^{12}CH_4$, Phys. Chem. Chem. Phys. **24**, 4157 (2022).

[54] K. Manamanni, T. Steshchenko, F. Wiotte, R. L. Targat, M. Abgrall, O. Lopez, E. Cantin, P. Éric Pottie, A. Amy-Klein, V. Roncin, and F. Du-Burck, Limitations due to residual interference in a fiber-based optical frequency reference at 1.55 μm, J. Opt. Soc. Am. B **39**, 438 (2022).

[55] C. Clivati, R. Ambrosini, T. Artz, A. Bertarini, C. Bortolotti, M. Frittelli, F. Levi, A. Mura, G. Maccaferri, M. Nanni, M. Negusini, F. Perini, M. Roma, M. Stagni, M. Zucco, and D. Calonico, A VLBI experiment using a remote atomic clock via a coherent fibre link, Sci. Rep. **7**, 40992 (2017).

[56] J. Serrano, P. Alvarez, M. Cattin, *et al.*, in *Int. Conf. Accelerator and Large Experimental Physics Control Systems (ICALEPCS), Kobe, Japan, 2009*, 978-4-9905391-0-8, TUC004 (CERN, Geneva, Switzerland, 2009).

[57] E. F. Dierikx, A. E. Wallin, T. Fordell, J. Myyry, P. Koponen, M. Merimaa, T. J. Pinkert, J. C. J. Koelemeij, H. Z. Peek, and R. Smets, White Rabbit precision time protocol on long-distance fiber links, IEEE Trans. Ultrason. Ferroelectr. Freq. Control **63**, 945 (2016).

[58] P. A. Williams, W. C. Swann, and N. R. Newbury, High-stability transfer of an optical frequency over long fiber-optic links, J. Opt. Soc. Am. B **25**, 1284 (2008).

[59] E. Cantin, M. Tønnes, R. Le Targat, A. Amy-Klein, O. Lopez, and P.-E. Pottie, An accurate and robust metrological network for coherent optical frequency dissemination, New J. Phys. **23**, 053027 (2021).

[60] C. E. Calosso, E. K. Bertacco, D. Calonico, C. Clivati, G. A. Costanzo, M. Frittelli, F. Levi, S. Micalizio, A. Mura, and A. Godone, Doppler-stabilized fiber link with 6 dB noise improvement below the classical limit, Opt. Lett. **40**, 131 (2015).

[61] A. Bercy, F. Stefani, O. Lopez, C. Chardonnet, P.-E. Pottie, and A. Amy-Klein, Two-way optical frequency comparisons at 5×10^{-21} relative stability over 100-km telecommunication network fibers, Phys. Rev. A **90**, 061802(R) (2014).

[62] D. Xu, O. Lopez, A. Amy-Klein, and P.-E. Pottie, Nonreciprocity in optical fiber links: Experimental evidence, Opt. Express **29**, 17476 (2021).

[63] S. Koke, A. Kuhl, T. Waterholter, S. M. F. Raupach, O. Lopez, E. Cantin, N. Quintin, A. Amy-Klein, P.-E. Pottie, and G. Grosche, Combining fiber Brillouin amplification with a repeater laser station for fiber-based optical frequency dissemination over 1400 km, New J. Phys. **21**, 123017 (2019).

[64] C. Clivati, M. Frittelli, D. Calonico, A. Mura, and F. Levi, in *2015 Joint Conference of the IEEE International Frequency Control Symposium & the European Frequency and Time Forum* (IEEE, 2015), p. 579.

[65] Consultative Committee for Time and Frequency (CCTF), Recommendation CCTF PSFS 2: Updates to the CIPM list of standard frequencies (2021).

[66] K. Szymaniec and S. E. Park, Primary frequency standard NPL-CsF2: Optimized operation near the collisional shift cancellation point, IEEE Trans. Instrum. Meas. **60**, 2475 (2015).

[67] J. Lodewyck, R. Le Targat, P.-E. Pottie, E. Benkler, S. Koke, and J. Kronjäger, Universal formalism for data sharing and processing in clock comparison networks, Phys. Rev. Res. **2**, 043269 (2020).

[68] https://www.bipm.org/en/bipm/tai/.

[69] M. Pizzocaro, P. Thoumany, B. Rauf, F. Bregolin, G. Milani, C. Clivati, G. A. Costanzo, F. Levi, and D. Calonico, Absolute frequency measurement of the $^1S_0$—$^3P_0$ transition of ^{171}Yb, Metrologia **54**, 102 (2017).

[70] H. R. Telle, B. Lipphardt, and J. Stenger, Kerr-lens, mode-locked lasers as transfer oscillators for optical frequency measurements, Appl. Phys. B **74**, 1 (2002).

[71] C. Grebing, A. Al-Masoudi, S. Dörscher, S. Häfner, V. Gerginov, S. Weyers, B. Lipphardt, F. Riehle, U. Sterr, and C. Lisdat, Realization of a timescale with an accurate optical lattice clock, Optica **3**, 563 (2016).

[72] N. Nemitz, T. Gotoh, F. Nakagawa, H. Ito, Y. Hanado, T. Ido, and H. Hachisu, Absolute frequency of ^{87}Sr at 1.8×10^{-16} uncertainty by reference to remote primary frequency standards, Metrologia **58**, 025006 (2021).

[73] H. Kim, M.-S. Heo, C. Y. Park, D.-H. Yu, and W.-K. Lee, Absolute frequency measurement of the ^{171}Yb optical lattice clock at KRISS using TAI for over a year, Metrologia **58**, 055007 (2021).

[74] W. F. McGrew, X. Zhang, H. Leopardi, R. J. Fasano, D. Nicolodi, K. Beloy, J. Yao, J. A. Sherman, S. A. Schäffer, J. Savory, R. C. Brown, S. Römisch, C. W. Oates, T. E. Parker, T. M. Fortier, and A. D. Ludlow, Towards the optical second: Verifying optical clocks at the SI limit, Optica **6**, 448 (2019).

[75] T. Kobayashi, D. Akamatsu, K. Hosaka, Y. Hisai, M. Wada, H. Inaba, T. Suzuyama, F.-L. Hong, and M. Yasuda, Demonstration of the nearly continuous operation of an ^{171}Yb optical lattice clock for half a year, Metrologia **57**, 065021 (2020).

[76] R. Tyumenev, M. Favier, S. Bilicki, E. Bookjans, R. L. Targat, J. Lodewyck, D. Nicolodi, Y. L. Coq, M. Abgrall, J. Guéna, L. D. Sarlo, and S. Bize, Comparing a mercury optical lattice clock with microwave and optical frequency standards, New J. Phys. **18**, 113002 (2016).

[77] J. Lodewyck, S. Bilicki, E. Bookjans, J.-L. Robyr, C. Shi, G. Vallet, R. L. Targat, D. Nicolodi, Y. L. Coq, J. Guéna, M. Abgrall, P. Rosenbusch, and S. Bize, Optical to microwave clock frequency ratios with a nearly continuous strontium optical lattice clock, Metrologia **53**, 1123 (2016).

[78] M. Barbiero, M. G. Tarallo, D. Calonico, F. Levi, G. Lamporesi, and G. Ferrari, Sideband-Enhanced Cold Atomic Source for Optical Clocks, Phys. Rev. Appl. **13**, 014013 (2020).

[79] M. Barbiero, D. Calonico, F. Levi, and M. G. Tarallo, Optically loaded strontium lattice clock with a single multi-wavelength reference cavity, IEEE Trans. Instrum. Meas. **71**, 1 (2022).

[80] R. Bondarescu, M. Bondarescu, G. Hetényi, L. Boschi, P. Jetzer, and J. Balakrishna, Geophysical applicability of atomic clocks: Direct continental geoid mapping, Geophys. J. Int. **191**, 78 (2012).

[81] R. Bondarescu, A. Schärer, A. Lundgren, G. Hetényi, N. Houlié, P. Jetzer, and M. Bondarescu, Ground-based optical atomic clocks as a tool to monitor vertical surface motion, Geophys. J. Int. **202**, 1770 (2015).

[82] G. Lion, I. Panet, P. Wolf, C. Guerlin, S. Bize, and P. Delva, Determination of a high spatial resolution geopotential model using atomic clock comparisons, J. Geod. **91**, 597 (2017).

[83] T. E. Mehlstäubler, G. Grosche, C. Lisdat, P. O. Schmidt, and H. Denker, Atomic clocks for geodesy, Rep. Progr. Phys. **81**, 064401 (2018).

[84] M. Takamoto, I. Ushijima, N. Ohmae, T. Yahagi, K. Kokado, H. Shinkai, and H. Katori, Test of general relativity by a pair of transportable optical lattice clocks, Nat. Photonics **14**, 411 (2020).

[85] C. Clivati, A. Meda, S. Donadello, S. Virzö, M. Genovese, F. Levi, A. Mura, M. Pittaluga, Z. Yuan, A. J. Shields, M. Lucamarini, I. P. Degiovanni, and D. Calonico, Coherent phase transfer for real-world twin-field quantum key distribution, Nat. Commun. **13**, 157 (2022).

Bibliography

[1] BIPM. *Bureau International des Poids et Mesures*. URL: https://www.bipm.org/en/home.

[2] Sébastien Bize. "Tests fondamentaux à l'aide d'horloges à atomes froids de rubidium et de césium". PhD thesis. Université Pierre et Marie Curie - Paris VI, Oct. 1, 2001. URL: https://tel.archives-ouvertes.fr/tel-00000981.

[3] L. Essen and J. V. L. Parry. "An Atomic Standard of Frequency and Time Interval: A Cæsium Resonator". In: *Nature* 176.4476 (Aug. 1955), pp. 280–282. ISSN: 0028-0836, 1476-4687. DOI: 10.1038/176280a0. URL: https://www.nature.com/articles/176280a0.

[4] S. A. Diddams et al. "Standards of Time and Frequency at the Outset of the 21st Century". In: *Science* 306.5700 (Nov. 19, 2004). Publisher: American Association for the Advancement of Science, pp. 1318–1324. DOI: 10.1126/science.1102330. URL: https://www.science.org/doi/10.1126/science.1102330.

[5] Michel Abgrall et al. "Atomic fountains and optical clocks at SYRTE: Status and perspectives". In: *Comptes Rendus Physique*. The measurement of time / La mesure du temps 16.5 (June 1, 2015), pp. 461–470. ISSN: 1631-0705. DOI: 10.1016/j.crhy.2015.03.010. URL: https://www.sciencedirect.com/science/article/pii/S1631070515000614.

[6] J. Guena et al. "Progress in atomic fountains at LNE-SYRTE". In: *IEEE Transactions on Ultrasonics, Ferroelectrics and Frequency Control* 59.3 (Mar. 2012), pp. 391–409. ISSN: 0885-3010. DOI: 10.1109/TUFFC.2012.2208. URL: http://ieeexplore.ieee.org/document/6174184/.

[7] J Guéna et al. "Contributing to TAI with a secondary representation of the SI second". In: *Metrologia* 51.1 (Feb. 1, 2014), pp. 108–120. ISSN: 0026-1394, 1681-7575. DOI: 10.1088/0026-1394/51/1/108. URL: https://iopscience.iop.org/article/10.1088/0026-1394/51/1/108.

[8] µquans. *µquans webpage*. URL: https://www.muquans.com/.

[9] iXblue. *iXblue webpage*. URL: https://www.ixblue.com/.

[10] Long-Sheng Ma et al. "Delivering the same optical frequency at two places: accurate cancellation of phase noise introduced by an optical fiber or other time-varying path". In: *Optics Letters* 19.21 (Nov. 1, 1994), p. 1777. ISSN: 0146-9592, 1539-4794. DOI: 10.1364/OL.19.001777. URL: https://www.osapublishing.org/abstract.cfm?URI=ol-19-21-1777.

[11] Albert A. Michelson and Edward D. Morley. "On the Relative Motion of the Earth and the Luminiferous Ether". In: *American Journal of Science* XXXIV.203 (Nov. 1887).

[12] LIGO Scientific Collaboration and Virgo Collaboration et al. "GW170814: A Three-Detector Observation of Gravitational Waves from a Binary Black Hole Coalescence". In: *Physical Review Letters* 119.14 (Oct. 6, 2017), p. 141101. DOI: 10.1103/PhysRevLett.119.141101. URL: https://link.aps.org/doi/10.1103/PhysRevLett.119.141101.

[13] Natale C. Pistoni and Mario Martinelli. "Polarization noise suppression in retracing optical fiber circuits". In: *Optics Letters* 16.10 (May 15, 1991), p. 711. ISSN: 0146-9592, 1539-4794. DOI: 10.1364/OL.16.000711. URL: https://www.osapublishing.org/abstract.cfm?URI=ol-16-10-711.

[14] E. I. Gordon. "A Review of Acoustooptical Deflection and Modulation Devices". In: *Applied Optics* 5.10 (Oct. 1, 1966). Publisher: Optica Publishing Group, pp. 1629–1639. ISSN: 2155-3165. DOI: 10.1364/AO.5.001629. URL: https://opg.optica.org/ao/abstract.cfm?uri=ao-5-10-1629.

[15] W J Riley. *Handbook of Frequency Stability Analysis*. Vol. 31. 1. U.S. Department of Commerce, National Institute of Standards and Technology, 1994. A49. ISBN: 3-01-975305-8. DOI: 10.1016/0148-9062(94)92706-5.

[16] Enrico Rubiola. "On the measurement of frequency and of its sample variance with high-resolution counters". In: *Review of Scientific Instruments* 76.5 (May 2005), p. 054703. ISSN: 0034-6748, 1089-7623. DOI: 10.1063/1.1898203. URL: http://aip.scitation.org/doi/10.1063/1.1898203.

[17] N. R. Newbury, P. A. Williams, and W. C. Swann. "Coherent transfer of an optical carrier over 251 km". In: *Optics Letters* 32.21 (Nov. 1, 2007), p. 3056. ISSN: 0146-9592, 1539-4794. DOI: 10.1364/OL.32.003056. URL: https://www.osapublishing.org/abstract.cfm?URI=ol-32-21-3056.

[18] Anthony Bercy. "Ultrastable optical fiber link : multiple-users dissemination, study of fundamental and technological limits and new applications". Theses. Université Paris 13 - Sorbonne Paris Cité, 2015. URL: https://hal.archives-ouvertes.fr/tel-01301488.

[19] C. E. Calosso et al. "Frequency transfer via a two-way optical phase comparison on a multiplexed fiber network". In: *Optics Letters* 39.5 (Mar. 1, 2014), pp. 1177–1180. ISSN: 1539-4794. DOI: 10.1364/OL.39.001177. URL: https://www.osapublishing.org/abstract.cfm?uri=ol-39-5-1177.

[20] C. E. Calosso et al. "Doppler-stabilized fiber link with 6 dB noise improvement below the classical limit". In: *Optics Letters* 40.2 (Jan. 15, 2015), p. 131. ISSN: 0146-9592, 1539-4794. DOI: 10.1364/OL.40.000131.

[21] Fabio Stefani et al. "Tackling the limits of optical fiber links". In: *Journal of the Optical Society of America B* 32.5 (May 1, 2015), pp. 787–797. ISSN: 0740-3224, 1520-8540. DOI: 10.1364/JOSAB.32.000787. URL: https://www.osapublishing.org/abstract.cfm?URI=josab-32-5-787.

[22] Anthony Bercy et al. "Two-way optical frequency comparisons at 5×10^{-21} relative stability over 100-km telecommunication network fibers". In: *Physical Review A* 90.6 (Dec. 22, 2014). ISSN: 1050-2947, 1094-1622. DOI: 10.1103/PhysRevA.90.061802. URL: https://link.aps.org/doi/10.1103/PhysRevA.90.061802.

[23] Anna Tampellini et al. "Effect of a timebase mismatch in two-way optical frequency transfer". In: *Metrologia* 54.6 (Dec. 1, 2017), pp. 805–809. ISSN: 0026-1394, 1681-7575. DOI: 10.1088/1681-7575/aa8a41. URL: https://iopscience.iop.org/article/10.1088/1681-7575/aa8a41.

[24] Won-Kyu Lee et al. "Hybrid fiber links for accurate optical frequency comparison". In: *Applied Physics B* 123.5 (May 2, 2017), p. 161. ISSN: 1432-0649. DOI: 10.1007/s00340-017-6736-5. URL: https://doi.org/10.1007/s00340-017-6736-5.

[25] Dan Xu et al. "Studying the fundamental limit of optical fiber links to the 10 $^{-21}$ level". In: *Optics Express* 26.8 (Apr. 16, 2018), p. 9515. ISSN: 1094-4087. DOI: 10.1364/OE.26.009515. URL: https://www.osapublishing.org/abstract.cfm?URI=oe-26-8-9515.

[26] Dan Xu et al. "Reciprocity of propagation in optical fiber links demonstrated to 1E-21". In: *Optics Express* 27.25 (Dec. 9, 2019), pp. 36965–36975. ISSN: 1094-4087. DOI: 10.1364/OE.27.036965. URL: https://www.osapublishing.org/abstract.cfm?URI=oe-27-25-36965.

[27] Dan Xu et al. "Non-reciprocity in optical fiber links: experimental evidence". In: *Optics Express* 29.11 (May 24, 2021). Publisher: Optical Society of America, pp. 17476–17490. ISSN: 1094-4087. DOI: 10.1364/OE.420661. URL: https://www.osapublishing.org/oe/abstract.cfm?uri=oe-29-11-17476.

[28] Etienne Cantin et al. "An accurate and robust metrological network for coherent optical frequency dissemination". In: *New Journal of Physics* (2021). ISSN: 1367-2630. DOI: 10.1088/1367-2630/abe79e. URL: http://iopscience.iop.org/article/10.1088/1367-2630/abe79e.

[29] Tomoya Akatsuka et al. "Optical frequency distribution using laser repeater stations with planar lightwave circuits". In: *Optics Express* 28.7 (Mar. 30, 2020), pp. 9186–9197. ISSN: 1094-4087. DOI: 10.1364/OE.383526. URL: https://www.osapublishing.org/oe/abstract.cfm?uri=oe-28-7-9186.

[30] Dan Xu et al. "Polarization scramblers to solve practical limitations of frequency transfer". In: *Journal of Lightwave Technology* (2021), pp. 1–1. ISSN: 0733-8724, 1558-2213. DOI: 10.1109/JLT.2021.3057804. URL: https://ieeexplore.ieee.org/document/9350164/.

[31] M. Fujieda et al. "Ultrastable Frequency Dissemination via Optical Fiber at NICT". In: *IEEE Transactions on Instrumentation and Measurement* 58.4 (Apr. 2009), pp. 1223–1228. ISSN: 0018-9456, 1557-9662. DOI: 10.1109/TIM.2008.2008088. URL: http://ieeexplore.ieee.org/document/4696007/.

[32] Cecilia Clivati et al. "Optical frequency transfer over submarine fiber links". In: *Optica* 5.8 (Aug. 20, 2018), pp. 893–901. ISSN: 2334-2536. DOI: 10.1364/OPTICA.5.000893. URL: https://www.osapublishing.org/optica/abstract.cfm?uri=optica-5-8-893.

[33] Jack K. Holmes and Srini Raghavan. "The mean cycle slip time for first-, second-, and third-order PLLs". In: *2009 IEEE Aerospace conference*. 2009 IEEE Aerospace conference. ISSN: 1095-323X. Mar. 2009, pp. 1–8. DOI: 10.1109/AERO.2009.4839416.

[34] Nicola Chiodo et al. "Cascaded optical fiber link using the internet network for remote clocks comparison". In: *Optics Express* 23.26 (Dec. 28, 2015), p. 33927. ISSN: 1094-4087. DOI: 10.1364/OE.23.033927. URL: https://www.osapublishing.org/abstract.cfm?URI=oe-23-26-33927.

[35] Olivier Lopez et al. "Cascaded multiplexed optical link on a telecommunication network for frequency dissemination". In: *Optics Express* 18.16 (Aug. 2, 2010), pp. 16849–16857. ISSN: 1094-4087. DOI: 10.1364/OE.18.016849. URL: https://www.osapublishing.org/abstract.cfm?uri=oe-18-16-16849.

[36] F. Guillou-Camargo et al. "First industrial-grade coherent fiber link for optical frequency standard dissemination". In: *Applied Optics* 57.25 (Sept. 1, 2018), pp. 7203–7210. ISSN: 2155-3165. DOI: 10.1364/AO.57.007203. URL: https://www.osapublishing.org/ao/abstract.cfm?uri=ao-57-25-7203.

[37] Olivier Lopez et al. "Frequency and time transfer for metrology and beyond using telecommunication network fibres". In: *Comptes Rendus Physique* 16.5 (June 2015), pp. 531–539. URL: https://hal.archives-ouvertes.fr/hal-01176012.

[38] REFIMEVE. *Reseau fibré metrologique à vocation européenne*. URL: https://www.refimeve.fr/index.php/en/.

[39] R. Santagata et al. "High-precision methanol spectroscopy with a widely tunable SI-traceable frequency-comb-based mid-infrared QCL". In: *Optica* 6.4 (Apr. 20, 2019), pp. 411–423. ISSN: 2334-2536. DOI: 10.1364/OPTICA.6.000411. URL: https://www.osapublishing.org/abstract.cfm?URI=optica-6-4-411.

[40] C. Lisdat et al. "A clock network for geodesy and fundamental science". In: *Nature Communications* 7 (Aug. 9, 2016), p. 12443. ISSN: 2041-1723. DOI: 10.1038/ncomms12443. arXiv: 1511.07735. URL: http://arxiv.org/abs/1511.07735.

[41] IQB. *Italian Quantum Backbone*. URL: https://www.inrim.it/en/node/654.

[42] CERN. *The White Rabbit Project*. URL: https://white-rabbit.web.cern.ch/.

[43] H. Jiang et al. "Long-distance frequency transfer over an urban fiber link using optical phase stabilization". In: *Journal of the Optical Society of America B* 25.12 (Dec. 1, 2008), p. 2029. ISSN: 0740-3224, 1520-8540. DOI: 10.1364/JOSAB.25.002029. URL: https://www.osapublishing.org/abstract.cfm?URI=josab-25-12-2029.

[44] Bérengère Argence et al. "Quantum cascade laser frequency stabilization at the sub-Hz level". In: *Nature Photonics* 9.7 (July 2015), pp. 456–460. ISSN: 1749-4885, 1749-4893. DOI: 10.1038/nphoton.2015.93. URL: http://www.nature.com/articles/nphoton.2015.93.

[45] C. Clivati et al. "Coherent Optical-Fiber Link Across Italy and France". In: *Physical Review Applied* 18.5 (Nov. 3, 2022), p. 054009. ISSN: 2331-7019. DOI: 10.1103/PhysRevApplied.18.054009. URL: https://link.aps.org/doi/10.1103/PhysRevApplied.18.054009.

[46] Gianni Di Domenico, Stéphane Schilt, and Pierre Thomann. "Simple approach to the relation between laser frequency noise and laser line shape". In: *Applied Optics* 49.25 (Sept. 1, 2010), pp. 4801–4807. ISSN: 0003-6935, 1539-4522. DOI: 10.1364/AO.49.004801. URL: https://www.osapublishing.org/abstract.cfm?URI=ao-49-25-4801.

[47] Xiaopeng Xie et al. "Phase noise characterization of sub-hertz linewidth lasers via digital cross correlation". In: *Optics Letters* 42.7 (Apr. 1, 2017), pp. 1217–1220. ISSN: 1539-4794. DOI: 10.1364/OL.42.001217. URL: https://www.osapublishing.org/ol/abstract.cfm?uri=ol-42-7-1217.

[48] Sebastian Koke et al. "Combining fiber Brillouin amplification with a repeater laser station for fiber-based optical frequency dissemination over 1400 km". In: *New Journal of Physics* 21.12 (Dec. 13, 2019), p. 123017. ISSN: 1367-2630. DOI: 10.1088/1367-2630/ab5d95. URL: https://iopscience.iop.org/article/10.1088/1367-2630/ab5d95.

[49] D.R. White. "The noise bandwidth of sampled data systems". In: *IEEE Transactions on Instrumentation and Measurement* 38.6 (Dec. 1989), pp. 1036–1043. ISSN: 0018-9456, 1557-9662. DOI: 10.1109/19.46397. URL: https://ieeexplore.ieee.org/document/46397/.

[50] D.W. Allan and J.A. Barnes. "A Modified "Allan Variance" with Increased Oscillator Characterization Ability". In: *Thirty Fifth Annual Frequency Control Symposium*. Thirty Fifth Annual Frequency Control Symposium. IEEE, 1981, pp. 470–475. DOI: 10.1109/FREQ.1981.200514. URL: http://ieeexplore.ieee.org/document/1537454/.

[51] Won-Kyu Lee et al. "The uncertainty associated with the weighted mean frequency of a phase-stabilized signal with white phase noise". In: *Metrologia* 47.1 (Feb. 2010), pp. 24–32. ISSN: 0026-1394, 1681-7575. DOI: 10.1088/0026-1394/47/1/004. URL: http://stacks.iop.org/0026-1394/47/i=1/a=004?key=crossref.4169a902d29e59d52e043b11026c2f8a.

[52] Erik Benkler, Christian Lisdat, and Uwe Sterr. "On the relation between uncertainties of weighted frequency averages and the various types of Allan deviations". In: *Metrologia* 52.4 (Aug. 1, 2015), pp. 565–574. ISSN: 0026-1394, 1681-7575. DOI: 10.1088/0026-1394/52/4/565. arXiv: 1504.00466. URL: http://arxiv.org/abs/1504.00466.

[53] RFI. *Investigators probe suspected sabotage of French fiber optic network*. Ed. by www.rfi.fr. Apr. 2022. URL: https://www.rfi.fr/en/science-and-technology/20220428-france-investigates-suspected-sabotage-of-fiber-optic-cables-that-disrupted-internet.

[54] G. E. P. Box et al. *Time Series Analysis*. Wiley, 2015, p. 709.

[55] Chang Xu. "Reconstruction of gappy GPS coordinate time series using empirical orthogonal functions". In: *Journal of Geophysical Research: Solid Earth* 121.12 (2016), pp. 9020–9033. ISSN: 2169-9356. DOI: https://doi.org/10.1002/2016JB013188. URL: https://agupubs.onlinelibrary.wiley.com/doi/abs/10.1002/2016JB013188.

[56] Ilaria Sesia et al. "An Efficient and Configurable Preprocessing Algorithm to Improve Stability Analysis". In: *IEEE Transactions on Ultrasonics, Ferroelectrics, and Frequency Control* 63.4 (Apr. 2016), pp. 575–581. ISSN: 0885-3010. DOI: 10.1109/TUFFC.2015.2496280. URL: http://ieeexplore.ieee.org/document/7313019/.

[57] Dai-Hyuk Yu, Marc Weiss, and Thomas E Parker. "Uncertainty of a frequency comparison with distributed dead time and measurement interval offset". In: *Metrologia* 44.1 (Feb. 2007), pp. 91–96. ISSN: 0026-1394, 1681-7575. DOI: 10.1088/0026-1394/44/1/014. URL: https://iopscience.iop.org/article/10.1088/0026-1394/44/1/014.

[58] Etienne Savalle et al. "Gravitational redshift test with the future ACES mission". In: *Classical and Quantum Gravity* 36.24 (Dec. 19, 2019), p. 245004. ISSN: 0264-9381, 1361-6382. DOI: 10.1088/1361-6382/ab4f25. arXiv: 1907.12320. URL: http://arxiv.org/abs/1907.12320.

[59] Claudio E. Calosso, Cecilia Clivati, and Salvatore Micalizio. "Avoiding Aliasing in Allan Variance: An Application to Fiber Link Data Analysis". In: *IEEE Transactions on Ultrasonics, Ferroelectrics, and Frequency Control* 63.4 (Apr. 2016), pp. 646–655. ISSN: 0885-3010. DOI: 10.1109/TUFFC.2016.2519265. URL: http://ieeexplore.ieee.org/document/7384737/.

[60] Lorenzo Galleani and Ilaria Sesia. "The Corrected Allan Variance: Stability Analysis of Frequency Measurements With Missing Data". In: *IEEE Transactions on Ultrasonics, Ferroelectrics, and Frequency Control* 66.10 (Oct. 2019), pp. 1667–1683. ISSN: 0885-3010, 1525-8955. DOI: 10.1109/TUFFC.2019.2927424. URL: https://ieeexplore.ieee.org/document/8756280/.

[61] G John Dick. "Local oscillator induced instabilities in trapped ion frequency standards". In: (1987), p. 16.

[62] Mads Tønnes et al. "Coherent fiber links operated for years: effect of missing data". In: *Metrologia* (Sept. 21, 2022). ISSN: 0026-1394, 1681-7575. DOI: 10.1088/1681-7575/ac938e. URL: https://iopscience.iop.org/article/10.1088/1681-7575/ac938e.

[63] P. Lemonde et al. "The sensitivity function: a new tool for the evaluation of frequency shifts in atomic spectroscopy". In: *Proceedings of the 1998 IEEE International Frequency Control Symposium (Cat. No.98CH36165)*. Proceedings of the 1998 IEEE International Frequency Control Symposium (Cat. No.98CH36165). ISSN: 1075-6787. May 1998, pp. 110–115. DOI: 10.1109/FREQ.1998.717890.

[64] L. Lo Presti, D. Rovera, and A. De Marchi. "A simple analysis of the Dick effect in terms of phase noise spectral densities". In: *IEEE Transactions on Ultrasonics, Ferroelectrics, and Frequency Control* 45.4 (July 1998).

Conference Name: IEEE Transactions on Ultrasonics, Ferroelectrics, and Frequency Control, pp. 899–905. ISSN: 1525-8955. DOI: 10.1109/58.710552.

[65] Mads Tønnes et al. "Scientific Data Processing of a Fiber Network for Optical Frequency Transfer: Methods and Studies". In: *URSI Radio Science Letters* 3 (2021), p. 3. DOI: 10.46620/21-0011.

[66] F. Riedel et al. "Direct comparisons of European primary and secondary frequency standards via satellite techniques". In: *Metrologia* 57.4 (Aug. 1, 2020), p. 045005. ISSN: 0026-1394, 1681-7575. DOI: 10.1088/1681-7575/ab6745. arXiv: 1910.06736. URL: http://arxiv.org/abs/1910.06736.

[67] Gérard Petit et al. "1×10^{-16} frequency transfer by GPS PPP with integer ambiguity resolution". In: *Metrologia* 52.2 (Apr. 1, 2015), pp. 301–309. ISSN: 0026-1394, 1681-7575. DOI: 10.1088/0026-1394/52/2/301. URL: https://iopscience.iop.org/article/10.1088/0026-1394/52/2/301.

[68] G Petit et al. "Continuous IPPP links for UTC". In: *Metrologia* 59.4 (Aug. 1, 2022), p. 045007. ISSN: 0026-1394, 1681-7575. DOI: 10.1088/1681-7575/ac7687. URL: https://iopscience.iop.org/article/10.1088/1681-7575/ac7687.

[69] D.W. Hanson. "Fundamentals of two-way time transfers by satellite". In: *Proceedings of the 43rd Annual Symposium on Frequency Control*. Proceedings of the 43rd Annual Symposium on Frequency Control. May 1989, pp. 174–178. DOI: 10.1109/FREQ.1989.68861.

[70] M Fujieda et al. "Carrier-phase two-way satellite frequency transfer over a very long baseline". In: *Metrologia* 51.3 (June 1, 2014), pp. 253–262. ISSN: 0026-1394, 1681-7575. DOI: 10.1088/0026-1394/51/3/253. URL: http://stacks.iop.org/0026-1394/51/i=3/a=253?key=crossref.0cfca314d2d9419542726a5df58013bc.

[71] Zhiheng Jiang et al. "Improving two-way satellite time and frequency transfer with redundant links for UTC generation". In: *Metrologia* 56 (Apr. 1, 2019), p. 025005. DOI: 10.1088/1681-7575/aafced. URL: http://adsabs.harvard.edu/abs/2019Metro..5625005J.

[72] Jean-Daniel Deschênes et al. "Synchronization of Distant Optical Clocks at the Femtosecond Level". In: *Physical Review X* 6.2 (May 11, 2016), p. 021016. DOI: 10.1103/PhysRevX.6.021016. URL: https://link.aps.org/doi/10.1103/PhysRevX.6.021016.

[73] E. Samain et al. "Time Transfer by Laser Link (T2L2) in non common view between Europe and China". In: *IEEE Transactions on Ultrasonics, Ferroelectrics, and Frequency Control* PP.99 (2018), pp. 1–1. ISSN: 0885-3010. DOI: 10.1109/TUFFC.2018.2804221.

[74] D. R. Gozzard et al. "Stabilized Free-Space Optical Frequency Transfer". In: *Physical Review Applied* 10.2 (Aug. 29, 2018), p. 024046. ISSN: 2331-7019. DOI: 10.1103/PhysRevApplied.10.024046. URL: https://link.aps.org/doi/10.1103/PhysRevApplied.10.024046.

[75] Martha I. Bodine et al. "Optical time-frequency transfer across a free-space, three-node network". In: *APL Photonics* 5.7 (July 1, 2020), p. 076113. DOI: 10.1063/5.0010704. URL: https://aip.scitation.org/doi/10.1063/5.0010704.

[76] Benjamin P. Dix-Matthews et al. "Point-to-point stabilized optical frequency transfer with active optics". In: *Nature Communications* 12.1 (Jan. 22, 2021). Number: 1 Publisher: Nature Publishing Group, p. 515. ISSN: 2041-1723. DOI: 10.1038/s41467-020-20591-5. URL: https://www.nature.com/articles/s41467-020-20591-5.

[77] "113 km Free-Space Time-Frequency Dissemination at the 19th Decimal Instability". In: (Mar. 22, 2022). arXiv: 2203.11272. URL: http://arxiv.org/abs/2203.11272.

[78] Marco Pizzocaro et al. "Intercontinental comparison of optical atomic clocks through very long baseline interferometry". In: *Nature Physics* 17.2 (Feb. 2021). Number: 2 Publisher: Nature Publishing Group, pp. 223–227. ISSN: 1745-2481. DOI: 10.1038/s41567-020-01038-6. URL: https://www.nature.com/articles/s41567-020-01038-6.

[79] Arne Bjerhammar. "On a relativistic geodesy". In: *Bulletin Géodésique* 59.3 (Sept. 1985), pp. 207–220. ISSN: 0007-4632, 1432-1394. DOI: 10.1007/BF02520327. URL: http://link.springer.com/10.1007/BF02520327.

[80] Pacome Delva, Heiner Denker, and Guillaume Lion. "Chronometric Geodesy: Methods and Applications". In: ed. by Seiichiro Himeno and Keiko Aoshima. ISBN 9789811336294 9789811336300. Singapore: Springer Singapore, 2019, pp. 25–85. DOI: 10.1007/978-3-030-11500-5_2. URL: http://link.springer.com/10.1007/978-3-030-11500-5_2.

[81] Sébastien Bize. "The unit of time: Present and future directions". In: *Comptes Rendus Physique* 20.1 (Jan. 2019), pp. 153–168. ISSN: 16310705. DOI: 10.1016/j.crhy.2019.02.002. URL: https://linkinghub.elsevier.com/retrieve/pii/S1631070519300167.

[82] Tetsushi Takano et al. "Real-time geopotentiometry with synchronously linked optical lattice clocks". In: *Nature Photonics* 10.10 (Oct. 2016), pp. 662–666. ISSN: 1749-4885, 1749-4893. DOI: 10.1038/nphoton.2016.159. arXiv: 1608.07650[physics]. URL: http://arxiv.org/abs/1608.07650.

[83] Tobias Bothwell et al. "JILA SrI optical lattice clock with uncertainty of 2×10^{-18}". In: *Metrologia* 56.6 (Oct. 2019), p. 065004. ISSN: 0026-1394. DOI: 10.1088/1681-7575/ab4089. URL: https://dx.doi.org/10.1088/1681-7575/ab4089.

[84] Boulder Atomic Clock Optical Network (BACON) Collaboration*. "Frequency ratio measurements at 18-digit accuracy using an optical clock network". In: *Nature* 591.7851 (Mar. 25, 2021), pp. 564–569. ISSN: 0028-0836, 1476-4687. DOI: 10.1038/s41586-021-03253-4. URL: http://www.nature.com/articles/s41586-021-03253-4.

[85] Jérôme Lodewyck et al. "Universal formalism for data sharing and processing in clock comparison networks". In: *Physical Review Research* 2.4 (Nov. 20, 2020), p. 043269. DOI: 10.1103/PhysRevResearch.2.043269. URL: https://link.aps.org/doi/10.1103/PhysRevResearch.2.043269.

[86] One Wiki to Rule Them All. *Palantíri*. URL: https://lotr.fandom.com/wiki/Palant%C3%ADri.

[87] One Wiki to Rule Them All. *Eye of Sauron*. URL: https://lotr.fandom.com/wiki/Eye_of_Sauron.

[88] One Wiki to Rule Them All. *Gandalf*. URL: https://lotr.fandom.com/wiki/Gandalf.

[89] One Wiki to Rule Them All. *Saruman*. URL: https://lotr.fandom.com/wiki/Saruman.

[90] Dan Xu et al. "Two-Branch Fiber Link for International Clock Networks". In: *IEEE Transactions on Instrumentation and Measurement* 68.6 (June 2019), pp. 2195–2200. ISSN: 0018-9456, 1557-9662. DOI: 10.1109/TIM.2018.2886865. URL: https://ieeexplore.ieee.org/document/8599074/.

[91] John M. Robinson et al. "Crystalline optical cavity at 4K with thermal-noise-limited instability and ultralow drift". In: *Optica* 6.2 (Feb. 20, 2019), pp. 240–243. ISSN: 2334-2536. DOI: 10.1364/OPTICA.6.000240. URL: https://www.osapublishing.org/optica/abstract.cfm?uri=optica-6-2-240.

[92] Sebastian M.F. Raupach and Gesine Grosche. "Chirped frequency transfer: a tool for synchronization and time transfer". In: *IEEE Transactions on Ultrasonics, Ferroelectrics, and Frequency Control* 61.6 (June 2014). Conference Name: IEEE Transactions on Ultrasonics, Ferroelectrics, and Frequency Control, pp. 920–929. ISSN: 1525-8955. DOI: 10.1109/TUFFC.2014.2988.

[93] Erik F. Dierikx et al. "White Rabbit Precision Time Protocol on Long-Distance Fiber Links". In: *IEEE Transactions on Ultrasonics, Ferroelectrics, and Frequency Control* 63.7 (July 2016), pp. 945–952. ISSN: 0885-3010. DOI: 10.1109/TUFFC.2016.2518122. URL: http://ieeexplore.ieee.org/document/7383303/.

[94] Cecilia Clivati et al. "Common-clock very long baseline interferometry using a coherent optical fiber link". In: *Optica* 7.8 (Aug. 20, 2020). Publisher: Optical Society of America, pp. 1031–1037. ISSN: 2334-2536. DOI: 10.1364/OPTICA.393356. URL: https://www.osapublishing.org/optica/abstract.cfm?uri=optica-7-8-1031.

[95] Filippo Levi et al. "Accuracy evaluation of ITCsF2: a nitrogen cooled caesium fountain". In: *Metrologia* 51.3 (June 1, 2014), pp. 270–284. ISSN: 0026-1394, 1681-7575. DOI: 10.1088/0026-1394/51/3/270. URL: https://iopscience.iop.org/article/10.1088/0026-1394/51/3/270.

[96] G Sagnac. "L'éther lumineux démontré par l'effet du vent relatif d'éther dans un interféromètre en rotation uniforme". In: *C. R. Acad. Sci.* 157 (1913), p. 708. URL: http://zelmanov.ptep-online.com/papers/zj-2008-07.pdf.

[97] Olivier Darrigol. "Georges Sagnac: A life for optics". In: *Comptes Rendus Physique*. The Sagnac effect: 100 years later / L'effet Sagnac : 100 ans après 15.10 (Dec. 1, 2014), pp. 789–840. ISSN: 1631-0705. DOI: 10.1016/j.crhy.2014.09.007. URL: https://www.sciencedirect.com/science/article/pii/S1631070514001340.

[98] CLONETS-DS. *Clock Network Services - Design Study*. URL: https://clonets-ds.eu/.

[99] Stephan Schiller. "Feasibility of giant fiber-optic gyroscopes". In: *Physical Review A* 87.3 (Mar. 20, 2013), p. 033823. DOI: 10.1103/PhysRevA.87.033823. URL: https://link.aps.org/doi/10.1103/PhysRevA.87.033823.

[100] C. Clivati et al. "Large-area fiber-optic gyroscope on a multiplexed fiber network". In: *Optics Letters* 38.7 (Apr. 1, 2013), p. 1092. ISSN: 0146-9592, 1539-4794. DOI: 10.1364/OL.38.001092. URL: https://www.osapublishing.org/abstract.cfm?URI=ol-38-7-1092.

[101] Ruyong Wang, Yi Zheng, and Aiping Yao. "Generalized Sagnac Effect". In: *Physical Review Letters* 93.14 (Sept. 27, 2004). ISSN: 0031-9007, 1079-7114. DOI: 10.1103/PhysRevLett.93.143901. URL: https://link.aps.org/doi/10.1103/PhysRevLett.93.143901.

[102] A. Ori and J. E. Avron. "Generalized Sagnac-Wang-Fizeau formula". In: *Physical Review A* 94.6 (Dec. 19, 2016), p. 063837. DOI: 10.1103/PhysRevA.94.063837. URL: https://link.aps.org/doi/10.1103/PhysRevA.94.063837.

[103] Richard S. Gross. "The excitation of the Chandler wobble". In: *Geophysical Research Letters* 27.15 (2000), pp. 2329–2332. ISSN: 1944-8007. DOI: 10.1029/2000GL011450. URL: https://onlinelibrary.wiley.com/doi/abs/10.1029/2000GL011450.

[104] A Simonelli et al. "Rotational motions from the 2016, Central Italy seismic sequence, as observed by an underground ring laser gyroscope". In: *Geophysical Journal International* 214.1 (July 1, 2018), pp. 705–715. ISSN: 0956-540X, 1365-246X. DOI: 10.1093/gji/ggy186. URL: https://academic.oup.com/gji/article/214/1/705/4993544.

[105] J. Belfi et al. "Analysis of 90 day operation of the GINGERINO gyroscope". In: *Applied Optics* 57.20 (July 10, 2018), p. 5844. ISSN: 1559-128X, 2155-3165. DOI: 10.1364/AO.57.005844. URL: https://opg.optica.org/abstract.cfm?URI=ao-57-20-5844.

[106] J. Belfi et al. "A 1.82 m2 ring laser gyroscope for nano-rotational motion sensing". In: *Applied Physics B* 106.2 (Feb. 2012), pp. 271–281. ISSN: 0946-2171, 1432-0649. DOI: 10.1007/s00340-011-4721-y. URL: http://link.springer.com/10.1007/s00340-011-4721-y.

[107] Giuseppe Marra et al. "Ultrastable laser interferometry for earthquake detection with terrestrial and submarine cables". In: *Science* (June 14, 2018), p. 4458. ISSN: 0036-8075, 1095-9203. DOI: 10.1126/science.

aat4458. URL: http://science.sciencemag.org/content/early/2018/06/13/science.aat4458.

[108] G. Marra et al. "Optical interferometry–based array of seafloor environmental sensors using a transoceanic submarine cable". In: *Science* 376.6595 (May 20, 2022), pp. 874–879. ISSN: 0036-8075, 1095-9203. DOI: 10.1126/science.abo1939. URL: https://www.science.org/doi/10.1126/science.abo1939.

[109] Yoshiyuki Kaneda. "Introduction to ocean floor networks and their scientific application". In: *Marine Geophysical Research* 35.3 (Sept. 2014), pp. 177–180. ISSN: 0025-3235, 1573-0581. DOI: 10.1007/s11001-014-9232-x. URL: http://link.springer.com/10.1007/s11001-014-9232-x.

[110] Olivier Lopez et al. "Simultaneous remote transfer of accurate timing and optical frequency over a public fiber network". In: *Applied Physics B* 110.1 (Jan. 1, 2013), pp. 3–6. ISSN: 0946-2171, 1432-0649. DOI: 10.1007/s00340-012-5241-0. URL: https://link.springer.com/article/10.1007/s00340-012-5241-0.

[111] Jorge C. Castellanos et al. "Optical polarization-based sensing and localization of submarine earthquakes". In: Optical Fiber Communication Conference. San Diego, California: Optica Publishing Group, 2022, M1H.4. ISBN: 978-1-55752-466-9. DOI: 10.1364/OFC.2022.M1H.4. URL: https://opg.optica.org/abstract.cfm?URI=OFC-2022-M1H.4.

[112] María R. Fernández-Ruiz et al. "Distributed acoustic sensing for seismic activity monitoring". In: *APL Photonics* 5.3 (Mar. 1, 2020), p. 030901. ISSN: 2378-0967. DOI: 10.1063/1.5139602. URL: http://aip.scitation.org/doi/10.1063/1.5139602.

[113] A. Sladen et al. "Distributed sensing of earthquakes and ocean-solid Earth interactions on seafloor telecom cables". In: *Nature Communications* 10.1 (Dec. 2019), p. 5777. ISSN: 2041-1723. DOI: 10.1038/s41467-019-13793-z. URL: http://www.nature.com/articles/s41467-019-13793-z.

[114] Peter Bormann and Domenico Giacomo. "The moment magnitude and the energy magnitude : common roots and differences". In: *Journal of Seismology* 15.2 (Dec. 2010). Publisher: Springer Verlag, pp. 411–427. DOI: 10.1007/s10950-010-9219-2. URL: https://hal.archives-ouvertes.fr/hal-00646919.

[115] B. L. N. Kennett and E. R. Engdahl. "Traveltimes for global earthquake location and phase identification". In: *Geophysical Journal International* 105.2 (May 1991), pp. 429–465. ISSN: 0956540X, 1365246X. DOI: 10.1111/j.1365-246X.1991.tb06724.x. URL: https://academic.oup.com/gji/article-lookup/doi/10.1111/j.1365-246X.1991.tb06724.x.

[116] ObsPy. *A Python Framework for Seismology*. Version 1.3.0. URL: https://docs.obspy.org/index.html.

[117] G. Ekström, M. Nettles, and A.M. Dziewoński. "The global CMT project 2004–2010: Centroid-moment tensors for 13,017 earthquakes". In: *Physics of the Earth and Planetary Interiors* 200-201 (June 2012), pp. 1–9. ISSN: 00319201. DOI: 10.1016/j.pepi.2012.04.002. URL: https://linkinghub.elsevier.com/retrieve/pii/S0031920112000696.

[118] Matteo Rossi et al. "Assessment of Distributed Acoustic Sensing (DAS) performance for geotechnical applications". In: *Engineering Geology* 306 (Sept. 2022), p. 106729. ISSN: 00137952. DOI: 10.1016/j.enggeo.2022.106729. URL: https://linkinghub.elsevier.com/retrieve/pii/S0013795222002149.

[119] D.W. Allan. "Statistics of atomic frequency standards". In: *Proceedings of the IEEE* 54.2 (1966), pp. 221–230. ISSN: 0018-9219. DOI: 10.1109/PROC.1966.4634. URL: http://ieeexplore.ieee.org/document/1446564/.

RÉSUMÉ

Les horloges atomiques sont les outils modernes de la mesure du temps. Depuis la redéfinition de la seconde en 1967 fondée sur l'interrogation d'une transition atomique du Césium 133, les horloges atomiques se sont considérablement améliorées. Cela a conduit à de nombreuses avancées technologiques au cours des 55 dernières années, dont beaucoup nécessitent un transfert précis des signaux de temps et de fréquence, un exemple important étant le système de positionnement global (GPS). Avec les récents progrès des horloges atomiques de dernière génération, dites optique, les moyens traditionnels de diffusion des signaux d'horloge(s) ne sont plus adaptés si on n'accepte pas de ne pas dégrader leurs performances. La mise en œuvre d'une nouvelle technologie a été développée à cette fin dans plusieurs pays du monde ces dernières années. Elle utilise les fibres optiques comme support pour transférer et comparer les signaux des références de fréquence atomique.
Dans cette thèse, j'aborderai la mise en œuvre d'un réseau de fibres optiques en France. Je discuterai des processus généraux de bruit de ces liaisons par fibre optique, et de leurs limites techniques et fondamentales. Des études approfondies de plusieurs applications d'un réseau de fibres sont présentées. Celles-ci incluent l'évaluation de la contribution de l'incertitude du réseau français de fibres optiques à la comparaison des horloges optiques. Ensuite, je présenterai une études sur l'utilisation de réseaux de fibres pour la détection de phénomènes géophysiques. Cela inclut la détection de l'effet Sagnac dans un lien à fibre déployé dans une topologie en anneau autour de Paris. Ensuite, je montrerai une étude de la détection des tremblements de terre avec le réseau de fibres français, et je discuterai des perspectives d'utilisation d'une telle technologie.

MOTS CLÉS

Métrologie, fréquence optique, transfert de fréquence optique, réseau fibré, geodétection, REFIMEVE

ABSTRACT

Atomic clocks are the modern tools of timekeeping. Ever since the redefinition of the second in 1967 based on an atomic transition of Cesium 133, the atomic clocks have improved drastically. This has lead to many technological advancements the last 55 years, many of which require precise transfer of time and frequency signals, a prominent example being the Global Positioning System (GPS). With the recent advancements of the last generation of state-of-the-art atomic clocks, so called *o*ptical clocks, traditional means of disseminating their signals without degrading their performance are no longer adequate. The implementation of a new technology for such purposes has in recent years been implemented in several countries around the world, which utilizes optical fibers as a medium to transfer and compare the signals of the atomic frequency references.
In this thesis, I discuss the exploitation of such an optical fiber network in France. I discuss the general noise processes of such fiber links, and their technical and fundamental limits. In-depth studies of several applications of a fiber network is presented. These include the evaluation of the uncertainty contribution of the French fiber network to the comparison of optical clocks. I also show studies of the use of fiber networks for the sensing of effects arising from the Earth. This includes the sensing of the Sagnac effect in a fiber link deployed in a ring topology around Paris, a study of the detection of earthquakes with the French fiber network, and a discussion of the prospects of the use of such a technology.

KEYWORDS

Metrology, optical frequency, optical frequency transfer, fiber network, geosensing, REFIMEVE